



Delft University of Technology

Neutron Depth Profiling Following the Lithium Distribution in Rechargeable Batteries

Verhallen, Tomas

DOI

[10.4233/uuid:debbe50e-27bb-4e57-805f-db30bb8a61bb](https://doi.org/10.4233/uuid:debbe50e-27bb-4e57-805f-db30bb8a61bb)

Publication date

2019

Document Version

Final published version

Citation (APA)

Verhallen, T. (2019). Neutron Depth Profiling: Following the Lithium Distribution in Rechargeable Batteries. <https://doi.org/10.4233/uuid:debbe50e-27bb-4e57-805f-db30bb8a61bb>

Important note

To cite this publication, please use the final published version (if applicable). Please check the document version above.

Copyright

Other than for strictly personal use, it is not permitted to download, forward or distribute the text or part of it, without the consent of the author(s) and/or copyright holder(s), unless the work is under an open content license such as Creative Commons.

Takedown policy

Please contact us and provide details if you believe this document breaches copyrights. We will remove access to the work immediately and investigate your claim.

This dissertation has been approved by the promotors.

Composition of the doctoral committee:

Rector Magnificus,	Delft University of Technology,	chairman
Prof. dr.ir. M. Wagemaker,	Delft University of Technology,	promotor
Prof. dr. E. H. Brück,	Delft University of Technology,	promotor

.....

Independent members:

Prof. dr. K. Edström,	Uppsala Universitet,	Sweden
Dr. C. Villevieille,		France
Prof. dr.ir. H van der Graaf,	Delft University of Technology,	
Prof. dr. F. M. Mulder,	Delft University of Technology,	
Dr. L. van Eijck,	Delft University of Technology,	

.....



REACTOR
INSTITUTE
DELFT



.....

Keywords;	Lithium; Neutron Depth Profiling; Batteries; Operando techniques;
Printed by;	GVO print
Cover design by;	Tomas Willem Verhallen
ISBN:	978-94-6332-520-2

Copyright © 2019 Tomas Willem Verhallen, unless otherwise indicated.

Neutron Depth Profiling; Following the Lithium Distribution in Rechargeable Batteries

Dissertation

for the purpose of obtaining the degree of doctor at Delft University of Technology
by the authority of the Rector Magnificus, Prof.dr.ir. T.H.J.J. van der Hagen, chair of
the Board for Doctorates to be defended publicly on

Wednesday, 10 July, 2019

at

12.30

by Tomas Willem VERHALLEN, Master of Science in Materials Science and
Engineering, Technical University Delft, the Netherlands,
born in Tiel, the Netherlands

Table of Contents

0. Summary	9
0. Samenvatting	13
1. Introduction	19
1.1 Batteries	20
1.1.1 Intercalation materials	27
1.1.2 Lithium metal anodes	30
1.1.3 Sulfur	32
1.2 Neutrons and batteries	34
1.3 References	37
2. Methods	45
2.1 Neutron Depth Profiling	45
2.1.1 Relating particle energy to depth.	50
2.1.2 Set-up geometry and intensity calibration	54
2.1.3 Energy straggling and other sources of error	58
2.1.4 Activation and noise	60
2.1.5 Pile up	61
2.1.6 Inverse algorithms	61
2.2 Experiment design	64
2.2.1 Ex-situ experiments	64
2.2.2 In-situ experiments	67
2.2.3 Operando experiments	69
2.3 Battery preparation	75
2.4 Conclusions	78
2.5 References	79
3. Exploring the Limits of Performance of High Rate Intercalation Materials	89
3.1 Introduction	89
3.2 Results and discussion	94
3.3 Consequences for application	105
3.4 Conclusions	109
3.5 Methods	111

3.5.1 Electrode preparation	111
3.5.2 Three phase 3D imaging	111
3.6 References	112
4. The Lightest Anode, Lithium Metal Electrochemically Plated on Copper	119
4.1 Introduction	119
4.2 Results	122
4.2.1 Synergy with optical methods	124
4.2.2 Salt concentration	126
4.2.3 Impact of current density	127
4.2.4 Evolution of the total amount of lithium during cycling	128
4.3 Morphology	132
4.4 Conclusion	136
4.5 Methods	137
4.6 References	137
5. Li-Sulfur Batteries, Dissolution and Performance	145
5.1 Introduction	145
5.2 Results and discussion	148
5.3 Conclusions	158
5.4 Methods	159
5.5 References	161
6. Next Generation NDP for Lithium Ion Batteries	167
6.1 Towards 3D NP	167
6.1.1 Preliminary results	170
6.1.1.1 Muons	171
6.1.1.2 Lithium	173
6.1.1.3 Boron	175
6.1.2 Discussion	179
6.2 Alternative routes to vacuum free NDP	180
6.3 Conclusions	185
6.4 References	185

Appendices & Other

A. Activation of elements of possible interest in battery research	193
B. Isotopes for NDP	195
C. Data Handling	196
C.1. Data import	196
C.2. TRIM/SRIM Manual	197
C.3. The mainline script.	202
D. Supporting Information to Chapter 3	204
E. Deactivation of the Matroesjka	208
F. Selected SLDs	209
References	210
Dankwoord	211
Acknowledgements	213
Publications	215
Curriculum Vitae	216



0. Summary

The sustainable energy transition relies on energy storage technology, both for stabilization of the electricity grid and to power personal vehicles. The successful exploitation of the light element lithium has led to batteries with unprecedented power to weight ratios. Nonetheless, several key challenges still inhibit further market penetration. Crucial to solving these challenges is profound understanding of the governing processes. Yet, due to the inherent difficulty to study light ions with conventional techniques, limited methodology is available that operando monitoring of lithium ion batteries. A non-invasive and versatile alternative is Neutron Depth Profiling. This technique provides information on the spatial and temporal lithium concentration during (dis)charge, highly complementary to microscopy and diffraction. The principle is based on the unique fingerprint of the ^6Li -lithium neutron capture reaction, producing energetic light ions that can be recorded by an energy sensitive detector outside the battery cell during operation. In this work NDP is used to shed new light on the key challenges in rechargeable lithium ion batteries.

An urgent challenge is to shorten charging times, which would increase the acceptance of the electric vehicle. The charge rates are limited by the internal resistance, lowering of which reduces heat production and thereby improving battery safety and cycle life. The internal battery resistance is a resulting property of the complex heterogeneous microstructure existing of active material, conductive additive and electrolyte which provides the required electronic and ion transport. Li-ion concentration profiles obtained ex situ with NDP allow recognizing which charge transport step is limiting when the voltage cut-off is reached, e.g. electron conduction, ion migration or solid state processes inside the active material. In the combination with FIB-SEM, which allows resolving the three phase 3D morphology, two types of electrodes were compared. In standard electrode the pores are of nanometer size. Here, attained through carbonate dissolution templating, the pores were hierarchical structured, i.e. micron sized 'ionic highways' with nanometer branches. Even though the porous network is vastly different, bulk values are equal, i.e. electrode thickness, active material and



carbon/binder volume fraction. This provides detailed understanding of the impact of key parameters such as the tortuosity for electron and Li-ion transport through the electrodes. The hierarchical pore network of the templated electrodes, containing micron sized pores, is shown to be more effective at high rate charge where the increase in electrolyte salt concentration increases viscosity. On the contrary, during discharge, the performance difference is smaller; this is attributed to the lack of lithium ions limiting the discharge rates in both cases. Surprisingly the carbonate templating method results in a better electronic conductivity of the CB network, enhancing the activity of LiFePO_4 near the electrolyte-electrode interface which in a large part is responsible for the improved rate performance both during charge and discharge. These changes are directly observed in NDP, demonstrating that standard electrodes provide a far from optimal charge transport network. Hence engineering the microstructure should unlock further performance improvements.

A crucial bottleneck in the development of post lithium ion battery technology is the reversible lithium-metal anode, as this would allow the use of high energy density cathodes based on the conversion reaction of lithium with oxygen or sulfur. Furthermore, a lithium metal anode can double pack level energy density when employing state of the art cathodes. Hence stabilizing metal anodes is considered an important stepping stone, however this goal is challenged by short circuits caused by dendrites and a short cycle life due to the reactivity with electrolytes. Strategies to form a dense, dendrite-free lithium metal layer are often rationalized using the Sand equation. This equation states that dendrite formation is initiated by electrolyte salt depletion due to the applied current, progressively stimulating structures protruding into the more salt rich regions of electrolyte. Hence a common approach is to increase electrolyte salt concentration or to lower the current density. With NDP we confirm that indeed increasing the salt concentration leads to denser lithium metal layers, however, when the current density is decreased, the plated lithium density also decreases. This phenomenon is rationalized by a denser nucleation induced by the larger overpotentials and faster cycling reduces SEI

Summary

thickening. Hence the concentration profile is shown to depend on the current density, electrolyte composition and cycling history, thereby providing insights in the dynamics of lithium metal anodes.

Lithium sulfur batteries are commercially interesting candidates to supersede the current Li ion technology, due to their high capacity and low material costs. Yet at present the use of Li-S batteries is limited due to their rapid capacity decay leading to a short cycle life. These problems originate from lithium polysulfide dissolution in the liquid electrolyte, the subsequent migration of which instigates loss of active material. Improvements rely on the stabilization of lithium anodes by electrolyte additives and chemisorption of polysulfides by metal oxide additives or physical confinement of polysulfide by hierarchically designed electrodes. NDP is used to probe Li concentration in three types of Li-S battery electrodes, evidence is presented for the migration, adsorption and confinement of polysulfides shifting the Li concentration across the cells, in relation to Li-S battery capacity and cyclability. These findings rationalize electrode design towards high energy-dense, safe and low-cost Li-S batteries.

The results demonstrated are obtained in a general purpose set up. However, this set-up relies on operating conditions which adversely affect battery performance, in turn compromising measurement validity. Since the demand for NDP measurements on battery systems is increasing, the development of specific set-ups is reasonable. Here new concepts are presented, especially focused at measuring at ambient pressure, thereby facilitating operando measurements. We conclude with a revolutionary concept based on a gas filled gridpix time projection chamber. A gridpix detector allows a 3D particle trace reconstruction. Hence a 3D spatial isotope specific, lithium-6, distribution is obtained. Using state of the art chips, this can be performed at high rates that allow following this distribution during (dis) charge. This method will allow a whole new range of topics to be studied especially concerning high capacity electrodes and solid electrolytes as their high lithium content increases the signal and allows faster measurements and higher resolution.



0. Samenvatting

De overgang naar hernieuwbare energie vereist efficiënte opslag van elektrische energie, voor de stabilisatie van het netwerk evenals voor het aandrijven van persoonlijk vervoer. The succesvolle exploitatie van het lichte element lithium heeft geleid tot batterijen met een ongeëvenaarde energie dichtheid. Desalniettemin zijn er een aantal sleutel uitdagingen die verdere markt penetratie verhinderen. Cruciaal bij het oplossen van deze uitdagingen is het begrijpen van de onderliggende processen. Echter, door de intrinsieke moeilijkheid van het bestuderen van lichte ionen met conventionele technieken, zijn er maar beperkt methodes beschikbaar die het toestaan om deze processen te meten in werkende batterijen. Een niet invasief en veelzijdig alternatief is Neutronen Diepte Profilering. Deze techniek levert de tijd en plaats afhankelijke concentratie van lithium (ionen en atomen) gedurende het laden en ontladen van de batterij. Deze informatie is zeer complementair aan traditionele technieken zoals Röntgen diffractie en elektronen microscopie. Het principe is gebaseerd op de unieke vingerafdruk van het ^6Li neutron invang reactie, deze produceert energieke, lichte ionen die gemeten kunnen worden buiten de batterij. In deze dissertatie is NDP gebruikt om nieuw licht te werpen op bestaande en toekomstige uitdagingen in de opslag van energie in lithium ion batterijen.

Op de korte termijn moeten de laadtijden van lithium ion batterijen drastisch ingekort worden, dit om de acceptatie van elektrisch vervoer mogelijk te maken. De laadsnelheden worden beperkt door de inwendige weerstand. Omdat deze leidt tot warmte productie en daarmee de veiligheid van de batterij en de levensduur van de batterij in gevaar brengt. De interne batterijweerstand is een resulterende eigenschap van de complexe heterogene microstructuur die elektronen en ionen transport mogelijk maakt, bestaande uit actief materiaal, geleidend additief en de porositeit. Lithium-ion concentratieprofielen verkregen met ex situ NDP maken het mogelijk te herkennen welke ladingtransportstap beperkend is wanneer de spanningslimiet wordt bereikt, d.w.z. elektronengeleiding, ion migratie of vaste stof processen binnen het actieve materiaal. In de combinatie met FIB-SEM, waarmee de driefasige morfologie in (3D) beeld kan worden gebracht,



werden twee typen elektroden vergeleken. Dit leverde een gedetailleerd onderzoek op naar hiërarchisch gestructureerde poriën versus homogene poriën, d.w.z. poriën van enkele micron tot nanometer afmetingen versus alleen poriën van enkele nanometer. De hiërarchische structuur wordt bereikt door middel van een sjabloon uit oplosbaar natrium carbonaat. Hoewel het poreuze netwerk enorm verschillend is, zijn de bulkwaarden gelijk, d.w.z. de elektrodedikte, het actieve materiaal en de volumefracties van koolstof en bindmiddel. Dit biedt een gedetailleerd inzicht in de impact van belangrijke parameters zoals de tortuositeit voor elektronen en lithium ionen in de poreuze elektroden.

Het hiërarchische porienetwerk van de sjabloon-elektroden, dat poriën van micron-grootte bevat, is voornamelijk effectief gebleken bij met hoge stroom opladen, wanneer, door de toename in de zoutconcentratie, de viscositeit van het elektrolyt wordt verhoogd. Integendeel, tijdens de ontlading van de batterij wordt de stroomdichtheid in beide gevallen belemmerd door de beperkte beschikbaarheid van lithium ionen en is het verschil in prestatie kleiner. Verrassenderwijs resulteert de werkwijze op basis van natrium carbonaat ook in een verbetering van de elektronische geleidbaarheid van het koolstof netwerk. Hierdoor wordt de activiteit van LiFePO_4 nabij het elektrode- elektrolyt interface verbeterd, hetgeen voor een deel verantwoordelijk is voor de verbeterde prestaties zowel tijdens het laden alsmede het ontladen van de batterij. Deze veranderingen worden direct waargenomen in NDP, wat aantoont dat in standaard elektroden het ladingtransportnetwerk verre van optimaal is. Vandaar dat verwacht wordt dat in de microstructuur nog verdere prestatieverbeteringen vergrendeld liggen.

Een sprong voorwaarts in de ontwikkeling van lithium ion batterijen zou een stabiele lithium-metaalanode zijn. Hierdoor kunnen kathodes met hogere energie dichtheid, op basis van de conversiereactie van lithium met zuurstof of zwavel, worden gebruikt. Daarnaast verdubbelt een lithiummetaalanode de energiedichtheid op cel niveau bij gebruik van standaard kathode materialen. Vandaar dat het stabiliseren van metaalanodes wordt beschouwd als een belangrijke opstap naar hogere energie dichtheid. Dit doel wordt

echter uitgedaagd door kortsluitingen vanwege dendrietvorming en de korte batterij levensduur veroorzaakt door de reactiviteit met elektrolyten. Strategieën om een dichte en dendrietvrije lithium metaal laag te vormen, worden vaak gerationaliseerd met behulp van de vergelijking van Sand. Deze vergelijking stelt dat dendrietvorming wordt geïnitieerd door elektrolytzoutdepletie vanwege de aangebrachte stroom, met een stimulerend effect op structuren die uitsteken in de meer zoutrijke gebieden van elektrolyt. Vandaar dat het een populaire benadering is om de elektrolytzoutconcentratie te verhogen of om de stroomdichtheid te verlagen. Met NDP bevestigen we dat inderdaad een verhoging van de zoutconcentratie leidt tot dichtere lithiummetaallagen, maar wanneer de stroomdichtheid wordt verlaagd, neemt ook de geplateerde lithiumdichtheid af. Dit fenomeen wordt gerationaliseerd door een meer compacte nucleatie die wordt veroorzaakt door de grotere overpotentialen die nodig zijn om hogere stroom mogelijk te maken. Dit beperkt de ruimte die beschikbaar is voor decompositie lagen. Daarmee is aangetoond dat het lithium concentratieprofiel van elektrochemisch gevormde laag afhangt van de stroomdichtheid, elektrolytsamenstelling en de voorgaande cyclussen, wat nieuwe inzichten oplevert voor verbeterde lithiummetaalanodes.

Lithiumzwavelaccu's zijn, vanwege de lage materiaal kosten en de hoge capaciteit, een commercieel interessant alternatief voor de huidige Li-ion-technologie. Echter is het op dit moment onmogelijk om rendabele Li-S-batterijen te introduceren vanwege hun snelle capaciteitsverval en korte levensduur. Deze problemen zijn het gevolg van de hoge oplosbaarheid van het lithium meervoudig zwavel, waarvan de migratie tot verlies van actief materiaal leidt. Verbeteringen berusten op de stabilisatie van lithiumanodes door elektrolyttoevoegingen en de chemisorptie van meervoudig zwavel aan metaaloxide toevoegingen of door fysische opsluiting van het zwavel door hiërarchisch ontworpen elektroden. Door NDP te gebruiken om de Li-concentratie in drie soorten Li-S-batterijelektroden te meten, wordt overtuigend bewijs gepresenteerd voor de migratie, adsorptie en opsluiting van polysulfiden die de Li-concentratie door de cellen verschuiven, in relatie tot Li-S-batterijcapaciteit en levensduur. Deze bevindingen rationaliseren het



ontwerp van elektroden naar hoog energierijke, veilige en goedkope Li-S-batterijen.

De getoonde resultaten worden verkregen in een algemene opstelling. Deze opstelling beïnvloedt de batterijprestaties negatief, hierdoor is de meetvaliditeit in gevaar. Omdat de vraag naar NDP-metingen aan batterijsystemen toeneemt, is het belangrijk specifieke opstellingen te ontwerpen die betrouwbare batterijprestaties garanderen. In dit werk worden nieuwe concepten gepresenteerd, voornamelijk gericht op het meten bij natuurlijke druk, waardoor operandi-metingen worden vergemakkelijkt. Bovendien wordt een revolutionair concept gepresenteerd dat gebaseerd is op een gas gevulde tijd projectiekamer met pixelchip detector, 'gridpix'. Een gridpix-detector maakt de 3D reconstructie van een triton pad mogelijk. Hierdoor kan de 3D isotoop specifieke concentratie in kaart worden gebracht. Met behulp van de nieuwste chips kan dit sneller worden uitgevoerd dan de (ont)laadsnelheid van een batterij. Met deze methode kan een hele reeks nieuwe onderwerpen worden bestudeerd, vooral met betrekking tot elektroden met een hoge capaciteit en vaste elektrolyten, omdat hun lithiumgehalte snellere metingen en een hogere resolutie mogelijk maakt.

1.

Introduction

1. Introduction

Our economy has prospered on liquid and gaseous hydrocarbon resources, which are straightforwardly transported and stored, allowing to be converted to energy where or whenever needed[4]. As a consequence these fossil fuels are used extensively to power transportation and produce electricity. The realization that fossil fuels are limited and produce harmful exhausts has ignited a drive to implement sustainable power sources such as wind turbines, solar panels, biomass reactors and hydroelectricity. Owing to government subsidies and industrial scaling, these resources are now cost effective and competitive with traditional electricity production[4-6]. However a complete transition towards sustainable supply is hindered by our ability to store energy as, contrary to traditional power generation, output from most renewable sources is inherently intermittent and uncontrollable[7-9]. Already viable products are reaching the consumer market. However to sustain this growth safety and reliability are of the utmost concern, while restricting to abundant and environmentally benign materials[11, 12].

On route to a complete transition three energy storage use cases can be recognized. Daily and seasonal fluctuations in energy production yield the first categories; long and short term stationary storage. For long term storage applications the design should optimize towards price, safety and scalability, leading to solutions such as pumping water back behind dams, termed pumped hydroelectricity[13], or producing energetic molecules such as hydrogen[14].

On a seasonal cycle the low cycle efficiency of these methods is acceptable, however, when energy is retrieved and stored daily, a higher efficiency is desired. Due to low entropy change, these efficiencies are straightforwardly attained by storing electrochemical energy in a battery[15].

For stationary applications weight is not an important design consideration, hence lithium ion batteries might not be the sole solution for this application. In electric vehicles, on the other hand, specific energy, per unit weight, is important factors as the added weight increases the energy demand,

furthermore space is limited[15, 16]. Common goals are safety and reliability while refraining from materials that are toxic or rare[17]. All battery architectures treated in the following chapters are envisioned to fit a niche within these last two categories.

1.1 Batteries

In a battery an electrochemical reaction is used to store electrical energy. The electrochemical process is sustained by three components, two electrodes, anode and cathode, separated by an electrolyte and separator, see **Figure 1.1**[10]. An electrolyte is usually a liquid, in which a salt is dissolved to allow ion conduction[18]. Both electrodes commonly consist of a mixture of active material, a binder and a conductive additive (carbon black) bonded to a metal foil. At both electrodes a part of the electrochemical reaction take place, termed half reactions. In one reaction an electron and ion is produced (oxidation) and in the other reaction electron and ion (or other positive charge) are consumed (reduction). The net balance of charges is zero. One reaction, however, is thermodynamically favored over the other. Thus in one direction energy is released from the system while in the opposite energy is stored. The balance of charges must be maintained, the reaction always involves a transfer of both the electron and the ion. Only ions can diffuse through the electrolyte, as it is not conductive for electrons and hence the electron must go via the metal foil, or current collector, through the external circuit. When the battery is charged, ions and electrons follow the blue arrows due to an electric potential applied externally. When a load is attached the battery is discharged, ion and electrons follow the red arrows in **Figure 1.1**. The energy stored is then released to the load via the electrons.

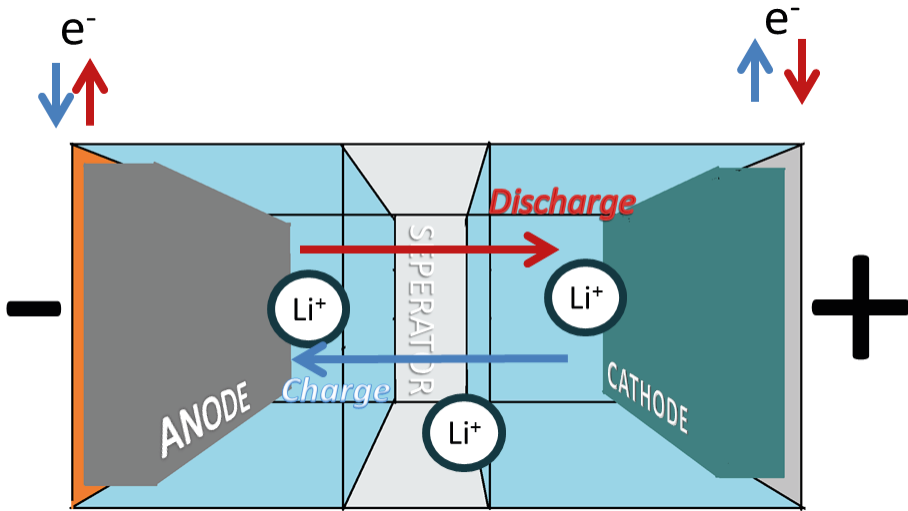
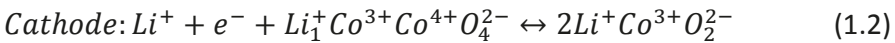


Figure 1.1 Schematic of a lithium ion battery in operation. Current collectors are far right and left, orange is copper foil and on the aluminum on the cathode side is indicated grey.

Among the first commercially exploited lithium ion batteries is a system based on a graphite anode vs a lithium cobalt oxide cathode[19]. Contrary to non-rechargeable lithium cells there are no metal electrodes, thus lithium is always present as an ion[19]. The lithium ion moves between the graphite atomic planes in the anode to the transition metal oxide layers in the cathode. This process is called intercalation or insertion, when lithium ions enter the material. The electrode active material provides a stable surrounding scaffold through which the lithium ion migrates[20]. The half reactions at the graphite anode and the LiCoO_2 cathode are;



Intercalation in graphite occurs around 0.2V[21] and in cobalt oxide at 4V[10] versus metallic lithium, yielding a 3.8 potential difference. To store energy the lithium ion is de-inserted from the oxide and moved to the graphite anode due to the potential applied on the electron. In the reverse reaction electrons are yielded at this potential. The voltages given are averages, they

depend on the chemical surrounding of the ion. The chemical potential is defined as the change in Gibbs free energy (G) with respect to the change in concentration of a species (n_i). Of course keeping all other contributions to the free energy constant, such as the concentrations of all other species (n_j) and the temperature (T) and pressure (p)[22];

$$\mu_i = \frac{\partial G}{\partial n_i} \Big|_{T,p,n_j=c} \quad (1.3)$$

The Gibbs free energy describes the total energy of a system. Constant temperature (T) and pressure (p) are realistic assumptions when considering normal battery operation condition. Hence for a battery the change in free energy is equal to the change in chemical potential of an ion moving from anode to cathode. If we consider a reversible process with negligible internal resistance we find[22];

$$z_i F (\phi_A - \phi_C) = \mu_A - \mu_C \quad (1.4)$$

F is Faraday's constant reflecting the electric charge associated with a mole of charges (electrons), z is the charge per ion and ϕ reflects the electron chemical potential, i.e. the voltage difference between anode and cathode. This voltage reflects the potential energy per electron. The number of electrons, or ions, stored per unit weight is given by;

$$C_{th} = \frac{1}{3.6} \frac{nF}{M_w} \quad (1.5)$$

Where n reflects the number of electrons involved in the reaction, F, Faradays' constant and M_w the molar weight of the surrounding atoms[23]. Multiplying the outcome of **equations 5** and **6** yields the energy density, the amount of electric energy stored per unit weight. For most applications energy density is the key performance indicator. Now we recognize two ways to improve this number; first is increasing the potential difference between anode and cathode and second is increasing the number of charges stored, i.e. the capacity.

Both properties are physically limited, on the anode side the chemical potential window is limited by the potential of the pure material, as the ions

Introduction

would form a coating if there is no thermodynamically favorable reaction. Lithium has the lowest electrode potential of all metals[24], resulting in the highest voltage difference between anode and cathode. On the cathode side, materials prone to accept electrons should be used, a property known as electronegativity. Here there are more options as even though electronegativity increases from left to right, with fluorine is the most electronegative element, metals increase in electron negativity when they are oxidized, see **Figure 1.2**[25].

Furthermore the amount of charge per unit volume or weight can be increased, by using small and light ions these are found top left, see **Figure 1.2**. Lithium is the lightest element solid at room temperature[26]. Altogether lithium makes an obvious choice to use as a charge carrier in a battery[27]. For both the anode and cathode, it is desired to use light materials that are sufficiently available and environmentally benign. The elements that fit these criteria are marked green.

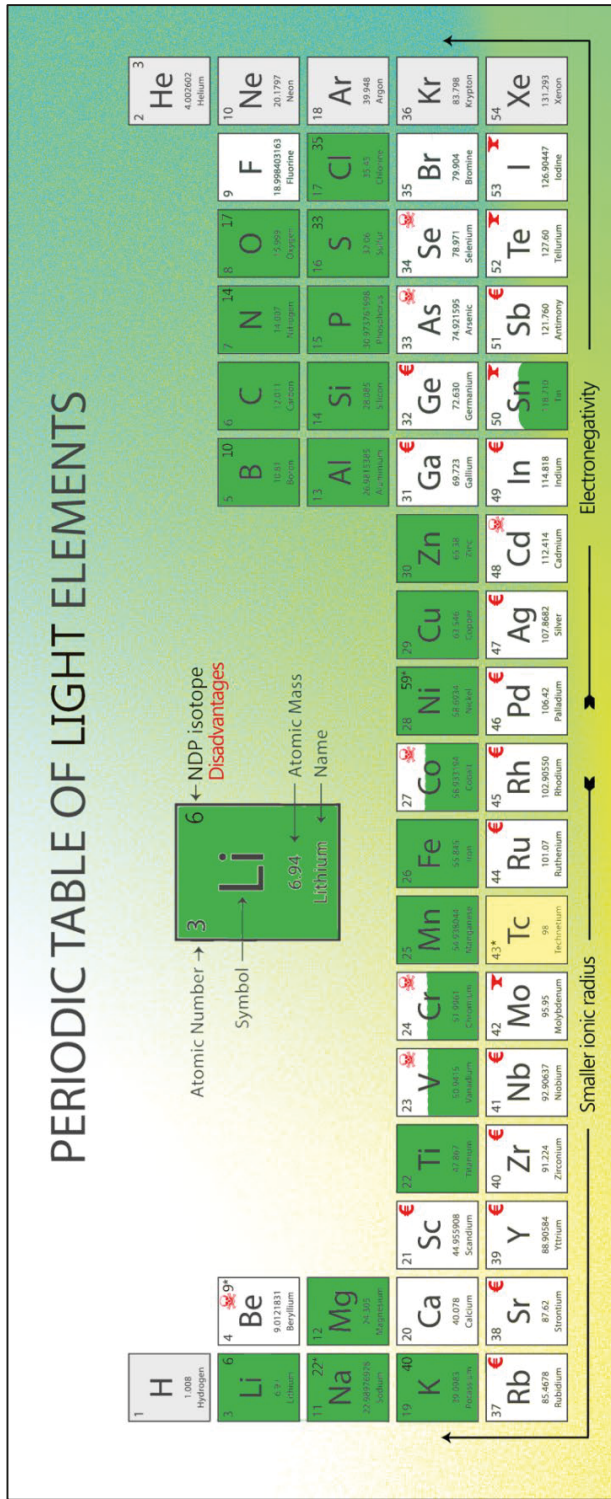


Figure 1.2 Infographic of desirable battery elements, in green. Materials are considered expensive when they are less abundant than Lithium[1] and/or currently not economically exploited. The whole fifth row is considered too heavy and rare to be used in competitive battery systems. Tin is the sole exception, which is actively researched as anode material due to its' high capacity through alloying with Li[2, 3]. Elements with carcinogenic or toxic oxidation states should be avoided, as these batteries are to be employed on a large scale and proper waste disposal cannot be ensured. Nevertheless some of these elements are currently used as alternatives are lacking or solely as model systems[10]. Gases are coloured grey and synthesized elements are in yellow.

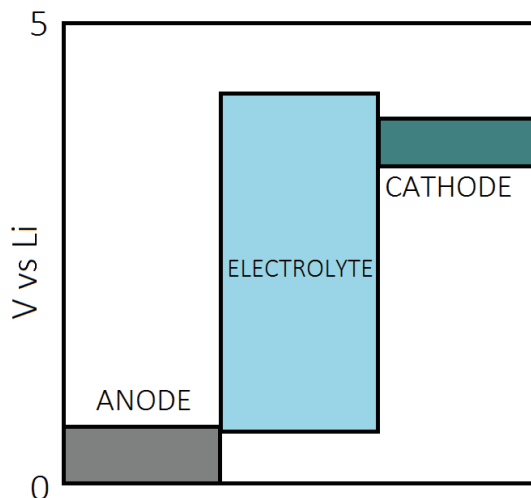


Figure 1.3 Schematic representation of the energy landscape in a typical lithium ion battery. The electrochemical stability window of the electrolyte, within the light blue box, limits the gap between anode (grey box) and cathode potential (green box). Nonetheless current commercial systems often exceed this limit on the anode side[28].

Multiple rechargeable lithium battery architectures are now intensively studied, the bulk of which are based on a liquid electrolyte. Liquids can completely wet the porous electrodes, thereby providing a bespoke electrode-electrolyte interface[15]. The solvent and salt are exposed to potential difference applied to the battery. Hence when this potential exceeds the stability window of the electrolyte components, they will accept or donate electrons instead of the electrode active materials[29]. For instance plain water splits around 1.2V[9, 14], therefore a high potential difference is typically attained through the use of electrochemically stable, but flammable, carbon based solvents and fluorinated salts[18, 29]. These combinations have allowed safe operation of voltage differences up until 3.5-4.1 V, between 0.3-0.8 and 4.3 V vs Li, as illustrates in **Figure 1.3**[10]. Note, that these numbers are highly system dependent, given by the catalytic activity of the electrode active materials[21].

However few commercial anode materials operate within this voltage limits owing to the high capacity, low price and voltage of graphite[21]. Hence decomposition occurs when the cell potential exceeds the limits of the electrolyte stability range at the end of charge[30]. This decomposition of the solvent and/or the salt is accompanied by the formation of a protective interface, termed solid electrolyte interphase (SEI). Much like the native oxide on an aluminum surface due to its' negligible electronic conduction should protect the electrolyte from further decomposition[21]. Furthermore, to allow battery operation the SEI layer should be penetrable for ions[12, 31, 32].

Currently scientific and commercial interests are shifting towards solid electrolytes, thereby aiming to avoid the flammability, toxicity and leaking potential of liquid electrolytes[33]. These electrolytes promise to be a safer alternative, deemed necessary in applications such as personal transportation which require sizeable batteries that will be used on a large scale. Currently polymer and inorganic solid electrolyte are studied, both systems show problems related to poor interface contact, this can be solved by applying pressure to the cell stack[34].

This work intends to focus on open questions in the lithium battery field around Li-ion transport in the electrode of different battery systems. The study of lithium ions in batteries is challenged due to the lack of electrons, restraining the possibilities offered by traditional techniques which are particularly sensitive to electrons[35]. Here, an alternative tool will be presented and further developed known as Neutron Depth Profiling. In the next chapters we will see how this technique can provide a unique view into the efficiency of charge transport in battery electrodes.

First an introduction to the field of these battery systems is given to provide the necessary framework to appreciate the results presented in the later sections. Starting with the work horse of today's electronic devices, battery systems based on intercalation materials, employing a graphite anode and a transition metal (Co, Ni, Mn) oxide or iron phosphate cathode are threatened. Next we look at the so-called beyond Li-ion systems. These batteries rely on a

conversion reaction between a light non-metal (i.e. O or S) and a lithium ion, hence their specific capacity is up to an order of magnitude higher[36, 37]. These cathodes would require a lithium metal anode or pre lithiated high capacity anode, to provide a lithium source[38, 39]. Even though increasing cycle numbers are reported[30], commercialization of these systems has proven difficult. This thesis will use neutron depth profiling to address the problems encountered and demonstrate possible routes of improvement for all these systems, intercalation cathodes, lithium metal anodes and sulfur cathodes.

1.1.1 Intercalation materials

The introduction of lithium cobalt oxide marked an important step in lithium ion battery research, it was the first intercalation oxide that was commercialized in secondary, or rechargeable, batteries[40]. Ever since it has been a race to find the next big leap in energy density. Research intensified with the hope of finding higher energy density, higher average voltage, improved rate capability and reduce the use of cobalt, as cobalt is toxic and relatively scarce[20]. Over the past forty years this has led to numerous cathode materials. These materials are traditionally classified based on their crystal structure leading to three categories; spinel, layered and olivine type structure, listed in the **Table 1.1**[28]. Voltages given are versus metallic Li. To find cell level energy densities the voltage difference between anode and cathode should be used. Moreover the weight of the inactive components, i.e. current collector, electrolyte and separator needs to be accounted for.

Table 1.1 Intercalation material classes

Structure	Li diffusion	Typical Material	Voltage[V]	Capacity[mAh/g]
Spinel	3D	LiNi _{0.5} Mn _{1.5} O ₄ [41]	4.6	175
		Li ₄ Ti ₅ O ₁₂ [42]	1.55	175
Layered	2D	LiCoO ₂ [40]	4.1	160
Olivine	1D	LiFePO ₄ [43]	3.4	175

The different structures lead to different (de)intercalation mechanisms. The positive lithium ions influence each other and their surroundings. This leads to changes the interatomic distances, sometimes promoting the separation into lithium rich and poor phases[34]. This behavior influences the voltage as the battery is (dis)charged, as shown at constant current in **Figure 1.4a**.

The spinel and olivine material classes, such LiFePO_4 , $\text{Li}_4\text{Ti}_5\text{O}_{12}$ generally transform through a first order phase transition[44, 45]. (De)lithiation is associated with a large amount of strain, deformation of the crystal lattice, which is accommodated by separating into a Li-rich and a Li –poor phase[46, 47]. Every next lithium ion is inserted at this interface hence every ion sees the same chemical environment leading to a characteristic flat voltage plateau. This interface is out of equilibrium and costs energy, leading to an overpotential and thus hysteresis[48]. For instance, in LiFePO_4 decreasing the particle size reduces the amount interface surface whilst shortening solid diffusion lengths, thereby positively influencing the rate capability[44, 49, 50]. This approach has proven to be particularly successful as the lower voltage of LiFePO_4 prevents electrolyte decomposition reduction and permits a higher overpotential hence allowing extremely fast charging[51, 52]. Furthermore other beneficial properties, it is not toxic and cobalt-free, lead to wide market acceptance especially in high rate applications[11].

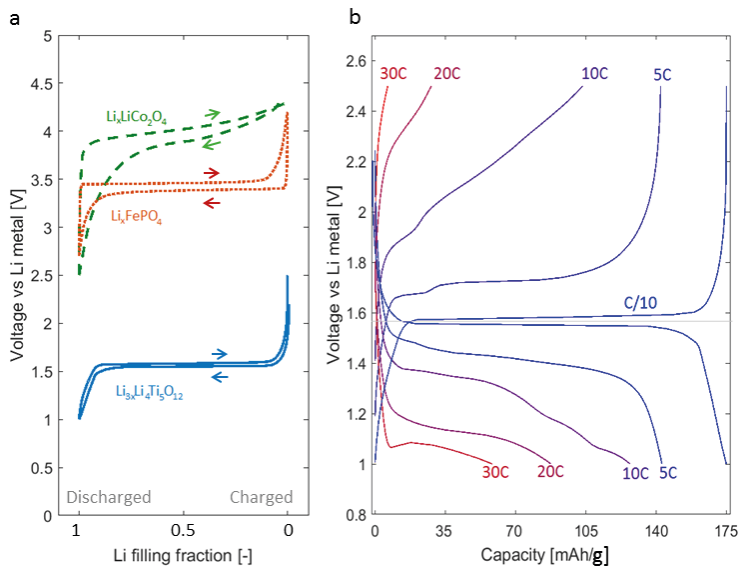


Figure 1.4 a) Charge – discharge curves of intercalation materials addressed in this thesis, as measured vs lithium foil at C/10. Charge is delithiation, thus $\text{LiFePO}_4 \rightarrow \text{FePO}_4$, $\text{Li}_2\text{Co}_2\text{O}_4 \rightarrow \text{LiCo}_2\text{O}_4$ and $\text{Li}_7\text{Ti}_5\text{O}_{12} \rightarrow \text{Li}_4\text{Ti}_5\text{O}_{12}$. **b)** Charge – discharge curves of $\text{Li}_4\text{Ti}_5\text{O}_{12}$ at higher currents.

Introduction

A notable exception in the spinel material class is lithium titanate, $\text{Li}_4\text{Ti}_5\text{O}_{12}$, where both phases have the same lattice parameter, hence there is no strain or stress associated with the phase transition. Consequently intercalation rates are high owing to a mobile interface and hysteresis is low. However, the equilibrium voltage of $\text{Li}_4\text{Ti}_5\text{O}_{12}$ is commonly considered inconvenient for practical applications as it is too high for an anode material and too low for a cathode. The high voltage spinel $\text{LiNi}_{0.5}\text{Mn}_{1.5}\text{O}_4$ on the contrary has a too high voltage, even though this allows high energy density, C-rates should be kept low as small overpotential triggers electrolyte decomposition[53]. Attempts are made to reduce materials surface reactivity and increase the electrolyte stability region[54-56].

In order to reduce strain on cobalt resources associated with the use of lithium cobalt oxide, the isostructural NMC or NCA cathodes were developed. In these layered oxides a large part of the cobalt has been replaced by a combination of manganese and nickel or nickel and aluminum[57]. In addition the equilibrium voltage is lowered due to the activation of $\text{Mn}^{3+}/\text{Mn}^{4+}$ and $\text{Ni}^{3+}/\text{Ni}^{4+}$ redox couples, which means a higher capacity is reached at 4.3 V. However as more lithium is extracted the more the oxygen ions start to repel one another, making these materials prone to oxygen evolution at the end of charge[34, 58]. To counteract these effects more lithium is introduced into the structure. These 'layered-layered', 'manganese rich' or 'lithium rich' material class, can be viewed as a spinel- layered hybrid, offering lithium ions the possibility to diffuse in three dimensions through the crystal[59], while simultaneously aiming to stabilize the anion layers.

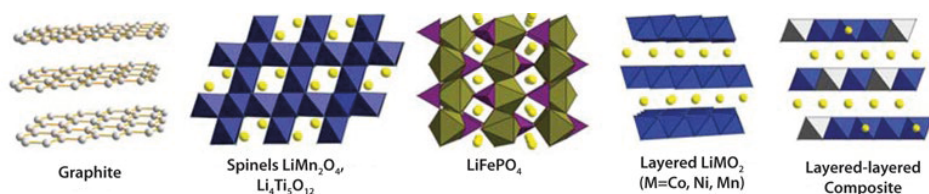


Figure 1.5. Intercalation materials available via Sigma Aldrich, a chemical supplier for research institutes[60], original **Figure** is published under a creative common license.

Although these are interesting developments, in this work we focus on the high rate intercalation materials, being LiFePO_4 and $\text{Li}_4\text{Ti}_5\text{O}_{12}$ [61]. Open questions are remaining around the relation between electrode morphology and the dominant charge transfer resistance. Here we will deepen the understanding of the processes that lead to higher power and energy density. As we will see neutrons can provide an ideal tool for this.

1.1.2 Lithium metal anodes

Graphite anodes have been meeting the required demands for the past 40 years now and even though the carbon is light and cheap, still 6 atoms are necessary to store 1 Li ion. The idea of using lithium metal as anode in a liquid electrolyte is tempting, for its' low potential and the immediate reduction of weight, however, has been abandoned multiple times[62, 63]. Uniform electrochemical plating of metallic lithium in organic electrolytes has proved to be challenging[64]. Small protrusion or in-homogeneities on the substrate instigate non uniform plating. Once this mossy lithium is formed, shown in **Figure 1.6a**, region 2, the chain of events continues in detrimental fashion. The inhomogeneous current distribution leads to concentration differences promoting the initiation and growth of structures protruding into the unaffected, relatively lithium rich electrolyte zones. These protruding structures are referred to as dendrites. They compromise battery operation as their large surface area consumes excessive amounts of electrolyte for SEI formation and, given enough time, they protrude the separator leading to short circuit[65-67]. The Sand equation is used to describe the time until the electrolyte salt is depleted, which can be related to the onset of dendritic growth, shown **Figure 1.6a**, region 1, and in the scheme **Figure 1.6c**[68].

$$t_{sand} = \pi D \left(\frac{z_i c_0 F}{2J t_a} \right)^2 \quad (1.6)$$

In this equation the sand time is related to the diffusion constant (D) of lithium ions multiplied, by the initial electrolyte concentration (c_0), Faradays constant (F) and the ion charge (z_i) which is divided by the current density (J) and the transference number (t_a). The transference number relates the mobility of the anion and cation in the electrolyte. This equation has been used to justify engineering approaches, such as more concentrated

electrolytes (increasing c_0) and metallic scaffolds to lower the current density[69, 70].

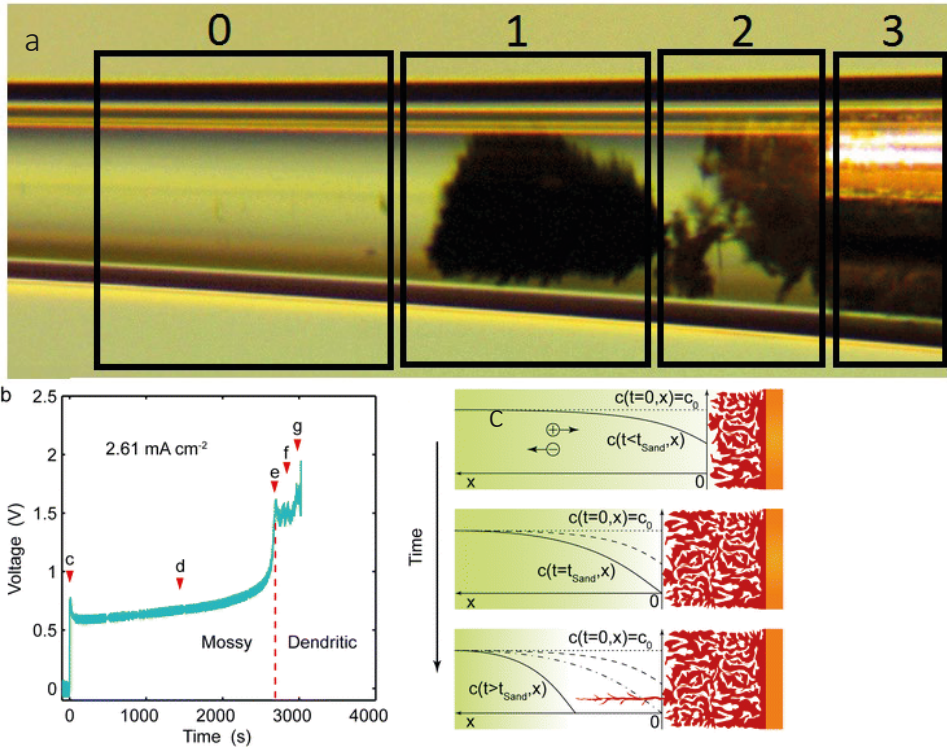


Figure 1.6 a) lithium plated in 1M LiFSI-DME electrolyte, in cell adapted to allow optical analysis of the layer grown. Region 3 is the original lithium electrode, region 2 the initial plating of ‘mossy lithium’, then Region 1 contains the propagating lithium dendritic structure in the lithium depleted electrolyte region. Region 0 is yet to be affected. There are movies: <http://energy.mit.edu/news/batteries-metal-reveals-dual-personality/>.

b) Typical voltage curve in a plating experiment. **c)** Scheme depicting the onset of dendritic growth with the aid of Sands’ equation. Photo courtesy to Peng Bai[67]. Original figures published under CC BY NC 3.0.

The renewed attention has led various new systems. Yet the onset and growth of these layers as a function of current density and previous cycles is still poorly understood. These highly unstable systems should be monitored in operando, i.e. in a working battery. This is not straightforward as few techniques are available that allow the quantitative determination of the

lithium spatial distribution while preserving a realistic environment. NDP can reveal exactly this, as detailed in chapter 4.

1.1.3 Sulfur

Intercalation oxides are limited by their biggest advantage, the 5-7 atoms that compile a stable scaffold is also heavy and increases costs. Hence a new mechanism is needed for the next big leap. For this the attention focuses on the top right of the periodic table, i.e. O,S,F,Cl, materials are light, abundant and highly electronegative. Theoretical discharge products, Li_2O , Li_2S , LiF and LiCl , allow for high capacity, i.e. 3350 mAh/g, 1675 mAh/g, 1410 mAh/g, 705 mAh/g respectively. These products are stable insulators, hence charging these chemistries requires a high overpotential[71]. Nevertheless, progress is made especially concerning the so called 'lithium-air' and the lithium sulfur systems[36, 37]. These systems have soluble intermediate products in common, which at least partially circumvents the nonconductive nature of the final discharge products. Especially popular in lithium air systems are 'redox mediators', these electrolyte additives are able to transport electrons from the carbon matrix to the surface of the discharge product, ensuring continuation of the reaction. The mobility of these mediators should be small, as they essentially undermine the primary function of the electrolyte, which is to prevent electron migration from anode to cathode[72]. Of the two systems lithium-sulfur batteries are considered to be closer to realization[71, 73].

Batteries based on a sulfur cathode are considered to be the prime candidate to power the beyond Li ion systems[74]. The large capacity per unit weight and the low price are the main advantages. The disadvantageous are the high overpotentials, low discharge potential and low volumetric energy densities, as these systems generally employ high carbon to sulfur ratio[75]. These are however negotiable when considering applications where price is the main selection criteria and space is abundant, i.e. such as electric grid stabilization. Already batteries employing two liquid electrodes and a highly conductive solid electrolyte are on the market for this purpose[76]. Operating above 300 degrees Celsius the battery active materials are of liquid sulfur and liquid

sodium[8]. In room temperature applications all solid state batteries generally suffer from poor contact[77].

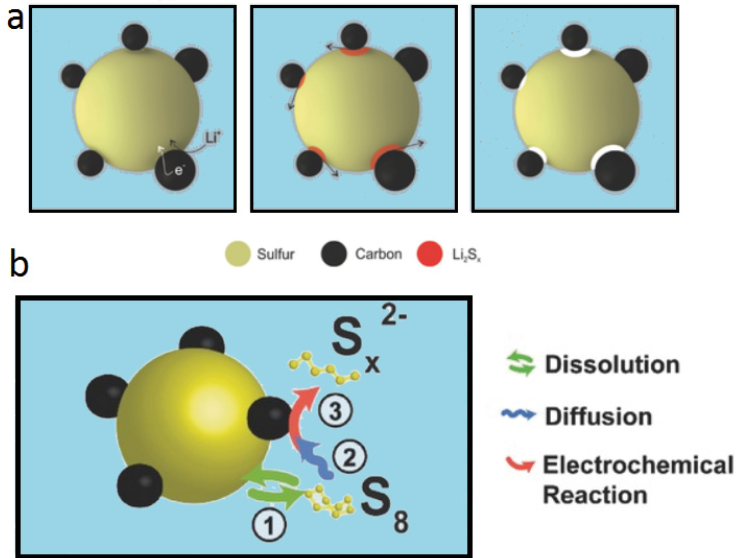


Figure 1.7 a) Discharge and charge without dissolution. **b)** Discharge with dissolution, physically separating the reaction process from the non-conductive particle. However the success of both systems is intimately related to the realization of a high capacity anode.

In a liquid electrolyte the active material displays an interesting property, it has the tendency to be partial soluble in the electrolytes used[75]. Elegantly shown by Harks et al. in an experiment where the cathode active material was electronically disconnected from the current collector still functioned and even provided a reasonable capacity[37]. At first glance this seems undesirable as dissolution of the cathode of course leads to capacity fade. However, solid sulfur is very poor electron conductor, hence a dissolution free battery would allow only the regions connected to the carbon matrix to react, thereby severely limiting the capacity, see **Figure 1.7a**. In general poor conductivity of an active material is solved by making a nano-sized powder, however the material evaporates easily so this is not advisable. Instead electrolytes are employed that allow a small degree of dissolution are used, this is enough to keep the reaction going and consume the micron sized

particles. Furthermore various methods are employed to bound the more soluble discharge products and reduce self-discharge and extensive anode consumption. Using NDP the lithium ions can be followed allowing to characterize and quantify the effectivity of these methods, as we will see in chapter 5.

1.2 Neutrons and batteries

Over centuries multiple methods have been developed in order to study the microstructure of materials. The fact that this structure, as influenced by the content, processing and treatment, gives rise to the desired mechanical properties was first quantified by Galileo in 17th century[78]. At first microscopes were used to unveil the details of this structure. Today also other particles such as electrons are used besides (high energy) photons to study materials and their properties. Like all particles, electrons are in some instances better described as wave, they can be focused. Moreover their wavelength depends on their kinetic energy, allowing to influence it[79]. This allows shorter wavelengths with higher magnification and larger depth of focus, ideal to study the details of rough surfaces, as commonly encountered material science and specifically in battery electrodes[89].

Contrary to visible light, high energy photons, x-rays, penetrate deep into the material where they interact with the electron cloud. Due to these interactions photons are scattered, diffracted or absorbed, each of which can be a tell tail sign revealing material characteristics. As both x-rays and electrons interact with the electron clouds of the atoms in the sample, they are particularly sensitive to heavier atoms which are accompanied by more electrons.

Neutrons are a neutral sub atomic particle. Normally they bond protons and stabilize the atom core[80]. Contrary to electrons they probe the structure of the atom core, making them element (and isotope) sensitive. The interaction probability is reflected by the scattering length, see **Figure 1.8**. Furthermore neutrons have a magnetic moment and hence interact with the materials magnetic properties. The information obtained with neutron techniques is unique and irreplaceable by electrons or x-rays. Especially for the direct study of light elements, which are common in energy storage applications, as they

are often undetectable with x-rays or electrons, being dwarfed by the strong interaction with the neighboring heavy elements[80-83].

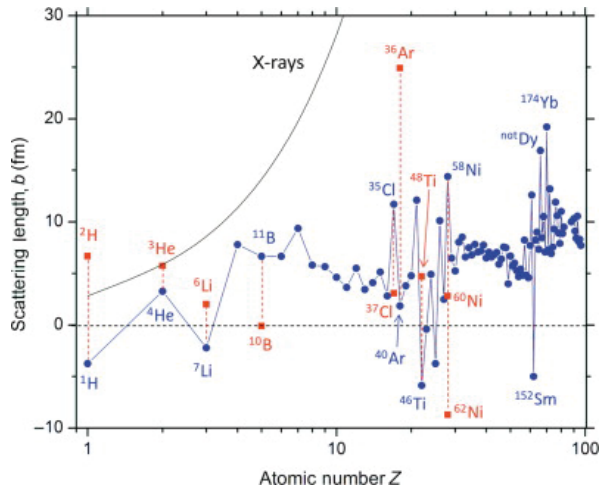


Figure 1.8 Scattering length densities of elements and selected isotopes. Black line indicates x-ray scattering length dependence with number of electrons. Reused with permission from ref [80].

Free neutrons are intrinsically unstable, they decay outside of the atom core with a half-life of 900s[84]. Hence they cannot be stored and must always be produced in order to do material science. One method to produce them is through nuclear fission, a process commonly used to fuel a nuclear reactor. Here a neutron induces a split of a uranium core producing free neutrons and two lighter elements, see **Figure 1.9b**[85, 86]. The reaction energy converted to kinetic energy of the products, in turn releasing this to the environment as heat. In an energy producing reactor this heat is harvested, in research this energy limits the neutron flux as the heat must be dissipated[86]. Only one neutron is needed to trigger the next reaction, the others radiate in all directions and few end up in one of the beamlines, see **Figure 1.9a**.

Uranium releases energy as the binding energy per nucleon is lower for the smaller elements. On the other side of the scale, concerning the light elements, this is also true, we witness the fusion of hydrogen every day, see the sun. Analogical to uranium, the stable isotope lithium-6 can also undergo a neutron capture reaction to produce lithium-7, this energy increase

however destabilizes the core causing it to decay into two new particles with known energy, similar to **Figure 1.9.b)**, however no neutrons are produced in this case. This process is the basis of neutron depth profiling[87]. The kinetic energy of these particles is high enough to pass through multiple microns of solid material. The resulting energy is measured allowing the determination of layer thickness through the energy loss of the particle[87]. The technique is highly selective as only few elements allow this capture. Moreover, the particle energies are high enough battery electrodes of commercially relevant thickness can be studied, to be extensively detailed in the following chapters.

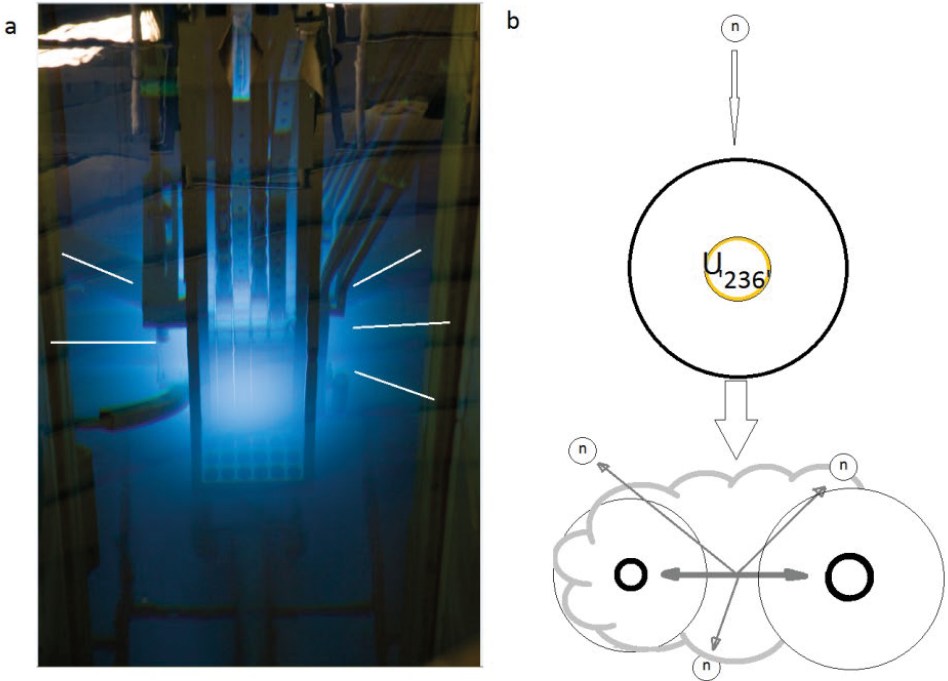


Figure 1.9.a) A close up of the reactor core in Delft, square rods contain uranium fuel, the blue light is due to Cherenkov radiation, photons emitted as particles are travelling faster than the speed of light in water. White lines indicate beamlines. **b)** Schematic representation of a fission reaction.

1.3 References

1. Gordon B. Haxel, et al., *Rare Earth Elements—Critical Resources for High Technology*, U.S. Geological, 2002.
2. Wang, J., et al., *Profiling lithium distribution in Sn anode for lithium-ion batteries with neutrons*. Journal of Radioanalytical and Nuclear Chemistry, 2014. **301**(1): p. 277-284.
3. Ferraresi, G., et al., *SnO₂ Model Electrode Cycled in Li-Ion Battery Reveals the Formation of Li₂SnO₃ and Li₈SnO₆ Phases through Conversion Reactions*. ACS Applied Materials & Interfaces, 2018. **10**(10): p. 8712-8720.
4. Shafiee, S. and Topal, E., *When will fossil fuel reserves be diminished?* Energy Policy, 2009. **37**(1): p. 181-189.
5. Ellabban, O., et al., *Renewable energy resources: Current status, future prospects and their enabling technology*. Renewable and Sustainable Energy Reviews, 2014. **39**: p. 748-764.
6. R. Bull, S., *Renewable energy today and tomorrow*. Vol. 89. 2001. 1216-1226.
7. Mulder, F.M., *Implications of diurnal and seasonal variations in renewable energy generation for large scale energy storage*. Journal of Renewable and Sustainable Energy, 2014. **6**(3): p. 033105.
8. Dunn, B., et al., *Electrical Energy Storage for the Grid: A Battery of Choices*. Science, 2011. **334**(6058): p. 928-935.
9. Armaroli, N. and Balzani, V., *Towards an electricity-powered world*. Energy & Environmental Science, 2011. **4**(9): p. 3193-3222.
10. Liu, C., et al., *Understanding electrochemical potentials of cathode materials in rechargeable batteries*. Materials Today, 2016. **19**(2): p. 109-123.
11. Whittingham, M.S., *Materials Challenges Facing Electrical Energy Storage*. MRS Bulletin, 2011. **33**(4): p. 411-419.
12. Thackeray, M.M., et al., *Electrical energy storage for transportation—approaching the limits of, and going beyond, lithium-ion batteries*. Energy & Environmental Science, 2012. **5**(7): p. 7854-7863.
13. Rehman, S., et al., *Pumped hydro energy storage system: A technological review*. Vol. 44. 2015.
14. Mulder, F.M., et al., *Efficient electricity storage with a battolyser, an integrated Ni-Fe battery and electrolyser*. Energy & Environmental Science, 2017. **10**(3): p. 756-764.
15. Reddy, T. B. and Linden, D., *Handbook of Batteries*. 2001: McGraw-Hill. 27.23.
16. Keshan, H., et al., *Comparison of lead-acid and lithium ion batteries for stationary storage in off-grid energy systems*. in *4th IET Clean Energy and Technology Conference (CEAT 2016)*. 2016.
17. Whittingham, M.S., *Lithium batteries and cathode materials*. Chemical reviews, 2004. **104**(10): p. 4271-4302.

18. Bagotsky, V.S., *Nonaqueous Electrolytes*, in *Fundamentals of Electrochemistry*. 2005, John Wiley & Sons, Inc. p. 127-137.
19. Ozawa, K., *Lithium-ion rechargeable batteries with LiCoO₂ and carbon electrodes: the LiCoO₂/C system*. *Solid State Ionics*, 1994. **69**(3): p. 212-221.
20. Tarascon, J.-M. and Armand, M., *Issues and challenges facing rechargeable lithium batteries*, in *Materials for Sustainable Energy*. 2012, Co-Published with Macmillan Publishers Ltd, UK. p. 171-179.
21. An, S.J., et al., *The state of understanding of the lithium-ion-battery graphite solid electrolyte interphase (SEI) and its relationship to formation cycling*. *Carbon*, 2016. **105**: p. 52-76.
22. Job, G. and Herrmann, F., *Chemical potential—a quantity in search of recognition*. *European Journal of Physics*, 2006. **27**(2): p. 353.
23. Eftekhari, A., *On the Theoretical Capacity/Energy of Lithium Batteries and Their Counterparts*. *ACS Sustainable Chemistry & Engineering*, 2018.
24. Fenton, W.M., et al., *Uses of Lithium Metal*, in *HANDLING AND USES OF THE ALKALI METALS*. 1957, AMERICAN CHEMICAL SOCIETY. p. 16-25.
25. Pauling, L., *THE NATURE OF THE CHEMICAL BOND. IV. THE ENERGY OF SINGLE BONDS AND THE RELATIVE ELECTRONEGATIVITY OF ATOMS*. *Journal of the American Chemical Society*, 1932. **54**(9): p. 3570-3582.
26. Shannon, R.D. and Prewitt, C.T., *Effective ionic radii and crystal chemistry*. *Journal of Inorganic and Nuclear Chemistry*, 1970. **32**(5): p. 1427-1441.
27. Nitta, N., et al., *Li-ion battery materials: present and future*. *Materials Today*, 2015. **18**(5): p. 252-264.
28. Blomgren, G.E., *The Development and Future of Lithium Ion Batteries*. *Journal of The Electrochemical Society*, 2017. **164**(1): p. A5019-A5025.
29. Kalhoff, J., et al., *Safer Electrolytes for Lithium-Ion Batteries: State of the Art and Perspectives*. *ChemSusChem*, 2015. **8**(13): p. 2154-2175.
30. Verma, P., et al., *A review of the features and analyses of the solid electrolyte interphase in Li-ion batteries*. *Electrochimica Acta*, 2010. **55**(22): p. 6332-6341.
31. Tarascon, J.-M. and Armand, M., *Issues and challenges facing rechargeable lithium batteries*, in *Materials for Sustainable Energy*. p. 171-179.
32. Yoshio, M., et al., *Lithium-Ion Batteries*. 2009: Springer-Verlag New York.
33. Janek, J. and Zeier, W.G., *A solid future for battery development*. *Nature Energy*, 2016. **1**: p. 16141.
34. Koerver, R., et al., *Chemo-mechanical expansion of lithium electrode materials – on the route to mechanically optimized all-solid-state batteries*. *Energy & Environmental Science*, 2018. **11**(8): p. 2142-2158.
35. Harks, P.P.R.M.L., et al., *In situ methods for Li-ion battery research: A review of recent developments*. *Journal of Power Sources*, 2015. **288**: p. 92-105.
36. Ganapathy, S., et al., *Nature of Li₂O₂ Oxidation in a Li–O₂ Battery Revealed by Operando X-ray Diffraction*. *Journal of the American Chemical Society*, 2014. **136**(46): p. 16335-16344.

37. Harks, P.P.R.M.L., et al., *The Significance of Elemental Sulfur Dissolution in Liquid Electrolyte Lithium Sulfur Batteries*. *Advanced Energy Materials*, 2017. **7**(3): p. 1601635-n/a.
38. Zuo, X., et al., *Silicon based lithium-ion battery anodes: A chronicle perspective review*. *Nano Energy*, 2017. **31**: p. 113-143.
39. Xu, W., et al., *Lithium metal anodes for rechargeable batteries*. *Energy & Environmental Science*, 2014. **7**(2): p. 513-537.
40. Mizushima, K., et al., *Li_xCoO₂ (0 < x < 1): A new cathode material for batteries of high energy density*. *Materials Research Bulletin*, 1980. **15**(6): p. 783-789.
41. Patoux, S., et al., *High voltage spinel oxides for Li-ion batteries: From the material research to the application*. *Journal of Power Sources*, 2009. **189**(1): p. 344-352.
42. Mei, J., et al., *Lithium-titanate battery (LTO): A better choice for high current equipment*. in *2016 International Symposium on Electrical Engineering (ISEE)*. 2016.
43. Padhi, A.K., et al., *Phospho-olivines as Positive-Electrode Materials for Rechargeable Lithium Batteries*. *Journal of The Electrochemical Society*, 1997. **144**(4): p. 1188-1194.
44. Li, Y., et al., *Current-induced transition from particle-by-particle to concurrent intercalation in phase-separating battery electrodes*. *Nature Materials*, 2014. **13**(12): p. 1149-1156.
45. Ganapathy, S., et al., *The Fine Line between a Two-Phase and Solid-Solution Phase Transformation and Highly Mobile Phase Interfaces in Spinel Li_{4+x}Ti₅O₁₂*. Vol. 7. 2016. 1601781.
46. Zhang, X., et al., *Rate-Induced Solubility and Suppression of the First-Order Phase Transition in Olivine LiFePO₄*. *Nano Letters*, 2014. **14**(5): p. 2279-2285.
47. Li, Z., et al., *Orientation-Dependent Lithium Miscibility Gap in LiFePO₄*. *Chemistry of Materials*, 2018. **30**(3): p. 874-878.
48. Dreyer, W., et al., *The thermodynamic origin of hysteresis in insertion batteries*. *Nat Mater*, 2010. **9**(5): p. 448-53.
49. Shahid, R. and Murugavel, S., *Particle size dependent confinement and lattice strain effects in LiFePO₄*. *Phys Chem Chem Phys*, 2013. **15**(43): p. 18809-14.
50. Li, Y., et al., *Effects of Particle Size, Electronic Connectivity, and Incoherent Nanoscale Domains on the Sequence of Lithiation in LiFePO₄ Porous Electrodes*. *Advanced Materials*, 2015. **27**(42): p. 6591-+.
51. Wagemaker, M., et al., *Dynamic Solubility Limits in Nanosized Olivine LiFePO₄*. *Journal of the American Chemical Society*, 2011. **133**(26): p. 10222-10228.
52. Wagemaker, M. and Mulder, F.M., *Properties and Promises of Nanosized Insertion Materials for Li-Ion Batteries*. *Accounts of Chemical Research*, 2013. **46**(5): p. 1206-1215.

53. Lu, W., et al., *In Situ Visualized Cathode Electrolyte Interphase on LiCoO₂ in High Voltage Cycling*. ACS Applied Materials & Interfaces, 2017. **9**(22): p. 19313-19318.
54. P. N. Nguyen, B., et al., *Manufacturing of LiNi_{0.5}Mn_{1.5}O₄ Positive Composite Electrodes with Industry-Relevant Surface Capacities for Lithium Ion-Cells*. Vol. 162. 2015. A1451-A1459.
55. Krause, L.J., et al., *Measurement of Li-Ion Battery Electrolyte Stability by Electrochemical Calorimetry*. Journal of The Electrochemical Society, 2017. **164**(4): p. A889-A896.
56. Hamenu, L., et al., *Benzotriazole as an electrolyte additive on lithium-ion batteries performance*. Journal of Industrial and Engineering Chemistry, 2017. **53**: p. 241-246.
57. Sun, Y.-K., et al., *High-energy cathode material for long-life and safe lithium batteries*. Nature Materials, 2009. **8**: p. 320.
58. Xiong, D.J., et al., *Measuring Oxygen Release from Delithiated LiNi_xMnyCo_{1-x-y}O₂ and Its Effects on the Performance of High Voltage Li-Ion Cells*. Journal of The Electrochemical Society, 2017. **164**(13): p. A3025-A3037.
59. Mohanty, D., et al., *Structural transformation of a lithium-rich Li_{1.2}Co_{0.1}Mn_{0.55}Ni_{0.15}O₂ cathode during high voltage cycling resolved by in situ X-ray diffraction*. Journal of Power Sources, 2013. **229**: p. 239-248.
60. Kinson, C.K. and Marca, M.D., *Electrode Materials for Lithium Ion Batteries*. Material Matters, 2012. **7**(4): p. 56-60.
61. Wang, C. and Hong, J., *Ionic/Electronic Conducting Characteristics of LiFePO₄ Cathode Materials: The Determining Factors for High Rate Performance*. Electrochemical and Solid-State Letters, 2007. **10**(3): p. A65-A69.
62. Lin, D., et al., *Reviving the lithium metal anode for high-energy batteries*. Nature Nanotechnology, 2017. **12**(3): p. 194-206.
63. Guo, Y., et al., *Reviving Lithium-Metal Anodes for Next-Generation High-Energy Batteries*. Advanced Materials, 2017. **29**(29).
64. Rao, B.M.L., et al., *Lithium-Aluminum Electrode*. Journal of The Electrochemical Society, 1977. **124**(10): p. 1490-1492.
65. Lv, S., et al., *Operando monitoring the lithium spatial distribution of lithium metal anodes*. Nature Communications, 2018. **9**(1): p. 2152.
66. Ding, F., et al., *Dendrite-Free Lithium Deposition via Self-Healing Electrostatic Shield Mechanism*. Journal of the American Chemical Society, 2013. **135**(11): p. 4450-4456.
67. Bai, P., et al., *Transition of lithium growth mechanisms in liquid electrolytes*. Energy & Environmental Science, 2016. **9**(10): p. 3221-3229.
68. Sand, H.J.S., III. *On the concentration at the electrodes in a solution, with special reference to the liberation of hydrogen by electrolysis of a mixture of copper sulphate and sulphuric acid*. The London, Edinburgh, and Dublin Philosophical Magazine and Journal of Science, 1901. **1**(1): p. 45-79.

69. Xu, Y., et al., *Honeycomb-like porous 3D nickel electrodeposition for stable Li and Na metal anodes*. Vol. 12. 2017.
70. Alvarado, J., et al., *High Concentrated Electrolytes for Li Metal Anodes*. Meeting Abstracts, 2017. **MA2017-02(5)**: p. 545.
71. Conder, J., et al., *Direct observation of lithium polysulfides in lithium-sulfur batteries using operando X-ray diffraction*. Nature Energy, 2017. **2**: p. 17069.
72. Chen, Y., et al., *Charging a Li-O₂ battery using a redox mediator*. Nature Chemistry, 2013. **5**: p. 489.
73. Zhang, S.S., *Liquid electrolyte lithium/sulfur battery: Fundamental chemistry, problems, and solutions*. Journal of Power Sources, 2013. **231**: p. 153-162.
74. Li, G., et al., *Lithium-Sulfur Batteries for Commercial Applications*. Chem, 2018. **4(1)**: p. 3-7.
75. Manthiram, A., et al., *Rechargeable Lithium-Sulfur Batteries*. Chemical Reviews, 2014. **114(23)**: p. 11751-11787.
76. Whittingham, M.S. and Huggins, R.A., *Measurement of Sodium Ion Transport in Beta Alumina Using Reversible Solid Electrodes*. The Journal of Chemical Physics, 1971. **54(1)**: p. 414-416.
77. Yu, C., et al., *Unravelling Li-Ion Transport from Picoseconds to Seconds: Bulk versus Interfaces in an Argyrodite Li₆PS₅Cl-Li₂S All-Solid-State Li-Ion Battery*. Journal of the American Chemical Society, 2016. **138(35)**: p. 11192-11201.
78. Plotnitsky, A., and Reed, D., *Mathematics, Demonstration, and Science in Galileo's Discourses Concerning Two New Sciences*. Johns Hopkins University Press, 2001. **9(1)**: p. 27.
79. Weinberger, P., *Revisiting Louis de Broglie's famous 1924 paper in the Philosophical Magazine*. Philosophical Magazine Letters, 2006. **86(7)**: p. 405-410.
80. Price, D.L. and Fernandez-Alonso, F., *Chapter 1 - An Introduction to Neutron Scattering*, in *Experimental Methods in the Physical Sciences*, 2013, Academic Press. p. 1-136.
81. Wang, H., et al., *In Situ Neutron Techniques for Studying Lithium Ion Batteries*, in *Polymers for Energy Storage and Delivery: Polyelectrolytes for Batteries and Fuel Cells*. 2012, American Chemical Society. p. 91-106.
82. Utsuro, M. and Ignatovich, V.K., *Reflection, Refraction, and Transmission of Unpolarized Neutrons*, in *Handbook of Neutron Optics*. 2010, Wiley-VCH Verlag GmbH & Co. KGaA. p. 31-70.
83. Rauch, H. and Waschkowski, W., *Neutron Scattering Lengths in ILL Neutron Data Booklet (second edition)*. 2003, Eds. Old City Publishing: Philadelphia. p. 1.1-1 1.1-17.
84. Bondarenko, L., et al., *Measurement of the neutron half-life*. JETP Lett.(USSR)(Engl. Transl.), 1978.
85. Meitner, L. and Frisch, O.R., *Disintegration of uranium by neutrons: a new type of nuclear reaction*. Garwin and Lincoln, 1939: p. 70-71.

86. Abderrahim, H.A., et al., *MYRRHA, a multipurpose hybrid research reactor for high-end applications*. Nuclear Physics News, 2010. **20**(1): p. 24-28.
87. Ziegler, J.F., et al., *Technique for determining concentration profiles of boron impurities in substrates*. Journal of Applied Physics, 1972. **43**(9): p. 3809-3815.
89. Shindo D. and Hiraga K. *Basis of High-Resolution Electron Microscopy. High-Resolution Electron Microscopy for Materials Science*. Springer, 1998. Tokyo

2.

Methods

2. Methods

The chapter aims at explaining neutron depth profiling technique and the data analysis. Also important aspects and considerations concerning operando battery preparation will be illustrated. Part of the text, especially section 2.2, is also found in;

Tomas Verhallen, Shasha Lv, Marnix Wagemaker; Operando Neutron Depth Profiling to Determine the Spatial Distribution of Li in Li-ion Batteries; Front. Energy Res., 03 July 2018 | <https://doi.org/10.3389/fenrg.2018.00062>

Figures 1 and 8 till 11 were originally published here, under CC BY license. The images can be reused and adapted for non-commercial purposes

2.1 Neutron Depth Profiling

A large part of this thesis is built around measurements using this technique. Furthermore a large degree of understanding and method development was part of this project, as such this chapter will read as a manual. It is a guidebook for future reference and contains practical examples. In the following part the physical processes of the technique will be explained, followed by a section devoted to relating depth to energy. These sections give an overview of the technique. The second subchapter will include case studies and advice on in operando experiments.

It is needless to mention that working with radiation requires understanding of the processes involved. Not only is radiation dangerous, side processes can deteriorate the sample[1] or produce noise and threaten the validity of the measurements.

Certain isotopes are able to undergo a neutron capture reaction[2]. These reactions are uncommon, though limiting the range of applications this also ensures and a selective probe with low noise. Three properties determine the usability of an isotope for neutron depth profiling, the natural abundance, the probability and the reaction energy. The probability, or capture cross-section, should be large as directly affects the measurement efficiency. The property is expressed in barns, this non-SI unit is equal to 10^{-28} m^2 [3]. The reaction energy is distributed between the reaction products while

conserving energy and momentum. When the neutron energy is negligible the particles move out in exactly opposite directions, with a kinetic energy inversely proportional to the particle weight[4]. As we will see the kinetic energy dictates the maximum depth probed[5].

Table 2.1. List of capture reactions relevant for NDP. Energies in keV are found within the brackets, all neutron capture cross sections are in barns and protons are abbreviated with p. Adapted from [2] and [6].

Element	%Abundance	Particles (Energies in keV)	Cross section
³ He	0.00014	p (572) + ³ H(191)	5333
⁶ Li	7.5	³ H(2727) + ⁴ He(2055)	940
⁷ Be	Radioactive	p(1438) + ⁷ Li (207)	48000
¹⁰ B	19.9	⁴ He(1472) + ⁷ Li(840) + γ [93.7%] ⁴ He(1777) + ⁷ Li(1013) [6.3%]	3837
¹⁴ N	99.6	¹⁴ C(42) + p (584)	1.83
¹⁷ O	0.038	¹⁴ C(404) + ⁴ He(1413)	0.24
²² Na	Radioactive	²² Ne(103) + p (2247)	31000
³³ S	0.75	³⁰ Si(411) + ⁴ He (3081)	0.19
³⁵ Cl	75.8	³⁵ S(17) + p (598)	0.49
⁴⁰ K	0.012	⁴⁰ Ar(56) + p (2231)	4.4
⁵⁹ Ni	Radioactive	⁵⁶ Fe(340) + ⁴ He(4757)	12.3

Lithium-6 is one of these isotopes. The isotope is 7.5% abundant in natural lithium[7, 8]. The capture cross section of lithium-6 is large, 940 barns[9]. The reaction produces two particles, a tritium ion or triton and an alfa particle, according to[3, 7]:



A typical set-up is depicted in **Figure 2.1**, adapted from [10]. A charged particle detector measures the kinetic energy of the incoming helium and triton particles, which has decreased because of interactions with the materials in the battery along their trajectory. The detector is placed at a well-defined distance, thereby decreasing the opening angle, indicated by the dotted grey lines, with the effect that only triton and alfa particle trajectories are recorded which make an approximate 90 degree angle with the sample plane. Hence the depth of the original lithium atom is related to the energy loss measured. The relation between energy loss and depth is quantified by the stopping power.

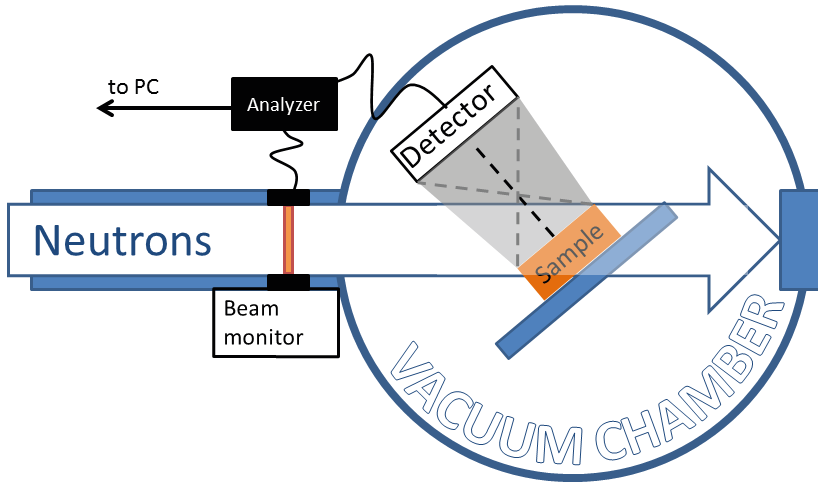


Figure 2.1. Schematic detailing the incoming neutron beam, the beam monitor, components of the set-up, i.e. sample and detector, and the range in which particles are detected and the maximum angle with the sample normal (dotted grey line).

Neutron Depth Profiling, NDP, thus allows to obtain a cross sectional averaged Li concentration profile as a function of depth, the axis perpendicular to the sample surface[7]. Moreover the technique is one of the most compact and economical among experimental neutron set-ups as a white beam is used and there are no neutron optics necessary[11, 12]. A major advantage of using neutrons is their large penetration depth in materials, allowing relatively simple sample environments[12]. Another advantage is that the technique is sensitive to ${}^6\text{Li}$ atoms regardless of their oxidation state. Furthermore the ${}^6\text{Li}$ consumption rate is negligible and NDP is considered a non-destructive technique.

However the relatively low beam intensity as compared to photon techniques is considered to be a common drawback of neutron techniques[13, 14]. Modern set-ups employ multiple detectors to improve counting statistics[15, 16]. Another strategy to increase the count rate is to enrich the ${}^6\text{Li}$ contents of the materials under investigation[17, 18] as the

natural abundance of the ^6Li isotope is only 7.5 % [19]. Hence replacing all ^7Li with ^6Li would increase count rates by a factor of 13.

An important implication of the geometrical resolution is that the detector is typically positioned at several centimeters from the sample. This requires the set-up to be in vacuum to avoid parasitic energy absorption of the ^3H and He particles by air [17-19]. The low pressure environment is one of the major obstacles for batteries containing liquid electrolytes [10, 20], as most electrolytes contain solvents with a low vapor pressure, the evaporation of which leads to contact loss between the electrodes and the electrolyte, severely hindering battery performance [10, 21]. To solve this Nagpure et al. suggested an experimental setup employing low density gases at atmospheric pressure [20]. Another approach is to work near the electrolyte vapor pressure, typically 0.1-0.3 bar, allowing the particles to reach the detector with an acceptable loss in kinetic energy. These and other strategies for measuring at ambient pressures will be further detailed in the last chapter.

Despite these challenges the technique is welcomed by the battery field, which is readily explained by the limited amount of techniques that are able to quantify both the amount and position of Li. Being a light element, lithium is difficult to detect with X-rays, furthermore techniques providing operando information on the electrochemical processes in these delicate and air sensitive batteries are limited. Hence previous operando NDP work has revealed a wealth of information. Oudenhoven et al. [18] were one of the first to demonstrate operando NDP on a lithium ion cell, performed in situ lithium metal plating from a LiCoO_2 cathode through a LIPON solid electrolyte in a thin film system using the increased depth resolution of the alpha spectrum. By using different isotopes the authors demonstrated that lithium ion exchange between cathode and electrolyte is almost non-existent in the pristine cell, due to a lack of lithium vacancies in the pristine cathode material [18]. The first operando study on a liquid electrolyte cell was performed by Liu et al. [22], their cell consisted of a 12.5 micron thick Sn anode. Their data clearly shows the expansion of the anode material, however the changes in the stopping power were not considered by the authors as the associated error

in depth would stay within 10%, which was deemed acceptable[22]. As shown recently, Li-metal plating is a process where full enrichment is achieved relatively straightforward[23]. Which, combined with the intrinsically high lithium densities in these systems, allows for a high time resolution, down to 60 seconds. In this thesis examples of intercalation materials such as LiFePO_4 are treated where these problems are irrelevant as the changes in stopping power and morphology are negligible[10]. However, as is typical for the low Li-density insertion hosts, the time resolution is poor, 60 minutes is too long to allow operando study of high rate materials[10, 21]. Hence for NDP on lithium ion batteries the following pattern is discerned; more lithium allows for higher time resolution but the interpretation of the data is complicated by the changing stopping power of the electrode mixture as influenced by the lithium concentration and the corresponding expansion.

The next section is dedicated to data interpretation. In the first 3 sub-sections the routine used in all experiments is explained, i.e. the experiments shown in this chapter and the chapters to come. The sub-section 2.1.4 will detail the measurement inaccuracy or the energy resolution. This is especially relevant when considering copper windows which due to the high stopping power force the signal to lower energies where the resolution is worse. Inversely, in the consideration of materials with a low stopping power a small energy deviation can lead to a large depth difference. Furthermore in measurements using lithium-6 a phenomenon known as pile up can arise, when the high intensity is flooding the detector.

In section 2.2 possibilities for experiment design and data interpretation are discussed, combining information from all these topics. First ex-situ measurements will be treated, necessary to understand the results of the next chapter. Secondly a guideline for in-situ measuring the depth resolved electrode porosity is provided. This extraordinary feature is realized through making use of the difference in stopping power between the pristine, dry, electrode as compared to the same electrode when infiltrated with electrolyte. Next it is demonstrated how this strategy can help in determining a more accurate stopping power for electrodes that display large changes in

morphology upon cycling, such as Li-air, Li-S, Li-metal and alloying anodes. In these type of electrodes the Li content significantly alters the stopping power due to expansion of the discharge products and low electron density of lithium. Hence an approach for calculating the stopping power during operando experiments is needed to make quantitative analysis possible[23, 29-31]. At last, a method for grouping operando measurements that encompass multiple cycles is shown thereby allowing higher time resolution in the study of intercalation materials. By means of these examples the aim of this chapter is to demonstrate the possibilities, measurement and data analysis strategies relevant to NDP for Li-ion battery work.

2.1.1 Relating particle energy to depth.

The stopping power determines the rate of energy loss as a function of particle energy given by the surrounding material. It is a material property as it depends on the density of charges, associated with the atoms. It is independent of the chemical nature of the surroundings, thus the stopping power of a mixture of materials is equal to the sum of the stopping power of the components times their volume ratio[32, 33]:

$$S_t = \frac{\partial E(E_n)}{\partial x} = \sum_{i=1}^n v_i \cdot S_i \quad (2.2)$$

Where S represents the stopping power, v the volume fraction and i the different components, which in a Li-ion battery electrode would typically be carbon black, binder, electrolyte and active material. Electrons make up most of the matter volume and therefore the electron density dominates the stopping power, especially at high particle energies[34]. At lower ^3H and alpha kinetic energies the type of bond of the electrons becomes relevant, where in the case of organic materials a correction factor of up to 20% is necessary to compensate for the decrease in electron energy with respect to the atomic state[32]. Only at low particle kinetic energies do the atom cores start to contribute significantly to the stopping power[35]. As a consequence the stopping power is strongly dependent on the particle energy, being large for small kinetic energies and small for large kinetic energies. The consequence is that the depth resolution increases with increasing depth, when ignoring energy dependent contributions that decrease the energy (and thus depth)

resolution. This results in more counts per detector energy channel for larger energies and lower counting rates at lower energies[10, 32]. As the amount of detected particles is a function of energy, an accurate determination of the stopping power is necessary to find accurate concentrations from NDP[32-36].

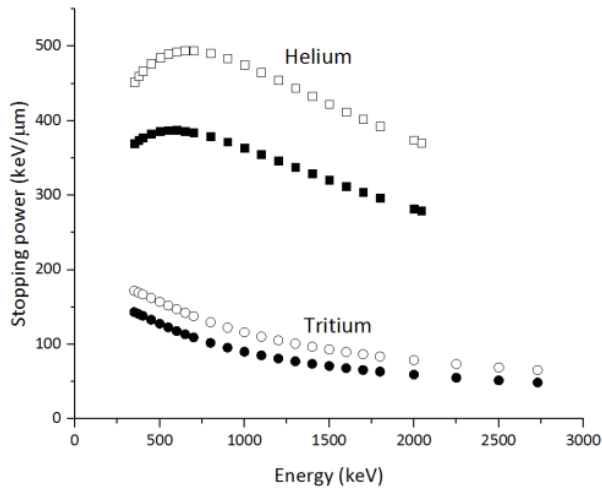


Figure 2.2. Stopping power versus particle energy of alphas and tritons in LiFePO_4 (open marker) and carbon (closed marker). Tritons are tritium ions.

In the relevant energy domain, the magnitude of the stopping power increases with decreasing particle energy, however for the low energies the inverse is true, see **Figure 2.2**. This data is obtained using the freely available software package SRIM[32] of which a short manual is found in **appendix C**[21]. The advantage of using these tables is that the values for each component can be calculated separately and then summed according to **equation 2.2**.

A consequence of the energy dependent nature of the stopping power is that a direct conversion between energy and depth yields a nonlinear depth axis and that the concentration profile needs to be corrected in a subsequent step. Here a set of equations is given that allow using a recursive method, based on a fixed depth step dx (**equation 2.3**). This results in a variable energy width (**equation 2.4**) from which the counts are assigned (**equation 2.5**).

Hence resulting in a linear depth axis which preserves the total counts, necessary to allow a correct estimation of the measurement accuracy.

$$dx = x_{n+1} - x_n \quad (2.3)$$

$$E_{n+1} = E_n - \frac{\partial E(E_n)}{\partial x} * dx \quad (2.4)$$

$$C_n = \int_{E_n}^{E_{n+1}} C(E) dE \quad (2.6)$$

The step size, dx, is chosen, based on statistics, sample thickness and the effects of straggling and detector noise, see section 2.1.3. Depending on the stopping power the resolution for ${}^3\text{H}^+$ can be around 50 nm and even better for He^{2+} . However practical considerations such as energy straggling, surface roughness and counting rate generally compromise the resolution.

Based on the kinetic energy of the ${}^3\text{H}$ and He particles after the capture reaction with ${}^6\text{Li}$, see **equation 2.1**, there is a maximum depth from which the triton and alpha particles can exit the sample. Due to the increased charge of the alpha (${}^4\text{He}^{2+}$) particle as compared to the ${}^3\text{H}^+$ particle, the stopping power is larger, and consequentially the depth resolution is larger. However, the escape depth for alphas is smaller making them more suitable for the study of thin layers[10, 32]. For energies smaller than the maximum energy of the alpha particle, 2056.12 keV, the measured signals overlap. The two signals must then be elucidated based on the ratio of the stopping power of the two particles[21, 36]. In which case **equation 2.6** needs an additional term reflecting the lithium concentration as measured through the alpha's. This value is however equal to the lithium concentration found using the triton spectra, as the same sample is probed. The helium count rate $C_{\text{He}}(E)$ can then be elucidated using the ratio of the stopping powers.

$$C_n = \int_{E_n}^{E_{n+1}} C(E) dE_{{}^3\text{H}} + \int_{E_n}^{E_{n+1}} C(E) dE_{\text{He}} \quad (2.7)$$

$$\text{With } \int_{E_n}^{E_{n+1}} C(E) dE_{\text{He}} = \frac{\partial E(E_n)_{3\text{H}}}{\partial E(E_n)_{\text{He}}} \int_{E_n}^{E_{n+1}} C(E) dE_{{}^3\text{H}} \quad (2.8)$$

To correctly interpret materials with covalent bonds, such as the electrolyte, a compound correction factor is calculated. This factor accounts for the fact that the electrons associated in a molecular bonds have significantly different binding energies[32]. The resulting table shows the stopping power due to electrons as well as due to atom cores, the contributions are independent and can thus be summed, similar to mixtures, see **appendix C**. The approach for a two component system is similar to that described by **equation (2.3-6)**, the difference lies in an extra parameter ρ , used to define the ratio between the two components (electrolyte and Li metal for instance for Li-metal anodes);

$$dx = x_{n+1} - x_n \quad (2.8)$$

$$E_{n+1} = E_n - \left(\rho_n * \frac{\partial E(E_n)}{\partial x_{Li}} + (1 - \rho_n) * \frac{\partial E(E_n)}{\partial x_{El}} \right) * dx \quad (2.9)$$

$$C_n = \int_{E_n}^{E_{n+1}} C(E) dE \quad (2.10)$$

The extra parameter results in an unsolvable set of equations, which can be resolved when the count rates of the individual components is known, where:

$$C_n = \rho_n C_{n,Li} + (1 - \rho_n) * C_{n,El} \quad (2.11)$$

This requires to measure the two components separately first. This method is only valid under the assumption that the measured concentration is solely due to the two components. This method will be illustrated in section 2.2.

Similarly the depth dependent porosity can be deduced. The stopping power will change through electrolyte wetting. As the amount of lithium contained within the electrolyte is considered negligible compared to pristine or discharged insertion hosts, the material quantity in both measurements, i.e. dry and filled with electrolyte is equal. Thus the integrated spectrum intensity is equal, and solely the stopping power is changed, spreading the signal. To find this addition in stopping power the equations must be solved in reverse order, starting from the counts obtained in the first measurement.

$$C_{n,dry} = C_{n,filled} = \int_{E_n}^{E_{n+1}} C(E) dE_{filled} \quad (2.12)$$

$$\Delta E_{El} = (E_{n+1} - E_n)_{filled} - (E_{n+1} - E_n)_{dry} \quad (2.13)$$

$$dx_{n,filled} = dx_{dry} + \Delta E_{El} / \frac{\partial E(E_n)}{\partial x_{El}} \quad (2.14)$$

$$\rho_n = 1 - \frac{dx_{dry}}{dx_{n,filled}} \quad (2.15)$$

Now due to the electrolyte filling the energy difference associated with the same amount of material, or counts, will be larger due to the larger stopping power, as is described by **equation 2.13**. This energy difference is divided by the stopping power associated with the electrolyte, resulting in a pore length, or addition to the depth increment, **equation 2.14**. The outcome of **equation 2.14** is a modified and non-linear depth axis, where the change in depth step reflects the local density. The application of this method will be shown in section 2.2.

2.1.2 Set-up geometry and intensity calibration

There is thus a relation between energy resolution and the material through the stopping power of the particle in the material. Furthermore the measurement intensity and accuracy are related through the set-up efficiency(ϵ), determined by the sample to detector distance (and their surface area). Increasing the sample to detector distance leads to higher resolution but fewer counts, as shown in **Figure 2.3**[2]. The measured intensity is further influenced by the neutron flux (\dot{n}), the reaction capture cross section (c_{sx}), the natural abundance(a) or enrichment degree of active isotope. Hence the absolute amount of atom x (N_x) can be found using equation 2.16:

$$N_x = \frac{c_x}{c_{sx} \cdot \epsilon \cdot a \cdot \dot{n}} \quad (2.16)$$

At the beam line in the flux is approximately 10^7 neutrons/cm²/s. Hence we can confirm that the technique is indeed non-destructive, as the absorption rate is one reaction per 10^{15} 6-lithium atoms per second. To find the counting rate we need to know the measurement efficiency or the probability of the particles to reach the detector. This can be calculated and measured. The set-up efficiency can be found algebraically as is explained by Maki et al.[36],

or using a Monte Carlo approach. The latter formed the basis for **Figure 2.3**. For this result 10^9 trajectories were modelled between a circular detector with a 1 cm diameter and equally sized sample. Obviously a 1 cm sample to detector spacing is not rational as the majority of counts will have travelled over 5% more than the expected path length. In Delft the sample to detector distance used is 4.5 cm, since this means the median error is 0.48%. The Canberra PIPS detector accuracy is rated at 12 keV for 5MeV alphas¹. Hence the geometrical error contribution is comparable for tritons who lost more than 2.7 MeV, assuming alphas and tritons are detected with equal accuracy.

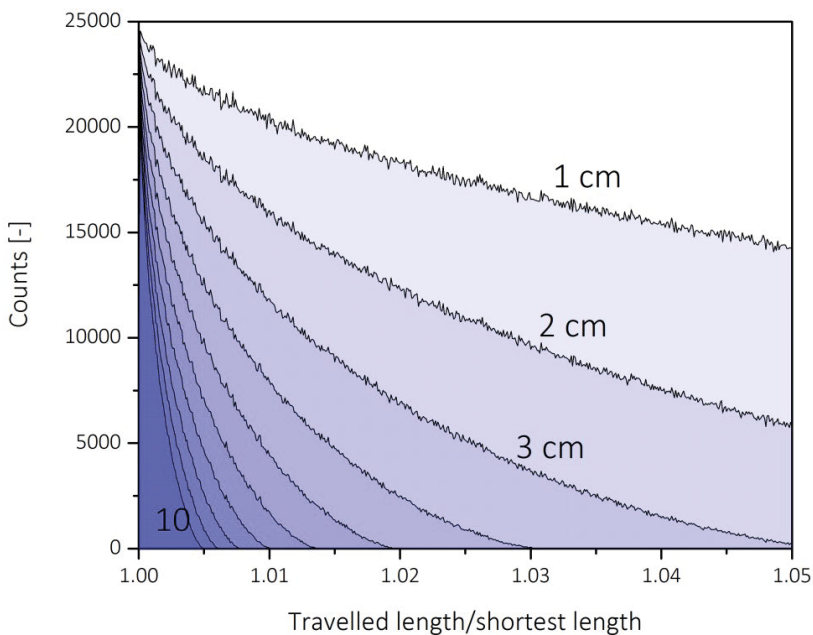


Figure 2.3. Monte Carlo simulation results for determining efficiency and accuracy as a function of sample to detector distance. Plotted are the number of particles that made it to the detector as a function of path length deviation. Bin size is 10^{-5} , 10^9 particles were emitted in random direction for a random location on the sample plane, sample plane and detector plane are circular (1 cm diameter), alignment is perfect.

¹ <https://www.mirion.com/products/passivated-implanted-planar-silicon-detectors>

Table 2.2 Measurement efficiency and accuracy versus sample to detector distance (LSD), related to **Figure 2.3**

LSD [cm]	1	2	3	4	5	6	7	8	9	10
ϵ [$\times 10^{-3}$]	25	7.4	3.4	1.9	1.2	0.86	0.64	0.49	0.39	0.31
Median error[%]	7.95	2.33	1.07	0.61	0.39	0.27	0.20	0.15	0.12	0.10

Alternatively the efficiency can be found through measuring a known sample. For this purpose samples are produced and sold by NIST², with known quantities of 10-Boron, e.g. the 1cm² SRM2137 with $1.018 \cdot 10^{15}$ ¹⁰B atoms. A measurement of SRM2137 is shown in **Figure 2.4**, here the background has been subtracted, revealing the lower energy ⁷Li peaks. Ideally you use a calibration sample with the same surface area as your intended windows or electrodes, as compared to the center the outer edges contribute less to the signal[6, 36], for this purpose larger silicon wafers are available with $9.85 \cdot 10^{15}$ ¹⁰B per cm², use a aluminum or copper window with a hole corresponding to the desired sample size. Furthermore it is advised to use sample sizes similar to the detector surface, thereby maximizing the resolution and count rate. Different isotopes have different neutron capture cross-sections as listed in table 2.1. Since the calibration samples contain 10-Boron instead of 6-Lithium, a correction is needed, which assuming equal geometries;

$$N_{Li} = \frac{C_{Li} \cdot c_{SSB} \cdot a_B \cdot N_B}{C_B \cdot c_{SSLi} \cdot a_{Li}} \quad (2.17)$$

Conversion from boron counts from SRM2137 to lithium concentration [mol/L] for natural lithium is achieved using the following relation[10]:

$$[Li^+] = 1.018 \cdot 10^{15} * \frac{3837}{940} * \frac{0.075}{A_{sample}} C_n * \frac{N_A}{dx} \quad (2.18)$$

Here C_n refers to local counts obtained via equations of **section 2.1.2**, N_A is Avogadro's number. The division with respect to the sample area and depth originates from the translation to concentration.

² https://www-s.nist.gov/srmors/view_detail.cfm?srm=2137

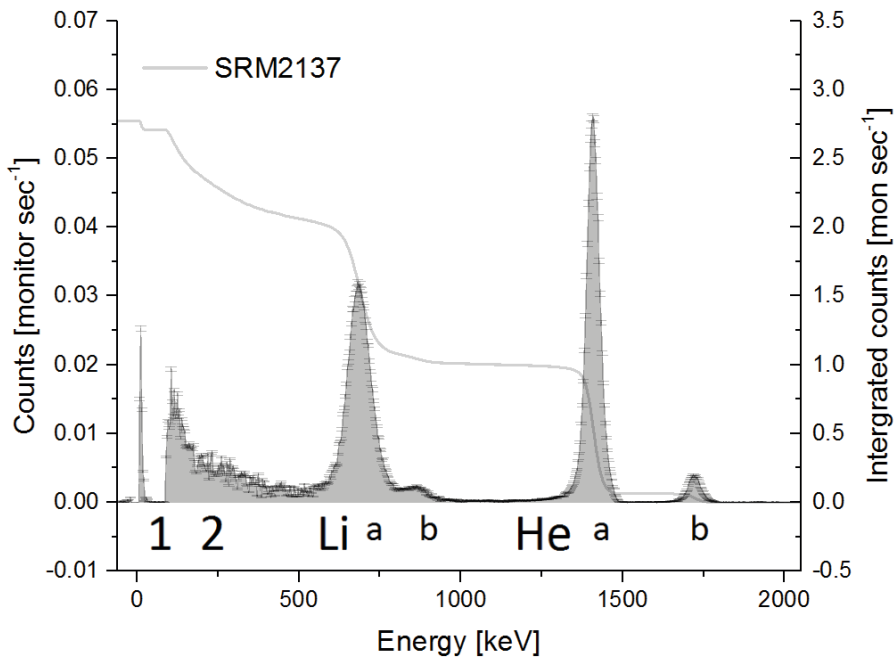


Figure 2.4. Measurement of SRM2137, with the four characteristic peaks of ^{10}B , see Table 2.1.3.I for the reaction details. The integrated intensity is shown in grey, indicating $1.018 \cdot 10^{15} \text{ }^{10}\text{B}$ atoms equal 1 monitor count. Numbers 1 and 2 indicate location of beam monitor and the region of low energy background noise.

The neutron flux is related to the reactor power. This varies slightly, hence a beam monitor is placed right at the neutron guide exit. This monitor is basically a second set-up containing a sample with a known Li concentration inside the beam and a pips detector[2, 18]. The count rate from the monitor count rate corrects for any fluctuations in the incoming neutron flux, the read-out software used in Delft (NDPinfo) performs this automatically. Currently the beam monitor is normalized such that $1 \text{ cnt} \cdot \text{mon}^{-1} \cdot \text{s}^{-1}$ is equal to $1.018 \cdot 10^{15} \text{ }^{10}\text{B}$ atoms, as is indicated in **Figure 2.4**.

Finally let us consider uncertainty in the counting statistics. Like other experiments where discrete hits are collected, the channels of a spectrum are Poisson distributed[36]. In a Poisson distribution the standard deviation

equals the square root of the measured value, in this case the total number of counts C ;

$$\sigma = \sqrt{C} \quad (2.18)$$

When σ is divided by C the relative error convenient in use for error propagation[37]. In most practical cases σ is small compared to other error contributions, otherwise measurements should be summed.

2.1.3 Energy straggling and other sources of error

So far we have mentioned detector and geometrical uncertainties yet the largest contribution to the energy inaccuracy is brought about by energy straggling. Due to the stochastic nature of the interaction between the particles and the medium, i.e. the surrounding electrode materials, energy loss is also distributed. This means particles, while originating from the same depth, arrive with varying energy. Visible in the case of SRM2137, where there is significant spread around the maximum dependent on particle Z , as shown in **Figure 2.3**, and **Figure 2.4** According to the Bohr model straggling could be approximated by[38]:

$$\sigma^2_{straggling} = 4\pi Z_1^2 Z_2 \rho_N x \quad (2.19)$$

Where Z_1 is the atomic number and ρ_N the atomic density of the host material and Z_2 the atomic number of the particle and x its' distance travelled through the host material. Although this equation is only accurate when considering low energy losses[36, 39] or low escape depths, small x , it accounts well for the differences visible in **Figure 2.4** and **Figure 2.5**. Moreover it is of important consideration when analyzing the alfa and triton signals as their spread is different, resulting in difficulties when subtracting an expected alfa signal based on triton data as explained in the previous section. Also the higher stopping power of the alphas deems this signal to be fit for the analysis of thin layers, however it is important to realize that straggling uncertainty does increase for the heavier particle.

Equation 2.19 ignores the particle energy itself. Straggling is proportional to the particle energy loss as shown in **Figure 2.6** for 2.727keV tritons, using TRIM[36]. The combined effects of straggling and geometrical error are well

quantified using the TRIM software package as described in chapter 6 and **Appendix C**. For more information readers are referred to some of the ground works on straggling, stopping power and the description of charged energetic particles in[35, 39, 40].

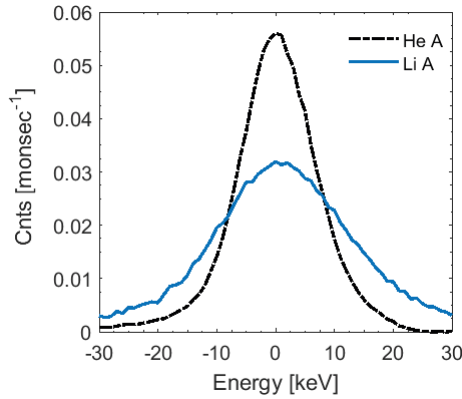


Figure 2.5 Enlargement of the helium and lithium particle peak, with their mean subtracted, arising from SRM2137, see full spectrum in **Figure 2.4**.

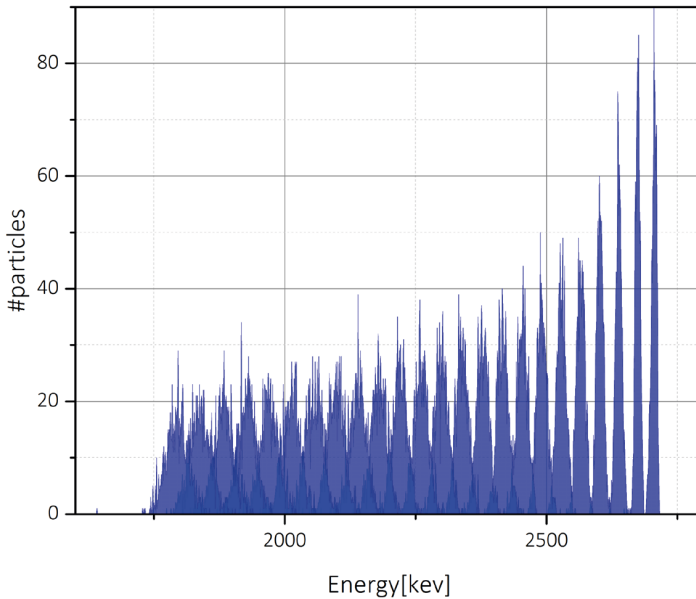


Figure 2.6 Histograms of 900 particle traces emitting every micron in a 25 micron LiPON sample and their energy at the detector modeled using TRIM,

the lowering of the maximum and the increasing overlap indicates that the energy spread is related to particle energy loss. Bin size is 1keV.

Lastly in the battery field being a practically study surfaces are never flat, but always rough, bend or wrinkled, this leads to the decay of intensity with energy, visible in **Figure 2.8**. Surface roughness and lack of flat substrates have not hindered valuable information being obtained using NDP in recent years, however the user is advised to exercise caution in data interpretation. All the errors described above are in the 10-20 keV region and are relevant when considering low density materials or flat surfaces. In the next section we will dive quickly in some of the undesired outcomes of these errors.

2.1.4 Activation and noise

Besides signal the detector is also picks up noise due to photons, most of those are created in the neutron reaction capture reaction and decay of ^{26}Al . This is followed by beta (4.6 MeV) decay with a half-life of 2.2 min, yielding ^{28}Si , in turn relaxing via prompt gamma emission of a 1778keV photon.³ The element is abundant in detector's field of view As the NDP chamber as well most of the battery packaging components are made out of aluminum. Furthermore the thermal neutron cross section is 12 barns for this reaction, this is relatively large. The short half-life results in a visible background increase during the first ten minutes of measuring. This is also an advantage, as a user will not need to wait too long, 30 minutes is advised, before it is safe to open the chamber.

Moreover the Copper isotopes 63 and 65 are prone to neutron capture. While the half-life of ^{66}Cu is short, 6.6 min that of ^{64}Cu is quite long, 12.7 hours. ^{64}Cu decays mostly through beta decay or positron emission, with <0.5% of the decays involving gamma emission. Using the NIST activation calculator, one is advised to store the measured samples for 5 days prior to disposal, assuming 10 mg of copper in the beam for 48 hours at 10^7 neutrons/cm²/s.

Many elements and isotopes are activated similarly when exposed to a neutron beam, appendix A contains a list of isotopes relevant for battery

³ <https://www.ornl.gov/PTP/PTP%20Library/library/DOE/bnl/nuclidedata/table.htm>

research that are prone to activation. It is in any case a good idea to check the materials used in a activation calculator such as BERAKT (Dutch) or NIST (freely available online). Moreover the radiation protection service (SBD) should be consulted when new set-ups or experiments are initiated, thereby ensuring your safety and that of your colleagues.

2.1.5 Pile up

Even though enriching with ${}^6\text{Li}$ can be effective, when high capacities are involved, the high intensity can flood the detector and electronics, as after every event the detector needs to return to equilibrium[41-43]. Although no new signals should be interpreted during this dead time, there is nonetheless a small window in which a multitude of charges may enter the detector and can be recorded as a single event, the energy assigned to this event will be equal to the sum of both events. This leads non-physical values of particle energies, which could be interpreted as a lithium concentration in post processing. An example is shown in **Figure 2.7**, were, to the right of the peak, an intensity is recorded, even though this regions corresponds to the lithium-free copper window. Thus users should be aware of this possibility to prevent erroneous interpretation. An important guideline is to make sure that the dead time is small compared to the measurement time. There are some instances where the issue is cannot be avoided. In the we will discuss inverse algorithms that are able to predict the shape and size of the NDP spectrum, even the part associated to pile up. Hence allowing to compensate for the effects in post processing.

2.1.6 Inverse algorithms

All the contributions to measurement error as discussed above can be effectively quantified using Monte Carlo algorithms, the next step is to predict the detector response. Modelling the detector response prior to measurement can be useful to aid experiment design and prevent misinterpretation. An example of such an inverse algorithm, based on the experiment shown in **Figure 2.7** is given here. This sample is a lithium-6 enriched metal foil on top of a copper window. Mathematically it can be described by a step function going from the ${}^6\text{Li}$ concentration in the metal to zero ${}^6\text{Li}$ concentration in the copper window. The first step is to account for

neutron beam intensity losses, through capture reactions neutron density decreases with depth causing the detection efficiency to reduce for lithium ions located deeper within the sample. Note that in most cases this effect is only minor but for samples with a high ${}^6\text{Li}$ concentration this becomes relevant. The next steps involve convolution with the geometrical error, detector uncertainty and the sample surface roughness, approximated by a Gaussian functions. The first two can be obtained from the shallow boron implanted silicon reference sample SRM2137 (NIST), where the peak width can be solely attributed to detector inaccuracy and geometrical error as straggling can be ignored as well as the surface roughness. The effects of straggling can be quantified using TRIM, the dominant reason for the spread shown in **Figure 2.4**. In this case the combined effect, sample surface roughness and straggling, are fitted to have equivalent standard deviation of 3.6 micron. Conversion from depth to energy is the inverse of the operations described in **section 2.1.2**. The anomalous concentration in the copper window, arising from the high ${}^6\text{Li}$ concentration and subsequent counting rates such that two particles are occasionally detected as a single particle having the sum of both kinetic energies. This phenomenon is referred to as ‘pile up’[43] and the intensity is given by the probability of a coincidence;

$$P(E_{12}) = P(E_1) \cdot P(E_2) \quad (2.20)$$

As the original spectrum is a probability distribution the chance of certain coincidence is found through convolution of the spectrum with itself. The intensity is related to the detector dead time. This leads to the blue line which closely resembles the measured data using only the sample surface roughness as a free parameter.

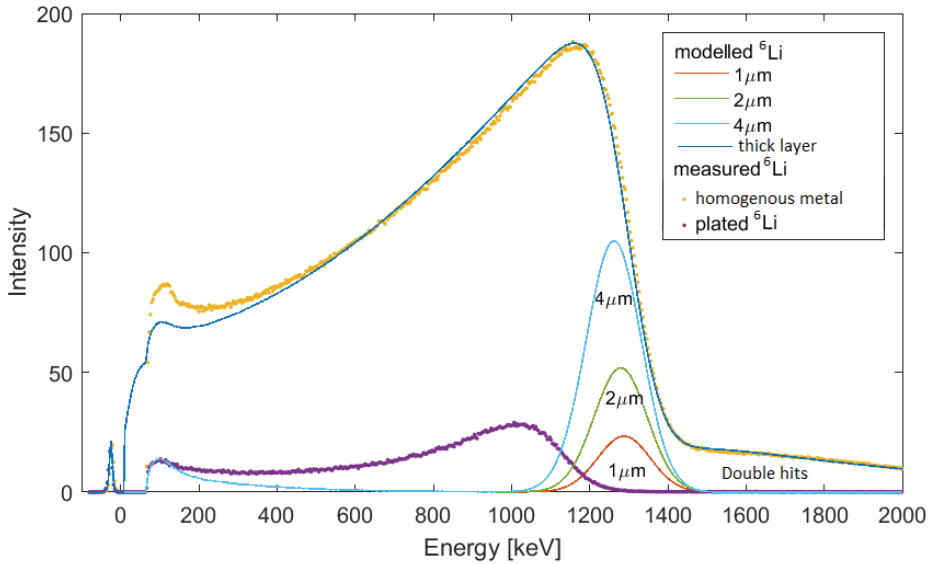


Figure 2.7. Modelling a neutron depth profiling measurement. The yellow dots reflect the measured spectrum obtained in 5 minutes where double hits indicates the region of the copper window. The purple dots reflect lithium-6 metal electrochemically plated on copper. Full lines are modelled detector responses for indicated layer thicknesses. Intensity is counts per monitor second. 1 count per monitor second is equivalent to 1.018×10^{15} ^{10}B atoms/cm². The width of a channel is 3.26 keV.

Clearly this inverse algorithm adequately predicts the detector response. The next step is to predict measurement accuracy as a function of a multiple factors such as window thickness and pressure[44]. The result can help interpret data or allow a preliminary study to determine whether the measurement accuracy can resolve the features of interest[6]. Using the present model the response to various thin layers is modelled, shown in **Figure 2.7**. With increasing thickness the peak broadens, however the height increase is more significant. This intensity increase is due to the spread in the signal which significantly overlap. The outcome shows that it is problematic to measure the ratio between components and calculate the stopping power by means of the approach detailed in section 2.1.1. as the measured intensity scales with the layer thickness. Further development of this inverse algorithm could lead to a fitting routine retrieving an estimation of the

lithium concentration profile shape, such a fitting routine based on a model is common in other disciplines[45, 46].

2.2 Experiment design

Three modes of operation are available, ex-situ, in-situ and operando. For ex-situ a battery is dismantled and the electrode of interest is harvested from the cell and placed in a sample stage of the measurement. During an in-situ measurement the battery remains intact yet cycling is paused and operando measurements occur while cycling[47]. All three modes of operation have their disadvantages. Metastable phases are only captured when measurements are adequately time resolved, however these measurements usually require significant alterations to cell design, which possibly hinder battery operation[14]. To illustrate the possibilities and stopping power strategies of operando NDP experiments four examples are discussed. Sample preparation for the batteries discussed in this subsection is found in 2.3.

2.2.1 Ex-situ experiments

The time resolution of a typical measurement with materials of low lithium concentration, e.g. intercalation cathode materials, can be insufficient. Measuring ex-situ is a potential alternative. Removing the electrolyte inhibits the movement of the lithium- ions in the electrode active material and thus prevents re-distribution. Note that this works only for cathode materials as anodes or materials with an equilibrium voltage lower than 2.94 V[55, 56] vs lithium will react with air.

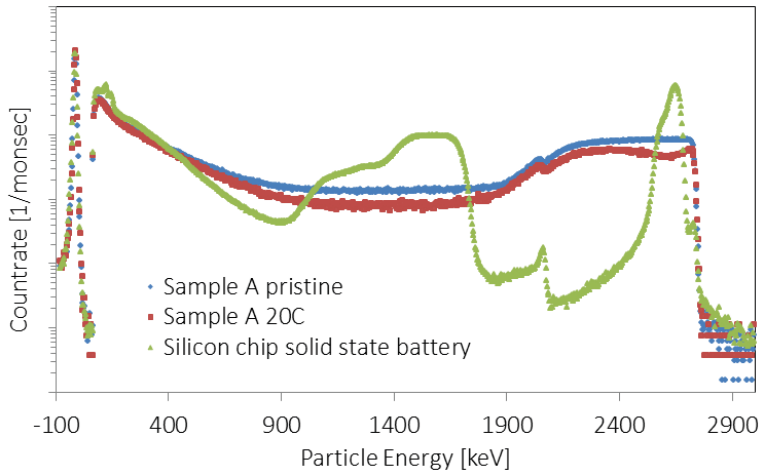


Figure 2.8. Selected ex-situ experiments, sample A is a LiFePO_4 electrode measured before and after a high rate charge. The green line is a thin film all solid state battery deposited on a silicon substrate.

Figure 2.8 shows three ex-situ measurements. During these measurements the samples are placed with the electrode facing the detector. When air stable materials are involved there is no need for a window and consequently both the alpha and triton particles are measured. The escape depth of the alpha particles is limited, approximately 6-8 microns. Due to the larger stopping power of the alpha ($^4\text{He}^{2+}$) particle, they are more suitable for the study of thin layers[10, 32]. This is illustrated by the green line in **Figure 2.8**. The triton signal is almost a single peak, whereas the alpha spectrum is clearly reflecting at least three different layers, i.e. from right to left; 2055 keV-lithium impurity on copper layer, 1750 keV start of the LiPON solid electrolyte and 1372-900 keV LiCoO_2 electrode. In the low energy regime, below 300 keV, we can discern a feature originating from the nitrogen capture reaction, which produces 500keV protons.

Moreover, ex-situ measurements allow to obtain information from thicker electrodes, 30 – 40 micron, approaching industrial sizes and allows the use of other (i.e. thicker) current collectors[59]. This increases the validity of the experiment. All neutron depth profiling results of the next chapter have been acquired using this method. Here the batteries were disassembled within minutes after reaching the desired state of charge or when the voltage

reached the charge or discharge cut-off voltage, 4.2V and 2.5V respectively. The electrode is carefully removed and rinsed using excessive amounts of DiMethyl Carbonate (DMC). Thereby ensuring that the Li-ion depth profiles are only due to the Li-ions in the active material. The removal of all LiPF_6 salt inhibits further charge transport between the LiFePO_4 particles. For the data interpretation the reference states are measured prior, i.e. the pristine state (blue diamonds in **Figure 2.8**) and the fully charged state. The measured Li-concentration of third measurement (i.e. the red squares in **Figure 2.8**) can then be expressed as the local cross sectional averaged state of charge is found.

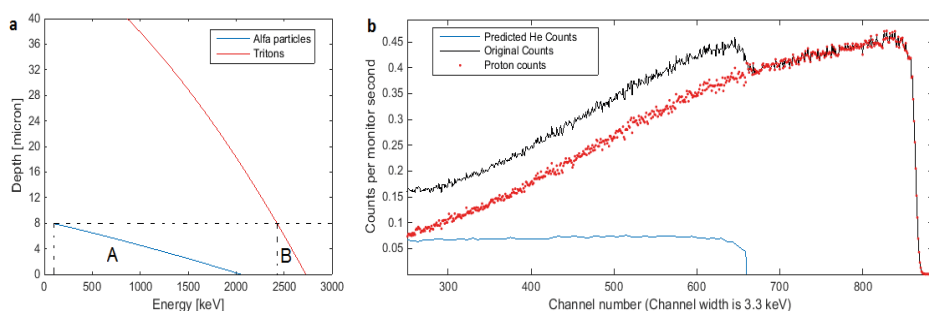


Figure 2.9.a) The energy versus depth relation for both triton and alpha particles as found using SRIM. **b)** A measurement on a pristine sample indicated in black and the resulting data after subtracting the alpha contribution in red.

For energies smaller than the maximum energy of the alfa particle, see **equation 2.1**, the measured signals overlap, see the small peak at 2055.12 keV in the red and blue line. This overlap can be avoided by using thinner electrodes[10, 57]. Alternatively the two signals can be disentangled based on the stopping power ratio. Here we make use of the fact that the concentration of lithium in first few micron of the electrode is measured twice. The alfa particles can only escape from the sample surface this will also be measured by the Tritons (^3H) from the alfa spectrum can be predicted. This expected Helium count rate is then subtracted from the signal to yield the counts from hydrogen only, depicted in **Figure 2.9b** and **equation 2.8**. In the ideal case users take into account that straggling is different for both

particles, this leads to the more smooth step at the beginning of the spectrum compared to the tritons[36]. This requires a deconvolution of the signal and a Gaussian function describing detector resolution and straggling. This operation is usually performed in Fourier space. A shortcut might be the use of a third Gaussian to describe the difference observed between the two particles. This method is not exact as straggling does increase with distance travelled and when lower energies are involved. Nonetheless the number of counts remain equal as the particles are inevitably sourced from the same sample. This discussion is circumvented when the measurement is binned, when a large step size is used referred to as Δx is **section 2.1.1**. It is important to note these effects in order to be able to explain features that might be encountered in the data processing. Furthermore any method which involves the subtraction of two signals increases the statistical uncertainties and a subsequent increasing measurement times is advised. This is achieved relatively straightforward as the sample is not expected to change or deteriorate as long as the electrolyte is removed[10, 58].

2.2.2 In-situ experiments

Arguably the difference between in-situ and operando measuring is obscured due to the relatively long measurement times and the fact that all data is based on a transverse average. Preventing local metastable phases from being resolved. However operando measurements require a low pressure environment, in-situ experiments could circumvent this problem by cycling at ambient pressures while measuring in a vacuum. Another case highlighting in-situ measurement is the following method developed to measure the depth dependent porosity using infiltration of a liquid, such as an electrolyte, in a porous Li containing medium, such as lithium battery electrode. In **Figure 2.10 a** two ^3H count rates versus particle kinetic energy loss are shown, one representing the dry electrode, in blue, and, in red, the same electrode impregnated by the electrolyte. The difference in NDP signal is due to the change in stopping power caused by the electrolyte filling the porous electrode. The data is corrected for the Al current collector, making direct comparison of the energy loss with and without the presence of the electrolyte possible. The electrode is built up by two layers of coating, the first layer on the Al current collector contains 60% of active material, 25%

carbon species, 15% PVDF binder and the second layer on top of that contains 80% of active material, 10% carbon and binder. The two layers can be distinguished by NDP based on the difference in Li density, reflected in the step in ^3H count rate, especially when the electrode pores are filled with the electrolyte.

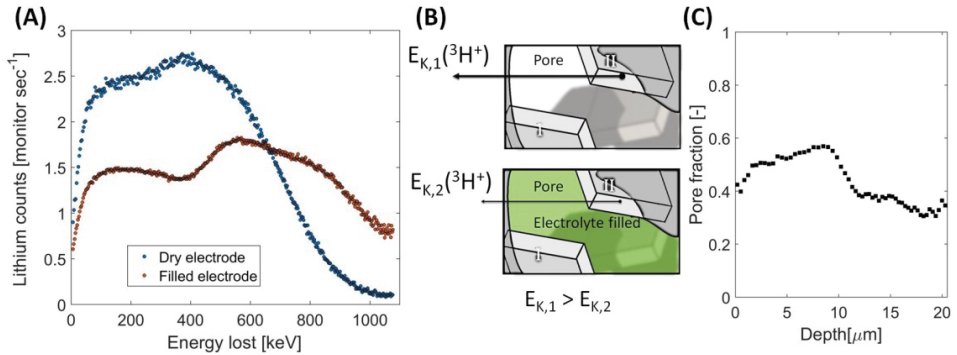


Figure 2.10 a) ^3H count rate versus particle kinetic energy loss, the raw NDP data, of a double layer LiFePO_4 electrode, measured without electrolyte (blue) and measured with electrolyte (red) **b)**. Schematic representation of the influence of the change in stopping power due to filling of the electrode pores with electrolyte. The tetragonal shapes indicate lithium containing active material, the arrows indicate particle kinetic energy, indicating that as the electrolyte fills the pores particles from crystallite II will lose more energy than without, allow discrimination between crystallite I & II. **c)** Local porosity distribution as a function of depth. The sudden change in the middle reflects the transition into the second layer.

The electrolyte fills the pores in the electrode that would otherwise not contribute to the stopping power as schematically indicated in **Figure 2.10b**. Hence the stopping power is increased and the signal is spread across a larger number of energy channels, as is described in **equations 2.11-15**. The total amount of lithium is only increased marginally ($\sim 5\%$) by adding the electrolyte[10]. Indeed the total amount of ^3H counts is equal and the increase in stopping power by adding the electrolyte results in a larger distribution in energy loss detected. This is a direct measure of the amount

and distribution of the electrolyte through the electrode, from which the depth resolved pore filling fraction can be determined.

The result, shown in **Figure 2.10c**, indicates that the porosity is much higher in the first layer. This demonstrates that an increased carbon content also increases the porosity due to the large carbon black porosity. This readily provides an additional explanation why high carbon content electrodes exhibit high rate capabilities[60, 61]. Also the porosity is relatively large in the vicinity of the interface between the two layers. This is probably a consequence of the double layer casting, where one layer is dried before the next is casted, resulting in more void space at the interface. For the second layer, having a closer to standard formulation of active material, carbon and binder, an average porosity of 0.36 is found, which is in good agreement with literature values[21, 62, 63]. Furthermore with this approach we measure the relevant porosity for the use as electrode porosity, the porosity that can be accessed by the electrolyte in question, which is different compared to what is measure by BET (Braun-Emmett-Teller) for instance[64]. Electrode porosity is a crucial electrode parameter as it strongly influences battery performance[65-69]. Generally, a larger porosity favors Li-ion transport allowing larger (dis)charge[62, 67] at the expense of the volumetric density[21, 70] and electrical conductivity of the electrode[69, 71]. The optimum seems to be reached by a certain porosity gradient[66, 72]. For measuring the porosity numerous methods are available, both bulk methods[73, 74] as well as methods with a submicron resolution, such as tomography[14, 75] and FIB-SEM[21, 76]. The advantage of using NDP is the combination of both length scales, as this measurement represents an average over 1.1 cm^2 electrode, the bulk average porosity is determined with a sub-micron resolution along an axis of interest. Moreover the measurement is performed in a non-destructive manner, allowing direct continuation of battery cycling, where the (de)lithiation as a function of depth and local porosity can now be studied.

2.2.3 Operando experiments

The ability to measure metastable phases might be limited due to the fact that transverse averaged distributions are probed. Instead instability of the

measured components versus air could be the dominant reason to study electrodes while cycling. Regardless of the operando set-up, a window is required to protect the unstable materials and supply electrons to the active material under study. This window is as thin as possible, reducing kinetic energy losses, while thick enough to withstand any pressure differences. For most cathode materials, aluminum is a straightforward choice[10], as it is used in industry and provides low density and reasonable strength. For most anodes, aluminum is not an option, as it is electrochemically active in the same voltage range[77]. Hence forcing the use of copper or a metallized Kapton film for strength, conductivity and low density and thus stopping power[22, 78]. Note that a layer solely made of Kapton does not inhibit moisture[79].

Here two examples will be used to demonstrate possibilities of operando NDP and the challenges involving good counting statistics and achieving quantitative results through calculating a dynamic stopping power. Firstly, the stopping strategy explained above will be used to determine more accurate stopping power when studying operando Li-metal plating. Here the large Li density results in high count rates and good time resolution during operando experiments, however changes in the morphology require stopping powers to be determined as a function of state of charge. Secondly, operando NDP of fast cycling $\text{Li}_4\text{Ti}_5\text{O}_{12}$ electrodes is achieved, where the challenge is the counting statistics and where the limited change in stopping power due to the Li-ion insertion and extraction allows straightforward determination of the Li density as a function of electrode depth.

In the study of lithium metal plating count rate are straightforwardly increased, as there is no lithium containing electrode, reducing one ^7Li reservoir and electrolyte enrichment is achieved by exposure to an abundance of ^6Li metal (96% pure), before use in the operando NDP cell, see the next subchapter for a more detailed description of sample preparation. Measurement times as short as 60 s can be achieved in these cells[23]. Although this intensity can lead to other specific difficulties, see **section 2.1.5**, the biggest challenge for these operando experiments is accurate calculation of the stopping power. Stopping powers of pure lithium and electrolyte are

obtained straightforwardly using SRIM, shown in **Figure 2.11**. However determining the thickness and the concentration of the plated lithium layer requires knowledge of the ratio between the two components. Our proposed strategy is as follows, by obtaining spectra of both components, the local volume fraction of lithium and electrolyte can be fitted for any third measurement, as is described in **equation 2.11-15** found in **section 2.1.1**. Obtaining the electrolyte spectra is straightforward as before cycling no lithium is plated and all counts are due to Lithium salts in the electrolyte.

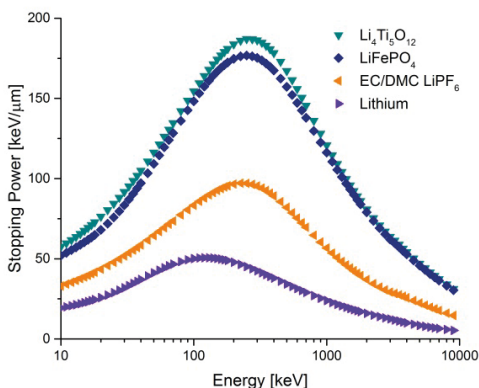


Figure 2.11 Selected stopping powers. The transition metal insertion hosts have twice as high stopping compared the commonly used EC/DMC electrolyte, which in turn is almost twice as high as metallic lithium.

Independently, a measurement of ${}^6\text{Li}$ -metal is performed to provide the second component for the stopping power calculation. As ${}^6\text{Li}$ metal is a strong thermal neutron absorber, even 40 micron of Li-metal that is observed results in approximately 40% absorption, which is worsened due to the 30 degree angle between sample and beam increases the effective length as seen for the beam, **Figure 2.1**. This effectively results in a decreased measurement efficiency of the deeper parts of the sample as demonstrated in **Figure 2.12a**. The Li density for the uncorrected data, grey triangles, decreases as a function of depth, whereas for the Li metal it should be constant at 4.64×10^{22} atoms per cm^3 , based on the ${}^6\text{Li}$ metal density (0.353 g/cm^3 [80]) and its molar weight 6.941 g/mol [81]. The first iteration, indicated by the black dots, corrects the count rate by the loss in neutron intensity

based on the ${}^6\text{Li}$ cross-section of 940 barns[9]. However, these atoms also absorb neutrons, thus a second iteration is necessary. Furthermore a small fraction is ${}^7\text{Li}$, hence the theoretical value, as is indicated by the dashed line in the **Figure 2.12a**, is obtained after the second iteration, indicated by the black squares, this results in the constant and correct Li density, accounting for both ${}^6\text{Li}$ and ${}^7\text{Li}$.

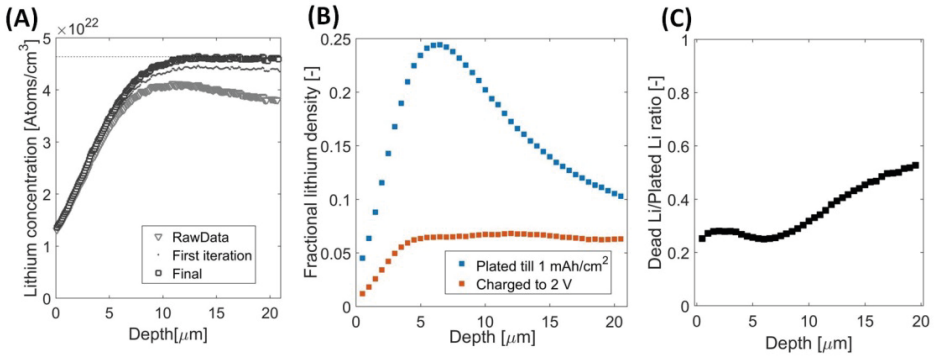


Figure 2.12 a). NDP spectra for lithium-6 metal foil, grey triangles indicate original, this data was corrected for reduced neutron intensity, dark grey dots, and finally for reduced neutron intensity and the small, unreactive ${}^7\text{Li}$ fraction, black squares. **b)** Lithium concentration after plating (blue) and stripping (red) at $1 \text{ mA}/\text{cm}^2$ for 1 hour. The unit of vertical axis, fractional lithium density is defined as the observed Li-density divided by the Li-density of Li-metal. **c)** Fraction of inactive Li, with respect to plated Li-metal with $1 \text{ mA}/\text{cm}^2$ for 1 hour on copper.

The concentration increase at the interface with the Cu current collector should resemble a step function however as shown in **Figure 2.12a**, smooth increase is observed. Firstly, this is the consequence of the larger stopping power of the copper current collector/window, which pushes the signal to lower energies. Secondly, the lower stopping power of the lithium metal spreads the measurement inaccuracies across multiple microns.

In **Figure 2.12** the ratio between Li-metal and electrolyte is shown at two moments during an operando Li-metal plating experiment. Firstly after a plating current of $1 \text{ mA}/\text{cm}^2$ for 1h, at this maximum capacity, only 30% of the volume is filled by Li-metal. From this data, averaged over approximately 1 cm^2 it is impossible to conclude if the Li-metal is plated as dense pillars or a

porous network. SEM images, performed ex-situ on layers that were plated in the same electrolyte on bare copper, e.g. shown in [27, 28], confirm that the electrochemically deposited Li-metal is highly porous. This porous layer will, to some extent, contain a solid electrolyte interphase, which is not taken into account in the stopping power analysis. The overall capacity as measured by NDP coincides with that applied electrochemically, indicating that no extra electrons are consumed by direct electrolysis of the electrolyte for instance. However it is difficult from NDP to obtain what fraction of Li is chemically decomposed. The lithium distribution after charge can be divided by the concentration after plating, as is shown in **Figure 2.12**, providing an indication of the local charging efficiency and thus the ratio between lithium metal plated and inactive Li-metal/SEI layer formed. In the first few microns, on the left side near the current collector, there is a small plateau after which the ratio increases with increasing depth, indicating an increase of inactive material towards the electrolyte/separator on the right side. This indicates that plating results in dendrite like growing structures, whereas stripping induces thinning of these structures, resulting in the observed inactive layer covering the copper current collector. Although inactive Li in the SEI/Li metal morphology is not taken into account at present, the distribution and growth can be measured after each charge. These possibilities indicate that operando NDP can be used to providing vital experimental data on the distribution and growth at intermediate states of inactive Li (SEI and dead Li-metal) upon cycling of Li metal anodes.

One of the major obstacles in the operando study of high rate intercalation materials with NDP is timeresolution. First and foremost the number of detectors can be increased or the neutron intensity via focusing optics. If the electrode can be cycled reversibly another approach is to accumulate statistics over several cycles[81]. Spinel $\text{Li}_4\text{Ti}_5\text{O}_{12}$ (LTO) shows almost no strain upon (de)lithiation and its relatively high voltage prevents decomposition of typical Li-ion battery electrolytes[82-84]. These properties ensure excellent rate capabilities, stable cycling and a long cycle life[62]. Previous measurements on another high rate material, LiFePO_4 [71], revealed that at high currents, 20C and larger[21], ionic conduction in the electrolyte is the limiting factor as indicated by the enormous differences in concentration and

local current near the electrolyte compared to the current collector. Similar limitations may be expected to arise in $\text{Li}_4\text{Ti}_5\text{O}_{12}$ electrodes at comparable C-rates and particle sizes.[85]. However the limited time resolution restricts measurement possibilities at high C-rates.

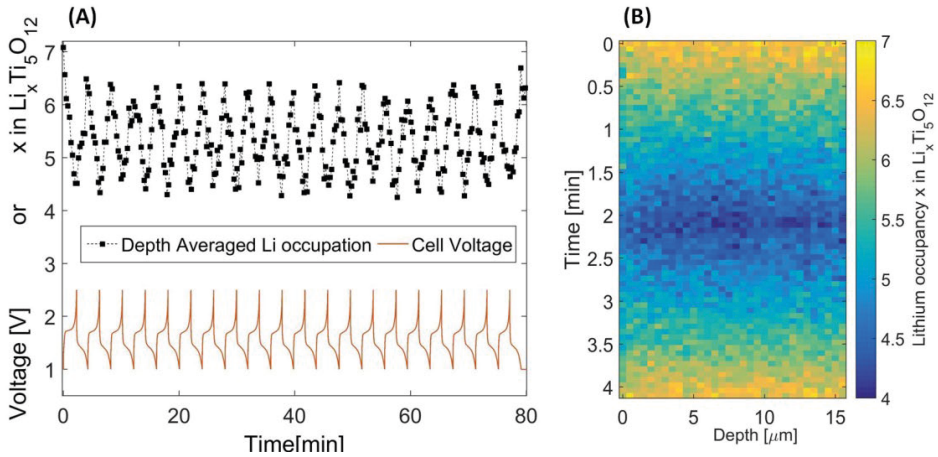


Figure 2.13 a) Reversible cycling of $\text{Li}_4\text{Ti}_5\text{O}_{12}$ during operando NDP experiments at a 30C rate. b) Operando NDP of $\text{Li}_4\text{Ti}_5\text{O}_{12}$ during 30C cycling, based on accumulated data over 20 cycles. The current collector at zero depth and the electrolyte/seperator at 15 micron depth.

Instead it is proposed to accumulate NDP measurements over several subsequent cycles at 30C, 0.0045 A/cm^2 , thereby achieving sufficient counting statistics in combination with the required time resolution (30 s in this case). The stable cycling of the $\text{Li}_4\text{Ti}_5\text{O}_{12}$ electrode in the operando NDP cell is demonstrated in **Figure 2.13a**, displaying almost no change in the voltage characteristic during the 20 cycles, even at the reduced pressure condition required for operando NDP operation. Furthermore, denoted by the black squares, the change in state of charge, reflected in terms of occupied sites, as obtained from the NDP spectra measured every 30s, confirms the consistent behavior, reaching a site occupancy of 4.2 to 6.5 almost every time. The local, depth dependent, site occupancy or state of charge is found by comparing measurements to the lithium distribution after a low rate (dis)charge when all available active material is either filled, $\text{Li}_x=7$, or emptied, $\text{Li}_x=4$, completely. This allows the direct study of the active

particle fraction as background noise due to the electrolyte lithium salt is subtracted. This method was previously described in [10].

Data obtained during these 20 charge-discharge cycles is ordered according to the voltage, where measurements within similar voltage ranges are averaged, reducing the noise, the result of which is shown in **Figure 2.13b**. The current collector is located on the left side at zero depth and the interface with the electrolyte at the right, approximately at 15 microns depth. Previous experiments observed large differences in concentration between the current collector and the interface with the electrolyte when LiFePO_4 electrodes were charged with a 20C rate [21, 86]. Close examination of **Figure 2.13b** and especially comparing electrolyte side and current collector side, reveals that there are almost no significant differences between these two regions of the electrode. The lithium concentration is in fact homogeneously distributed throughout the electrode as opposed to that for LiFePO_4 electrodes (by ex-situ measurements). This signifies the excellent rate performance of $\text{Li}_4\text{Ti}_5\text{O}_{12}$ electrodes, potentially explained by a better Li-ion transport network available through the particles [87, 88] or/and transport is facilitated due to a different morphology even though the particle size is comparable [62, 63]. The particle size could also govern the kinetics, allowing a homogenous distribution since the larger particles do not have enough surface sites to accommodate larger reaction rates [89, 90]. The differences between the rate limiting mechanisms testifies to the extraordinary nature of these high rate insertion materials.

2.3 Battery preparation

Sample preparation steps are found in all chapters, concisely explaining the relevant steps. In this section those the choices are elaborated. Aforementioned in the introduction, batteries contain two electrodes coated on current collectors which are separated by an electrolyte/separator. The active materials are mixed with a conductive additive (some form of carbon) and a binder, which are dissolved in a solvent to produce an adhesive slurry. Carbon additives are used in many shapes and sizes, their properties directly affect the electrode performance as we saw in section 2.2.2. and numerous examples can be found in literature [71, 94, 95]. Small particles are

considered desirable for achieving efficient percolation, however the large surface areas consume a large amount of binder. The chemically inert thermoplastic poly vinyl difluoride (PVDF) is commonly used as a binder for cathode materials. PVDF is solvated using N-Methyl-2-Pyrrolidone (NMP), which is carcinogenic and evaporates slowly[96]. Even though the slightest ingress of water is detrimental to the performance of lithium ion batteries[97], some water based binders have been developed. A notable example is the biodegradable Carboxyl Methyl Cellulose (CMC)[98] or E466, used in toothpaste and gluten-free additive in sauces and candy⁴. Anode materials such as Lithium titanate ($\text{Li}_4\text{Ti}_5\text{O}_{12}$) and silicon are sometimes bonded using CMC, as it is unstable versus higher potentials used on the cathode side[96, 98].

These components are then thoroughly mixed to achieve homogeneity and adequate solvation of the binder. Ideally, active material quantities are maximized while maintaining percolation of the carbon matrix and proper adhesion. Although it is tempting to increase the relative quantity of carbon and binder as it lowers current density which in turn increases rate capability and active material utilization, showcasing your material. The slurry is coated on the current collector by means of a thin application methods also common in other fields, referred to as ‘tape casting’ or ‘doctor blade method’[99, 100]. In practice a well-defined slit moves relative to a flat surface spreading the slurry with the slit thickness. This coating is dried in an oven placed inside a fume hood for evacuation of the NMP or alternatively in air if the solvents are harmless. The drying process reduces the thickness. Fast drying and thick coatings generally lead to delamination whereas slow drying allows agglomeration of active material or carbon nano powder.

Current collectors are almost exclusively made from aluminum (cathode side) and Copper on the anode side, owing to their respective stability windows and availability[91]. For LiFePO_4 it is considered to beneficial use carbon-coated aluminum foil allowing improved adhesion and lowers resistance[21, 59]. Separators can be glass fibre as well as polymer (Teflon, polyethylene) based, higher energy density can be achieved using polymer separators as

⁴ https://en.wikipedia.org/wiki/Carboxymethyl_cellulose, retrieved 25-09-2018

they are thinner[92]. Liquid electrolytes are usually based on a combination of two organic polar solvents, such as Ethylene Carbonate (EC) and DiMethyl Carbonate (DMC), in which a salt, LiPF_6 , is dissolved. The combination of solvents allows optimizing viscosity while maintaining a large electrochemical stability window and desirable SEI forming properties. Furthermore the mixture should prevent pitting corrosion of the aluminum foil as well[93].

In this work electrode thicknesses are limited by the escape depth of the tritons, since thicker coatings would render part of the electrode outside of the field of view. Hence coating thicknesses should be below 20 micron (in-situ/operando) or below 35 micron (ex-situ). Ex-situ coatings, shown in chapter 3, were applied on carbon coated aluminum foil.

All examples of section 2.2 are based on measurements on pouch cells[23, 48-50], also known as coffee bag cells[51], their flexible design allows the straightforward sealing of current collector window[52], as is also described in [53]. Also pouch cell type constructions are common practice in industrial applications[54]. Moreover reducing the amount of material is advisable as neutron activation can lead to samples emitting hazardous radiation. Pouch cells introduce negligible background by other isotopes as they consist from plastic coated aluminum foil.

The electrodes used in this chapter are prepared by NMP based slurries cast onto 11 micron aluminum foil, in the last example of 2.2.3. a 90 % $\text{Li}_4\text{Ti}_5\text{O}_{12}$ (Phostech), 3% SuperP carbon and 7% PVDF binder was used and the in-situ example, the double layer electrode was built from a first coating of 60% LiFePO_4 (Phostech) active material, 25% carbon species (of which 10% SuperP and 15% KS4 (Timcal)) and 15% PVDF binder and the second layer containing 80% of active material, 10% SuperP carbon and binder. The second layer was applied when the first was dry. NMP-based slurries in this work are dried at 70°C within one hour and then left for 24h to finish drying at room temperature. Particle sizes of commercial powders are poorly defined, but XRD refinement showed an domain size of approximately 140nm for both the LiFePO_4 and the $\text{Li}_4\text{Ti}_5\text{O}_{12}$ [62, 63]. In the second example bare 10 micron copper foil was used as current collector and window and ^6Li -enriched Li-metal foil was used as counter electrode. 1M LiPF_6 in EC/DMC (Sigma Aldrich)

served as the electrolyte in all examples. By measuring around the electrolyte vapor pressure in the NDP setup, contact loss between the electrodes of the pouch cell, signified by an increase in the overpotential, is avoided.

2.4 Conclusions

Direct observation of lithium concentration versus electrode depth in working Li-ion batteries is possible through the capture reaction of the thermal neutrons by the ${}^6\text{Li}$ isotope. The charged particles produced in this reaction lose energy due to stopping power of the sample environment. This energy loss is measured by an energy sensitive detector placed at certain distance from the sample is a direct measure for the original ions depth. The particle kinetic energy limits the escape depth and therefore the depth of view. Although the large attenuation length of neutrons in most materials allows diverse sample environments, the effective measurements require thorough experiment design.

The low pressure environment hampers battery performance. Reducing the vacuum, or increasing the pressure can mitigate the effects yet does increase straggling and thus measurement inaccuracy. Proper understanding and models can predict the outcome and help validation of experiments. Some key features might be difficult to resolve without a high vacuum.

Here in-situ or ex-situ measurements could be a viable alternative. The lack of a window in ex-situ measurements allows the largest depth view. Furthermore this method allows the use of the alpha particles, which in spite of the increased straggling allow higher depth resolution due to the increased stopping power. Measurement time is straightforwardly extended allowing depth resolution even when quantities are minute. However this method is limited to air stable samples, thereby limiting the application to cathode materials.

The combination ex-situ and in-situ measurements on the same electrode allow the quantification of the pore distribution, due to the change in NDP signal due to filling of the porous electrode. This is of particular importance in the study of lithium ion battery electrodes where porosity has a direct

influence on the energy density and charge transport, hence determining the rate capability of battery electrodes.

Accurate determination of the stopping power of the battery electrode, which may change upon cycling, is vital to achieve the quantitative Li density as a function of depth. In particular for the cases that electrochemical cycling leads to large changes in the composition, a stopping power calculation strategy is developed to result in quantitative results. This is demonstrated lithium metal plating, where operando NDP is able to provide insight in the growth and development of the evolution of inactive Li.

Increasing time resolution can be achieved through ^6Li enrichment. This is an effective method due to the low natural abundance (7.5%) but not always practical to achieve. Also high count rates can flood the detector. Here we demonstrate that accumulation of NDP data over repeated battery cycling enables operando investigations of intercalation materials at a rate of 30C, avoiding complexity of ^6Li homogenization that comes along with enrichment and allowing for the use of commercially produced powders.

2.5 References

1. Tan, C., et al., *Gamma radiation effects on Li-ion battery electrolyte in neutron depth profiling for lithium quantification*. Journal of Radioanalytical and Nuclear Chemistry, 2015. **305**(2): p. 675-680.
2. Downing, R.G., et al., *Neutron Depth Profiling: Overview and Description of NIST Facilities*. Journal of Research of the National Institute of Standards and Technology, 1993. **98**(1): p. 109-126.
3. Ziegler, J.F., et al., *Technique for determining concentration profiles of boron impurities in substrates*. Journal of Applied Physics, 1972. **43**(9): p. 3809-3815.
4. Tomandl, I., et al., *High resolution imaging of 2D distribution of lithium in thin samples measured with multipixel detectors in sandwich geometry*. Review of Scientific Instruments, 2017. **88**(2): p. 023706.
5. Fink, D., *Neutron Depth Profiling*. 1996: Hahn-Meitner Institute fur Kernforschung.
6. Shi, C., et al., *Inverse iteration algorithm for neutron depth profiling*. Journal of Radioanalytical and Nuclear Chemistry, 2018. **317**(1): p. 81-85.
7. Whitney, S.M., et al., *Benchmarking and analysis of ^6Li neutron depth profiling of lithium ion cell electrodes*. Journal of Radioanalytical and Nuclear Chemistry, 2009. **282**(1): p. 173.

8. Whitney, S., et al., *Neutron Depth Profiling Applications to Lithium-Ion Cell Research*. Journal of the Electrochemical Society, 2009. **156**(11): p. A886-A890.
9. Kopecky, J., et al., *Atlas of neutron capture cross sections*. 1997, International Atomic Energy Agency.
10. Zhang, X.Y., et al., *Direct Observation of Li-Ion Transport in Electrodes under Nonequilibrium Conditions Using Neutron Depth Profiling*. Advanced Energy Materials, 2015. **5**(15): p. 1500498.
11. Utsuro, M. and Ignatovich, V.K., *Reflection, Refraction, and Transmission of Unpolarized Neutrons*, in *Handbook of Neutron Optics*. 2010, Wiley-VCH Verlag GmbH & Co. KGaA. p. 31-70.
12. Wang, H., et al., *In Situ Neutron Techniques for Studying Lithium Ion Batteries*, in *Polymers for Energy Storage and Delivery: Polyelectrolytes for Batteries and Fuel Cells*. 2012, American Chemical Society. p. 91-106.
13. M. Itkis, D., et al., *Probing Operating Electrochemical Interfaces by Photons and Neutrons*. Vol. 2. 2015.
14. Harks, P.P.R.M.L., et al., *In situ methods for Li-ion battery research: A review of recent developments*. Journal of Power Sources, 2015. **288**: p. 92-105.
15. Parikh, N.R., et al., *Neutron depth profiling by coincidence spectrometry*. Nuclear Instruments and Methods in Physics Research Section B: Beam Interactions with Materials and Atoms, 1990. **45**(1): p. 70-74.
16. Mulligan, P.L., et al., *A multi-detector, digitizer based neutron depth profiling device for characterizing thin film materials*. Review of Scientific Instruments, 2012. **83**(7): p. 8.
17. Downing, R., J. Maki, and R. Fleming, *Analytical applications of neutron depth profiling*. Journal of Radioanalytical and Nuclear Chemistry, 1987. **112**(1): p. 33-46.
18. Oudenhoven, J.F.M., et al., *In Situ Neutron Depth Profiling: A Powerful Method to Probe Lithium Transport in Micro-Batteries*. Advanced Materials, 2011. **23**(35): p. 4103-+.
19. Hutchison, D.A., *Natural Abundance of the Lithium Isotopes*. Physical Review, 1954. **96**(4): p. 1018-1021.
20. Nagpure, S.C., et al., *Neutron depth profiling of Li-ion cell electrodes with a gas-controlled environment*. Journal of Power Sources, 2014. **248**: p. 489-497.
21. Liu, Z., et al., *Relating the 3D electrode morphology to Li-ion battery performance; a case for LiFePO₄*. Journal of Power Sources, 2016. **324**: p. 358-367.
22. Liu, D.X., et al., *In Situ Quantification and Visualization of Lithium Transport with Neutrons*. Angewandte Chemie-International Edition, 2014. **53**(36): p. 9498-9502.
23. Lv, S., et al., *Operando monitoring the Lithium spatial distribution of Li-metal anodes*. Nature Communications, 2018: p. in press.

24. Zhang, S.S., *Problem, Status, and Possible Solutions for Lithium Metal Anode of Rechargeable Batteries*. ACS Applied Energy Materials, 2018. **1**(3): p. 910-920.
25. Liu, D.X., et al., *In Situ Neutron Depth Profiling of Lithium Transport within Aluminum and Tin*. Meeting Abstracts, 2015. **MA2015-01**(2): p. 649.
26. Cheng, X.-B., et al., *Toward Safe Lithium Metal Anode in Rechargeable Batteries: A Review*. Chemical Reviews, 2017. **117**(15): p. 10403-10473.
27. Bieker, G., et al., *Electrochemical in situ investigations of SEI and dendrite formation on the lithium metal anode*. Physical Chemistry Chemical Physics, 2015. **17**(14): p. 8670-8679.
28. Zhang, W., et al., *A "cation-anion regulation" synergistic anode host for dendrite-free lithium metal batteries*. Science Advances, 2018. **4**(2).
29. Asadi, M., et al., *A lithium–oxygen battery with a long cycle life in an air-like atmosphere*. Nature, 2018. **555**: p. 502.
30. Kang, H.S., et al., *A Scaled-Up Lithium (Ion)-Sulfur Battery: Newly Faced Problems and Solutions*. Advanced Materials Technologies, 2016. **1**(6): p. 1600052.
31. Wang, J., et al., *Profiling lithium distribution in Sn anode for lithium-ion batteries with neutrons*. Journal of Radioanalytical and Nuclear Chemistry, 2014. **301**(1): p. 277-284.
32. Ziegler, J.F., et al., *SRIM - The stopping and range of ions in matter (2010)*. Nuclear Instruments & Methods in Physics Research Section B-Beam Interactions with Materials and Atoms, 2010. **268**(11-12): p. 1818-1823.
33. Ziegler J.F., *The Stopping and Range of Ions in Matter*. 1985, Boston, MA: Springer.
34. Lindhard, J., et al., *RANGE CONCEPTS AND HEAVY ION RANGES (NOTES ON ATOMIC COLLISIONS, II)*. Kgl. Danske Videnskab. Selskab. Mat. Fys. Medd., 1963: p. Medium: X; Size: Pages: 1-42.
35. Wilson, W.D., et al., *Calculations of nuclear stopping, ranges, and straggling in the low-energy region*. Physical Review B, 1977. **15**(5): p. 2458-2468.
36. Maki, J.T., et al., *Deconvolution of neutron depth profiling spectra*. Nuclear Instruments and Methods in Physics Research Section B: Beam Interactions with Materials and Atoms, 1986. **17**(2): p. 147-155.
37. Ord, J.K., *Handbook of the Poisson Distribution*. Journal of the Operational Research Society, 1967. **18**(4): p. 478-479.
38. Bohr, N., *LX. On the decrease of velocity of swiftly moving electrified particles in passing through matter*. London, Edinburgh, and Dublin Philosophical Magazine and Journal of Science, The, 1915. **30**(178): p. 581.
39. Inokuti, M., *Inelastic Collisions of Fast Charged Particles with Atoms and Molecules---The Bethe Theory Revisited*. Reviews of Modern Physics, 1971. **43**(3): p. 297-347.
40. Chu, W.-K., *Calculation of Energy Straggling for Protons and Helium Ions*. Vol. 13. 1976. 2057-2060.

- 
41. Verhallen, T.W., et al., *Operando Neutron Depth Profiling to Determine the Spatial Distribution of Li in Li-ion Batteries*. *Frontiers in Energy Research*, 2018. **6**(62).
 42. Lv, S., et al., *Operando monitoring the lithium spatial distribution of lithium metal anodes*. *Nature Communications*, 2018. **9**(1): p. 2152.
 43. Wetjen, M., et al., *Quantifying the Distribution of Electrolyte Decomposition Products in Silicon-Graphite Electrodes by Neutron Depth Profiling*. *Journal of The Electrochemical Society*, 2018. **165**(10): p. A2340-A2348.
 44. Coakley, K.J., et al., *Modeling detector response for neutron depth profiling*. *Nuclear Instruments and Methods in Physics Research Section A: Accelerators, Spectrometers, Detectors and Associated Equipment*, 1995. **366**(1): p. 137-144.
 45. Krouglov, T., et al., *Structural transitions of hard-sphere colloids studied by spin-echo small-angle neutron scattering*. *Journal of Applied Crystallography*, 2003. **36**(6): p. 1417-1423.
 46. Andersson, R., et al., *Analysis of spin-echo small-angle neutron scattering measurements*. *Journal of Applied Crystallography*, 2008. **41**(5): p. 868-885.
 47. Conder, J., et al., *Do imaging techniques add real value to the development of better post-Li-ion batteries?* *Journal of Materials Chemistry A*, 2018. **6**(8): p. 3304-3327.
 48. Yu, D.Y.W., et al., *Effect of electrode parameters on LiFePO₄ cathodes*. *Journal of the Electrochemical Society*, 2006. **153**(5): p. A835-A839.
 49. Mohanty, D., et al., *Structural transformation of a lithium-rich Li_{1.2}Co_{0.1}Mn_{0.55}Ni_{0.15}O₂ cathode during high voltage cycling resolved by in situ X-ray diffraction*. *Journal of Power Sources*, 2013. **229**: p. 239-248.
 50. Gustafsson, T., et al., *The polymer battery as an environment for in situ X-ray diffraction studies of solid-state electrochemical processes*. *Electrochimica Acta*, 1992. **37**(9): p. 1639-1643.
 51. Singh, M., et al., *Thick Electrodes for High Energy Lithium Ion Batteries*. *Journal of The Electrochemical Society*, 2015. **162**(7): p. A1196-A1201.
 52. Villevieille, C., *Electrochemical characterization of rechargeable lithium batteries*. 2015, book chapter, Elsevier. p. 183-232.
 53. Zhang, X., et al., *Rate-Induced Solubility and Suppression of the First-Order Phase Transition in Olivine LiFePO₄*. *Nano Letters*, 2014. **14**(5): p. 2279-2285.
 54. Trask, S.E., et al., *From coin cells to 400 mAh pouch cells: Enhancing performance of high-capacity lithium-ion cells via modifications in electrode constitution and fabrication*. *Journal of Power Sources*, 2014. **259**: p. 233-244.
 55. Ganapathy, S., et al., *Operando Nanobeam Diffraction to Follow the Decomposition of Individual Li₂O₂ Grains in a Nonaqueous Li-O₂ Battery*. *The Journal of Physical Chemistry Letters*, 2016. **7**(17): p. 3388-3394.

56. Ganapathy, S., et al., *Nature of Li₂O₂ Oxidation in a Li–O₂ Battery Revealed by Operando X-ray Diffraction*. Journal of the American Chemical Society, 2014. **136**(46): p. 16335-16344.
57. Nagpure, S.C., et al., *Neutron depth profiling technique for studying aging in Li-ion batteries*. Electrochimica Acta, 2011. **56**(13): p. 4735-4743.
58. Li, Y., et al., *Fluid-enhanced surface diffusion controls intraparticle phase transformations*. Nature Materials, 2018.
59. Li, T., et al., *Carbon-coated aluminum foil as current collector for improving the performance of lithium sulfur batteries*. International Journal of Electrochemical Science, 2017. **12**(4): p. 3099-3108.
60. Kang, B. and Ceder, G., *Battery materials for ultrafast charging and discharging*. Nature, 2009. **458**: p. 190.
61. Liu, H., et al., *Capturing metastable structures during high-rate cycling of LiFePO₄ nanoparticle electrodes*. Science, 2014. **344**(6191).
62. Singh, D.P., et al., *Templated spinel Li₄Ti₅O₁₂ Li-ion battery electrodes combining high rates with high energy density*. Electrochemistry Communications, 2013. **35**: p. 124-127.
63. Singh, D.P., et al., *Facile Micro Templating LiFePO₄ Electrodes for High Performance Li-Ion Batteries*. Advanced Energy Materials, 2013. **3**(5): p. 572-578.
64. Klinkenberg, L.J., *The Permeability Of Porous Media To Liquids And Gases, in Drilling and Production Practice*. 1941, American Petroleum Institute: New York, New York.
65. Strobridge, F.C., et al., *Mapping the Inhomogeneous Electrochemical Reaction Through Porous LiFePO₄-Electrodes in a Standard Coin Cell Battery*. Chemistry of Materials, 2015. **27**(7): p. 2374-2386.
66. Liu, L., et al., *Experimental and Simulation Investigations of Porosity Graded Cathodes in Mitigating Battery Degradation of High Voltage Lithium-Ion Batteries*. Journal of The Electrochemical Society, 2017. **164**(13): p. A3163-A3173.
67. Just, P., *A method to quantify coating thickness and porosity of electrodes for lithium-ion-batteries*. Measurement, 2016. **89**: p. 312.
68. Fongy, C., et al., *Electronic and Ionic Wirings Versus the Insertion Reaction Contributions to the Polarization in LiFePO₄ Composite Electrodes*. Journal of the Electrochemical Society, 2010. **157**(12): p. A1347-A1353.
69. Fongy, C., et al., *Ionic vs Electronic Power Limitations and Analysis of the Fraction of Wired Grains in LiFePO₄ Composite Electrodes*. Journal of the Electrochemical Society, 2010. **157**(7): p. A885-A891.
70. Singh, M., et al., *Effect of Porosity on the Thick Electrodes for High Energy Density Lithium Ion Batteries for Stationary Applications*. Batteries, 2016. **2**(4): p. 35.

71. Wang, C. and Hong, J., *Ionic/Electronic Conducting Characteristics of LiFePO₄ Cathode Materials: The Determining Factors for High Rate Performance*. Electrochemical and Solid-State Letters, 2007. **10**(3): p. A65-A69.
72. Du, Z., et al., *Understanding limiting factors in thick electrode performance as applied to high energy density Li-ion batteries*. Journal of Applied Electrochemistry, 2017. **47**(3): p. 405-415.
73. Li, X., et al., *Mesoporous silicon sponge as an anti-pulverization structure for high-performance lithium-ion battery anodes*. Nature Communications, 2014. **5**: p. 4105.
74. DuBeshter, T., et al., *Measurement of Tortuosity and Porosity of Porous Battery Electrodes*. Journal of The Electrochemical Society, 2014. **161**(4): p. A599-A605.
75. Ge, M., et al., *Large-Scale Fabrication, 3D Tomography, and Lithium-Ion Battery Application of Porous Silicon*. Nano Letters, 2014. **14**(1): p. 261-268.
76. Hutzenlaub, T., et al., *Three-dimensional electrochemical Li-ion battery modelling featuring a focused ion-beam/scanning electron microscopy based three-phase reconstruction of a LiCoO₂ cathode*. Electrochimica Acta, 2014. **115**: p. 131-139.
77. Rao, B.M.L., R.W. Francis, and H.A. Christopher, *Lithium-Aluminum Electrode*. Journal of The Electrochemical Society, 1977. **124**(10): p. 1490-1492.
78. Wang, C., et al., *In Situ Neutron Depth Profiling of Lithium Metal–Garnet Interfaces for Solid State Batteries*. Journal of the American Chemical Society, 2017. **139**(40): p. 14257-14264.
79. Shiang, W.R. and Woo E.P., *Soluble copolyimides with high modulus and low moisture absorption*. Journal of Polymer Science Part A: Polymer Chemistry, 1993. **31**(8): p. 2081-2091.
80. Lord, A.M.J.a.M.P., *Macmillan's Chemical and Physical Data*. 1992, London, UK: Macmillan.
81. Meija, J., et al., *Atomic weights of the elements 2013 (IUPAC Technical Report)*, in *Pure and Applied Chemistry*. 2016. p. 265.
82. Wang, S., et al., *Lithium titanate hydrates with superfast and stable cycling in lithium ion batteries*. Nature Communications, 2017. **8**(1): p. 627.
83. Tang, Y., et al., *Li₄Ti₅O₁₂ hollow microspheres assembled by nanosheets as an anode material for high-rate lithium ion batteries*. Electrochimica Acta, 2009. **54**(26): p. 6244-6249.
84. Odziomek, M., et al., *Hierarchically structured lithium titanate for ultrafast charging in long-life high capacity batteries*. Nature Communications, 2017. **8**: p. 15636.
85. Yu, Y.-S., et al., *Dependence on Crystal Size of the Nanoscale Chemical Phase Distribution and Fracture in Li_xFePO₄*. Nano Letters, 2015. **15**(7): p. 4282-4288.

86. Zhang, X., et al., *Direct Observation of Li-Ion Transport in Electrodes under Nonequilibrium Conditions Using Neutron Depth Profiling*. *Advanced Energy Materials*, 2015. **5**(15): p. 1500498.
87. Lee, K.T., et al., *Proof of Intercrystallite Ionic Transport in LiMPO₄ Electrodes (M = Fe, Mn)*. *Journal of the American Chemical Society*, 2009. **131**(17): p. 6044-6045.
88. Tanida, H., et al., *Elucidating the Driving Force of Relaxation of Reaction Distribution in LiCoO₂ and LiFePO₄ Electrodes Using X-ray Absorption Spectroscopy*. *The Journal of Physical Chemistry C*, 2016. **120**(9): p. 4739-4743.
89. Wang, C., et al., *A robust strategy for crafting monodisperse Li₄Ti₅O₁₂ nanospheres as superior rate anode for lithium ion batteries*. *Nano Energy*, 2016. **21**: p. 133-144.
90. Vasileiadis, A., et al., *Towards optimal performance and in-depth understanding of spinel Li₄Ti₅O₁₂ electrodes through phase field modeling*. 2018.
91. Yoshio, M., et al., *Lithium-Ion Batteries*. 2009: Springer-Verlag New York.
92. Reddy, T.B.L., D. , *Handbook of Batteries*. 2001: McGraw-Hill. 27.23.
93. Kalhoff, J., et al., *Safer Electrolytes for Lithium-Ion Batteries: State of the Art and Perspectives*. *ChemSusChem*, 2015. **8**(13): p. 2154-2175.
94. Zhu, J., et al., *The application of graphene in lithium ion battery electrode materials*. *SpringerPlus*, 2014. **3**: p. 585.
95. Wang, R., et al., *Performance-Enhanced Activated Carbon Electrodes for Supercapacitors Combining Both Graphene-Modified Current Collectors and Graphene Conductive Additive*. *Materials*, 2018. **11**(5): p. 799.
96. Pohjalainen, E., et al., *Water soluble binder for fabrication of Li₄Ti₅O₁₂ electrodes*. *Journal of Power Sources*, 2013. **226**: p. 134-139.
97. Aurbach, D. and Y. Gofer, *The Correlation Between Surface Chemistry, Surface Morphology, and Cycling Efficiency of Lithium Electrodes in a Few Polar Aprotic Systems*. *Journal of the Electrochemical Society*, 1989. **136**(11): p. 3198-3205.
98. Li, J., R. Lewis, and J. Dahn, *Sodium carboxymethyl cellulose a potential binder for Si negative electrodes for Li-ion batteries*. *Electrochemical and Solid-State Letters*, 2007. **10**(2): p. A17-A20.
99. Hu, L., et al., *Thin, flexible secondary Li-ion paper batteries*. *ACS nano*, 2010. **4**(10): p. 5843-5848.
100. Berni, A., M. Mennig, and H. Schmidt, *Doctor Blade*, in *Sol-Gel Technologies for Glass Producers and Users*, M.A. Aegerter and M. Mennig, Editors. 2004, Springer US: Boston, MA. p. 89-92.

3.

Exploring the Limits of Performance of
High Rate Intercalation Materials

3. Exploring the Limits of Performance of High Rate Intercalation Materials

In this chapter an example is demonstrated that combines the measurement of the Li-ion distribution using neutron depth profiling with 3D electron microscopy, in tailored samples. The aim is to provide insight in the rate limiting step in relation to electrode morphology. The body of this chapter is based on the results of a collaboration between Northwestern University and the TU Delft, where Northwestern provided FIB-SEM analysis and we were responsible for the battery electrodes, electrochemical analysis and performed neutron depth profiling.

*Tomas W. Verhallen, Zhao Liu, Deepak P. Singh, Hongqian Wang, Marnix Wagemaker, Scott Barnett; Relating the 3D electrode morphology to Li-ion battery performance; a case for LiFePO₄, Journal of Power Sources, 324, (2016), p358–367
DOI:10.1016/j.jpowsour.2016.05.097*

Figures 2-7 are re-used from this work, for which I have permission being a co-author. If you wish to use one of those figures please contact the publisher (Elsevier).

3.1 Introduction

Driven by electrification of mobile transport and increasing demands of portable electronic devices Li-ion battery research focuses on improvement of the energy and power density, while ensuring a stable, long cycle life and the use of abundant, environmentally benign materials. A high energy density requires high lithium capacities of both positive and negative electrode materials and a large difference in potential. Power density is the rate at which this energy can be extracted. This requires a low internal resistance provided by facile charge transport, both ionic and electronic through the battery electrode morphology[1]. The internal resistance of the battery is dominated by the resistance of the rate limiting charge transport step[2, 3]. This resistance causes the voltage polarization that scales with the (dis)charge current, leading to higher external potentials during charge and lower during discharge, often referred to as overpotential. This reduces the energy efficiency and moreover the effective capacity as the cell potential is

restricted by the stability window of the electrolyte to prevent detrimental electrolyte decomposition. Hence to reach higher currents and higher power densities, improvement of the rate limiting charge transport step is required. Alternatively, lowering the internal resistance allows to design thicker electrodes, increasing the relative amount of active materials on pack level, thereby increasing the effective energy density. Li-ion battery electrodes based on liquid electrolytes typically consist of a solid state storage (active) material, an electron conducting phase, and a binder that together form the porous structure to be soaked with an organic electrolyte. Given this structure, contributions to the internal resistance include (1) the electronic resistance of the contact between the active electrode material and the current collector, (2) the ionic network formed by the liquid electrolyte in the pores of the porous composite electrodes connecting the active electrode material and the electrolyte, (3) the electrochemical reaction allowing the ion to enter the active electrode material and simultaneous reorganisation of the liquid electrolyte solvent molecules and (4) the solid state transport and phase nucleation/transformation kinetics within the active electrode material[3, 4].

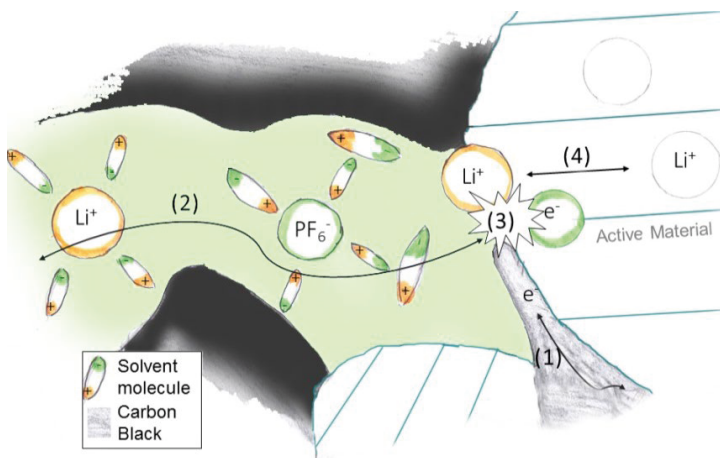


Figure 3.1. Contributions to charge transfer resistance for a porous electrode in liquid electrolyte. Electronic (1) and Ionic (2) resistance to providing reactants to a charge transfer site (3) followed by solid state diffusion of products into the solid material(4). Upon charge these process occur in reverse order.

Hence improving the performance of these battery systems starts with an accurate determination of the rate limiting step. To provide insight in the kinetic and thermodynamic processes in batteries it is essential to observe the Li-ion distribution depending on the electrochemical conditions and depending on the structure and morphology of the electrodes. In the following sections we will demonstrate this process for the common intercalation electrode material LiFePO_4 . The material was proposed by Padhi et al.[5] in 1997, since then it has been intensively studied and today serves as an established model system[3]. For LiFePO_4 the initial hurdle of poor intrinsic electronic and solid state ionic conduction were overcome by reducing the particle size in combination with carbon or metallic conductive coatings[6-8]. Further studies attempting to improve the material properties lead to numerous insights on a wide range of length scales. Submicron crystallites tend to (de)lithiate via a particle-by-particle, or mosaic mechanism at low rates[9-12], concentrating the current to a small fraction of the particles in an electrode, leading to large local differences in state of charge[13, 14]. Whereas for higher rates the behaviour moves towards a more concurrent transformation of the particles[10, 15]. The region of this transition is difficult to pinpoint, as it is related to the particle size and the kinetics of the local environment[3, 16-19].

Inside the particle the nucleation barrier for the first order phase transition in LiFePO_4 is predicted[20] and observed[3, 13] to decrease for smaller particles and also the particle shape and nature of the surface has been recently shown to affect the transformation[16, 21]. At higher discharge rates the particle is predicted[10, 22-24] and observed[15, 25] to convert via a solid solution mechanism precluded by a range of metastable phases[26, 27], these solid solution and metastable phase regimes are considered to be responsible for the inherently fast (dis)charging of LiFePO_4 electrodes, at least qualitatively supporting a Butler-Volmer relation between charge transfer over the electrolyte electrode interface and the overpotential[15, 23].

On an electrode level, however, studies recognize the ionic transport through the porous electrode structure as being rate limiting at higher rates[3, 16, 28-

34]. This is consistent with the direct observation that increasing the electrode loading density (proportional to the electrode thickness) results in a decrease in capacity at the same C-rate[28, 35] and the observation that for thick electrodes particles near the electrolyte lithiate preferentially[3, 16, 34]. However contradictory reports have shown that the most resistive process in an electrode is the electronic conduction between the LiFePO_4 particle surface and the nearest branch of the percolating carbon network[17].

In summary we can discern the following pattern, when decreasing the (effective) particle size or increasing the current it seems that the bulk electrode properties, conduction of ions or electrons, start to become the dominant resistance. Or inversely upon decreasing the electrode dimensions or loading density the particles become rate limiting. Even though many of the elementary processes that constitute the (dis)charging process are understood, commercial electrodes are characterized by a high loading density, thick layers (~ 100 micron[36]), and subject to a dynamic current range. Hence it remains questionable whether we can quantify the above effects across the relevant length scales and can improve new electrodes accordingly, until ultimately providing a universal understanding of the limits of lithium battery electrodes. Neutron depth profiling provides the opportunity to answer these questions as it allows the unique possibility to explore a bulk property, lithium concentration, on a small length scale with sub-micron accuracy, as will be demonstrated in the following section(s). Here a comparison of two iron phosphate based electrodes prepared using different techniques is demonstrated. The differences on a micron level are studied using FIB-SEM whereas the electrochemical implications are studied on a bulk level using NDP.

In a recent study we have used a cheap and scalable templating technique, based on carbonate templates, improving the high rate capacity retention significantly in both LiFePO_4 and $\text{Li}_4\text{Ti}_5\text{O}_{12}$ electrodes[36, 37]. Importantly, the applied templating method leads to only a marginal increase in the porosity, resulting in a combination of large tap density (high volumetric energy density) and improved power density. Interpretation of the electrochemical data has indicated an improved tortuosity of the electrolyte network

throughout the electrode, a better ionic wiring provided by increased interconnectivity of the electrolyte filled pores in the electrode as induced by the template[30, 31]. Surprisingly, also an improvement of the electronic conductivity was suggested, which could not be explained by the applied templating approach. The importance of the electronic conductivity in battery electrodes was also recently demonstrated by the direct observation of Li concentration profiles, probed by operando neutron depth profiling[3].

To provide insight in the kinetic and thermodynamic processes in batteries it is essential to observe the Li-ion distribution depending on the electrochemical conditions and depending on the structure and morphology of the electrodes. As outlined in the introduction it is evident that the overall charge transport properties of an electrode depend on the detailed 3D electrode morphology including: the porosity, tortuosity of both ionic and electronic conducting phases, active material grain size and shape. The diversity in reported results and the large amount of parameters involved make it difficult if not impossible to unambiguously establish the relation between the rate limiting step, the applied current and the electrode morphology, a prerequisite for reaching optimal kinetic battery performance. This has initiated several studies to reconstruct the 3D Li-ion battery electrode microstructure aiming to find a correlation with the electrode performance. The benefits of characterizing the 3D microstructure of Li-ion battery electrodes are two-fold. Firstly, it is considered an effective tool to quantitatively assess complex microstructural characteristics[36, 38-40]. On the other hand, the 3D electrode reconstruction provides realistic microstructural input for 3D computational modelling of the electrode electrochemical process[41-43]. Recently, 3D reconstruction resolving all three phases; oxide particles, carbonaceous materials and electrolyte filled pores has been achieved, allowing detailed quantitative analysis of the facets of charge transport in the electrode[43-45]. To date, although there are a few reports on three-phase 3D microstructure of LiFePO₄ electrode[44, 45], limited analysis was performed to investigate the correlation between electrode 3D microstructure with charge transport mechanisms. This analysis is hindered by the large number of variables that together determine the microstructure and the subsequent transport properties. Ideally this number

is reduced by preparing electrodes of similar structure which fundamentally differ on a few key aspects, thereby isolating certain properties and their effect on the electrochemical properties. By combining detailed three-phase 3D reconstruction of carbonate templated and pristine LiFePO_4 electrodes with direct measurement of Li-ion gradients under variable conditions, using focused ion beam-scanning electron microscopy (FIB-SEM) and NDP respectively, the present research reveals the origin of the improved rate performance of the template electrodes. The results give insight in the role of electronic and ionic transport in typical Li-ion battery electrodes and how the 3D electrode morphology can be tailored to improve Li-ion battery performance.

3.2 Results and discussion

Figure 3.2. shows charge voltage profiles at different charge rates and the charge and discharge capacity retention under variable rate for the standard and templated LiFePO_4 electrodes, both having tap densities close to 2.0 g/cm^3 . As reported previously[21,30], templating results in lower overpotentials indicating a lower internal resistance to charge transport and consistently larger charge and discharge capacities, in particular exposed at high rates.

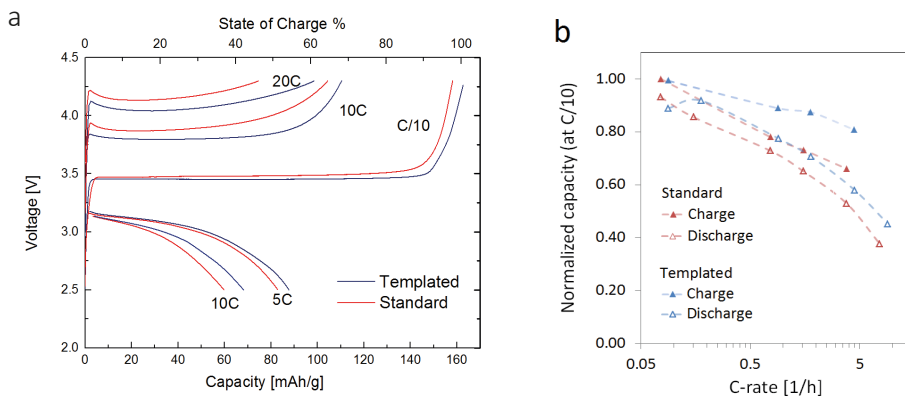


Figure 3.2. (a) Voltage profiles for templated and standard electrodes at different charge rates. (b) Capacity as a function of (dis)charge rate for both templated and standard electrodes.

To investigate what differences are responsible for the improved charge transport, cross-sectional SEM images were obtained and the corresponding 3D reconstruction of the resin-infiltrated samples is determined, both for the templated and standard electrodes as shown in **Figure 3.3**. The silicone resin infiltration allows good image contrast among LiFePO_4 particles (white), carbon and binder domain (CB, black), and resin-infiltrated pores (grey). The microstructures differ clearly in two aspects; in the templated electrodes the LiFePO_4 particles and carbon/binder phase are densely packed and surrounded by large micron-size pores (indicated with red dashed circle in **Figure 3.3. (a)** and **(c)**) accompanied by small nanometre-size pores, whereas in the standard sample all three phases were homogeneously distributed. This observation is confirmed by the cumulative feature size distribution of all three phases in both electrodes shown in **Figure 3.4**. The broad distribution in electrolyte feature size demonstrates that these pores are present throughout the analysed volume. As expected the size distributions of the other two phases are practically identical, since the same LiFePO_4 and carbon powders were used in both samples. The micron-size pores are formed due to the dissolution of the NaHCO_3 and could play a critical role in improving rate performance in templated sample[29]. Bae et al. reported that, by introducing a multiple length-scales pore network, for example dual-scale porosity, the electrode kinetics can be effectively improved and results in an enhanced rate performance[46]. However, Fukutsuka et al. have shown that Li ion conductivities do not depend on pore size in regular free-standing membranes[47].

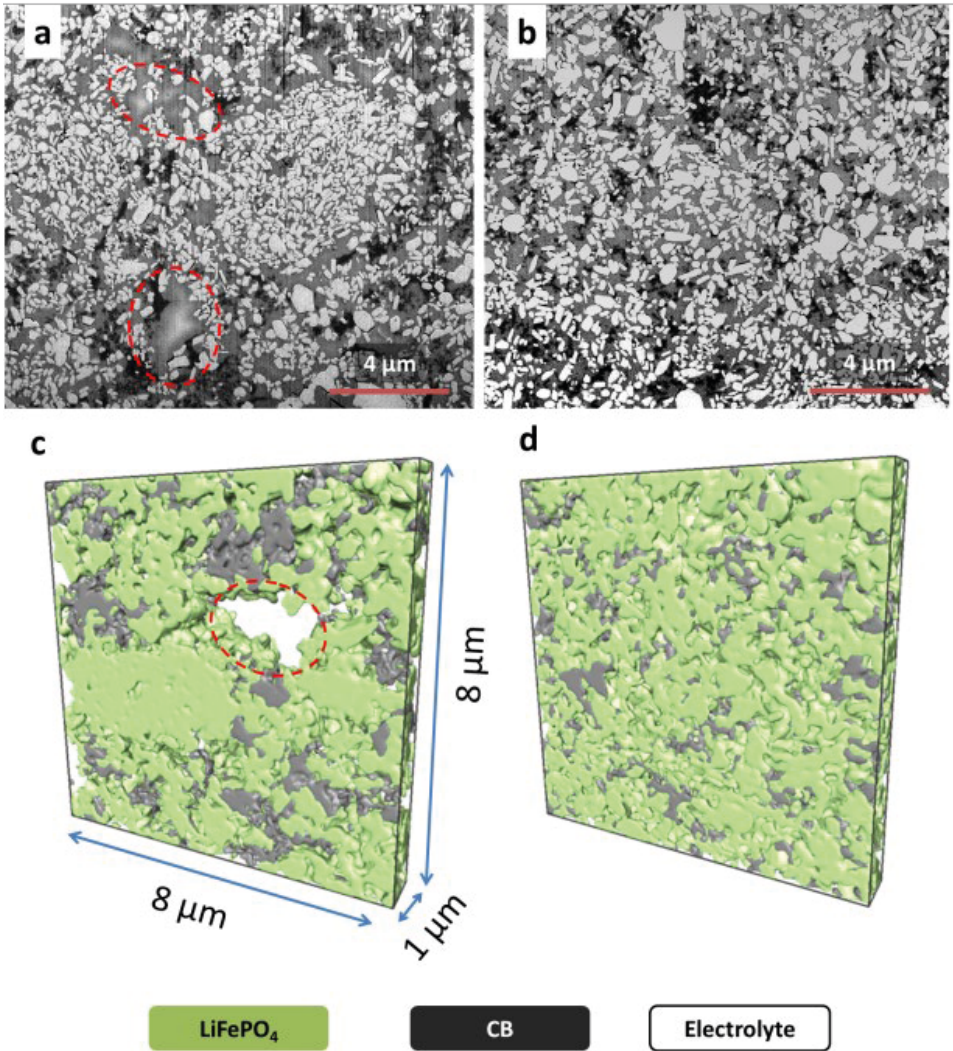


Figure 3.3 Cross-sectional SEM images and 3D reconstructions (a fraction of the whole reconstruction) of (a),(c) templated and (b), (d) standard cathode. The red dashed circles indicate the resin filled micron-size pores formed after dissolution of NaHCO₃ template.

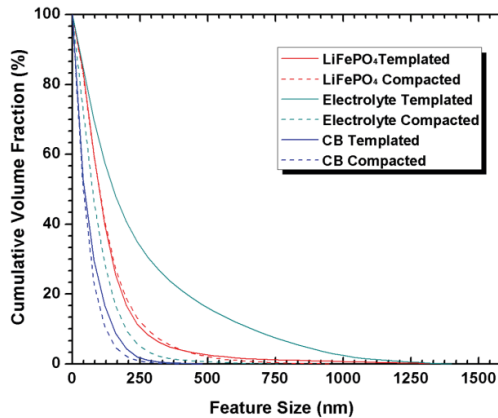


Figure 3.4 Cumulative feature size distribution of LiFePO₄, electrolyte and CB in both templated and standard electrodes.

Table 3.1 summarizes microstructural parameters of both electrodes obtained from the analysed volume. The determination of the interfacial surface area is useful for accurately modelling of the charge transfer process and the strain/stress distribution in the active material during charge/discharge processes[41, 43, 48, 49]. Ideally one would like to maximize the interface between the LiFePO₄ and the electrolyte to improve ionic charge transport, as well as maximize contact of the LiFePO₄ with the CB to improve the electronic charge transport.

Table 3.1. Microstructural parameters calculated from LiFePO₄ templated and standard cathode 3D reconstruction

	Templated	Standard
Volume Fraction (%)		
LiFePO ₄	50.3	52.5
Electrolyte	40.5	38.2
Carbon and Binder	9.2	9.3
Interfacial area (μm^{-1})		
LiFePO ₄	8.25	8.93
Electrolyte	2.9	2.95
CB SA _i	5.91	6.14
LiFePO ₄ /Electrolyte	5.63	6.06
LiFePO ₄ /CB	2.62	2.87
Electrolyte/CB	0.28	0.08

The volume fraction calculations on each phase agree well with prior work on similar samples[29], which not only validates the segmentation process but also indicates that the as-obtained reconstruction volume can be obtained with excellent statistics to represent the whole electrode. For both templated and standard electrodes, the active material occupies more than 50% of the volume. Thus, consistent with previous work[21,30], the templating does not negatively influence the volumetric energy density. Also a similar active fraction has previously been reported for high power commercial LiFePO_4 cells[45]. Also the templating method leads to a marginal ($\sim 2\%$) increase in porosity. The calculation of the CB volume shows nearly identical values in both electrodes. All the interphase areas are lower in the templated electrode. This supports the above mentioned notion that the templated electrode is locally densely packed, whereas the standard sample is more homogenous.

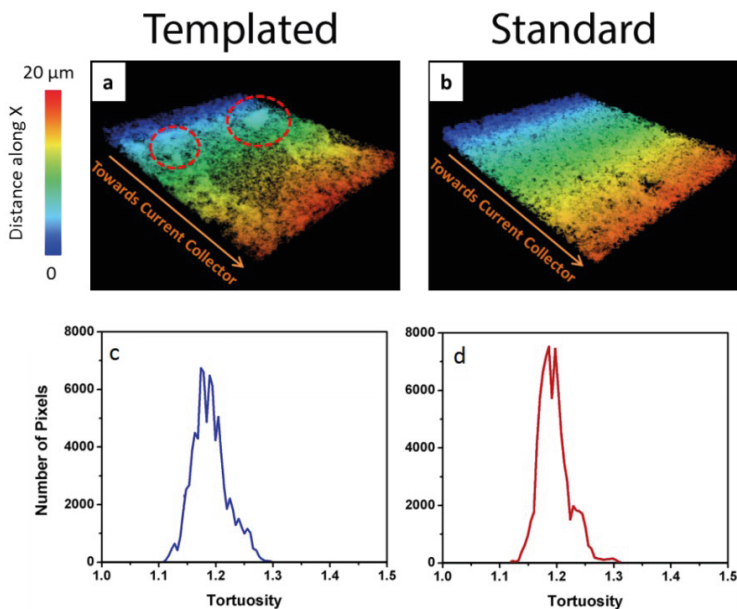


Figure 3.5 Three-dimensional distance map of electrolyte in the direction towards the current collector (along X direction) for (a) templated and (b) standard electrode (a thin slice along X-Z plane); (c) and (d) Histograms of the tortuosity distribution of electrolyte corresponding to X=14,5 micron,

the end of the analysed volume; Red dashed circle in (a) indicates the micron-size pores in the templated electrode.

In-depth knowledge of the electrode transport properties was gained via the quantitative analysis on the connectivity and tortuosity of electrolyte and CB phases. The analysis on the 3D electrolyte distance map and tortuosity distribution is shown in **Figure 3.6**. The connectivity of the percolated electrolyte volume towards the current collector is $\sim 100\%$ for both templated and standard electrodes, which indicates that the electrolyte accessibility in both electrodes is similar. Almost all active material particles are somewhere connected to the electrolyte. It is not known which surfaces are touching the electrolyte and this could be relevant as in LiFePO_4 lithium diffusion is strictly one dimensional[50]. Earlier work[37], using a simple model with diffusivities corrected with a Bruggeman exponent had suggested a lower tortuosity for the templated sample. However, despite the substantial differences in electrode structure, there were no differences in the measured directional tortuosity of the electrolyte networks in the templated and standard electrodes. Although the micron-size pores (indicated in red dashed circle) are visible in the distance map of the templated sample, it does not improve the Li^+ ion diffusion significantly in terms of propagation distance. **Figure 3.6.c–d** depicts the tortuosity distribution at the plane ($X=14.5 \mu\text{m}$) close to the current collector. The tortuosity distributions of the two samples are quite similar, the values are ranging from 1.1 to 1.3. Note that the presented geometric tortuosity calculation does not account for effects of the pore size on transport properties, compared to a diffusion-based calculation or a full 3D simulation[18].

The CB phase connectivity was significantly higher for the templated electrode (Table 1). **Figure 3.6.a-b** depict the 3D reconstruction of the CB phase in the templated and standard electrode and demonstrates percolated, unknown and isolated portions, see also **table 3.2**. Clearly, the CB phase in the standard sample has more isolated regions (11%) than in templated sample (6.7%). These isolated regions are unfavorable, because they cannot contribute during cycling and hence result in a lower power

density. This is consistent with the higher capacities achieved even at slow charging for the templated electrodes as observed in **Figure 3.2.a** and consistent with NDP measurements for which also similar quantities of unreacted material have been found in empty, charged, electrodes, see Figures Appendix D.

Table 3.2. Electronic connectivity of CB phase in templated and standard electrodes

	Templated	Standard
Percolated (%)	89.2	83.6
Unknown (%)	4.1	5.4
Isolated (%)	6.7	11

The CB phase tortuosity, measured directionally towards the separator, was found to be ~36% percent lower (2.2) for the templated sample, compared to the standard sample (3.0). **Figures 3.6.c-f** show the 3D distance map and spatially resolved tortuosity distribution of CB phase in templated and standard samples. The longest electron transport path in the standard sample is 55 μm , while it is 38 μm in the templated sample. The higher tortuosity in the standard sample will result in a higher electronic resistance and hence larger overpotential during (dis)charge. Moreover, the CB phase tortuosity distribution in the standard sample is more heterogeneous than in the templated sample. The large isolated fraction and spread in electron path length in the standard sample could explain why large local differences in the state of charge have been reported[13, 14].

As the differences in terms of interfacial area and volume fractions are small, these electrodes are ideal for studying the observed differences in connectivity and tortuosity. To gain more insight in how these 3D electrode structural features influence the electrode performance, neutron depth profiling (NDP) is used; this technique allows direct, non-destructive and continuous measurement of the lithium concentration depth profile in Li-ion electrodes on the micron scale.[3, 51-53]. This distribution of Li-ions as a function of electrode depth, reflects the in-electrode-plane averaged state of (dis)charge and allows studying of electrode transport phenomena.

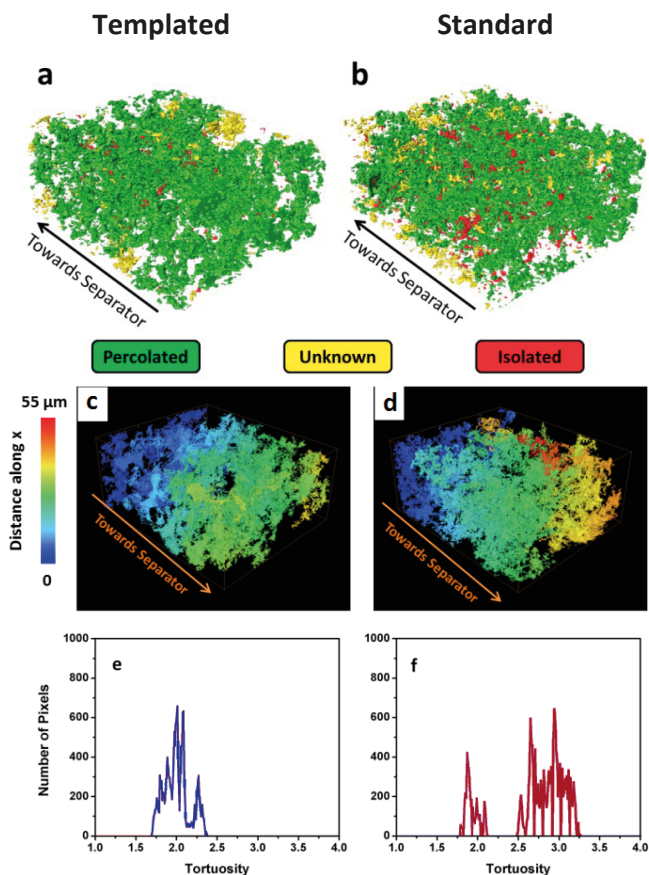


Figure 3.6. 3D image reconstructions showing the directional connectivity of the CB phase of the templated (a) and standard (b) electrode. Three-dimensional distance map of CB in the direction towards the separator (along X direction) for (a) templated and (b) standard electrodes; (e) and (f) Histograms of the tortuosity distribution of CB corresponding to $x=0$, the start of the analysed volume.

Previous work has shown that at high (dis)charge rates, the activity of the electrode material is limited to the part of the electrode located near the electrolyte, indicating that ionic conduction through the electrode morphology is the rate limiting charge transport mechanism[3, 4, 16, 25, 54, 55]. This is supported by the present NDP results in **Figures 3.6.a-d** showing the average state of (dis)charge as a function of electrode depth after (dis)charging with various rates until reaching the cut off voltage, for

electrodes with a thickness of approximately 35 μm . After charging at 20C (**Figure 3.6.a**) and after discharge at 10C (**Figure 3.6.b**) and 5C (**Figure 3.6.d**), the part of the electrode near the electrolyte reaches the highest state of (dis)charge. Near the electrolyte, the active material can still be supplied with Li-ions from the electrolyte (in the separator) during discharge and vice versa during charge. Further from the electrolyte, however, Li-ion transport within the electrode's electrolyte phase limits (dis)charge, leading to high internal resistance at these high rates.

In contrast to 10C discharging, at 10C charging (**Figure 3.6.c**) a depth independent state of charge is observed for both the standard and templated electrodes. This indicates that the Li-ion transport through the electrolyte (located in the pores of the electrode) is better during charge as compared to discharge. Upon discharge, the electrolyte at the current collector will be depleted, whereas upon charge, the electrolyte will be saturated. Simulations have shown, that even at a relatively low discharge rate (C/7) the molarity locally could drop to 0.2 molar (starting at a 1.0 molar equilibrium concentration)[16]. Assuming that the electrolyte has the optimal molarity with respect to Li-ion conductivity, both depletion and saturation lead to a decrease in the ionic conductivity of the electrolyte[56], depletion through the reduction in available Li-ions and saturation through the increase of the viscosity, lowering the Li-ion diffusivity. As such, a battery containing an electrolyte of non-optimal concentration would show either a higher charge or discharge capacity compared to a battery containing standard electrolyte, this has been recently demonstrated by Kitada et al.[54] It should be expected, that upon electrolyte depletion (discharge) the Li-ion conductivity will drop more dramatically, explaining the better Li-ion transport during charge which results in the higher state of charge reached at fast charging as compared to discharging (see **Figure 3.7**)[55].

Consistent with the electrochemical results in **Figure 3.2** the depth dependent state of (dis)charge shown in **Figure 3.7.a-d** display a larger state of (dis)charge after high rate (dis)charge throughout the electrodes. **Figure 3.7.a** and **b** proves that templating improves the state of (dis)charge both near the current collector and near the electrolyte, indicating that not only

the Li-ion transport is improved, but also the electronic transport. Although the templating does not improve the tortuosity of the porous electrolyte network, as concluded from the 3D image reconstruction result in **Table 3.2**, it is possible that the presence of larger voids, introducing a multiple length-scale pore network, may be responsible for the better ionic transport[46]. As discussed above, during discharge the improved ionic transport is not effective, most likely because of depletion of the electrolyte. The increase in state of (dis)charge near the electrolyte side indicates that templating also improves electronic transport. For 20C charge the state of charge throughout the electrode is enhanced by the templating whereas on 10C and 5C discharge templating mainly improves the state of discharge near the electrolyte side requiring an improved electronic connection with the current collector. Indeed templating results in a significantly better tortuosity of the CB network as observed in **Figure 3.7**, which appears in large part to be the origin for the higher charge capacity of the templated electrodes.

In **Figure 3.7.e-f** the state of (dis)charge profiles are shown at approximately 50% state of charge and discharge at C/5 for both electrodes. The absence of a distribution in the state of (dis)charge as a function of depth in the templated electrodes confirms the better charge transport characteristics due to the templating. An interesting observation is that at C/5 charging the gradient in the standard electrode is reversed compared to 10C charging shown in **Figure 3.7.a**. Apparently, it is easier to delithiate the current collector side of the electrode, indicating that electronic transport is limiting at C/5 where Li-ion transport appears limiting at 20C. This is consistent with recent findings where it was shown that the rate limiting process actually depends on the (dis)charge rate, for the considered LiFePO_4 electrodes being nucleation at low rates, ionic transport through the electrolyte in the pores of the electrode at high rates, and electronic transport limitations at medium rates[3]. Recently Li et al.[17] also indicated that electronic transport may be rate limiting at specific conditions, demonstrating that the most resistive process in a LiFePO_4 electrode appears to be the electronic conduction

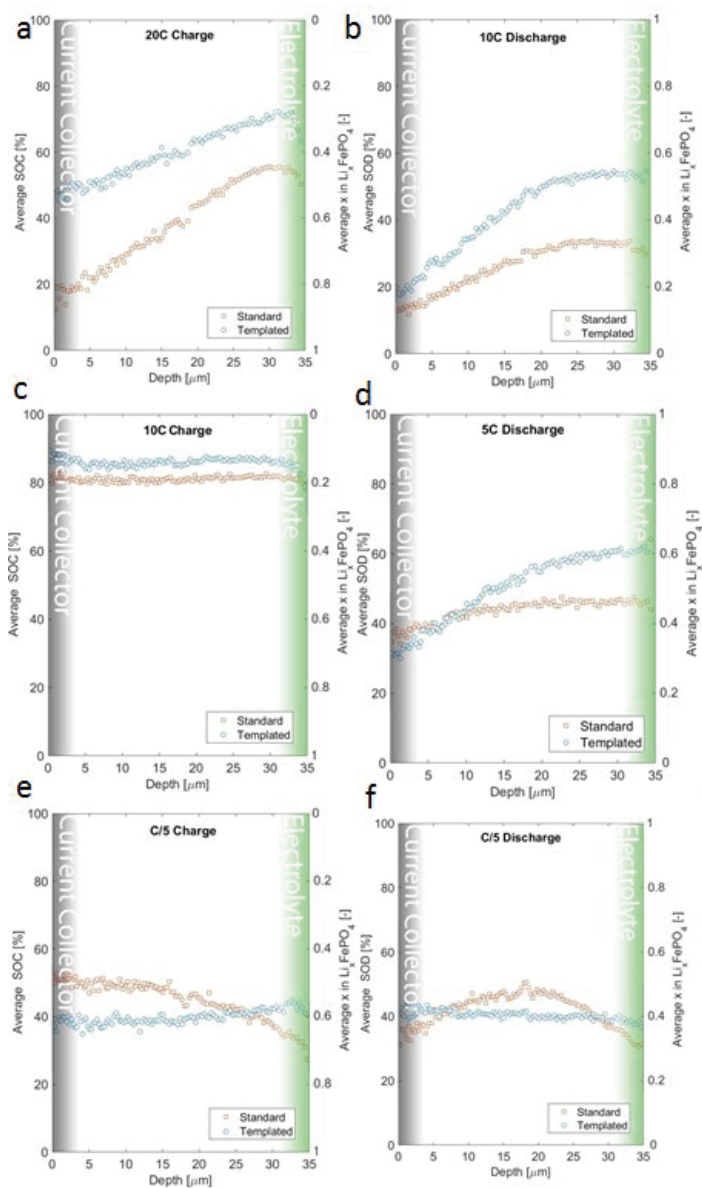


Figure 3.7. State of (dis)charge profiles after cycling at high rates for both templated and standard electrodes. e-f) State of (dis)charge profiles at approximately 50% state of (dis)charge during C/5 (dis)charging. The grey shade marks the location of the current collector and the green shade at approximately 35 μm the interface with the electrolyte.

between the LiFePO_4 particle surface and the nearest branch of the percolating carbon network. An interesting observation in **Figure 3.7.f** is the maximum in the state of discharge of the standard electrodes during C/5 discharge. This reflects the competition between ionic and electronic transport, apparently having a similar resistance at this discharge rate and for this specific electrode (3D structure and thickness). Again reflecting the differences between charge and discharge, demonstrating the importance of ionic limitations even at low discharge rates.

3.3 Consequences for application

The measurements presented in **Figure 3.7**, show that lithium ion concentration is not homogenous throughout the electrode layer. Instead a C-rate dependent distribution is measured, leading to a depth dependent state of charge. Now it is interesting to relate these lithium distributions to practical battery behaviour. Irregular loading (acceleration) and regenerative braking causes (dis)charge pulses in EV applications[57], leading to specific distributions of the ions in the active electrode material. In turn affecting the diffusion lengths and internal resistance.

To mimic this effect of irregular loading, an experiment is performed from 50% State Of Charge (SOC). In the experiment the available capacity when discharging at a high C-rate (5C) from 50% SOC as a function of (charge or discharge) current used to attain this state of charge. This experiment should indicate whether the distributions reported in **Figure 3.7**, affect the battery behaviour. To disentangle any effects unrelated with the lithium distribution in the active material a resting step is introduced, allowing electrolyte concentration gradients and the 'activated' particle fraction to relax[58]. To determine the necessary length of the rest period the following experiment is performed; a 2C charge or 2C discharge to 50% of the electrode capacity is followed by a rest period and a discharge at 5C to cut-off voltage 2.7V. Thus the time of the rest phase is varied and we follow the discharge capacity of the 5C discharge step, see **Figure 3.8**.

During charge and discharge the battery is out of thermodynamic equilibrium. Hence when disconnected from the load or power source, the battery components will equilibrate, the rate of these processes depends on

the energy barrier to be overcome and the energy penalty associated with the non-equilibrated state. One of the reasons why this work on LiFePO_4 demonstrates such clear results is the first order phase transition associated with (de)lithiation, allowing a mixture of Li-rich or Li-poor particles to be in thermodynamic equilibrium, hence there is no energy gained upon redistribution. A significant difference with respect to layered oxide cathodes, where the solid solution thermodynamics and the associated relation between lithium concentration and potential, remains a driving force to equilibrate the lithium concentration in active material particles[58, 59].

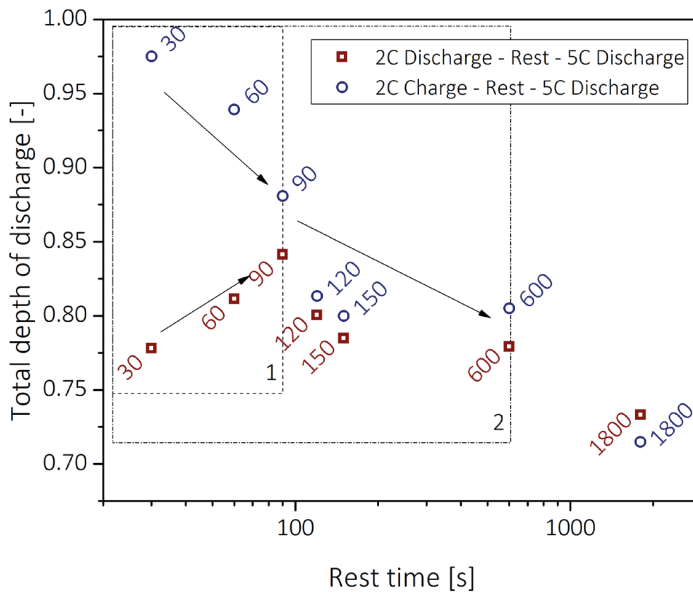


Figure 3.8 Discharge capacity versus the time between charge or discharge to 50% of the capacity. Red squares show charge followed by discharge, blue circles reflect discharge followed by discharge, when the capacity (y-axis) reaches 1 it means a full discharge to LiFePO_4 .

As detailed in the introduction the phase transition proceeds through (de)intercalation of the active material, in general this process is fast[15, 24-27]. The energy associated with the interface between the two phases can cause the activated particles to exchange with their neighbours, resulting in a mixture of particles either completely lithium rich or lithium poor after a

short rest[58]. Relaxation of inhomogeneity's in the electrolyte salt concentration is also expected to be a quick process, the driving force is small but the barrier to diffusion is low.

At short rest times, region 1, the electrolyte concentration is present[16], which favours reversing the direction of the current, hence in this time domain charge–rest-discharge leads to more capacity than the discharge–rest-discharge. This effect is clear up until 90s rest time. Here a maximum is reached in the discharge–rest-discharge curve. Having metastable, active particles can be expected to constitute an advantage as there is no overpotential needed to initiate the reaction[11, 12, 14]. Apparently this advantage outweighs any disadvantages associated to the concentration gradient in the electrolyte at around 90s. After two minutes both curves more or less align, indicating that electrolyte concentration gradients have homogenised at this time scale. Furthermore the capacity changes little between 150-600s an indication that most particles are out of a metastable state, region 2, a result confirmed in [12] where after 3 minutes only a small fraction of particles contain both phases. This result is important in the design of the aforementioned experiment, indicating that a rest time of 10 minutes should be sufficient to probe any effects associated with the lithium distribution. Certainly the rest time in between (dis)charge steps influences the following cycles and hence the notion of state of charge becomes more flexible at these discharge rates.

To answer the question posed at the start of this section, a test is performed where the (dis)charge rate of the first step is varied and, the rest time and discharge rate are constant. Plotted with black dots in **Figure 3.9**, a clear relation is seen between the C-rate of the first 'write' step and the capacity available when the battery, after a 10min rest, is discharged at 5C. The trend being that upon charge higher currents increase the subsequent discharge capacity and, inversely, higher discharge rates reduce the subsequent capacity. Even though these electrodes are thinner compared to those shown **Figure 3.6**, the results are consistent. Similar to what has been reported by Newman et al. in [60], yet owing to the NDP results we understand that with consecutive discharge the available capacity is located in a deeper region of

the electrode which requires a longer diffusion path which at these rates is the limiting factor, hence the 5C discharge capacity is lower. Whereas after a high rate charge the available capacity is located closer to the electrode electrolyte interface, reducing diffusion lengths. Note that the dotted line reflecting the 5C discharge capacity reached from a full C/10 charge is surpassed on each measurement. This is consistent with the rate limiting step being the salt concentration build up in the liquid electrolyte in the pores of the electrode. The rest period allows the concentration to equilibrate, after which discharge is restarted with 'refreshed' electrolyte, having higher conductivity due to lowered viscosity[61].

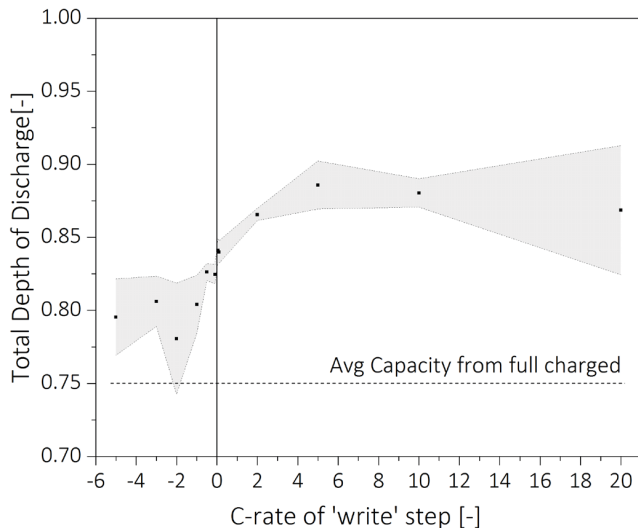


Figure 3.9. Memory effect in LiFePO_4 data is averaged from 8 batteries, error bar reflects the variance in the underlying data set. Y-axis values reflect total depth of discharge. The capacity of the 5C discharge is related to the c-rate of the previous cycle. The dotted line reflects the average capacity reached at 5C discharge after a C/10 full charge.

Both results in **Figures 3.8** and **3.9** are indicative of a memory effect where the cycle history affects the current battery properties. Similar effects have been previously reported[62] but never been related on electrode scale lithium distributions. Moreover in commercial batteries the cathode capacity is over dimensioned to compensate for ions lost in the formation of the Solid

Electrolyte Interphase layer, hence the remaining 80-90% is free to be stored as the lithium is replenished[63]. This means the described effect could be more significant in commercial applications. It demonstrates how valuable techniques like NDP are, in studying electrode materials and understanding battery behaviour.

3.4 Conclusions

Three-phase 3D reconstruction using FIB-SEM has been employed to investigate the origin of the improved rate performance of LiFePO_4 templated electrodes as compared to standard LiFePO_4 electrodes. Microstructural parameters were determined, including volume fraction, surface area, and feature size distributions of the active LiFePO_4 material, CB and the porous structure, where the latter is filled with electrolyte during battery operation. Due to the analogous electrode formulations most of these parameters, including the interphase areas, are found to be similar. This represents an almost ideal case study for direct comparison between the tortuosity and connectivity of templated and non-templated electrodes, giving unique insight in the origin of the differences in electrochemical performance, and more general in the relation between the electrode morphology and battery performance.

The CB and electrolyte connectivity, tortuosity, and tortuosity distributions were analyzed for both electrodes from the 3D images and compared. The connectivity calculation shows a fully percolated electrolyte phase for both templated and the standard electrodes. For the tortuosity in the electrolyte phase no significant differences were found between the two electrodes in contrast to what was concluded previously[36, 37]. Nevertheless it is proposed that the hierarchical interconnected porosity in the templated electrodes improves the ionic transport throughout the electrodes, partially responsible for the better rate performance. This is especially observed upon charge where direct observation of the average state of charge as a function of depth in the electrode by NDP reveals that, compared to the standard LiFePO_4 electrodes, the templated electrodes show much more charge activity near the current collector side. This is much less obvious during discharge, most likely due to electrolyte depletion reducing the conductivity

of the electrolyte, the apparent origin of the asymmetric charge-discharge performance.

Although the same amount of CB was used in both electrode formulations, the connectivity calculation based on the three-phase 3D reconstruction reveals that the CB network is more percolating in the templated electrodes, which must result in a higher electrical conductivity. Moreover, the tortuosity distribution of the electronic network is more homogeneous in the templated electrode making a larger part of the active material well connected to the CB network. This demonstrates that a lower electronic resistivity of the templated electrode is for a large part responsible for the improved capacities during charge and discharge at high rates. This is consistent with the larger charge and discharge activity in the templated electrode near the electrolyte/separator directly observed with NDP. The shift of the most active electrode region from the current collector side towards the electrolyte/separator side upon higher (dis)charge rates is consistent with recent findings[3], indicating that the rate limiting step for the charge transport in electrodes depends on the (dis)charge rate itself.

These results illustrate that typical electrodes have a far from optimal charge transport network, and that surprisingly the carbonate templating method results in a better electronic conductive CB network, in a large part responsible for the improved rate performance. Further improvement of the ionic and electronic network appears possible, signifying the importance of developing cheap and scalable methods to improve the charge transport in electrodes that will enable improved power and energy density of Li-ion batteries.

Moreover the measured NDP spectra have indicated an unobserved memory effect, as the rate limiting step of the previous cycle influences the distribution of lithium ions, which influences the internal resistance via the diffusion length through the pore network. Potentially having large implications for situations where the amount of ions exceeds the storage capacity as is the case for commercial electrodes, where part of the lithium reservoir is consumed in the formation of the SEI. Indicating the importance of the insights obtained using the NDP.

3.5 Methods

3.5.1 Electrode preparation

The preparation method of both the conventional, referred to as standard, as well as the enhanced electrode can be found in previous work[37] and in **Appendix D**. For both electrodes the compacting pressure, current collector and compositions are the same, the difference is the 40 %wt. NaHCO_3 (Aldrich) which is added to the templated electrode slurry, which, after pressing, is allowed to react with demineralized water under the formation of water soluble NaOH and gaseous CO_2 . The gas formation is visible as small bubbles are exiting the electrode, leaving channels that will later be filled with electrolyte.

3.5.2 Three phase 3D imaging

In order to provide contrast between the different carbon based materials, in the carbon black and the PVDF binder, a two part commercial silicone resin was used in preparation for the FIB-SEM process. A more thorough description of the sample preparation can be found in [42, 43] and in appendix D. The as-collected 2D image sequences were aligned, cropped and stacked into a 3D microstructure using a method previously described[38]. Each sample volume was cropped into the identical size ($14.5 \mu\text{m} \times 12.3 \mu\text{m} \times 6.4 \mu\text{m}$, $1140 \mu\text{m}^3$). Image segmentation was performed via multi-level Otsu's method to attribute different grey scale intensity values to different phases, where white (grey scale intensity: 255) is assigned to LiFePO_4 particles, grey (127) to resin-infiltrated porosity, and black (0) to carbon and binder[64]. It is noted that the resin-infiltrated porosity corresponds to regions which normally are occupied by the liquid electrolyte; hence this region will be referred to as electrolyte in the following text. After segmentation, the noise filter built in ImageJ (National Institutes of Health, MD, USA) was used on images that needed further noise reduction and Amira 5.5.0 (FEI Visualization Sciences Group, MA) was used for 3D visualization[65]. The goal is to quantitatively analyse microstructural parameters such as volume fraction, surface area, feature size distribution, directional connectivity, tortuosity, and tortuosity distribution from 3D reconstruction volume. The 3D surface mesh was created via a marching cube algorithm to obtain the surface area[66]. Interfacial surface area density

(SA_i) was then calculated by normalizing the surface area of each phase to the total reconstruction volume. The feature size distribution of each phase was calculated via the method introduced by Münch et al[67]. Connectivity and tortuosity are two important parameters that represent transport properties of the electrode, which were used to analyse electrolyte (ionic transport) and CB phase (electrical transport). The phase connectivity is determined by running a connected component labelling algorithm (function “bwlabeln” in MATLAB) through the 3D volume. By definition, there are three types of regions presented in the results. The region fully connected to target plane is defined as “Percolated”, and region which touch other faces (neither source plane nor the target plane) but not the percolating volume are labelled as “Unknown”. Regions that are completely isolated from the percolating and unknown regions are defined as “Isolated”. Tortuosity and tortuosity distribution were calculated via a geometric method, namely the directional propagation method, introduced by Chen-Wiegart et al[68].

3.6 References

1. Thorat, I.V., et al., *Understanding Rate-Limiting Mechanisms in LiFePO₄ Cathodes for Li-Ion Batteries*. Journal of The Electrochemical Society, 2011. **158**(11): p. A1185-A1193.
2. Jow, T.R., et al., *Factors Limiting Li⁺ Charge Transfer Kinetics in Li-Ion Batteries*. Journal of The Electrochemical Society, 2018. **165**(2): p. A361-A367.
3. Zhang, X.Y., et al., *Direct Observation of Li-Ion Transport in Electrodes under Nonequilibrium Conditions Using Neutron Depth Profiling*. Advanced Energy Materials, 2015. **5**(15): p. 1500498.
4. Ogihara, N., et al., *Impedance Spectroscopy Characterization of Porous Electrodes under Different Electrode Thickness Using a Symmetric Cell for High-Performance Lithium-Ion Batteries*. Journal of Physical Chemistry C, 2015. **119**(9): p. 4612-4619.
5. Padhi, A.K., et al., *Phospho-olivines as Positive-Electrode Materials for Rechargeable Lithium Batteries*. Journal of The Electrochemical Society, 1997. **144**(4): p. 1188-1194.
6. Huang, H., et al., *Approaching theoretical capacity of LiFePO₄ at room temperature at high rates*. Electrochemical and Solid-State Letters, 2001. **4**(10): p. A170-A172.
7. Ravet, N. et al. in 196th Electrochemical Society Meeting, Honolulu, *Hawaii Abstract 127* (Electrochemical Society, Pennington, New Jersey, 1999).

8. Herle, P.S., et al., *Nano-network electronic conduction in iron and nickel olivine phosphates*. Nature Materials, 2004. **3**(3): p. 147-152.
9. Delmas, C., et al., *Lithium deintercalation in LiFePO₄ nanoparticles via a domino-cascade model*. Nature Materials, 2008. **7**(8): p. 665-671.
10. Li, Y., et al., *Current-induced transition from particle-by-particle to concurrent intercalation in phase-separating battery electrodes*. Nature Materials, 2014. **13**(12): p. 1149-1156.
11. Ferguson, T.R. and Bazant, M.Z., *Nonequilibrium Thermodynamics of Porous Electrodes*. Journal of The Electrochemical Society, 2012. **159**(12): p. A1967-A1985.
12. Chueh, W.C., et al., *Intercalation Pathway in Many-Particle LiFePO₄ Electrode Revealed by Nanoscale State-of-Charge Mapping*. Nano Letters, 2013. **13**(3): p. 866-872.
13. Robert, D., et al., *Multiscale phase mapping of LiFePO₄-based electrodes by transmission electron microscopy and electron forward scattering diffraction*. ACS Nano, 2013. **7**(12): p. 10887-10894.
14. Ouvrard, G., et al., *Heterogeneous behaviour of the lithium battery composite electrode LiFePO₄*. Journal of Power Sources, 2013. **229**: p. 16-31.
15. Zhang, X., et al., *Rate-Induced Solubility and Suppression of the First-Order Phase Transition in Olivine LiFePO₄*. Nano Letters, 2014. **14**(5): p. 2279-2285.
16. Strobridge, F.C., et al., *Mapping the Inhomogeneous Electrochemical Reaction Through Porous LiFePO₄-Electrodes in a Standard Coin Cell Battery*. Chemistry of Materials, 2015. **27**(7): p. 2374-2386.
17. Li, Y., et al., *Effects of Particle Size, Electronic Connectivity, and Incoherent Nanoscale Domains on the Sequence of Lithiation in LiFePO₄ Porous Electrodes*. Advanced Materials, 2015. **27**(42): p. 6591-+.
18. Kehrwald, D., et al., *Local tortuosity inhomogeneities in a lithium battery composite electrode*. Journal of the Electrochemical Society, 2011. **158**(12): p. A1393-A1399.
19. Katayama, M., et al., *X-ray absorption fine structure imaging of inhomogeneous electrode reaction in LiFePO₄ lithium-ion battery cathode*. Journal of Power Sources, 2014. **269**: p. 994-999.
20. Cogswell, D.A. and Bazant, M.Z., *Coherency Strain and the Kinetics of Phase Separation in LiFePO₄ Nanoparticles*. ACS Nano, 2012. **6**(3): p. 2215-2225.
21. Li, Y., et al., *Dichotomy in the Lithiation Pathway of Ellipsoidal and Platelet LiFePO₄ Particles Revealed through Nanoscale Operando State-of-Charge Imaging*. Advanced Functional Materials, 2015. **25**(24): p. 3677-3687.
22. Cogswell, D.A. and Bazant, M.Z., *Theory of Coherent Nucleation in Phase-Separating Nanoparticles*. Nano Letters, 2013. **13**(7): p. 3036-3041.
23. Bai, P., et al., *Suppression of Phase Separation in LiFePO₄ Nanoparticles During Battery Discharge*. Nano Letters, 2011. **11**(11): p. 4890-4896.

- 
24. Malik, R., et al., *Kinetics of non-equilibrium lithium incorporation in LiFePO₄*. Nat Mater, 2011. **10**(8): p. 587-590.
 25. Liu, H., et al., *Capturing metastable structures during high-rate cycling of LiFePO₄ nanoparticle electrodes*. Science, 2014. **344**(6191).
 26. Orikasa, Y., et al., *Direct observation of a metastable crystal phase of Li_xFePO₄ under electrochemical phase transition*. Journal of the American Chemical Society, 2013. **135**(15): p. 5497-5500.
 27. Orikasa, Y., et al., *Transient phase change in two phase reaction between LiFePO₄ and FePO₄ under battery operation*. Chemistry of Materials, 2013. **25**(7): p. 1032-1039.
 28. Yu, D.Y.W., et al., *Effect of electrode parameters on LiFePO₄ cathodes*. Journal of the Electrochemical Society, 2006. **153**(5): p. A835-A839.
 29. Gaberscek, M, et al., *Electrochemical kinetics of porous, carbon-decorated LiFePO₄ cathodes: Separation of wiring effects from solid state diffusion*. Physical Chemistry Chemical Physics, 2007. **9**(15): p. 1815-1820.
 30. Fongy, C., et al., *Electronic and Ionic Wirings Versus the Insertion Reaction Contributions to the Polarization in LiFePO₄ Composite Electrodes*. Journal of the Electrochemical Society, 2010. **157**(12): p. A1347-A1353.
 31. Fongy, C., et al., *Ionic vs Electronic Power Limitations and Analysis of the Fraction of Wired Grains in LiFePO₄ Composite Electrodes*. Journal of the Electrochemical Society, 2010. **157**(7): p. A885-A891.
 32. Johns, P.A., et al., *How the electrolyte limits fast discharge in nanostructured batteries and supercapacitors*. Electrochemistry Communications, 2009. **11**(11): p. 2089-2092.
 33. Danilov, D. and Notten, P.H.L., *Mathematical modelling of ionic transport in the electrolyte of Li-ion batteries*. Electrochimica Acta, 2008. **53**: p. 5569-5578.
 34. Liu, J., et al., *Visualization of charge distribution in a lithium battery electrode*. Journal of Physical Chemistry Letters, 2010. **1**(14): p. 2120-2123.
 35. Singh, M., et al., *Effect of Porosity on the Thick Electrodes for High Energy Density Lithium Ion Batteries for Stationary Applications*. Batteries, 2016. **2**(4): p. 35.
 36. Singh, D.P., et al., *Facile Micro Templating LiFePO₄ Electrodes for High Performance Li-Ion Batteries*. Advanced Energy Materials, 2013. **3**(5): p. 572-578.
 37. Singh, D.P., et al., *Templated spinel Li₄Ti₅O₁₂ Li-ion battery electrodes combining high rates with high energy density*. Electrochemistry Communications, 2013. **35**: p. 124-127.
 38. Wilson, J.R., et al., *Three-dimensional reconstruction of a solid-oxide fuel-cell anode*. Nature Materials, 2006. **5**(7): p. 541-544.
 39. Liu, Z., et al., *Relating the 3D electrode morphology to Li-ion battery performance; a case for LiFePO₄*. Journal of Power Sources, 2016. **324**: p. 358-367.

40. Chen-Wiegart, Y., et al., *3D analysis of a LiCoO₂-Li(Ni_{1/3}Mn_{1/3}Co_{1/3})O₂ Li-ion battery positive electrode using x-ray nano-tomography*. *Electrochemistry Communications*, 2013. **28**: p. 127-130.
41. Wiedemann, A.H., et al., *Effects of three-dimensional cathode microstructure on the performance of lithium-ion battery cathodes*. *Electrochimica Acta*, 2013. **88**: p. 580-588.
42. Hutzenlaub, T., et al., *Three-dimensional reconstruction of a LiCoO₂ Li-ion battery cathode*. *Electrochemical and Solid-State Letters*, 2012. **15**(3): p. A33-A36.
43. Hutzenlaub, T., et al., *Three-dimensional electrochemical Li-ion battery modelling featuring a focused ion-beam/scanning electron microscopy based three-phase reconstruction of a LiCoO₂ cathode*. *Electrochimica Acta*, 2014. **115**: p. 131-139.
44. Ender, M., et al., *Three-dimensional reconstruction of a composite cathode for lithium-ion cells*. *Electrochemistry Communications*, 2011. **13**(2): p. 166-168.
45. Ender, M., et al., *Quantitative characterization of LiFePO₄ cathodes reconstructed by FIB/SEM tomography*. *Journal of the Electrochemical Society*, 2012. **159**(7): p. A972-A980.
46. Bae, C.J., et al., *Design of battery electrodes with dual-scale porosity to minimize tortuosity and maximize performance*. *Advanced Materials*, 2013. **25**(9): p. 1254-1258.
47. Fukutsuka, T., et al., *Ion Transport in Organic Electrolyte Solution through the Pore Channels of Anodic Nanoporous Alumina Membranes*. *Electrochimica Acta*, 2016. **199**: p. 380-387.
48. Malavé, V., et al., *A computational model of the mechanical behavior within reconstructed Li_xCoO₂ Li-ion battery cathode particles*. *Electrochimica Acta*, 2014. **130**: p. 707-717.
49. Goldin, G.M., et al., *Three-dimensional particle-resolved models of Li-ion batteries to assist the evaluation of empirical parameters in one-dimensional models*. *Electrochimica Acta*, 2012. **64**: p. 118-129.
50. Ouyang, C., et al., *First-principles study of Li ion diffusion in LiFePO₄*. *Physical Review B - Condensed Matter and Materials Physics*, 2004. **69**(10): p. 1043031-1043035.
51. Oudenhoven, J.F.M., et al., *In Situ Neutron Depth Profiling: A Powerful Method to Probe Lithium Transport in Micro-Batteries*. *Advanced Materials*, 2011. **23**(35): p. 4103-+.
52. Wang, J., et al., *Profiling lithium distribution in Sn anode for lithium-ion batteries with neutrons*. *Journal of Radioanalytical and Nuclear Chemistry*, 2014. **301**(1): p. 277-284.
53. Liu, D.X., et al., *In Situ Quantification and Visualization of Lithium Transport with Neutrons*. *Angewandte Chemie-International Edition*, 2014. **53**(36): p. 9498-9502.

- 
54. Kitada, K., et al., *Factors determining the packing-limitation of active materials in the composite electrode of lithium-ion batteries*. Journal of Power Sources, 2016. **301**: p. 11-17.
 55. Roberts, M.R., et al., *Direct observation of active material concentration gradients and crystallinity breakdown in LiFePO₄ electrodes during charge/discharge cycling of lithium batteries*. Journal of Physical Chemistry C, 2014. **118**(13): p. 6548-6557.
 56. Valøen, L.O. and Reimers, J.N., *Transport properties of LiPF₆-based Li-Ion battery electrolytes*. Journal of the Electrochemical Society, 2005. **152**(5): p. A882-A891.
 57. H. J. Rajmakers, L., et al., *Non-Zero Intercept Frequency: An Accurate Method to Determine the Integral Temperature of Li-Ion Batteries*. Vol. 63. 2016. 1-1.
 58. Tanida, H., et al., *Elucidating the Driving Force of Relaxation of Reaction Distribution in LiCoO₂ and LiFePO₄ Electrodes Using X-ray Absorption Spectroscopy*. The Journal of Physical Chemistry C, 2016. **120**(9): p. 4739-4743.
 59. Jia, J.F., et al., *Relaxation-Induced Memory Effect of LiFePO₄ Electrodes in Li-Ion Batteries*. Acs Applied Materials & Interfaces, 2017. **9**(29): p. 24561-24567.
 60. Srinivasan, V. and Newman, J., *Existence of path-dependence in the LiFePO₄ electrode*. Electrochemical and Solid State Letters, 2006. **9**(3): p. A110-A114.
 61. Valøen, L.O. and Reimers, J.N., *Transport properties of LiPF₆-based Li-ion battery electrolytes*. Journal of the Electrochemical Society, 2005. **152**(5): p. A882-A891.
 62. Sasaki, T., Y. Ukyo, and P. Novak, *Memory effect in a lithium-ion battery*. Nat Mater, 2013. **12**(6): p. 569-75.
 63. Shanmukaraj, D., et al., *Sacrificial salts: Compensating the initial charge irreversibility in lithium batteries*. Electrochemistry Communications, 2010. **12**(10): p. 1344-1347.
 64. Otsu, N., *THRESHOLD SELECTION METHOD FROM GRAY-LEVEL HISTOGRAMS*. IEEE Trans Syst Man Cybern, 1979. **SMC-9**(1): p. 62-66.
 65. Abràmoff, M.D., P.J. Magalhães, and S.J. Ram, *Image processing with imageJ*. Biophotonics International, 2004. **11**(7): p. 36-41.
 66. Lorensen, W.E. and H.E. Cline, *MARCHING CUBES: A HIGH RESOLUTION 3D SURFACE CONSTRUCTION ALGORITHM*. Computer Graphics (ACM), 1987. **21**(4): p. 163-169.
 67. Münch, B. and L. Holzer, *Contradicting geometrical concepts in pore size analysis attained with electron microscopy and mercury intrusion*. Journal of the American Ceramic Society, 2008. **91**(12): p. 4059-4067.
 68. Chen-Wiegart, Y., et al., *Tortuosity characterization of 3D microstructure at nano-scale for energy storage and conversion materials*. Journal of Power Sources, 2014. **249**: p. 349-356.

4.

The Lightest Anode, Lithium Metal
Electrochemically Plated on Copper

4. The Lightest Anode, Lithium Metal Electrochemically Plated on Copper

Currently the lithium metal anode is in a true renaissance. It has regained a lot of scientific attention recently as successful implementation could mark the end of the lithium ion battery. In the first chapter, the general introduction, sulfur and oxygen have been mentioned as opportunities to increase energy density. These systems however benefit from a lithium metal anode to achieve their potential. Stable lithium metal anodes have been a research topic since the 1970s and progress is only barely made. In this chapter it is demonstrated how Neutron Depth Profiling can be used to shed new light on the matter. The work presented here is based on the following publications;

Shasha Lv, Tomas Verhallen, Alexandros Vasileiadis, Frans Ooms, Yaolin Xu, Zhaolong Li, Zhengcao Li and Marnix Wagemaker; **Operando monitoring the lithium spatial distribution of lithium metal anodes**; Nature Communications, volume 9, (2018)

The paper is published open access, under a CC BY 4.0 license, <http://creativecommons.org/licenses/by/4.0/>, Figures 4.1 till 4.6 are re-used from this paper, Figure 4.6 has been adapted, it no longer shows lithium presence in the copper current collector.

Tomas Verhallen, Shasha Lv, Marnix Wagemaker; Operando Neutron Depth Profiling to Determine the Spatial Distribution of lithium in Li-ion Batteries; Front. Energy Res., 03 July 2018

4.1 Introduction

Based on their large gravimetric and volumetric energy densities, Li-ion batteries are the technology of choice for portable electronics and electrical mobility[1-3]. The specific weight of the positive and negative electrodes in Li-ion batteries are the decisive factor in the energy density. Li-ion insertion chemistries are approaching their limit and hence intensive research is directed towards high capacity alternatives; the Li-S and Li-O₂ conversion cathodes[4-7], and lithium metal having the highest specific capacity (3860 mAh·g⁻¹). This ultimate anode offers a capacity ten times larger than the

current standard, the graphite anode (370 mAh g^{-1}), and the lowest possible redox potential (-3.04 V versus standard hydrogen). For these reasons lithium metal was already vigorously studied in the early stages of lithium battery research[8, 9]. However, dendrite formation and the associated safety risks shifted the focus to intercalation alternatives, such as graphite[10].

The major challenges for lithium metal anodes are safety and cyclability, due to its tendency to form dendritic and porous deposits, directly related to its low potential and subsequent reactivity towards common electrolytes[2, 8, 11, 12]. Dendrites are branched, needle-like structures able to protrude the separator, causing internal short-circuit when they reach the cathode. This induces spontaneous and rapid self-discharge, leading to local heating, potentially instigating gas production and violent cell failure. Recently, a diversity of promising strategies have been proposed, either aiming at prevention, suppression or blocking dendrite formation[12-15]. These strategies are mainly based on insights gained through employing microscopic and optical techniques[12-15]. Pei et al.[16] demonstrated using SEM that the lithium metal nuclei density is proportional to the cubic power of the overpotential, consistent with classical nucleation and growth theory. Cryogenic TEM revealed the preferred growth facets of lithium metal and the nature of the Solid Electrolyte Interphase (SEI) nanostructures in various electrolytes[17]. SEM and optical studies have shown a correlation between the current density and the plated lithium metal microstructure in line with the Chazalviel model[18]. This model allows to calculate the time it takes to deplete the surface of the anode of lithium ions at a certain current density. This time is commonly referred to as Sand's time[19, 20]. When the electrolyte close to the plated surface is depleted of ions, the process continues inhomogeneously and the self-amplified growth of dendrites is induced[18, 19, 21]. Below this critical current, lithium deposits dominantly as whiskers in carbonaceous electrolytes[19], which is believed to be the result of the formation of the SEI on the surface, resulting in porous lithium metal/SEI heterogeneous morphologies. However, over a number of cycles dendrites can grow at currents far below the critical current density[12-15, 22, 23]. During battery operation fresh lithium metal surface is exposed to

the electrolyte. This induces SEI formation through electrolyte reduction. These processes continuously follow each other adding to a complex microstructure of SEI and metallic lithium. The resistance of this layer lowers the coulombic efficiency and raises the internal resistance, reducing the capacity and eventually leading to complete failure. Additionally, the microstructural evolution during stripping may leave electronically isolated regions of lithium metal. This so called “dead” lithium metal contributes to capacity loss, and could play an important role in the penetration of dendrites. Therefore, the evolution of the lithium metal microstructure should be monitored from the onset to assess the safety risks and energy storage efficiency of lithium metal batteries.

This has motivated the use and development of several microscopic and spectroscopic characterization approaches, mostly under *ex-situ* or *in-situ* conditions[12, 13, 24] as *operando* characterization is more challenging. *In-situ* TEM microscopic studies have been able to observe the local plating reactions, including local dendrite growth and SEI formation[25-31] Typically, these *in-situ* open cell TEM as well as SEM[32, 33] experiments are limited to low volatile electrolytes (e.g. ionic liquids and solid electrolytes). Recently nanoscale imaging was achieved with *in-situ* TEM for liquid cells[34] which allowed detailed local characterization of the lithium metal plating[29] and SEI phases[35, 36], although care should be taken for the potential influence of the electron beam on the system[37, 38]. *In-situ* and *operando* optical microscopy as well as using laser scanning confocal microscopy has been used to observe the evolution of dendrites giving direct insight in the factors that influence dendritic deposition of lithium[19, 21, 39-42]. *Operando* ^7Li NMR spectroscopy and electron paramagnetic resonance spectroscopy have been shown to be promising approaches to monitor the nature of the lithium species[43, 44] whereas *in-situ* ^7Li NMR imaging was shown to be able to measure the lithium metal microstructure buildup with sub-micron resolution[44]. Synchrotron hard X-ray micro tomography experiments were able to observe lithium dendritic structures in polymer cells[45, 46]. Despite these crucial advances in *in-situ* and *operando* characterizations, lithium metal research would benefit from the development of quantitative and non-invasive techniques that operate under realistic *operando* battery conditions.

Developing understanding of the lithium anode microstructures is challenged by the difficulty to detect Li, both its quantitative distribution and chemical form, in particular during battery operation[12-15, 47].

Here we apply Neutron Depth Profiling (NDP) to provide quantitative, non-invasive *operando* measurements of the Li-ion concentration as a function of depth in lithium metal anodes, allowing complementary insights to microscopic and spectroscopic techniques[47-51]. Focusing on the plating and stripping activity in liquid electrolyte symmetric cells, utilizing asymmetric cells employing bare copper foil current collectors NDP will allow to follow the lithium (dis)charge efficiency as a function of current density, cycling history and salt concentration.

4.2 Results

Lithium metal cells employing a LiPF_6 EC/DMC liquid electrolyte will be used to investigate lithium plating and stripping on a copper current collector. ^6Li enriched lithium metal was used (95% ^6Li and 5% ^7Li), because natural lithium consists of only 7.5% of the isotope, this significantly increases counting rates especially at the start of discharge where at the onset of growth, little lithium is present. There is no reason to assume that this enrichment influences the metal and plating reactions. The electrolyte is enriched by bringing the electrolyte in contact with excess enriched lithium metal of the same source. Since the ^4He particles are not able to pass the copper current collector, only the ^3H particles, tritons, are detected during the experiments. The depth as shown in **Figure 4.1.b** is measured starting from the interface with the copper current collector and chamber atmosphere, which is kept at 200 mTorr. Positioned at approximately 12 μm , the interface of the copper current collector with the interior of the cell is observed by the count rate increase hence reflecting the presence of Li. The 12 μm thick copper foil results in a loss of 1040 keV of the initial 2727 keV of the ^3H . The conversion from energy to depth, background and intensity correction are performed as described in the methods chapter 2 and some specific details are found at the end of this chapter. In **Figure 4.1.b** the lithium density normalized to lithium metal is shown, hence it should be read as the fractional density with respect to lithium metal. The depth resolution for these systems is

The lightest anode

approximately 1 micron, which is dictated by the stochastic nature of the interactions of the ^3H particles with gas and current collector along the path between the lithium in the electrode and the detector referred to as straggling, see chapter 2. Nonetheless NDP results allow for unique insights in lithium density or approximate porosity of the deposited lithium metal.

In **Figure 4.1.b** *operando* NDP results are shown for 4 subsequent electrochemical cycles, plating and stripping at 1 mA cm^{-2} up to a capacity of 1 mAh cm^{-2} during which measurements are recorded every minute. During plating, discharge, the detected lithium density on the $12 \mu\text{m}$ thick copper current collector increases, whereas the lithium density decreases during the stripping or charging.

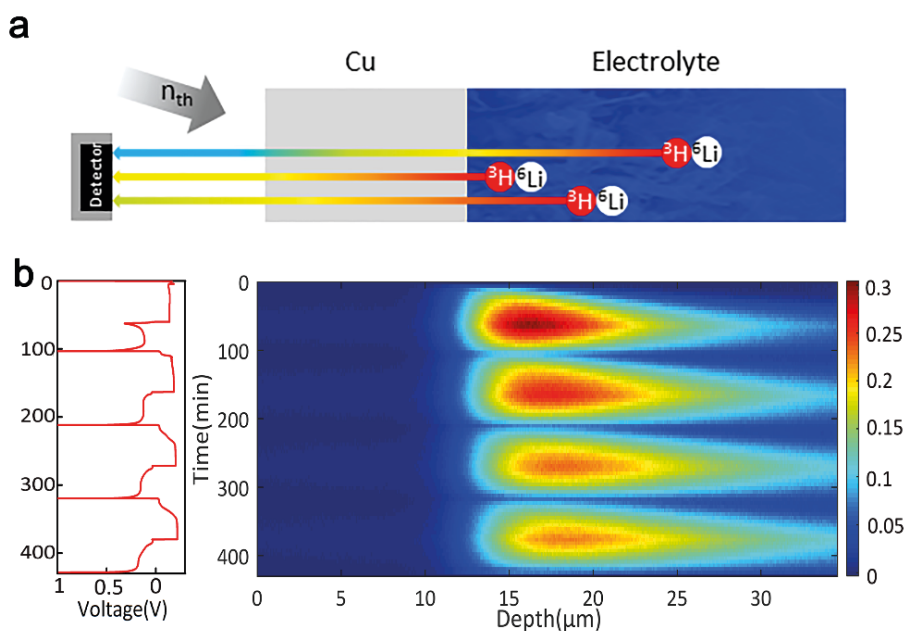


Figure 4.1 a) Principle of operando Neutron Depth Profiling (NDP). **b)** Operando NDP measurements of 4 plating and stripping cycles at 1.0 mA cm^{-2} current density, showing the fractional Li-density as a function of depth perpendicular to the copper current collector. The fractional lithium density is obtained by normalizing the measured lithium density by the lithium metal density.

The maximum fractional density is approximately 0.3, which, assuming this all to be lithium metal, results in a minimum porosity of the deposited lithium of 0.7 (70%). The plated capacity, 1 mAh cm^{-2} , would correspond to a solid lithium metal film thickness of approximately $5 \text{ }\mu\text{m}$, however, in this case distributed over a $20 \text{ }\mu\text{m}$ thick layer as observed in **Figure 4.1.b**. Clearly, straightforward plating in carbonate electrolytes results in a highly porous lithium metal film. Moreover using NDP the growth rate can be determined, amounting to $0.23 \text{ }\mu\text{m}\cdot\text{min}^{-1}$ for 0.1 fractional density and $0.11 \text{ }\mu\text{m}\cdot\text{min}^{-1}$ for 0.2 fractional density. Such quantitative *operando* information on the lithium density and porosity of electrochemically plated Li is unprecedented, illustrating the added value of NDP for the characterization of lithium metal plating reactions.

4.2.1 Synergy with optical methods

From the lithium density profiles in **Figure 4.1.b** we know that repeated cycling leads to less dense and thicker lithium deposits. However with NDP no information on the morphology is obtained. The density profiles are a combination of electrochemical plated Li and counts from the lithium containing inorganic compounds produced in the reduction of the EC/DMC electrolyte, i.e. Li_2O and Li_2CO_3 for carbonate electrolytes[17, 52-54].

To obtain microstructural insights, ex-situ SEM measurements were performed at different deposition capacities, shown in **Figure 4.2a-h**. At first, $0.1 \text{ mAh}\cdot\text{cm}^{-2}$ and at $0.2 \text{ mAh}\cdot\text{cm}^{-2}$, the lithium is plated in separated groups, consistent with previous work[55]. At a capacity of $0.5 \text{ mAh}\cdot\text{cm}^{-2}$ elongated lithium deposits as well as connected, 'mossy', lithium structures are formed and at $1.0 \text{ mAh}\cdot\text{cm}^{-2}$ approximately 200 nm wide needle-like tips are observed. **Figure 4.2.f** shows that after stripping a porous microstructure remains. The tilted SEM image at $1 \text{ mAh}\cdot\text{cm}^{-2}$, **Figure 4.2.g**, clearly shows a porous morphology, with dendrites extending approximately $13 \text{ }\mu\text{m}$ into the electrolyte. This is in good agreement with the average thickness of the lithium density observed with *operando* NDP, where one, plating and stripping, cycle at $1 \text{ mAh}\cdot\text{cm}^{-2}$ is displayed in **Figure 4.2.i**. The dense lithium region observed by NDP in **Figure 4.2.b** corresponds to the more dense mossy lithium deposits observed by SEM, whereas the low density tails extending

far into the electrolyte corresponds to the dendrites observed by SEM. After stripping some material is covering the current collector, as shown in **Figure 4.2.f**. The nature of this species is difficult to characterize, although a deposit of SEI species and disconnected, 'dead', lithium metal is most likely.

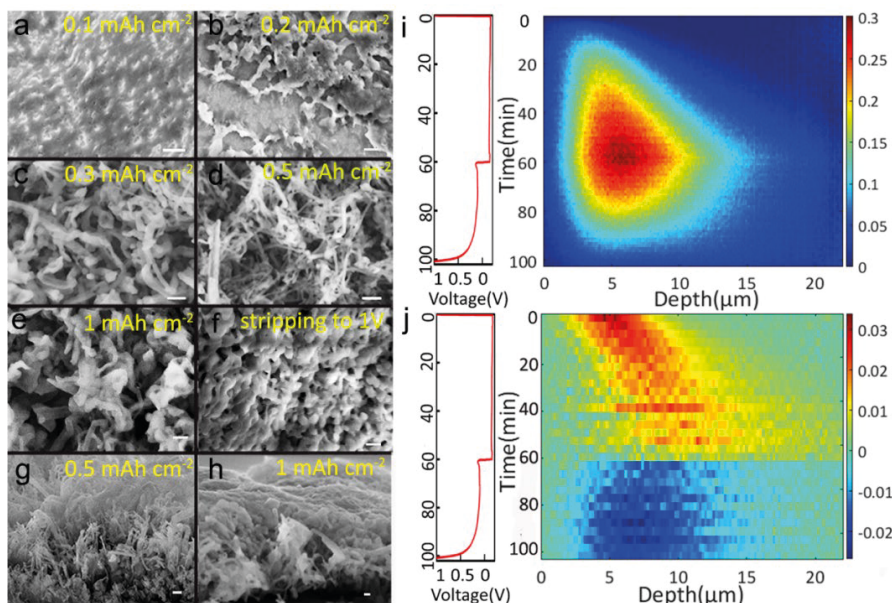


Figure 4.2. Li-density and lithium metal plating/stripping activity by operando NDP compared to ex-situ SEM. **a)** SEM measurement showing the lithium metal morphology plated with $1\text{mA}\cdot\text{cm}^{-2}$ at various capacities; **a)** 0.1, **b)** 0.2, **c)** 0.3, **d)** 0.5 and **e)** $1\text{mAh}\cdot\text{cm}^{-2}$ and **f)** after stripping. In **g)** and **h)** cross sections are shown for 0.5 and $1\text{mAh}\cdot\text{cm}^{-2}$. The scale bar in **a-b)** is $5\ \mu\text{m}$ and in **c-h)** $1\ \mu\text{m}$. **i)** Displays the lithium density versus time during the first cycle at $1\text{mAh}\cdot\text{cm}^{-2}$ and **j)** the local plating and stripping activity, the derivative of the results shown in **Figure i**. In **i)** and **j)** zero depth is the end of copper current collector and start of the electrolyte/SEI/lithium metal.

From the 2D lithium density in **Figure 4.2.i** the plating and stripping process appears to be asymmetric. This can be more clearly visualized by calculating the derivative of the lithium densities versus time, hence resulting in the local change in lithium density, shown in **Figure 4.2.j**. This provides direct insight in the distribution of the plating and stripping activity, where a plating current is indicated in red stripping current in blue. During plating at $1\ \text{mA}\ \text{cm}^{-2}$ lithium

deposition is localized within 5 μm in depth, the position of which progressively moves away from the copper current collector into the electrolyte. This is consistent with growth from the root of the porous lithium, where the top is pushed into the electrolyte, as observed by various reports based on optical analysis[12, 14, 15, 19, 30]. The localized growth indicates, that root growth dominates over thickening of the connected porous branches, since this would result in a homogeneous lithium plating activity. In contrast, the stripping activity is more homogeneously distributed over the thickness of the deposited lithium metal film. This indicates thinning of the connected porous branches is occurring throughout the deposited lithium metal film. Not only does this indirectly prove that the grown layer is indeed porous and contact with the electrolyte is available throughout the layer, also this thinning is likely to result in regions of disconnected lithium metal. The lack of contact to the copper current collector results in so called “dead” lithium which lowers the available lithium for the electrochemical process, indicating that the fundamental origin of “dead” lithium is the homogeneous stripping activity throughout the depth. Thereby, the plating and stripping activity observed by operando NDP provides a transverse average of the growth and stripping mechanism and is, thus, independent of local inhomogeneity.

4.2.2 Salt concentration

The local ion concentration in the electrolyte is among the key parameters that determine the growth mechanism and corresponding lithium metal morphology. Above critical current densities, the electrolyte ions are depleted at the metal surface, inducing inhomogeneous lithium metal plating[18, 19, 21]. Avoiding ion depletion could be an effective strategy to prevent lithium dendrite formation. A straightforward approach is to increase the salt concentration in the electrolyte. To investigate the influence of the LiPF_6 concentration in the EC/DMC electrolyte, the molarity was raised from 1 to 2 molar. **Figure 4.3** shows the comparison of the lithium density between 1 and 2 molar LiPF_6 electrolytes from NDP at different plating capacities and after stripping at $1 \text{ mA}\cdot\text{cm}^{-2}$ during the first plating/stripping cycle. Even though the increase in concentration is small, the higher concentration increases the plating density resulting in a thinner deposited layer.

The lightest anode

Concentrated electrolytes have been shown to reduce the thickness of the SEI layer[56] yet the quantitative relation between the density or porosity of a lithium metal film and the electrolyte concentration has not been reported before.

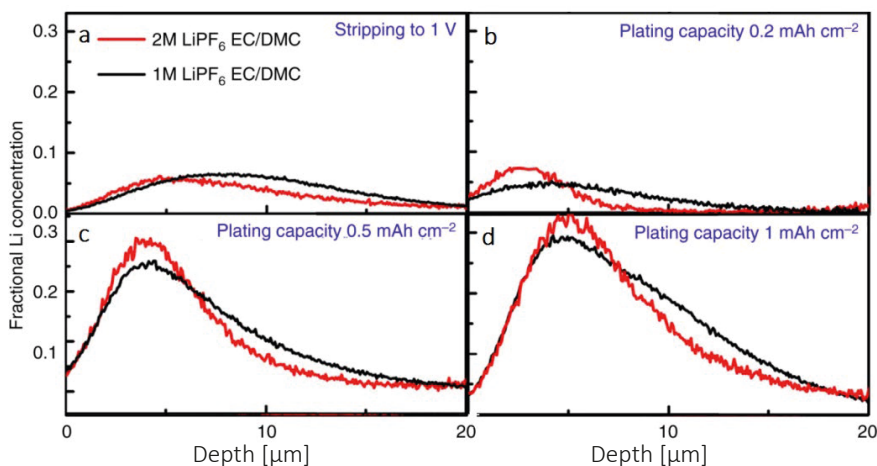


Figure 4.3 Impact of the Li-salt concentration on the Li-density distribution. lithium density at different stages of the first plating cycle (**b-d**) and **a**) at the end of stripping at 1 mA cm^{-2} comparing 1 molar and 2 molar LiPF_6 in EC/DMC. The depth is measured starting from the interface of the copper current collector with the electrolyte/SEI/Lithium metal.

4.2.3 Impact of current density

Alternative to raising the salt concentration, the applied current can be lowered thereby decreasing the ion depletion rate. In **Figure 4.4** *operando* NDP results are shown of the first plating/stripping cycle at a current density of 0.5 and $2 \text{ mA}\cdot\text{cm}^{-2}$ applied for 2 and 0.5 hour respectively, hence both result in $1 \text{ mAh}\cdot\text{cm}^{-2}$ total plated capacity. Consistently, the plating and stripping activity demonstrates that plating occurs much more localized and closer to the current collector at $2 \text{ mA}\cdot\text{cm}^{-2}$ compared to $0.5 \text{ mA}\cdot\text{cm}^{-2}$ current density. This experiment shows that a larger current density results in more compact lithium metal plating. This is somewhat counterintuitive as higher currents should be expected to induce ion concentration gradients in the electrolyte. However, Pei et al.[16] showed that classic nucleation theory is followed in ether-based electrolytes, hence the lithium nuclei size are

inversely proportional to the overpotential and, consequently, the number of lithium nuclei is proportional to the cubic power of the overpotential. The higher overpotential associated with $2 \text{ mA}\cdot\text{cm}^{-2}$ leads to a larger amount of nuclei and can therefore be expected to result in denser plating, in particular in the vicinity of the copper current collector. Concurrently, the elongated plating time at $0.5 \text{ mA}\cdot\text{cm}^{-2}$ can be expected to result in more SEI formation and hence in a more porous layer. These NDP results indicate the strong relationship between the current and the resulting lithium metal density, even at these relatively low current densities. These findings even suggest the existence of an optimal current, resulting in the largest plated metal density, motivating further systematic studies on the relationship between the lithium metal morphology and the current density. Again proving the extraordinary value of NDP as such insights are extremely difficult to attain from comparing ex-situ SEM images or other microscope techniques.

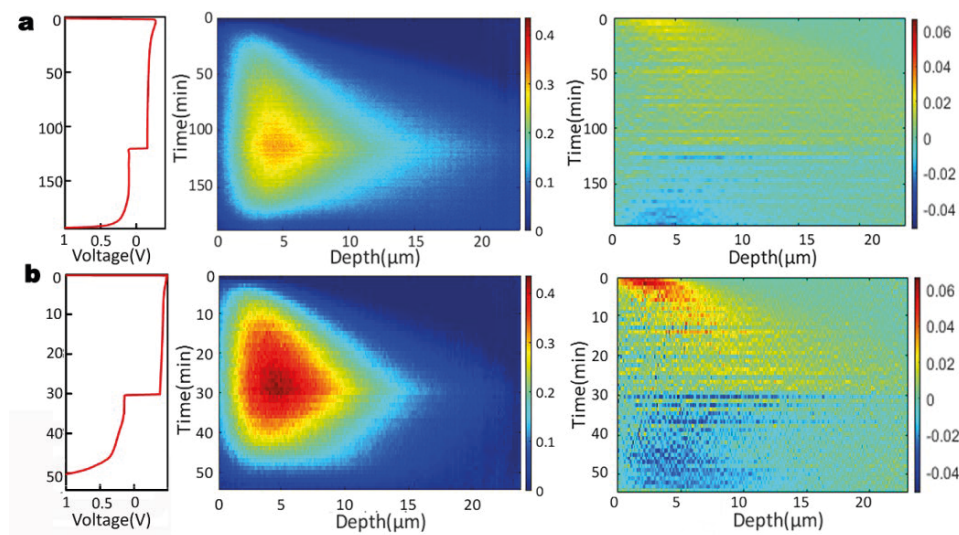


Figure 4.4. Impact of the current density on the Li-density distribution. **a)** Operando NDP measurements of the first plating and stripping cycle including the plating and stripping activity at $0.5 \text{ mA}\cdot\text{cm}^{-2}$ and **b)** at $2 \text{ mA}\cdot\text{cm}^{-2}$. The depth is measured starting from the interface of the copper current collector with the electrolyte/SEI/Lithium metal.

4.2.4 Evolution of the total amount of lithium during cycling

High density growth is desirable to attain the excellent gravimetric energy density of lithium anodes. Consequently the amount of electrolyte interface, resulting in electrolyte decomposition and the formation of “dead Li”, should be minimized. NDP allows to monitor the capacity loss due to SEI formation as well as “dead” lithium metal formation over repeated cycling. By integrating the lithium density profiles obtained by the *operando* NDP, the evolution of inactive lithium after each cycle can be monitored. To investigate the influence of current density and cycling history, two *operando* NDP cycling experiments were performed, shown in **Figure 4.5**, one starting with 5 cycles at $0.5 \text{ mA}\cdot\text{cm}^{-2}$ followed by 5 cycles at $2 \text{ mA}\cdot\text{cm}^{-2}$ and the other experiment starting with 5 cycles at $2.0 \text{ mA}\cdot\text{cm}^{-2}$ followed by 5 cycles at $0.5 \text{ mA}\cdot\text{cm}^{-2}$ all up to a $1 \text{ mAh}\cdot\text{cm}^{-2}$ plating capacity.

The lithium efficiency and the Coulombic efficiency of the two experiments are shown in **Figure 4.5.b** and **c**. The Coulombic efficiency, the ratio of charge stored during discharge and charge, does not allow to distinguish between reactions that involve Li-ion transfer and those that do not, i.e. electrochemical versus direct chemical reactions. Owing to the data obtained with NDP the amount of inactive Li can be quantified, hence allowing to determine the lithium efficiency and thus unravel electron transfer and lithium transfer. The difference between the Coulombic efficiency and the lithium efficiency quantifies the amount of irreversible reactions that do not involve Li-ion transfer, such as direct electrolyte reduction. This does rely on the assumption of a side reaction-free counter electrode. During the first cycle of both current densities a large amount of inactive lithium is observed, becoming smaller for each subsequent cycle up to the 5th cycle. As a consequence, the initially small lithium efficiencies, increase during the first 5 cycles for both current densities. Also the Coulombic efficiencies increase, until stabilizing around 80%, hence indicating that SEI is still continuously formed. The main difference between the first 5 cycles is that the lithium efficiency increases to values around 100% for $2 \text{ mA}\cdot\text{cm}^{-2}$ which is significantly larger than the efficiency for $0.5 \text{ mA}\cdot\text{cm}^{-2}$. This indicates that the lithium stripping is more efficient at a larger current density. For both current densities the Coulombic efficiency is below the lithium efficiency, demonstrating that direct reduction of the electrolyte continuously plays a

significant role. These experiments show a marked difference for the two experiments, indicating that the current at which the initial layer is formed has a significant impact on subsequent performance.

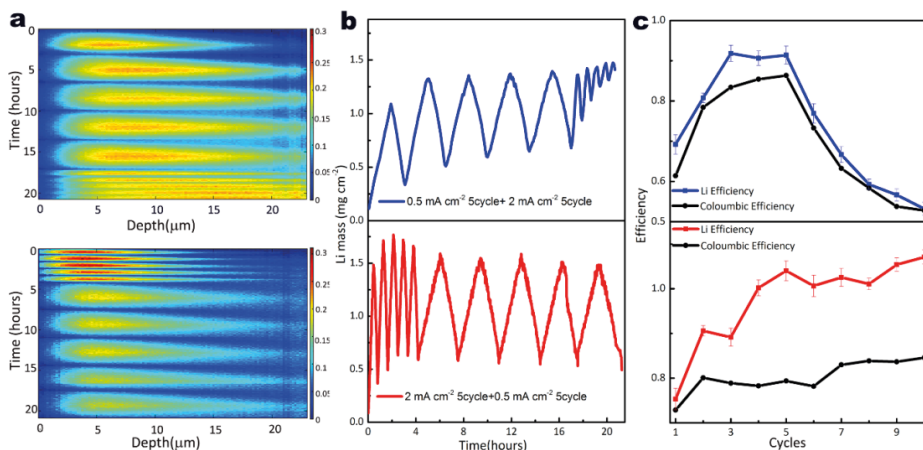


Figure 4.5 Evolution of the total amount of Li. **a)** Operando NDP for 5 plating/stripping cycles at 2 mA·cm⁻² followed by 5 cycles at 0.5 mA·cm⁻² and for 5 plating/stripping cycles at 0.5 mA·cm⁻² followed by 2 cycles at 0.5 mA·cm⁻² all up to 1 mAh·cm⁻² plating capacity. The depth is measured starting from the interface of the copper current collector with the electrolyte/SEI/Lithium metal. **b)** Integrated amount of lithium from the operando NDP experiments in **a**. **c)** Coulombic Efficiency and lithium efficiency during the cycling.

In **Figure 4.5b** large differences are observed between the two experiments. In the first case, where a low current is followed by a high current, the amount of inactive lithium shows an increase in the initial 5 cycles, followed by a second similar increase in the last 5 cycles. This is further reflected in the dramatic drop in lithium efficiency observed in **Figure 4.5.c**, which is accompanied by a strong decrease in Coulombic efficiency. In contrast, when the high current is followed by low current cycling, there is no increase in inactive Li. Instead the inverse is shown as the amount of active lithium increases, which implies that it is possible to reactivate a fraction of the 'dead' lithium. Hence resulting in an efficiency exceeding 100%, whereas the Coulombic efficiency remains constant. Clearly, slow cycling is more

reversible when preceded by high current cycling. These experiments show the importance of formation cycling under controlled conditions for these relatively unstable systems.

in **Figure 4.6**, the lithium density profiles after each plating cycle and after each stripping cycle of both experiments are plotted. Clearly the lithium distributions after plating **Figure 4.6a** look rather similar, even though the low current cycling progressively leads to a less dense and more distributed lithium layer. It is predominantly the stripping efficiency that shows remarkable deterioration after the fifth cycle. On the contrary, in **Figure 4.6c**, the distribution after plating is changing with each progressing cycle, achieving a reduced density and becoming more spread. Whereas the lithium density after stripping is more or less similar, some increase in efficiency can be spotted for the deeper regions in **Figure 4.6d**.

These observations prove that cycling history has a drastic impact on the morphology of plated lithium metal. Based on these observations, we propose the following mechanism, schematically shown in the second row of **Figure 4.6**. At low current densities, owing to a reduced number of lithium metal nuclei a more porous network is formed. Consequently more SEI is able to form as exposure is lengthened and the larger amount of available space between the branches of the network. The less dense lithium metal morphologies are more susceptible for leaving inactive lithium metal upon stripping, as this process occurs homogenous throughout the porous layer as shown in **Figure 4.2**. As a consequence a larger inactive lithium density after stripping is observed and a low lithium efficiency is attained. Moreover, during subsequent plating at a higher current density, the thick SEI/inactive lithium metal morphology formed, promotes inhomogeneous plating, leading to penetration of this SEI morphology. This will expose lithium metal to fresh electrolyte and hence initiate further SEI formation and formation of “dead” lithium metal, explaining the rapid rise of the amount of inactive lithium observed in **Figure 4.5.b**.

In contrast, the denser nucleation and growth of lithium metal at $2 \text{ mA}\cdot\text{cm}^{-2}$ is less susceptible to dead lithium-metal formation and leaves less volume for SEI formation which consequentially passivates, consistent with the stable

lithium and Coulombic efficiency in **Figure 4.5**. Perhaps the most interesting result is that this more dense morphology promotes dense plating near the current collector, even when a lower current density is applied. Moreover this is observed to revive some of the inactive Li. The reactivated lithium may originate from reconnecting “dead” lithium metal, enabling subsequent stripping, or from reversible capacity stored in the SEI[57].

Hence, we conclude that the current dependent lithium metal plating during the initial cycles, templates the SEI that forms during the first cycles. The SEI morphology formed during these initial cycles, strongly influences the lithium metal plating-morphology on subsequent cycling. These results indicate the potential opportunities of formation-cycling strategies to form SEI morphologies in-situ that are more stable upon subsequent cycles.

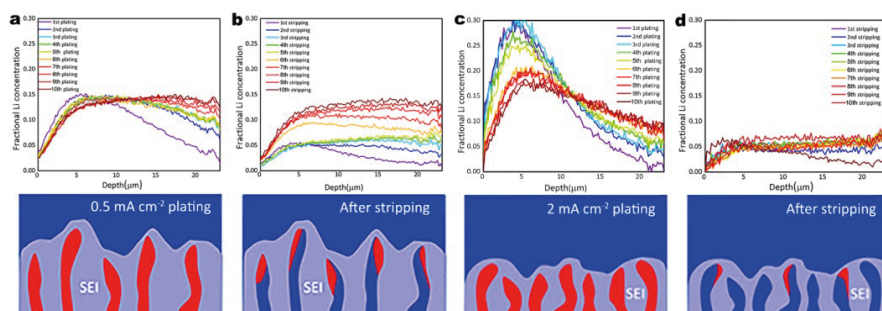


Figure 4.6.a) Fractional lithium density after plating and **b)** after stripping for 5 cycles at $0.5 \text{ mA}\cdot\text{cm}^{-2}$ followed by 5 cycles at $2.0 \text{ mA}\cdot\text{cm}^{-2}$ and **c)** after plating and **d)** after stripping for 5 cycles at $2.0 \text{ mA}\cdot\text{cm}^{-2}$ followed by 5 cycles at $0.5 \text{ mA}\cdot\text{cm}^{-2}$. The depth is measured starting from the interface of the copper current collector with the electrolyte/SEI/Lithium metal. **e-h)** Schematic representation of the plating and stripping process at 0.5 and $2.0 \text{ mA}\cdot\text{cm}^{-2}$ based on the evolution of the Li-density observed with NDP.

4.3 Morphology

The work presented in the previous sections has provided insightful data on the formation and density of plated lithium metal under various conditions, i.e. current density, salt concentration and behavior across cycles. Especially in this last part where the results highlight the importance of the electrochemical formation during the initial cycles, the lack of further details

on the microstructure, i.e. porosity, dendrite thickness and pore volume, is a significant drawback. In this respect small angle scattering techniques, i.e. **SAXS (Small Angle X-ray Scattering)**, **SANS (Neutron)** and **SESANS (Spin Echo)**, could prove a valuable addition. These techniques employ the small angle region containing information on large structures, i.e. beyond lattice spacing, such as particle sizes and particle to particle distances. The same pouch cell batteries can be used, facilitating the experimental synergy.

SESANS is sensitive at length scales from 20 nm up to 20 micron[58]. The technique employs a polarized monochromatic neutron beam, where, in a quantum mechanical framework, a single neutron can be described by a superposition of two eigenstates, spin up and spin down in a magnetic field, as described in **equation 4.1**;

$$|\Psi\rangle = c_1|\downarrow\rangle + c_2|\uparrow\rangle \text{ with } c_1^2 + c_2^2 = 1 \quad (4.1)$$

When a neutron enters a magnetic field these two eigenstates are either accelerated or decelerated, depending on the spin direction. This leads to a split in the position of the neutron in the direction of the beam, however if the front of this magnetic field is not perpendicular but tilted with respect to the neutron path as shown in **Figure 4.7**, the eigenstates are shifted perpendicular to the beam as well[59]. This is analogous to birefringence.

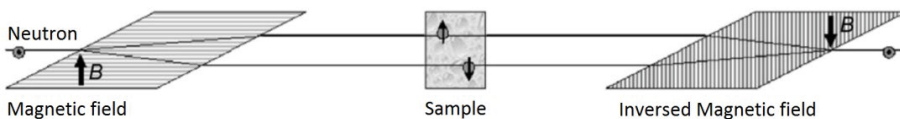


Figure 4.7 Splitting of neutron eigenstates, depicted here is the situation where both states undergo the same phase change, hence the original polarization is obtained, if not a decrease in measured.

After the sample position the neutron passes an inversed, though equal in magnitude, magnetic field region returns the original superposition. The magnetic field strength determines the distance of the shift; referred to as the spin echo length[58, 60]. For small lengths, the two states pass through the same material, hence the polarization is unchanged and equal to 1, see **Figure 4.8**. However if the sample, positioned in the middle of the setup, has

an inhomogeneity on the length scale of the spin-echo length, the two spin-states will experience this difference in composition of the material. As is shown in **Figure 4.8**, where a measurement of 1 micron diameter Teflon filter/separator is used, shows a steep drop until 2 micron, after which the depolarization remains equal, a signature for no correlations being present beyond this length scale. Thus for certain spin-echo lengths the chance increases for the two states to transverse different materials, giving rise to a relative phase change. This yields information on the sample morphology perpendicular to the beam. The shape of the polarization as a function of spin-echo length directly reflects the scattering length density correlation function[58, 61, 62].

The change in polarization is dependent on the wavelength squared, the sample thickness and phase fraction and the difference in the neutron Scattering Length Density also squared (SLD)[63], typical SLDs can be found in the appendix. Furthermore to achieve high intensity, incoherent contributions should be reduced as well as absorption processes. An infamous incoherent scattering isotope is ^1H , see the appendix F for some relevant scattering length densities. Deuterated electrolyte is available albeit at high costs. Alternatively fluorinated electrolytes could be a cheap improvement. However any electrolyte change is likely to influence the performance, hence 'off the shelf' electrolytes were used in this first experiment. Following similar reasoning, Teflon (C_2F_4)_n separators are used, reducing hydrogen content with respect to the more conventional Solupor[®] and Celgard[®] separators[64, 65]. Whatman[®] glass fiber separators are not used as their structure is expected to closely resemble that of the porous mossy lithium. These Teflon separators have a high SLD, $4.8 \cdot 10^{-6} \text{ \AA}^{-2}$, compared to natural metallic lithium and electrolyte, being $-0.88 \cdot 10^{-6}$ and $2.0 \cdot 10^{-6} \text{ \AA}^{-2}$ respectively. The pouch cells were cycled for 3 cycles with 1mA and until 3mAh in order to have grown a layer about 60 micron thick. Furthermore one pouch was continuously exposed to this current until short circuit occurred after 90 hour.

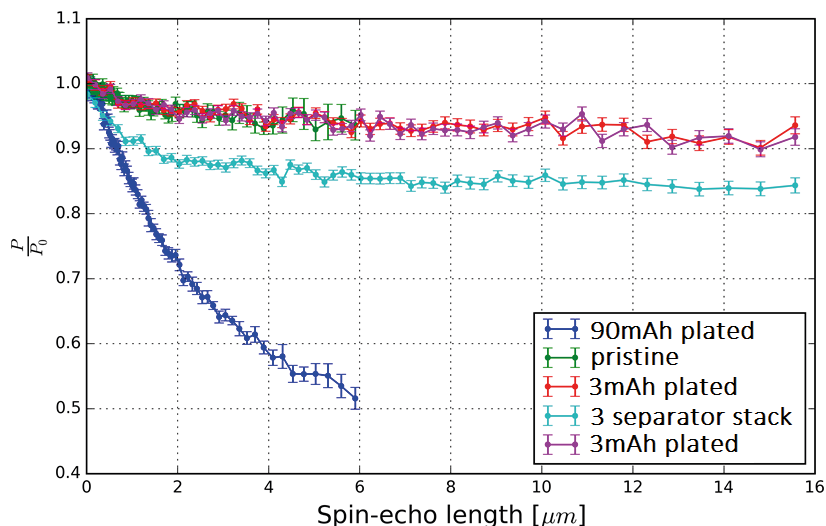


Figure 4.8. SESANS preliminary results. All measurements are of complete battery pouches, i.e. 2 copper current collectors, separator and lithium metal anode, except ‘separator 3x’. In many of the results the structure of the separator is the major contributor to the depolarization, except for the dark blue line which contains lithium plated on copper for 90 hours at 1mA.

Figure 4.8 shows the results of these first SESANS measurements on lithium metal plating. First of all, the Teflon separator is responsible for most of the scattering intensity as all curves follow this line. As the pristine cell follows this curve we can conclude that either no structure is there, or the combination of layer thickness and contrast, i.e. difference in SLD should be increased. The clear exception is in 90mAh discharged sample, the blue line. Not only is the layer thicker in this measurement, as it extends into the Teflon separator, the contrast is also increased. The continuous decrease in the line indicates correlated lengths to be present on all scales. This is a characteristic of a fractal structure[63, 66]. Hence indicating that these dendrite grows in all directions without being hindered by the surroundings or limited by the structure of Teflon separator. Hence we demonstrate that SESANS allows the none destructive measurement of dendritic structures in a working pouch cell battery using standard electrolyte. Moreover we show that by tailoring the hydrogen content of electrolyte versus separator lithium dendrite growth can be studied in a specific region of interest. Furthermore the technique

would be especially interesting when systems intrinsically low in hydrogen, such as solid electrolytes are studied.

4.4 Conclusion

Operando observation of the onset of failure mechanisms in lithium metal anodes is crucial, however challenged by the difficulty to measure lithium under realistic working conditions. Neutron Depth Profiling (NDP) is demonstrated to provide quantitative measurement of the depth resolved lithium density. This allows to monitor the spatial distribution during various electrochemical conditions. The present measurements give insight in the growth mechanism and the distribution of the activity, which promote the formation of isolated regions of inactive lithium metal. Although increasing the current density is generally expected to result in less dense microstructures, at the currents investigated, increasing the current leads to more compact microstructures, rationalized by more dense nucleation induced by larger overpotentials and the shorter cycles reduce SEI thickening. The impact of the salt concentration on the lithium metal distribution is studied, indicating that the porous lithium metal structure is more dense at larger salt concentrations.

The amount of inactive Li, both in the SEI and as dead lithium metal, is directly monitored by the *operando* NDP measurements. An interesting finding is that after relatively fast cycling, subsequent slow cycling is able to activate a fraction of the inactive lithium metal or SEI formed during the initial cycles. The results indicate a current dependent lithium metal morphology, formed during initial cycles. The resulting SEI morphology has large impact upon subsequent cycling, indicating strong memory effects that can be used to improve performances. As we effectively measure the coulombic efficiency through the lithium efficiency, the ratio between the lithium metal oxidized and reduced, allowing direct comparison with the current supplied. This offers new possibilities to assess the formation of the SEI and dead lithium during battery operation. Furthermore we show the ability of spin echo small angle scattering to further study the dendrite formation, providing a larger depth of view as well as providing details on the structure.

4.5 Methods

A pouch cell was fabricated with approximately 10 μm thick copper foil as the working electrode and the window towards the NDP detector. The separator used was a 300 μm glass fiber (Whatman) sandwiched between two 25 μm PE (Celgard) sheets. 500 μL conventional carbonate electrolyte (1 M LiPF₆ in 1:1 v/v ethylene carbonate and dimethyl carbonate, EC:DMC) was added to the separator sandwich. Approximately 500 μm lithium metal foil, 95% wt% ⁶Li and 5% wt% ⁷Li (density 0.47 g cm⁻³), serves as the counter electrode. The deposition of lithium onto the copper working electrode was performed with different current densities up to a capacity of 1 mAh·cm⁻², followed by lithium stripping up to 1 V at different current densities.

Electrodes for microscopy were prepared by discharging the pouch cell to different capacity states. Before SEM imaging, the electrodes were rinsed with dimethyl carbonate (DMC) in a glove box under dry argon atmosphere and dried several times in a vacuum chamber. Subsequently, samples were transferred into a SEM (JEOL JSM-6010LA) machine under dry argon conditions. Images were taken using an accelerating voltage of 10 kV.

4.6 References

1. Armand, M. and Tarascon, J.M., *Building better batteries*. Nature, 2008. **451**(7179): p. 652-657.
2. Dunn, B., et al., *Electrical Energy Storage for the Grid: A Battery of Choices*. Science, 2011. **334**(6058): p. 928-935.
3. Chu, S. and Majumdar, A., *Opportunities and challenges for a sustainable energy future*. Nature, 2012. **488**(7411): p. 294-303.
4. Manthiram, A., et al., *Rechargeable Lithium–Sulfur Batteries*. Chemical Reviews, 2014. **114**(23): p. 11751-11787.
5. Seh, Z.W., et al., *Designing high-energy lithium-sulfur batteries*. Chemical Society Reviews, 2016. **45**(20): p. 5605-5634.
6. Christensen, J., et al., *A Critical Review of Li/Air Batteries*. Journal of the Electrochemical Society, 2012. **159**(2): p. R1-R30.
7. Kraytsberg, A. and Ein-Eli, Y., *Review on Li-air batteries-Opportunities, limitations and perspective*. Journal of Power Sources, 2011. **196**(3): p. 886-893.
8. Tarascon, J.M. and Armand, M., *Issues and challenges facing rechargeable lithium batteries*. Nature, 2001. **414**(6861): p. 359-367.

9. Yu, Y.-S., et al., *Dependence on Crystal Size of the Nanoscale Chemical Phase Distribution and Fracture in Li_xFePO_4* . Nano Letters, 2015. **15**(7): p. 4282-4288.
10. Mizushima, K., et al., *Li_xCoO_2 ($0 < x < 1$): A new cathode material for batteries of high energy density*. Materials Research Bulletin, 1980. **15**(6): p. 783-789.
11. Goodenough, J.B. and Park, K.-S., *The Li-Ion Rechargeable Battery: A Perspective*. Journal of the American Chemical Society, 2013. **135**(4): p. 1167-1176.
12. Xu, W., et al., *Lithium metal anodes for rechargeable batteries*. Energy & Environmental Science, 2014. **7**(2): p. 513-537.
13. Lin, D., et al., *Reviving the lithium metal anode for high-energy batteries*. Nature Nanotechnology, 2017. **12**(3): p. 194-206.
14. Cheng, X.-B., et al., *Toward Safe Lithium Metal Anode in Rechargeable Batteries: A Review*. Chemical Reviews, 2017. **117**(15): p. 10403-10473.
15. Lang, J., et al., *High performance lithium metal anode: Progress and prospects*. Energy Storage Materials, 2017. **7**: p. 115-129.
16. Pei, A., et al., *Nanoscale Nucleation and Growth of Electrodeposited Lithium Metal*. Nano Letters, 2017. **17**(2): p. 1132-1139.
17. Li, Y., et al., *Atomic structure of sensitive battery materials and interfaces revealed by cryo-electron microscopy*. Science, 2017. **358**(6362): p. 506-510.
18. Chazalviel, J.N., *ELECTROCHEMICAL ASPECTS OF THE GENERATION OF RAMIFIED METALLIC ELECTRODEPOSITS*. Physical Review A, 1990. **42**(12): p. 7355-7367.
19. Bai, P., et al., *Transition of lithium growth mechanisms in liquid electrolytes*. Energy & Environmental Science, 2016. **9**(10): p. 3221-3229.
20. Sand, H.J.S., III. *On the concentration at the electrodes in a solution, with special reference to the liberation of hydrogen by electrolysis of a mixture of copper sulphate and sulphuric acid*. The London, Edinburgh, and Dublin Philosophical Magazine and Journal of Science, 1901. **1**(1): p. 45-79.
21. Brissot, C., et al., *Dendritic growth mechanisms in lithium/polymer cells*. Journal of Power Sources, 1999. **81**: p. 925-929.
22. Guo, Y., et al., *Reviving Lithium-Metal Anodes for Next-Generation High-Energy Batteries*. Advanced Materials, 2017. **29**(29).
23. Chang, H.J., et al., *Correlating Microstructural Lithium Metal Growth with Electrolyte Salt Depletion in Lithium Batteries Using Li-7 MRI*. Journal of the American Chemical Society, 2015. **137**(48): p. 15209-15216.
24. Verma, P., et al., *A review of the features and analyses of the solid electrolyte interphase in Li-ion batteries*. Electrochimica Acta, 2010. **55**(22): p. 6332-6341.
25. Mehdi, B.L., et al., *Observation and Quantification of Nanoscale Processes in Lithium Batteries by Operando Electrochemical (S)TEM*. Nano Letters, 2015. **15**(3): p. 2168-2173.

26. Huang, J.Y., et al., *In Situ Observation of the Electrochemical Lithiation of a Single SnO₂ Nanowire Electrode*. *Science*, 2010. **330**(6010): p. 1515-1520.
27. Liu, X.H., et al., *Lithium fiber growth on the anode in a nanowire lithium ion battery during charging*. *Applied Physics Letters*, 2011. **98**(18).
28. Liu, X.H., et al., *Anisotropic Swelling and Fracture of Silicon Nanowires during Lithiation*. *Nano Letters*, 2011. **11**(8): p. 3312-3318.
29. Zeng, Z., et al., *Visualization of Electrode-Electrolyte Interfaces in LiPF₆/EC/DEC Electrolyte for Lithium Ion Batteries via in Situ TEM*. *Nano Letters*, 2014. **14**(4): p. 1745-1750.
30. Lin, D., et al., *Layered reduced graphene oxide with nanoscale interlayer gaps as a stable host for lithium metal anodes*. *Nature Nanotechnology*, 2016. **11**(7): p. 626-+.
31. Yan, K., et al., *Selective deposition and stable encapsulation of lithium through heterogeneous seeded growth*. *Nature Energy*, 2016. **1**.
32. Dollé, M., et al., *Live Scanning Electron Microscope Observations of Dendritic Growth in Lithium/Polymer Cells*. *Electrochemical and Solid-State Letters*, 2002. **5**(12): p. A286-A289.
33. Sagane, F., et al., *In-situ scanning electron microscopy observations of Li plating and stripping reactions at the lithium phosphorus oxynitride glass electrolyte/Cu interface*. *Journal of Power Sources*, 2013. **225**: p. 245-250.
34. Unocic, R.R., et al., *Direct Visualization of Solid Electrolyte Interphase Formation in Lithium-Ion Batteries with In Situ Electrochemical Transmission Electron Microscopy*. *Microscopy and Microanalysis*, 2014. **20**(4): p. 1029-1037.
35. Sacci, R.L., et al., *Nanoscale Imaging of Fundamental Li Battery Chemistry: Solid-Electrolyte Interphase Formation and Preferential Growth of Lithium Metal Nanoclusters*. *Nano Letters*, 2015. **15**(3): p. 2011-2018.
36. Sacci, R.L., et al., *Direct visualization of initial SEI morphology and growth kinetics during lithium deposition by in situ electrochemical transmission electron microscopy*. *Chemical Communications*, 2014. **50**(17): p. 2104-2107.
37. Rosso, M., et al., *Dendrite short-circuit and fuse effect on Li/polymer/Li cells*. *Electrochimica Acta*, 2006. **51**(25): p. 5334-5340.
38. Leenheer, A.J., et al., *Lithium Electrodeposition Dynamics in Aprotic Electrolyte Observed in Situ via Transmission Electron Microscopy*. *ACS Nano*, 2015. **9**(4): p. 4379-4389.
39. Liu, S., et al., *Lithium Dendrite Formation in Li/Poly(ethylene oxide)-Lithium Bis(trifluoromethanesulfonyl)imide and N-Methyl-N-propylpiperidinium Bis(trifluoromethanesulfonyl)imide/Li Cells*. *Journal of the Electrochemical Society*, 2010. **157**(10): p. A1092-A1098.
40. Steiger, J., et al., *Mechanisms of dendritic growth investigated by in situ light microscopy during electrodeposition and dissolution of lithium*. *Journal of Power Sources*, 2014. **261**: p. 112-119.

41. Nishikawa, K., et al., *Li dendrite growth and Li⁺ ionic mass transfer phenomenon*. Journal of Electroanalytical Chemistry, 2011. **661**(1): p. 84-89.
42. Nishikawa, K., et al., *In Situ Observation of Dendrite Growth of Electrodeposited Li Metal*. Journal of the Electrochemical Society, 2010. **157**(11): p. A1212-A1217.
43. Bhattacharyya, R., et al., *In situ NMR observation of the formation of metallic lithium microstructures in lithium batteries*. Nature Materials, 2010. **9**(6): p. 504-510.
44. Chandrashekar, S., et al., *Li-7 MRI of Li batteries reveals location of microstructural lithium*. Nature Materials, 2012. **11**(4): p. 311-315.
45. Harry, K.J., et al., *Detection of subsurface structures underneath dendrites formed on cycled lithium metal electrodes*. Nature Materials, 2014. **13**(1): p. 69-73.
46. Shui, J.-L., et al., *Reversibility of anodic lithium in rechargeable lithium-oxygen batteries*. Nature Communications, 2013. **4**.
47. Zhang, X.Y., et al., *Direct Observation of Li-Ion Transport in Electrodes under Nonequilibrium Conditions Using Neutron Depth Profiling*. Advanced Energy Materials, 2015. **5**(15): p. 1500498.
48. Nagpure, S.C., et al., *Neutron depth profiling technique for studying aging in Li-ion batteries*. Electrochimica Acta, 2011. **56**(13): p. 4735-4743.
49. Oudenhoven, J.F.M., et al., *In Situ Neutron Depth Profiling: A Powerful Method to Probe Lithium Transport in Micro-Batteries*. Advanced Materials, 2011. **23**(35): p. 4103-+.
50. Liu, D.X., et al., *In Situ Quantification and Visualization of Lithium Transport with Neutrons*. Angewandte Chemie-International Edition, 2014. **53**(36): p. 9498-9502.
51. Liu, Z., et al., *Relating the 3D electrode morphology to Li-ion battery performance; a case for LiFePO₄*. Journal of Power Sources, 2016. **324**: p. 358-367.
52. Aurbach, D., et al., *THE SURFACE-CHEMISTRY OF LITHIUM ELECTRODES IN ALKYL CARBONATE SOLUTIONS*. Journal of the Electrochemical Society, 1994. **141**(1): p. L1-L3.
53. Aurbach, D., et al., *IDENTIFICATION OF SURFACE-FILMS FORMED ON LITHIUM IN PROPYLENE CARBONATE SOLUTIONS*. Journal of the Electrochemical Society, 1987. **134**(7): p. 1611-1620.
54. Peled, E., et al., *Advanced model for solid electrolyte interphase electrodes in liquid and polymer electrolytes*. Journal of the Electrochemical Society, 1997. **144**(8): p. L208-L210.
55. Zhang, S.S., *Problem, Status, and Possible Solutions for Lithium Metal Anode of Rechargeable Batteries*. ACS Applied Energy Materials, 2018. **1**(3): p. 910-920.
56. Alvarado, J., et al., *High Concentrated Electrolytes for Li Metal Anodes*. Meeting Abstracts, 2017. **MA2017-02**(5): p. 545.

57. Rezvani, S.J., et al., *Is the Solid Electrolyte Interphase an Extra-Charge Reservoir in Li-Ion Batteries?* *Acs Applied Materials & Interfaces*, 2017. **9**(5): p. 4570-4576.
58. Bouwman, W.G., et al., *Real-space neutron scattering methods*. Nuclear Instruments and Methods in Physics Research Section A: Accelerators, Spectrometers, Detectors and Associated Equipment, 2008. **586**(1): p. 9-14.
59. Gähler, R., et al., *Space-time description of neutron spin echo spectrometry*. *Physica B: Condensed Matter*, 1996. **229**(1): p. 1-17.
60. Bouwman, W.G., et al., *SESANS studies of colloid phase transitions, dairy products and polymer fibres*. *Physica B: Condensed Matter*, 2004. **350**(1): p. 140-146.
61. Andersson, R., et al., *Analysis of spin-echo small-angle neutron scattering measurements*. *Journal of Applied Crystallography*, 2008. **41**(5): p. 868-885.
62. Krouglov, T., et al., *Structural transitions of hard-sphere colloids studied by spin-echo small-angle neutron scattering*. *Journal of Applied Crystallography*, 2003. **36**(6): p. 1417-1423.
63. Teixeira, J., *Small - angle scattering by fractal systems*. *Journal of Applied Crystallography*, 1988. **21**(6): p. 781-785.
64. Sarachan, K.L., et al., *Small-angle scattering contrast calculator for protein and nucleic acid complexes in solution*. *Journal of Applied Crystallography*, 2013. **46**(6): p. 1889-1893.
65. Seidlmayer, S., et al., *In Operando Small-Angle Neutron Scattering (SANS) on Li-Ion Batteries*. *Journal of The Electrochemical Society*, 2015. **162**(2): p. A3116-A3125.
66. Zhou, Z., et al., *From nanopores to macropores: Fractal morphology of graphite*. *Carbon*, 2016. **96**: p. 541-547.

5.

Li-Sulfur Batteries,
Dissolution and Performance

5. Li-Sulfur Batteries, Dissolution and Performance

So far lithium was studied in solid phases, both metals as well as ionic compounds. However the concentration in the electrolyte can also be probed, thereby allowing to study dissolution processes. Even though active material dissolution is generally avoided some lithium battery systems cannot work without. The cathode material sulfur is functionalized by active material dissolution, thereby circumventing the electronically insulating material property. However, the dissolution behavior needs to be controlled as otherwise active material is lost and charge is shuttled from cathode to anode. The content of this chapter is drawn from;

Spatio-temporal Quantification of lithium both in Electrode and in Electrolyte with atomic precision via Operando Neutron Absorption.

Tomas W. Verhallen‡, Peter-Paul R.M.L. Harks‡, Chandramohan George, Marnix Wagemaker* and Fokko M. Mulder* *Submitted*

5.1 Introduction

Among the various battery chemistries available today, the high theoretical energy density (2600 Wh/kg), availability, environmental benignity (low toxicity) and low cost of sulfur make lithium-sulfur (Li-S) batteries highly attractive to supersede the current Li ion technology[1-3]. Especially for applications where volumetric energy density is not the most critical design parameter in large scale grid stabilization purposes[4, 5].

Despite these merits, Currently the Li-S battery system suffers from rapid capacity fading and poor round-trip efficiency[1, 2], which seem inherently linked to the material properties of sulfur, i.e. dissolution of the intermediate lithium polysulfide species in battery electrolyte and Li metal corrosion via polysulfide accumulation[1, 2]. However, this soluble intermediates allow to circumvent the materials' extremely low electronic conductivity, which would otherwise render it unsuitable as active material. A conductive matrix, most commonly carbon, is providing both a pathway for electrons and reaction sites, such that the migrated Li ions can shorten the sulfide backbone till the solid product Li_2S_2 is formed[6].

A typical discharge curve of a Li-S battery consists of a high (≈ 2.3 V) and a low (≈ 2.0 V) voltage plateau, attributed to a solid (S_8) \rightarrow dissolved (Li_2S_6) \rightarrow solid (Li_2S_2/Li_2S) process with a gradual decrease in the sulfur chain length. The high plateau is ascribed to the reduction of the cyclic S_8 ring to soluble long chain polysulfides (Li_2S_x , $4 < x < 8$), while the low voltage plateau is believed to correspond to further reduction of polysulfides to solid Li_2S_2/Li_2S [7-9]. Since the intermediate active materials are dissolved, they are no longer confined to the cathode section and instead they are able to migrate to the anode section, where they undergo parasitic reactions. This not only severely limits the practical performance of Li-S batteries but serves also as root cause for battery self-discharge.

A common approach to mitigate this problem is to add additives such as lithium nitrate ($LiNO_3$) to the electrolyte[10]. These additives facilitate the formation of a passivating layer consisting of S and electrolyte species through chemical reactions between $LiNO_3$ and Li anode. This layer prevents Li metal from being directly exposed to polysulfides, while allowing Li-ion conduction, due to Li_3N species[11]. However, the $LiNO_3$ depletes because of its continuous consumption, induced by the morphological changes during cyclic Li re-deposition, causing repetitive break-down of the passivating layer.

More importantly, this additive alone cannot inhibit the active material from diffusing out of the electrode region. Aiming to avoid active material loss, efforts are focused on physically encapsulating polysulfide active material within hollow carbon structures. Yet the weak interaction between carbon and polysulfides yielded little improvements in terms of cycle life, especially when benchmarked against the current Li-ion cells[12, 13].

Recently, chemical bonding strategies for immobilizing polysulfides have been developed, which are based on the strong interactions between polar functional groups and polysulfides[9, 14]. Functional groups (e.g. oxygen, boron, nitrogen and sulfur) are introduced to electrodes via the conductive additive (carbon matrix), or by dispersing polymer or (transition) metal oxide additives (e.g. TiO_2 and $Li_4Ti_5O_{12}$). Their addition has offered considerable improvements in the performance of Li-S batteries, reflected by the increased battery cycle life[15, 16]. The beneficial effects are attributed to

their high polarity which should yield a high chemical affinity towards polysulfide species[17]. Direct experimental observations are still thinly spread.

Among the reasons, there is the intrinsic difficulty to study light ions, such as lithium, using methods based on X-rays or electrons[18-20]. For example, in situ diffractometric techniques are helpful in understanding formation of crystalline Li_2S and Li_2S_2 through disproportionation in both electrode and glass fiber separator[6, 21]. Yet, the non-crystalline polysulfide chains and nano-crystalline particles cannot be resolved[6, 21, 22]. Alternatively, inelastic methods based on photon absorption, i.e. UV-VIS, XAS, XANES and RIXS, have been employed thereby allowing the study of in operando observations of dissolved polysulfide species[7, 23-26]. This strive for operando measurements is paramount, as these dynamic and delicate processes escape the probing ability of ex-situ methods and electrochemical testing[16, 18]. However these intense and energetic probes increase the risk of degradation[22].

Neutron Depth Profiling (NDP) allows for the absolute detection of Li with atomic selectivity, independent of the oxidation state or phase. This ability allows for the simultaneous detection of lithium in both electrode and electrolyte, which makes NDP a unique battery diagnostic method to unravel the space and time dependent lithium density, resulting from the complex electrochemical processes taking place across battery electrodes[27]. Moreover the low energy of the neutrons and the techniques selectivity suppresses undesired energy exchange between probe and sample.

Here three electrode configurations are studied that are designed to unveil the key processes that take place in solution and on the surfaces: a carbon/sulfur electrode (termed: CS electrode), a carbon/sulfur electrode with 10w% $\text{Li}_4\text{Ti}_5\text{O}_{12}$ added (LTO + CS electrode) and a carbon/sulfur electrode sandwiched with an $\text{Li}_4\text{Ti}_5\text{O}_{12}$ membrane (CS electrode + membrane). By looking at the local lithium concentration as a function of electrode depth, and distinguishing Li concentration in electrodes from electrolyte, direct evidence for active Li containing material dissolution and

migration, and polysulfide adsorption by metal oxides within and across electrodes is related to Li-S battery capacity.

5.2 Results and discussion

To reveal electrode-wide dynamics that dictate the fate of lithium polysulfides in Li-S batteries, we investigated three groups of electrodes. **Figure 5.1** reports the averaged NDP profiles of the pristine cells obtained during their initial, pre-discharge resting time. Although no current was drawn from the cells, i.e. no lithiation occurred, the measured curves still reveal the presence of Li across the entire thickness of the electrodes in all types of electrodes. This is due to Li from the battery electrolyte (LiTFSI and LiNO_3 in TEGDME) that is infiltrated into the porous network of electrodes, as can be seen in the standard CS electrode, indicated by the black squares, that demonstrates a nearly constant lithium concentration of 0.8 molar.

The primary role of $\text{Li}_4\text{Ti}_5\text{O}_{12}$ in these electrodes is to confine polysulfide. Owing to its' lithium content, the use of $\text{Li}_4\text{Ti}_5\text{O}_{12}$ offers another experimental advantage in NDP as it can serve as a marker indicating electrode lateral dimensions, as is demonstrated in **Figure 5.1**. The lithium concentration in the electrolyte should be close to 1.2 molar whereas pure $\text{Li}_4\text{Ti}_5\text{O}_{12}$ contains over 30 mol/l. Therefore the $\text{Li}_4\text{Ti}_5\text{O}_{12}$ containing electrodes and the $\text{Li}_4\text{Ti}_5\text{O}_{12}$ membrane are distinguishable from the electrolyte, which is the only lithium containing component before discharge. As the CS electrode and CS region in the CS with LTO membrane electrode stack (blue triangles) are similar (same batch), the measured Li-concentration up to 10 micron in both electrodes is comparable. Indeed, the cell containing CS electrode with an LTO membrane shows a strong Li increase after ~ 15 micron where the LTO membrane is located, which, due to the rough interface of the electrode and membrane leads to a sloping concentration. The CS+LTO electrode, indicated by the red spheres, shows a small step at 7 micron, marking the dimensions of the electrode. The 10wt% of LTO in this electrode occupies 6% of the volume, thereby increasing the lithium concentration to 1.7 molar, high enough to be distinguished from the electrolyte contribution. The Li-concentration in the CS+LTO electrode converges with increasing depth towards the same concentration as the CS electrode, representing the concentration in the

separator. In conclusion, by addition of $\text{Li}_4\text{Ti}_5\text{O}_{12}$ to the electrodes, the pristine electrode layer thickness can be deduced.

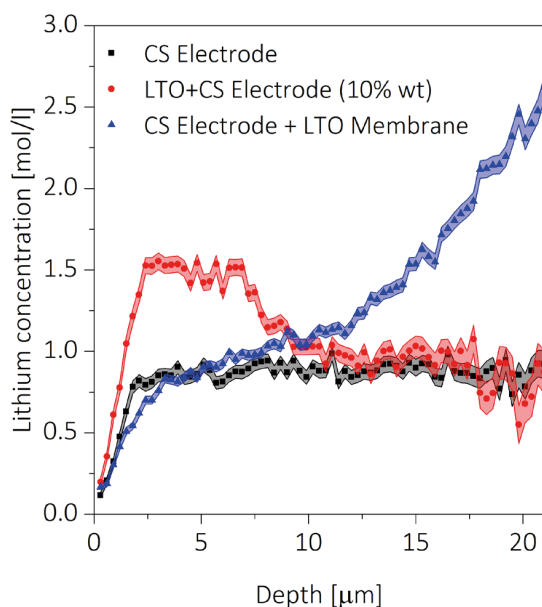


Figure 5.1. Pristine cells with different electrodes, measurements obtained during the rest period before discharge. The end of the aluminum current collector/window is at 0 micron depth, from which the porous electrode starts. The error bars increase with depth as the subtracted background is larger for lower energies hence the signal to noise ratio decreases while the measurement uncertainty increases.

As we focus on the role of $\text{Li}_4\text{Ti}_5\text{O}_{12}$ in this type of batteries, the results on the CS electrode will be discussed later. The results on the additive cells are given in **Figure 5.2**. These color contour images show lithium concentration versus time and electrode depth during L-S battery discharge. It is the measured Li concentration profile during discharge, after subtracting by the lithium concentration in the electrolyte from the reference cell as well as the background noise. This subtraction highlights the change in lithium concentration over time, both in the electrode and in the electrolyte. The discharge voltage and plateaus are characteristic of a Li-S battery, see the bottom panels. The battery discharge cut-off voltage was set to 1.7V, in order

to prevent electrochemical activity of $\text{Li}_4\text{Ti}_5\text{O}_{12}$, as well as decomposition of LiNO_3 . Therefore, the recorded lithium concentration increase is solely due to the electrochemical activity of sulfur forming discharge products, soluble and solid, polysulfide species.

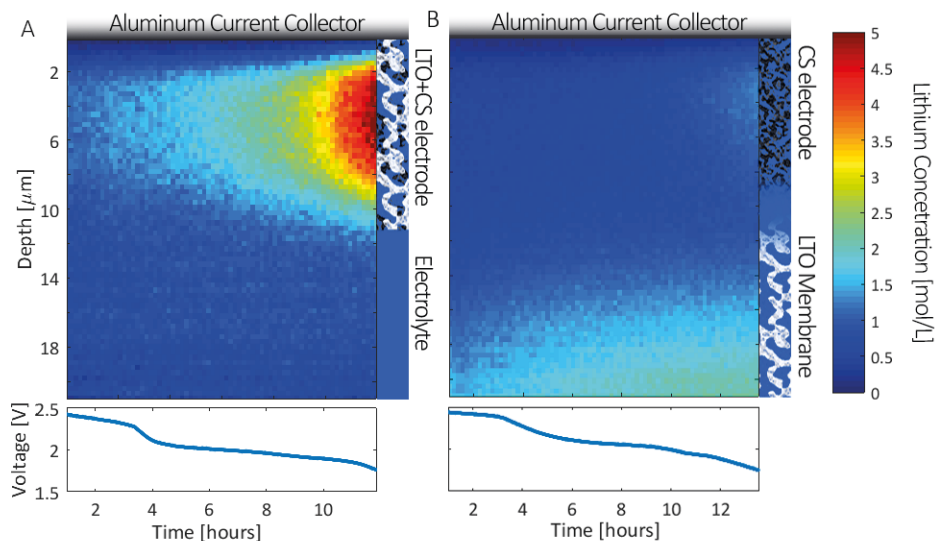


Figure 5.2 shows the increase in lithium concentration with time versus depth at a constant current discharge. The aluminum current collector/window is at the top of the plot, whereas the electrolyte (and membrane) are found below. **A** depicts the LTO+CS electrode and **B** The standard CS electrode and LTO membrane.

Figure 5.2A shows the cell containing CS+LTO electrode. Surprisingly most of the lithium concentration increase takes place at the end of discharge. This contradicts the view that sulfur reduction should occur at a constant rate since a constant current is applied. This indicates that the oxidized Li is stored in the electrolyte in the form of soluble polysulfide species. Furthermore these species rapidly diffuse and equilibrate in the electrolyte, since no significant concentration change is observed in the first ~ 20 micron visible with NDP. The electrolyte layer is extending into a 250 micron thick separator which poses a significant reservoir.

Nevertheless, in this electrode a high lithium concentration is attained at the end of discharge. During the process the electrode layer thickness slightly

increases, reaching 11 micron at the end of charge. This is a 50 % increase when compared to **Figure 5.1**, where the original layer thickness can be deduced from the $\text{Li}_4\text{Ti}_5\text{O}_{12}$ additive. This is consistent with the 80% volume change reported elsewhere[28], proving that even though the active material is deposited from soluble products, these solid deposits can apparently strain the carbon host matrix. However, even though this observation is consistent with previous reports[29], it should be noted that the validity of this observation is complicated by the expected but unknown decrease in electrode porosity, thereby increasing the total stopping power and thus apparent layer thickness.

Figure 5.2B shows the cell containing CS electrode with LTO membrane. The increased lithium concentration due to the LTO membrane at depths above 10 micron is obvious when compared to the same region in panel **A**. In this case, lithiation of the electrode does not progress as significant as in the CS+LTO electrode, even though the same constant current C-rate is applied. Especially in the first half of the discharge there is no visible concentration increase in the electrode region ($< 10 \mu\text{m}$), however, there is a pronounced concentration increase within the LTO membrane. This means that a large fraction of the oxidized Li is actually stored within the membrane, instead of the electrode region. We can safely rule out the possibility of intercalation or lithiation of $\text{Li}_4\text{Ti}_5\text{O}_{12}$ particles as the cell potential is well above 1.55V, see bottom panels, where intercalation in $\text{Li}_4\text{Ti}_5\text{O}_{12}$ typically occurs. Therefore, it can be rationalized that the accumulation of Li in the LTO membrane is not a result of an electrochemical process but is due to the adsorption of Li polysulfides. They migrate from the electrode and are absorbed in the LTO membrane, thereby preventing further migration to the anode. To our knowledge, this is the first direct evidence of the ability of $\text{Li}_4\text{Ti}_5\text{O}_{12}$ to bond the dissolute Li-polysulfide species. In the second half of discharge, the electrode region does show an increase in lithium concentration. This lithiation might result from low solubility solid products, which accept electrons and deposit on the carbon matrix and are therefore restricted to the electrode region. However, the concentration of lithium in the membrane does not decrease, which indicates that the absorbed species are relatively stable and do not re-dissolve to keep the reaction going. Hence the



final concentration attained in the carbon-sulfur electrode with LTO membrane is much lower, which also corroborates its relatively low capacity. This can explain why a Li-S electrode design involving cathode interlayers offers sub-optimal battery performance, if the interlayer does not provide sufficient electron conductivity for the reduction of polysulfides or other properties aiding the re-dissolution, i.e. lower polysulfide affinity.

These results indicate that lithiation proceeds sequentially in the electrode and the electrolyte/membrane region. To explore this behavior further the counts from the two different regions in the cell are summed; the region from 0-12 micron represents the entire host matrix (CS or CS + LTO) available in electrodes for lithiation and the region from 12-28 micron encompasses the measureable domain part of the electrolyte or the membrane only. This summation simultaneously increases the measurement statistics. Next the measured increase in Li concentration is related to the current that was retrieved from the battery during discharge, thereby elucidating differences in applied current and allowing a direct comparison to the cell electrochemistry.

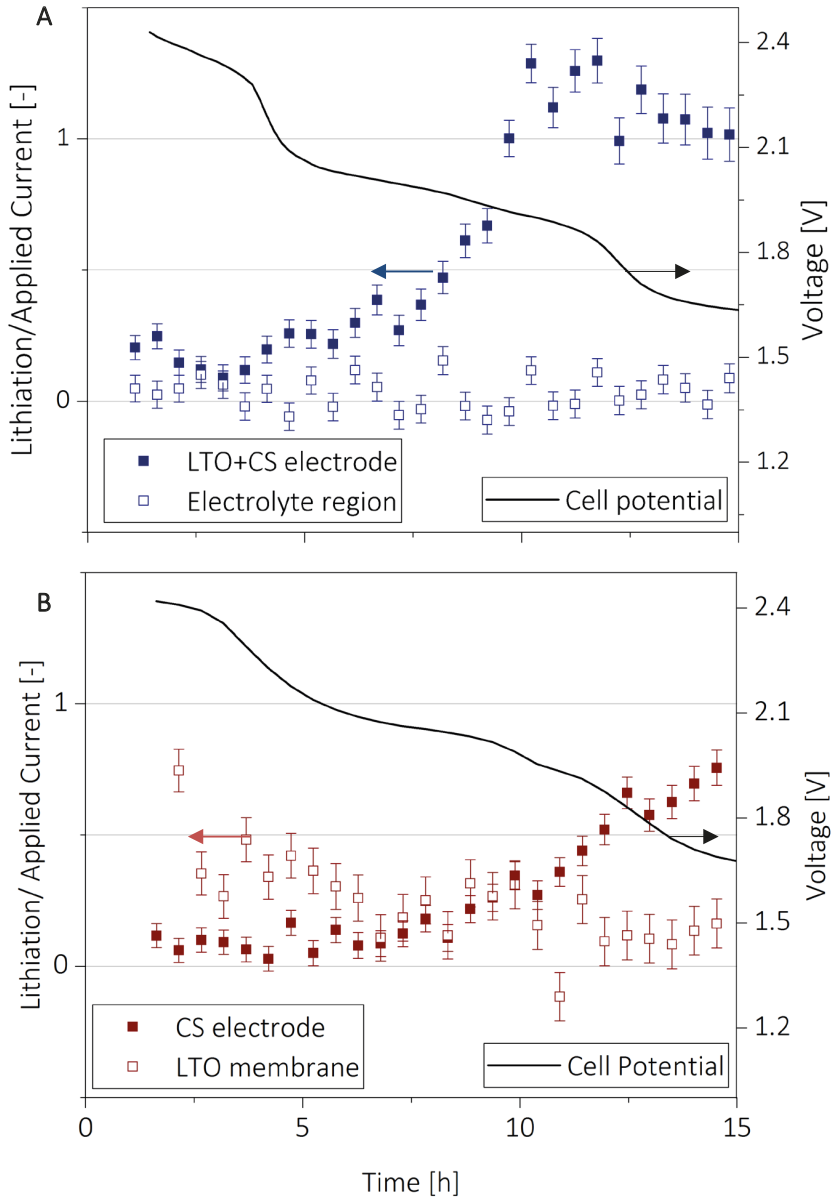


Figure 5.3. Regional lithiation defined as the Li concentration increase per time unit divided by the current and plotted versus discharge time. **(a)** Here blue symbols reflect composite electrode cell and **(b)** red symbols the standard electrode with membrane, filled squares indicate electrode region whereas open spheres denoted electrolyte and electrolyte/membrane

region. Data has been binned, error bars reflect the spread in the data of one point.

The ratio between lithiation and the applied current should ideally be 1, then for every electron a lithium is transported and stored in the measurable domain. Lower values are a direct indication of polysulfide migration. During initial stages of discharge, at the first plateau 2.5-2.3V, the lithium increase is slower than the applied current in both cases. Although the increase in lithium concentration is lower than expected due to the diffusion of PS, in both electrodes the regions that contain $\text{Li}_4\text{Ti}_5\text{O}_{12}$ do show lithiation. In **Figure 5.3a**, the CS+LTO electrode, shows significant electrochemical activity whereas the electrolyte region barely changes. Even more obvious is the change in the LTO region in the CS with LTO membrane electrode, **Figure 5.3b**. Here, because of the high $\text{Li}_4\text{Ti}_5\text{O}_{12}$ concentration (85%) in the membrane, more surface area is available, which shows why lithiation proceeds more readily at this stage of discharge. As the cell potential window rules out electrochemical activity of the $\text{Li}_4\text{Ti}_5\text{O}_{12}$, the sole explanation for the observed lithiation are adsorbed polysulfide species. A direct indication that indeed this oxide (LTO) can retain lithium sulfur based solutes. However, it should be noted that absorption of polysulfides onto $\text{Li}_4\text{Ti}_5\text{O}_{12}$ does not occur on par with the applied current, a ratio <1 , which can be explained by a lack of available surface sites. Even though there is room for optimization here, as currently commercial $\text{Li}_4\text{Ti}_5\text{O}_{12}$ nanopowder is used, which is not intended for this application, clearly the material adsorbs lithium polysulfides.

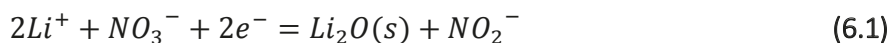
In the second stage of discharge, when the voltage reaches at 2V plateau a clear shift is seen. The CS + LTO electrode shows a sudden increase in lithiation speed halfway through the second plateau, the relative lithiation even exceeds 1. This reveals that solid compounds are formed, rapidly consuming the polysulfide species present in the electrolyte in the porous networks of the electrode as well as on the surface of the $\text{Li}_4\text{Ti}_5\text{O}_{12}$ particles. Together with two Li ions from the electrolyte these species are reduced to insoluble products, which are subsequently deposited on the carbon substrate. Furthermore the consumption of soluble and adhered polysulfide species lowers the local PS concentration and results in a net influx of these

species from the electrolyte reservoir, atop of the applied current, hence leading to a 'surplus' in lithiation speed. The fact that the observed value surpasses 1 proves that solid sulfur compounds are formed and that at this stage no capacity is dissipating in soluble products.

The concentration gradient is relaxed during the end of the second plateau, which entails an equilibration of all fluxes, i.e. electrochemical processes combined with relaxation of the dissolved Li_2S_n concentration gradient. Demonstrating that even on these long time scales and relatively low currents ($C/20$), this will lead to a concentration difference of polysulfides in the electrolyte in the electrode region and outside of it.

In **Figure 5.3b**, the CS electrode with LTO membrane also shows a jump in lithiation speed, albeit somewhat later in the discharge process, but it remains much lower than the CS+LTO electrode. The ratio between lithium concentration increase and applied current never reaches 1, a clear indication of soluble products, and consequently charge capacity, is leaving the measurement scope. Even though there is an obvious transition in this voltage plateau, the activity is moving from the membrane to the electrode, the contribution to the current of the membrane does not become negative. Hence the otherwise mobile polysulfide species, formed during the first stages of discharge, are irreversibly trapped in the membrane. The $\text{Li}_4\text{Ti}_5\text{O}_{12}$ membrane is incapable of supplying the adhered lithium sulfides with electrons, therefore, these polysulfides that cannot be further reduced. This explains the poor capacity obtained for this cell compared to the CS+LTO electrode.

To exclude the scenario that significant regions of the carbon matrix are outside of the window of measurement, the potential was decreased further (to $\sim 1.6\text{V}$), such that the NO_3^- anions become instable, forming lithium oxide according to;



This would cause solid deposition of Li_2O on the carbon host, and the exchange of NO_3^- with NO_2^- ions in solution. Hence this insoluble lithium

oxide is only formed on the carbon electrode matrix. Therefore at 1.6 V the lithiation (normalized to the current) in the electrode should be found to be ~ 1 for both electrode configurations. This is the case for both cells, proving that the electrodes are fully within the window of measurement.

The additive free cells, that is the CS electrode, generally performed poorly, especially in the first cycle. This result is, by itself, not enough to deduce any beneficial properties or positive influence of the LTO membrane or LTO + CS electrode, however an interesting result was obtained when a cell was paused mid -discharge, while it was entering the second plateau, shown in **Figure 5.4**.

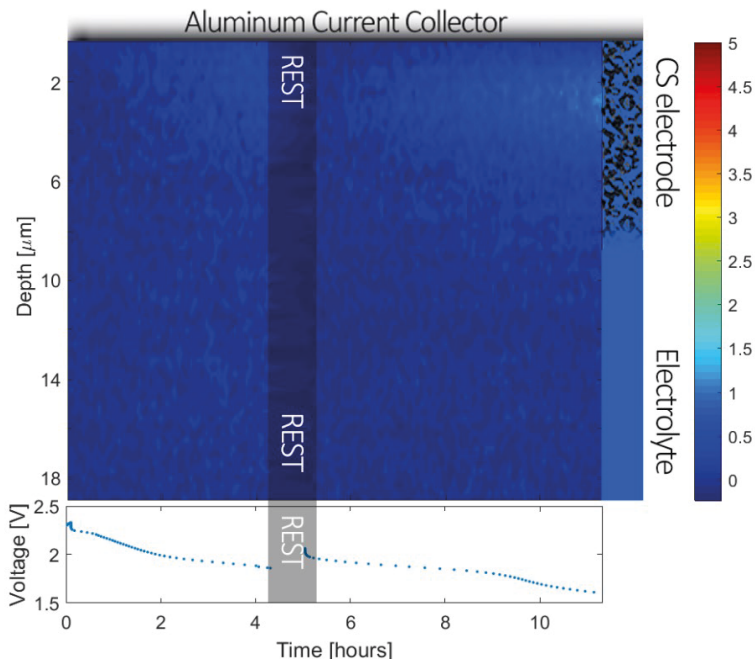


Figure 5.4 NDP result of the CS electrode. Lithiation degree is low as indicated by the light blue colors.

The first plateau ~ 2.4 V was relatively short and the cell quickly entered the second plateau, after approximately 2 hours. Nonetheless the CS electrode is lithiated, whereas the comparable CS electrode + LTO membrane needs almost 8 hours to reach a similar concentration in the electrode. Hence it seems that the rapid voltage drop allows an earlier onset of solid sulfur

deposition. However, when after 4 hours discharge was stopped and the cell was left to rest for 1 hour, all this capacity had left the measurement scope. This concentration increase and decrease might be explained by soluble polysulfide species diffusing slowly outward of the porous network, however this was not observed in the cells containing $\text{Li}_4\text{Ti}_5\text{O}_{12}$ additive. An alternative explanation could be that the solid deposits are re-dissolved with the aid of sulfide (S_8) rings from the available uncycled sulfur. This observation helps to explain the large experimental discrepancies in the reported onset of solid deposition[7, 13, 28, 30].

Based on our NDP spatio-temporal measurements, we were able to generate a comprehensive picture of Li-S batteries at work, as sketched in **Figure 5.5**. Starting from the rest period, where at OCP dissolved S_8 rings are in an equilibrium concentration with the electrolyte. As soon as the circuit is closed, electrons are supplied, allowing these rings to open and form PS complexes. This initiates progressive dissolution of the sulfur active material, see **Figure 5.5B**. These complexes are molecules or possibly ionized to Li^+ and S_n^{2-} . From the results shown in **Figure 5.2 and 5.3**, we can confirm that the soluble polysulfides migrate out of the electrode and are adsorbed at $\text{Li}_4\text{Ti}_5\text{O}_{12}$ sites. In the case of CS+ LTO membrane, the diffusion is observed by a subpar lithiation speed and through the lithium concentration increase in the LTO membrane, which at this voltage can only be attributed to adsorbed lithium polysulfide species. This adsorption process also takes place in the CS+LTO electrode, but to a smaller extent due to the lower $\text{Li}_4\text{Ti}_5\text{O}_{12}$ loading. In the last step (**Figure 5.5C**) the dissolved polysulfide species react to form solid compounds which can only occur on a conducting surface, leading to a lithium ion concentration increase in the electrode region. When the available polysulfide species are consumed, which in the LTO + CS cell leads to a higher Li end-concentration, as adsorbed polysulfide can diffuse over the $\text{Li}_4\text{Ti}_5\text{O}_{12}$ surface to be reduced at the carbon matrix, whereas in the CS+LTO membrane electrode they are simply contained by the membrane, unable to participate in further reactions. Due to the conversion of dissolved polysulfide into solid products, the concentration in the electrode area decreases, hence it becomes thermodynamically favorable for polysulfide species from the electrolyte to diffuse towards the electrode region. This

additional flux is registered atop of the reaction necessary to sustain the applied current.

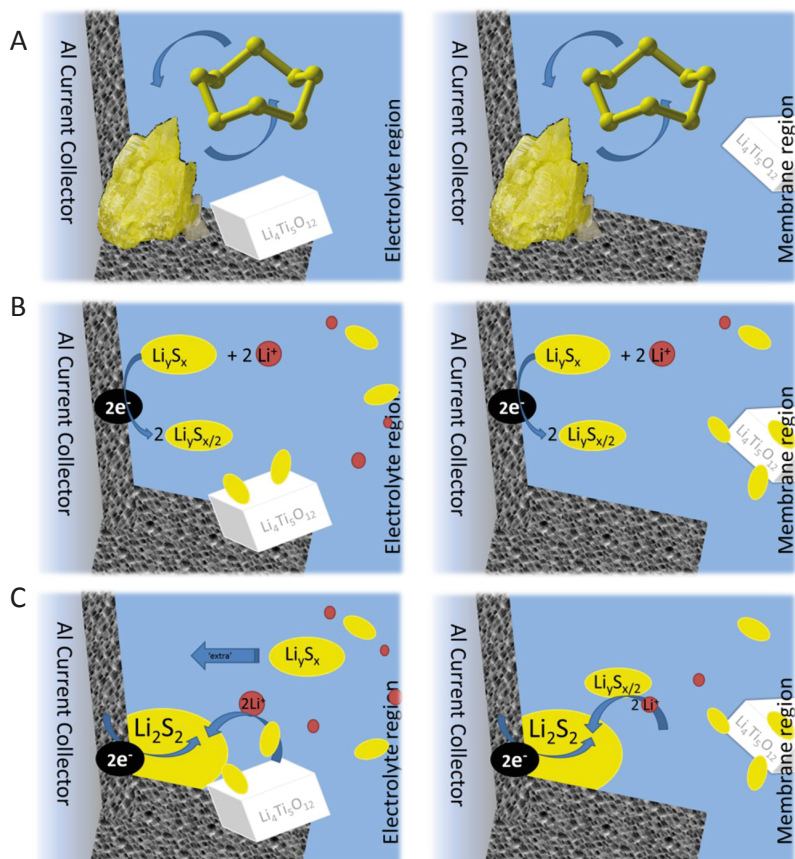


Figure 5.5A-C. Schematic representation of the (electro)chemical processes in the sulfur electrodes during discharge as derived from the operando NDP measurements.

5.3 Conclusions

Neutron depth profiling (NDP) allowed to find real-time evidence for polysulfide migration during different stages of the Li-S cell discharge process. Moreover, as NDP enables us to measure Li concentration both in electrode and electrolyte simultaneously, we succeeded to present the first in operando evidence of polysulfide adsorption on metal oxide ($\text{Li}_4\text{Ti}_5\text{O}_{12}$). By comparing the electrochemical processes and the diffusional behavior of

active material in Li-S batteries in three electrode types of Li-S based cells, it is concluded;

- (i) The utilization of the Li-S capacity is highly dependent on the availability of sulfur, the migration and adsorption of polysulfides and the applied current, demonstrating the importance of operando methods to probe the inner mechanistic processes.
- (ii) Volume expansion can be in part offset by the dissolution of polysulfide, however the formation of solid products can strain the host matrix significantly.
- (iii) Trapping of polysulfides by using a metal oxide membrane interlayer does not necessarily improve the capacity of a Li-S battery. Instead ideally trapping-agents are mixed in the electrode matrix, where material can transfer electrons to the adhered species. Hence providing a catalytic function and aiding polysulfide redox reaction towards solid deposition.

Hence, for the design of commercial sulfur batteries, finding the optimum ratio between sulfur and adsorbing additive for dissolution and confinement and reutilization of polysulfide, is paramount. NDP will be an important tool to unambiguously prove the effectiveness of different cells. Thereby leading to a cell-design with negligible capacity fade due to the polysulfide shuttle. The crucial step towards realizing commercially viable Li-S batteries.

5.4 Methods

Electrodes were prepared by the conventional slurry based process. A slurry was prepared by mixing Sulfur (Sigma Aldrich), Ketjen black (Akzo Nobel), KS4 graphite (Timcal) and PVDF (Kynar Flex) in a weight ratio of 60:15:10:15 in N-methyl pyrrolidone (NMP, from Sigma Aldrich). For the $\text{Li}_4\text{Ti}_5\text{O}_{12}$ containing electrodes, 10 wt.% pure LTO (particle size ~ 150 nm, Süd-Chemie) was applied to the mixture, at the expense of sulfur. The slurry was then casted onto Al-foil using a doctor blade. LTO membranes were prepared by mixing $\text{Li}_4\text{Ti}_5\text{O}_{12}$ and PVDF in a weight ratio of 85:15, without a conductive additive. The semiconducting $\text{Li}_4\text{Ti}_5\text{O}_{12}$ intrinsic low electronic conductivity and low

operating potential should prevent electrochemical energy storage in the membrane and thereby solely showcasing the polysulfide confinement ability. The slurry was subsequently casted on a glass plate and then immersed in demineralized water to phase invert the polymer, which produced a free-standing membrane which is self-detachable from the glass substrate.

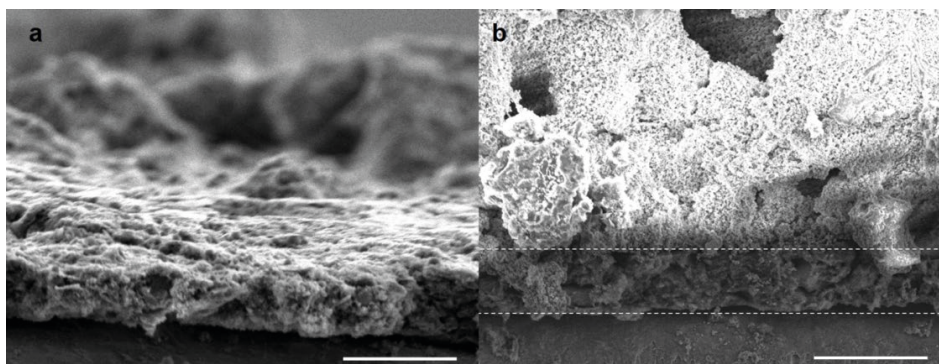


Figure 5.6 Scanning electron microscopy cross-sectional view of the electrodes on Al-foil applied in this study. a) A LTO + CS electrode, containing 10 w% LTO, and b) a CS electrode covered by an LTO membrane with the electrode region clarified by the dashed lines. The scale bars represent 10 μm .

The cells were assembled inside an Ar filled glovebox with oxygen and water content less than 1 ppm. Lithium foil was used as the counter and reference electrode, combined with a glass fiber (Whatman) separator (~ 250 micron thick) and the working electrodes to make up the cell. As electrolyte a solution of 1M LiTFSI in TEGDME was used, with 1 wt.% LiNO_3 additive. The galvanostatic cycling experiments were performed with a programmable Maccor 4000 series galvanostat. The cells were discharged to 1 V and charged to 3.8 V vs. Li^+/Li^0 at various C-rates ($1\text{C} = 1675 \text{ mA}\cdot\text{g}^{-1}$). Prior to electrochemical measurements, the electrodes were shortly dried at 60°C in a vacuum oven.

Pouch cells or coffee bag cells, similar to industrial practice were used in the neutron depth profiling set-up[31, 32]. Their simplicity allows straightforward sealing of the current collector and the pouch material, enabling it to be used

as a window for the ^3H ions[33, 34]. A window diameter of 16 mm was used, whilst electrodes were cast within a 13 mm diameter to facilitate alignment. Despite the high capacity and associated volume change of sulfur (80%)[28] a constant energy to depth conversion is used, rationalized by the mere minor differences in the stopping power between the lithiated sulfur and the pristine material, especially in relation to the other constituents, see **Figure 5.2**.

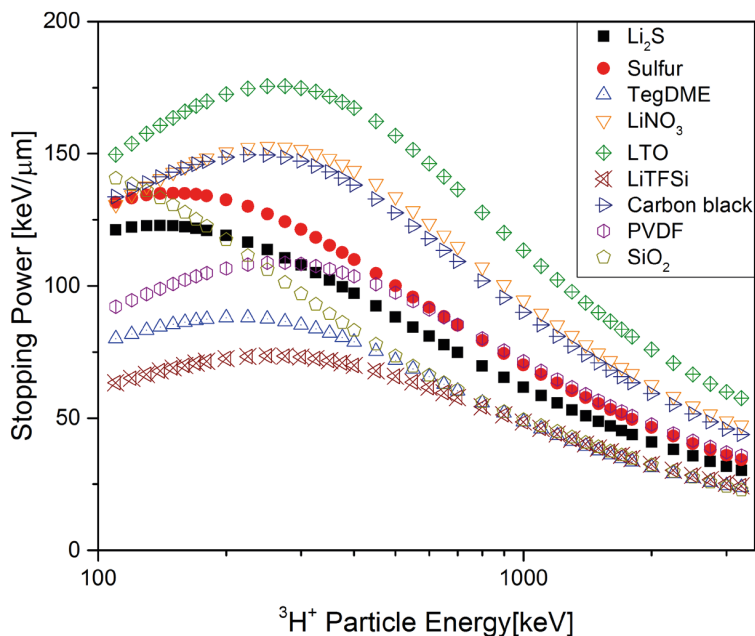


Figure 5.7 The stopping powers of all cell constituents.

5.5 References

1. Kang, H.S., et al., *A Scaled-Up Lithium (Ion)-Sulfur Battery: Newly Faced Problems and Solutions*. *Advanced Materials Technologies*, 2016. **1**(6): p. 1600052.
2. Harks, P.P.R.M.L., et al., *The Significance of Elemental Sulfur Dissolution in Liquid Electrolyte Lithium Sulfur Batteries*. *Advanced Energy Materials*, 2017. **7**(3): p. 1601635-n/a.
3. Manthiram, A., et al., *Rechargeable Lithium–Sulfur Batteries*. *Chemical Reviews*, 2014. **114**(23): p. 11751-11787.
4. Dunn, B., et al., *Electrical Energy Storage for the Grid: A Battery of Choices*. *Science*, 2011. **334**(6058): p. 928-935.

5. Armaroli, N. and Balzani, , *Towards an electricity-powered world*. Energy & Environmental Science, 2011. **4**(9): p. 3193-3222.
6. Conder, J., et al., *Direct observation of lithium polysulfides in lithium–sulfur batteries using operando X-ray diffraction*. Nature Energy, 2017. **2**: p. 17069.
7. Zhao, E., et al., *Advanced characterization techniques in promoting mechanism understanding for lithium–sulfur batteries*. Advanced Functional Materials, 2018. **28**(38): p. 1707543.
8. Fang, R., et al., *More Reliable Lithium–Sulfur Batteries: Status, Solutions and Prospects*. Advanced Materials, 2017. **29**(48): p. 1606823.
9. Pang, Q., et al., *A Comprehensive Approach toward Stable Lithium–Sulfur Batteries with High Volumetric Energy Density*. Advanced Energy Materials, 2016. **7**(6): p. 1601630.
10. Aurbach, D., et al., *On the Surface Chemical Aspects of Very High Energy Density, Rechargeable Li–Sulfur Batteries*. Journal of The Electrochemical Society, 2009. **156**(8): p. A694-A702.
11. Park, K. and J.B. Goodenough, *Dendrite-Suppressed Lithium Plating from a Liquid Electrolyte via Wetting of Li₃N*. Advanced Energy Materials, 2017. **7**(19): p. 1700732.
12. Chen, R., et al., *From a historic review to horizons beyond: lithium–sulphur batteries run on the wheels*. Chemical Communications, 2015. **51**(1): p. 18-33.
13. Zhang, S.S., *Liquid electrolyte lithium/sulfur battery: Fundamental chemistry, problems, and solutions*. Journal of Power Sources, 2013. **231**: p. 153-162.
14. Pang, Q., et al., *Advances in lithium–sulfur batteries based on multifunctional cathodes and electrolytes*. Nature Energy, 2016. **1**: p. 16132.
15. Liu, X., et al., *Nanostructured Metal Oxides and Sulfides for Lithium–Sulfur Batteries*. Advanced Materials, 2017. **29**(20): p. 1601759.
16. Fan, X., et al., *Advanced chemical strategies for lithium–sulfur batteries: A review*. Green Energy & Environment, 2018. **3**(1): p. 2-19.
17. Qu, Q., et al., *Strong Surface-Bound Sulfur in Conductive MoO₂ Matrix for Enhancing Li–S Battery Performance*. Advanced Materials Interfaces, 2015. **2**(7): p. 1500048.
18. Conder, J. and C. Villevieille, *Is the Li–S battery an everlasting challenge for operando techniques?* Current Opinion in Electrochemistry, 2018. **9**: p. 33-40.
19. Zhang, X.Y., et al., *Direct Observation of Li-Ion Transport in Electrodes under Nonequilibrium Conditions Using Neutron Depth Profiling*. Advanced Energy Materials, 2015. **5**(15): p. 1500498.
20. Zhu, W., et al., *Application of Operando X-ray Diffraction and Raman Spectroscopies in Elucidating the Behavior of Cathode in Lithium-Ion Batteries*. Frontiers in Energy Research, 2018. **6**(66).

21. Waluś, S., et al., *New insight into the working mechanism of lithium–sulfur batteries: in situ and operando X-ray diffraction characterization*. Chemical Communications, 2013. **49**(72): p. 7899-7901.
22. Paoella, A., et al., *Transient existence of crystalline lithium disulfide Li₂S₂ in a lithium-sulfur battery*. Journal of Power Sources, 2016. **325**: p. 641-645.
23. Patel, M.U.M., et al., *Li-S Battery Analyzed by UV/Vis in Operando Mode*. ChemSusChem, 2013. **6**(7): p. 1177-1181.
24. Gorlin, Y., et al., *Understanding the charging mechanism of lithium-sulfur batteries using spatially resolved operando X-ray absorption spectroscopy*. Journal of The Electrochemical Society, 2016. **163**(6): p. A930-A939.
25. Pang, Q., et al., *Surface-enhanced redox chemistry of polysulphides on a metallic and polar host for lithium-sulphur batteries*. Nature Communications, 2014. **5**: p. 4759.
26. Kavčič, M., et al., *Operando Resonant Inelastic X-ray Scattering: An Appropriate Tool to Characterize Sulfur in Li–S Batteries*. The Journal of Physical Chemistry C, 2016. **120**(43): p. 24568-24576.
27. Verhallen, T.W., S. Lv, and M. Wagemaker, *Operando Neutron Depth Profiling to Determine the Spatial Distribution of Li in Li-ion Batteries*. Frontiers in Energy Research, 2018. **6**(62).
28. Wang, D.-W., et al., *Carbon–sulfur composites for Li–S batteries: status and prospects*. Journal of Materials Chemistry A, 2013. **1**(33): p. 9382-9394.
29. Tonin, G., et al., *Multiscale characterization of a lithium/sulfur battery by coupling operando X-ray tomography and spatially-resolved diffraction*. Scientific Reports, 2017. **7**(1): p. 2755.
30. Nelson, J., et al., *In Operando X-ray Diffraction and Transmission X-ray Microscopy of Lithium Sulfur Batteries*. Journal of the American Chemical Society, 2012. **134**(14): p. 6337-6343.
31. Gustafsson, T., et al., *The polymer battery as an environment for in situ X-ray diffraction studies of solid-state electrochemical processes*. Electrochimica Acta, 1992. **37**(9): p. 1639-1643.
32. Trask, S.E., et al., *From coin cells to 400 mAh pouch cells: Enhancing performance of high-capacity lithium-ion cells via modifications in electrode constitution and fabrication*. Journal of Power Sources, 2014. **259**: p. 233-244.
33. Lv, S., et al., *Operando monitoring the Lithium spatial distribution of Li-metal anodes*. Nature Communications, 2018: p. in press.
34. Zhang, X., et al., *Rate-Induced Solubility and Suppression of the First-Order Phase Transition in Olivine LiFePO₄*. Nano Letters, 2014. **14**(5): p. 2279-2285.

6.

Next Generation NDP,
for Lithium Ion Batteries

6. Next Generation NDP for Lithium Ion Batteries

The results so far demonstrated have been obtained in a general purpose set-up. However, these set-ups employ operating conditions which harm battery performance, thereby threatening measurement validity. As the demand for NDP measurements increases, the development of battery specific set-ups becomes reasonable. Here the most recent efforts of the reactor institute on new set-ups will be discussed, especially focused around measuring at ambient pressure, thereby avoiding electrolyte evaporation.

6.1 Towards 3D NP

We have seen neutron depth profiling to be a technique that allows quantitative determination of lithium and boron with respect to depth. This non-destructive technique is based on a neutron capture reaction. The reaction energy is distributed between a light ion (H , 3H , α) and a recoil nucleus, see **equation 6.1**[1, 2]. The lighter ion kinetic energy is high enough to reach an energy sensitive detector placed at a distance such that the recorded particles must have left the sample plane perpendicular, enforcing the relation between measured energy and depth. To minimize particle energy loss and straggling, the sample is placed in vacuum[3-5]. These reactions are unique and isotope specific, intrinsically allowing high selectivity and low noise, while leaving the other battery components unperturbed.



The technique has recently gained in scientific interest as it allows to follow the lithium ion movement during (dis)charge in lithium ion batteries. This has provided unprecedented insights regarding diffusion, transfer and cycling efficiency of ions in batteries[3, 6-10]. However a number of issues limit application of this technique. Firstly the principal of operation is now intrinsically one dimensional whereas the challenges of future batteries are multidimensional, for instance homogenous lithium metal plating and microstructural aging in high capacity materials[11-15]. Secondly counting rates are too low and hence exposure times typically do not permit the study of new materials allowing fast charging[5, 6, 10]. Lastly the low pressure

environment is a major obstacle batteries for based on liquid electrolyte, as battery performance is hindered due to electrolyte evaporation[5].

In recent years various techniques have been applied to study of lithium ion battery electrode morphologies in 3 dimensions, aiming to understand charge transfer processes and guide electrode development[16]. As we have seen in **chapter3**, high resolutions, ~ 10 nm, can be obtained using scanning electron microscopy, and in combination with a focused ion beam a 3d image is reconstructed by milling thin layers, < 10 nm[17, 18]. This destructive technique is limited to ex-situ/post mortem imaging and specific information on lithium content cannot be obtained, unless when combined with other techniques[10]. Alternatively X-ray based techniques can allow in-situ and in operando microscopy battery electrodes[19, 20]. The resolutions are limited by the spot size, which can be below 50 nm[21-23]. Furthermore, the combination of x-ray microscopy with x-ray absorption allows to simultaneously obtain chemical and morphological information[24]. In inverse space higher resolutions can be obtained[25], however obtaining in enough information to compile a three dimensional image requires long measurement time[26], hampering in-situ operation. X-rays however do not allow for direct measurement of lithium ions and contrast differences are required to resolve the various electrode phases in microscopy[27, 28]. Especially in liquid based systems the beam intensity can lead to damage to electrolyte, hindering the electrochemical processes[29].

The unique fingerprint of the neutron capture reactions allow to record a specific picture of the distribution of light ions. This has motivated researchers to design set-ups that measure element distributions in multiple directions based on the ${}^6\text{Li}$ capture reaction[30-33]. Typically a millimeter sized pin hole is used to scan the surface, significantly reducing counting rates and obtaining a millimeter resolution in x and y at best[31-33]. Tomandl et al. used sandwich arrangement of two timepix2 detectors to obtain a resolution close 30 micron, however no depth information is recorded[30]. This techniques are clearly still in a development stage but show concentration differences across the electrode (i.e. in x and y). Hence this need of an 3D sensitive type of NDP is clearly demonstrated.

For a fully three dimensional measurement complete particle tracks need to be recorded with a large opening angle allowing high count rates. Gas filled time projection chambers (TPC) allow particle energy and trajectory to be determined. Their principal is based on the ion-electron pairs produced by the particle moving through a gas[34], see **Figure 6.1**. The pairs are separated due to an electric field, forcing the electrons to drift to a pixel chip detector. On top of this Timepix detector a micromesh is placed, a combination is known as Gridpix TPC. This micromesh grid allows a potential to be applied such that the incoming electrons are accelerated, leading to an electron avalanche which triggers the pixel below[35]. These hits form a 2d projection of the track. Furthermore each pixel can record either the time of arrival (TOA) or the time above a certain threshold (TOT) with 10 nanosecond increments. As the electron drift velocity is known, the arrival time provides the remaining coordinate of the particle trajectory. Alternatively the time over threshold is related to the total number of ion-electron pairs and thus to particle energy. The energy lost in the sample and the angle at the point of entry can be determined using either way. This information forms the basis to the reconstruction of the isotope presence in 3D.

Recently a new generation of Timepix chips is available, referred to as Timepix3. This chip records with nanosecond increments (640 MHz)[36] and allows simultaneous read and write, eliminating death time. A consortium from Bonn university, CERN and Nikhef aims to provide ready to use Gridpix TPC's based on this Timepix3 chip for various charged particle applications. Furthermore they are assembling so-called 'quads', assemblies of 4 chips enabling an active area of 10.24 cm^2 . These technical developments permit recording the emitted particles in 3 dimensions allowing the reconstruction of 3D isotope specific images revolutionizing the neutron depth profiling technique. Moreover the detection rates will be sufficient to allow time resolved operando measuring, without vacuum and high freedom in sample environment.

Now we intend to apply of these Gridpix TPC's in depth profiling. The advent of high capacity anodes and cathodes will increase the lithium concentration and therefore counting rates. Together with the increased opening angle this

will lead to sufficient statistics to follow the lithium distribution in 3D in batteries in operando. This is highly relevant as dramatic morphological changes and the associated failure mechanisms, e.g. dendrites and SEI build up, spoil commercial exploitation of these high energy density systems. As aforementioned in operando 3D characterisation is actively pursued with various probes, the proposed technique however is unique owing to its' high isotope selectivity allowing to directly probe the most active battery component, lithium. Moreover through isotope enrichment, ^6Li and ^7Li , labelling selective parts is possible, allowing to probe specific battery components without limiting battery operation.

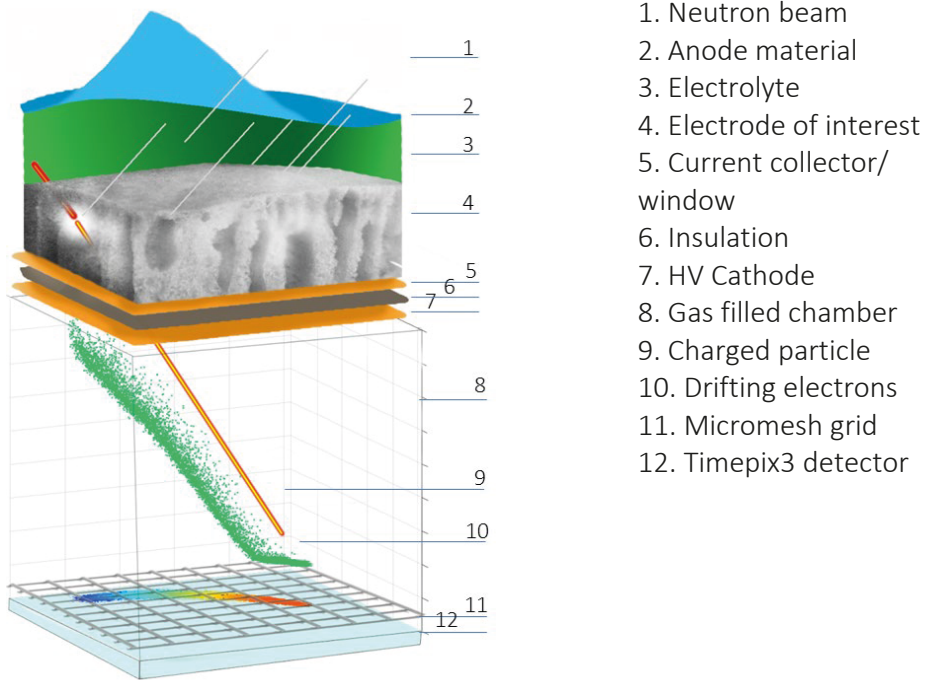


Figure 6.1. Sketch illustrating the operating principle of the gridpix NDP set up.

6.1.1 Preliminary results

With the development of quad assembled gridpix TPCs underway, the feasibility of the proposed set-up is studied using a single timepix1 chip, see **Figure 6.1**. The active volume or drift volume is 16x16x50mm, all the area above the reflective silicon chip. To explore the possibilities and limitations of

such a set-up, various experiments were performed. Here a selection of the methods used and their results are presented according to the source of the ionizing particle. In these detectors specific gases are used as the ingress of electronegative species, e.g. O_2 , can trap electrons and act as a center for recombination; detrimental for the principal of operation[36]. Even though these gasses for TPCs are well understood, the application here requires exposure to neutrons thereby limiting the application of certain noble gasses. The activation of these gasses poses a safety concern which should be avoided. Besides pollution of the gas, heterogeneities in the drift electric field also hamper operation. Hence the set-up must be characterized.

6.1.1.1 Muons

A good start for this characterization is the measurement of muons[37, 38]. A muon is particle equal in charge as an electron and about two hundred times heavier, created when a pion interacts with the outer atmosphere. It has half-life is 2.2 μs and reaches the earth's surface owing to its relativistic velocity[39, 40]. Their intensity approximates $1 \text{ min}^{-1}\text{cm}^{-2}$ [37, 38]. The advantage of these particles is their global availability and straight trajectory, allowing to demonstrate the homogeneity of the electric field across the drift volume. A typical muon trajectory is shown in **Figure 6.2**. Being a minimal ionizing particle only few primary electrons are freed. Hence a gas is used with high ionization density, argon/isobutene 95/5, but shows large lateral diffusion. This leads to the characteristic spherical spread, especially visible in the blueish pixels owing to the longer drift times as they originated from the top of the volume.

The muon intensity is small. The timepix1 chip can record 11810 increments of 10 nanoseconds, which equals a recording window of 0.1 milliseconds, after which readout consumes the next 30 milliseconds, the chance that a muon passes when the detector is recording is impractically small. Hence a set-up utilizing a double scintillator is used. One below and one above the detector, this allows to start recording only when a muon has passed. Since the particle is travelling at relativistic speeds it passes all three components more or less simultaneously, but the electrons need time to reach the chip, giving the control system time to respond. After 1 microsecond the

measurement is stopped and the chip is read. The recorded time of arrival on all pixels are plotted in a histogram, **Figure 6.2.b**. The peak around 930 ns is caused by primary electrons formed close to the chip. Due to the delay in the electronic circuit, these electrons have already reached the chip when the measurement is started.

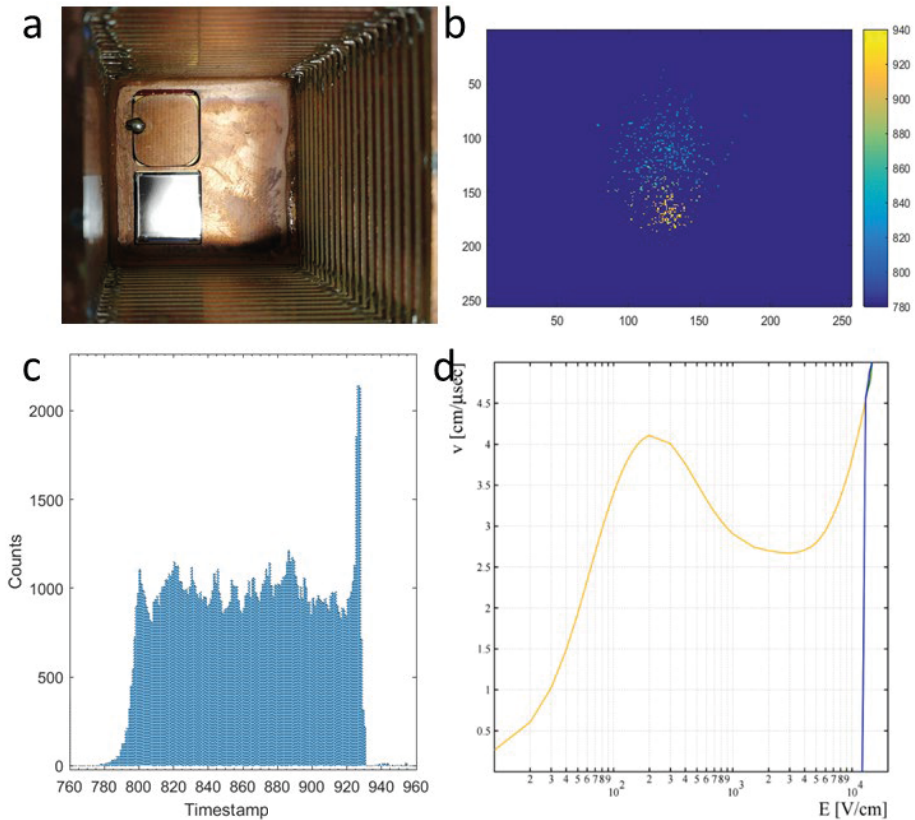


Figure 6.2.a) View into the detector with the 16x16mm gridpix chip bottom left. **b)** typical trajectory with in yellow the last recorded pixels (near the chip) and in blue the pixels associated to the point of entry. **c)** Histogram of the time of arrival of pixels during the measurement. **d)** Electron drift velocity as calculated using MAGBOLTZ[41].

From **Figure 6.2.c**, the time difference between front and back is found to be 1400 ns. The electron drift velocity is calculated at various electric field strengths using the MAGBOLTZ software package[41]., the result is shown in

Figure 6.2.d. The applied field strength was 200V/cm leading to a drift velocity of 4.1 cm per microsecond, yielding 5.75 cm which considering diffusion and straggling is expected.

6.1.1.2 Lithium

Next we move a sample with a stronger resemblance to battery application. A difficulty is the relatively small active volume compared to triton projected range. A 2.7 MeV triton travels approximately 5 cm in this gas, see **Figure 6.3.a**. In the envisioned application there will be a number of layers separating the sample, i.e. the electrode material and battery interior, from the high voltage cathode and the active gas volume. First there is the battery current collector/substrate, second an insulating layer and thirdly a cathode foil, to which high voltage is applied, to instigate electron drift. These layers reduce the particle energy and range, reducing the size of the necessary active volume. Alternatively, gasses with higher charge density can be used to increase the stopping power and reduce the necessary detection volume.

Here, to mimic the influence of various substrates a standard LiFePO_4 coating was tested behind an 11 micron aluminum foil and a 10 micron copper foil, reducing the particle energy to 2.2 MeV and 1.45 MeV respectively, see **Figure 6.3**. The start and the end of the measured trajectory is used to calculate the track length, as based on the time of arrival and corresponding pixel coordinates. Using the relation between range and particle energy found using SRIM, as presented in **Figure 6.3.a**, this is converted to an energy spectrum as depicted in **Figure 6.3.b** Even though the same area was measured behind the substrate, as verified by the similar intensities, the spectra obtained clearly differ. This is an artefact caused by the small detector size as compared to the range of the more energetic particles, causing part of their trajectory to lie outside the field of view thus making it unfeasible to correctly assess the path length of these particles. In the copper foil the particles lose more energy and as such a larger degree of particle traces lie within the field of view, see highlighted trace in **Figure 6.3.c**.

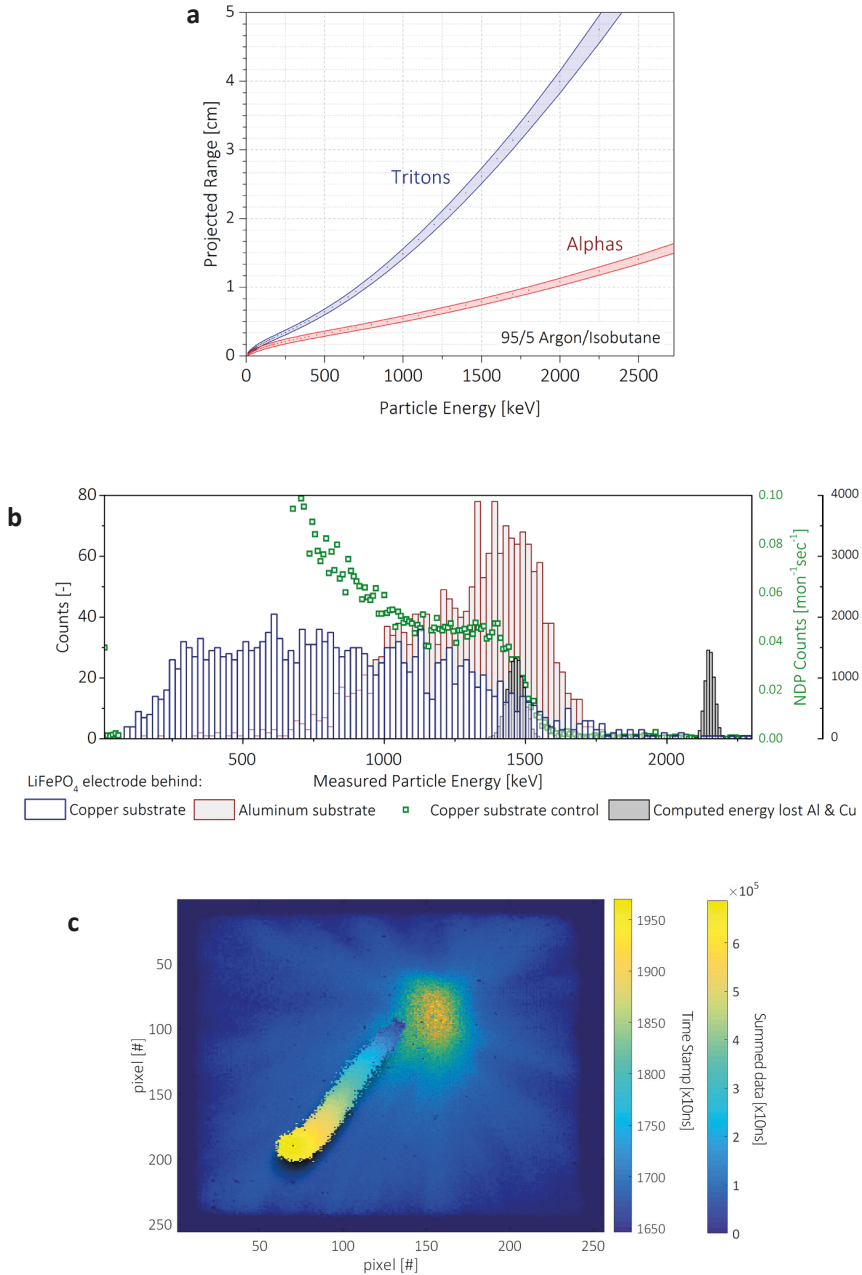


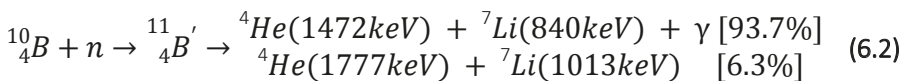
Figure 6.3.a. Projected range of tritons and alphas in Argon Isobutene gas mixture, calculated using SRIM, error bar reflects straggling which intrinsically limits the attainable resolution[42]. **b.** Measured spectra from a LiFePO₄ electrode (3x3mm) placed behind various substrates and compared

with a spectrum obtained traditionally, all were obtained over three hours. The energy lost, calculated using SRIM, is added to depict intrinsic error due to straggling. **c.** Measured time of arrival from a (3x3mm) LiFePO₄ electrode placed behind copper foil. Size and shape are visible in the sum of all data, highlighting the origin of traces. A single triton trace is showed on top of this data, reflecting the high ionization density.

Now comparison with the standard NDP set-up is possible, depicted by the green squares. The silicon chip detector used in the traditional set-up is sensitive to betas and photons leading to noise in low energy regime. Here the new set-up has a clear advantage as differing ionization profiles allow straightforward separation from the particle traces. Furthermore from the sum of all traces, **Figure 6.3.c.**, the sample location can be easily determined allowing particles a different origin to be ignored. The accuracy in which the particle origin is determined greatly effects the resolution of this set-up. However from this image containing a mere 1823 verified particle traces a clear sample location and size can be determined.

6.1.1.3 Boron

The active volume is small relative to the track length of the 2.7 MeV tritons. Hence further 2-dimensional characterization is performed with less energetic particles. Boron-10 has been an important isotope in past neutron depth profiling applications[2]. The neutron capture reaction is;



The cross section for this reaction is 4 times larger than lithium and the isotope abundancy is higher, being approximately 20% in natural samples. Hence, in parallel, it will be interesting to explore whether the different particles can be recognized.

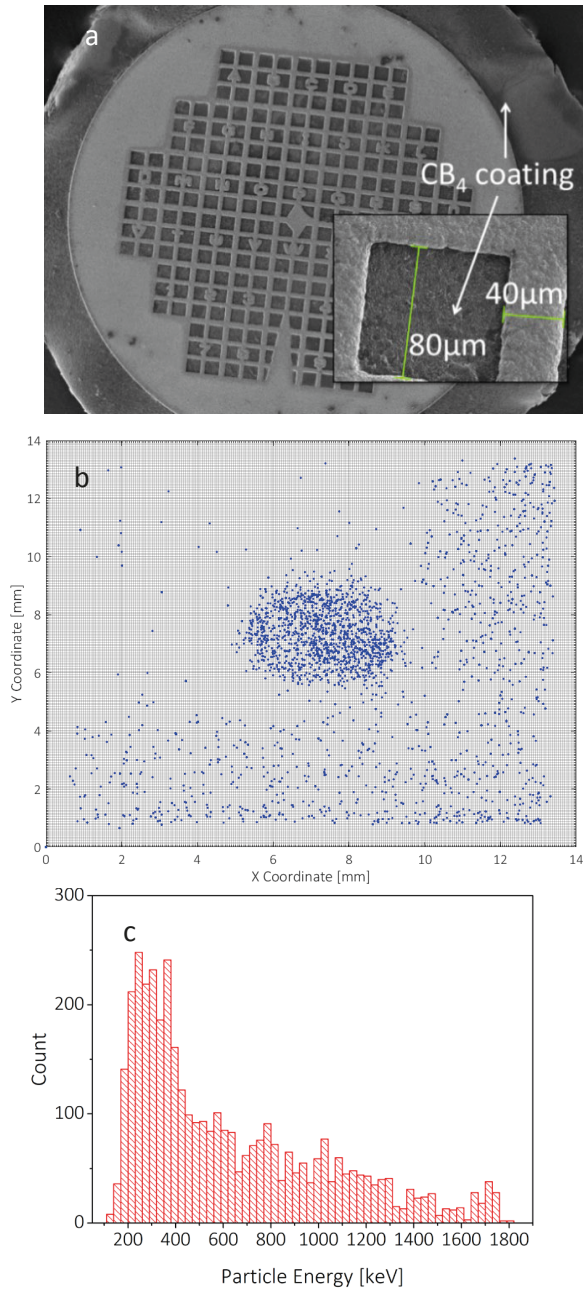


Figure 6.4.a) TEM-grid solidified in a boron carbide coating. **b)** Scatter plot of the starts of the tracks recorded, in total 4700 particles were measured. Grid squares are pixel sized. **c)** Particle energies interpreted from track lengths.

The ^{10}B based sample is made with the aim to further detail the lateral resolution. For this purpose a 2.3 mm TEM grid is stuck in a straightforward coating on the basis of NMP, PVDF and boron carbide (CB_4). The TEM grid is decorated with letters and numbers as they are designed for holding samples. Besides these indications the grid consists of equally spaced square holes, see **Figure 6.4.a**. Although these holes are slightly larger than a pixel, the walls are below the pixel size, hence it is not expected that the resolution is adequate to retrieve the pattern. In any case it is difficult to attain adequate statistics, as the death time of timepix1 exceeds 99.5%. Hence when the starts of all traces, plotted **Figure 6.4.b**, are compared to the SEM picture, the resemblance is still poor, the 4500 tracks recorded do not allow to obtain a clear image. More surprisingly the energy resolution in **Figure 6.4.c**, is also poor, time of arrival does not allow to determine the particle type, however the range of low energy alpha and lithium particles is similar. This seems counterintuitive as lithium atoms are heavier than helium, however the energy of the lithium produced is right below the Bragg peak, whereas the energy of the alpha is before the Bragg peak, see **Figure 6.6a** and **b**. A Bragg peak refers to the large increase in stopping power protons and ions experience as their energy decreases, this leads losing almost all their energy near the end of their trajectory[43-45]. The peak energy is particle specific, being higher for lithium particle. Hence the peculiarity occurs that 600 keV particles have equal track lengths, as they experience similar stopping power, see **Figure 6.5**. However their ionization profiles are, for the same reason entirely different. The helium should attain its' maximum in stopping power somewhere along the track whereas the lithium stopping power is almost constantly decreasing. The stopping power is directly related to ionization and thus production of primary electrons. Hence when a recording the time over threshold an energy loss can be determined along the particle track. The measured rate of energy loss is related to track orientation and stopping power.

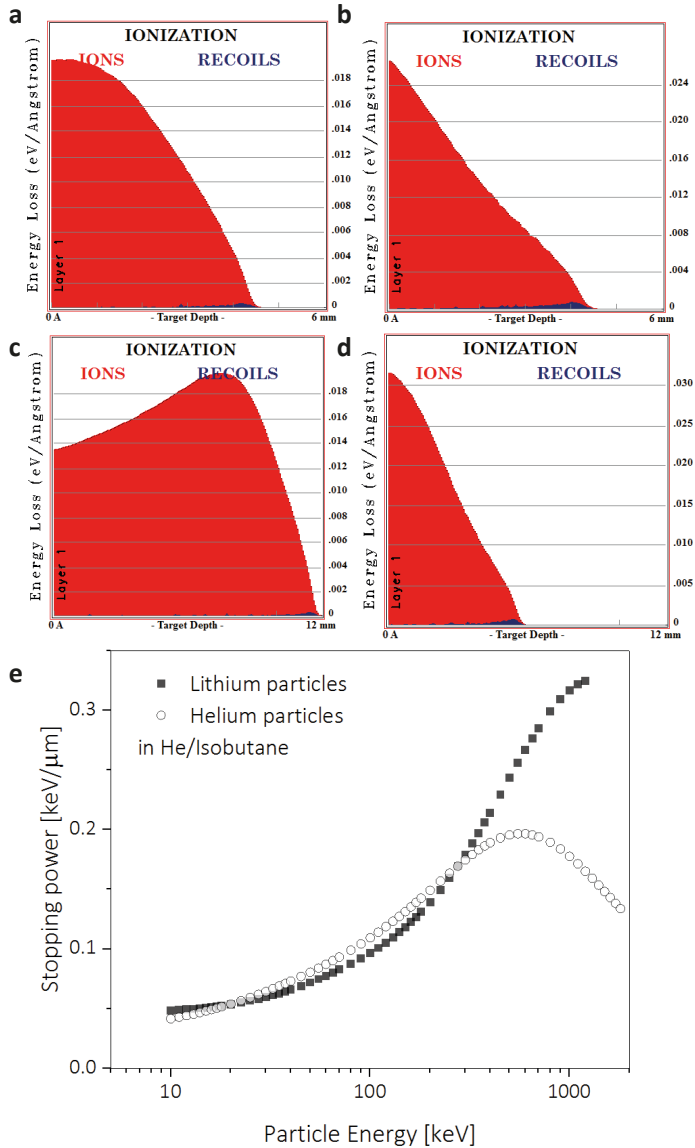


Figure 6.5. Calculated energy loss in Helium/isobutane 79.9/20.1 gas mixture, in eV/Å for He, **a)** and **c)**, and Li, **b)** and **d)**, particles. In **a)** and **b)** particle energy is 600 keV, in **c)** 1772 keV and in **d)** 1012 keV **e)** Stopping power of He and Li particles in Helium/isobutene 79.9/20.1 gas mixture, as a function of particle energy.

In **Figure 6.6e-h** this comparison demonstrated. Two tracks are shown in **Figures e and f**, their shape and length differs only marginally. However when looking a transverse sum, the ionization along the trajectory, the vastly differing energy loss profiles emerge. The red blocks show a slight, near linear increase toward a maximum half way, after which it drops rapidly towards the end, clearly resembling the simulated He spectrum shown in **Figure 6.6.c**. Even though the blue squares show significantly more noise, the trends is a clear constant decay, similar to what is expected from the lithium particles. The scatter is reminiscent from the conversion between polar coordinates and Cartesian axes and is reduced by binning the data.

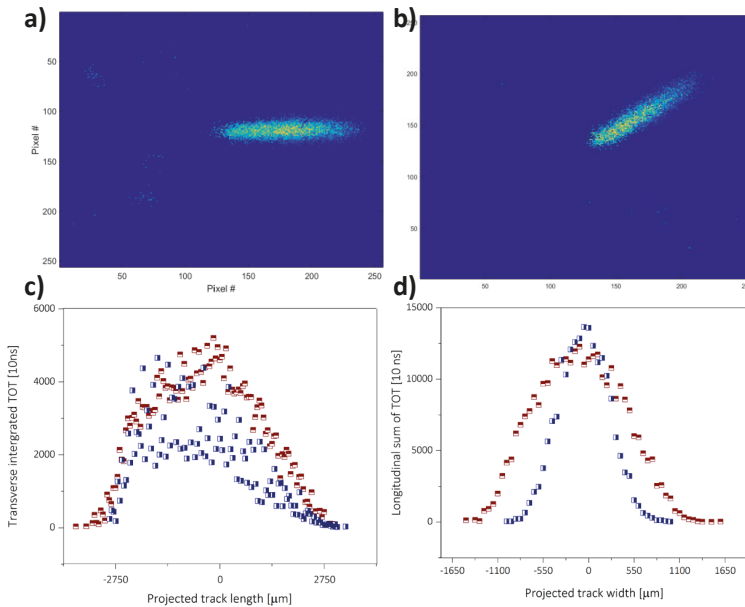


Figure 6.6 Measured energy loss reflected by time over threshold, in **a)** and **b)** and transverse **(c)** and longitudinal **(d)** integrated values of traces plot in **a)** (horizontal red squares) and **b)** (vertical blue squares).

6.1.2 Discussion

A new principle for NDP has been demonstrated using a particle trace detector based on a Timepix1 chip. A method to measure particle track length, point of entry and particle energy and type was shown. These steps provide sufficient information to disentangle the 3D distribution. Although the principle is shown to be feasible, the trail set-up has shortcomings.

Firstly, owing to the relatively large dead time collecting 4000-5000 tracks consumes approximately thirty hours, while as shown above this is insufficient for satisfactory x-y resolution. Similar to the first example, where a double scintillator was used to record muons efficiently, this can be improved by designing a trigger. The ratio between measurement and readout time remains a detrimental issue. Secondly the active area is too small to stop the tritons completely.

Yet the unique operating principle provides sufficient beneficial properties. Lateral information is now obtained and the large opening angle allows faster regular, i.e. 1D, NDP. Furthermore the use of a timepix chip allows to discriminate the tritons from other radiation, this allows the effectively measure at much lower particle energies where the signal of a traditional silicon chip detectors is poor due to noise from beta and gamma radiation emitted in the chamber. Also vacuum operation is no longer a necessity.

6.2 Alternative routes to vacuum free NDP

The ideal sample to detector distance decreases the opening angle such that the detector resolution and the geometrical resolution are equal. However as straggling and geometrical errors are path length and thus energy dependent a trade-off needs to be made, this has led to the present length of 45mm and approximately 12 degrees[1, 46-48], see **Figure 2.1**. Here two alternatives are described that allow the use of a similar opening angle whilst operating at ambient pressures.

Firstly the stopping power of the gas could be decreased[49]. Hydrogen and helium both provide a significant decrease in electron density with respect to air. Although there is no difference in the total amount of charge the distribution of these charges significantly alters the stopping power[43], see **Figure 6.7**. As this is lower for helium, this gas is most suited.

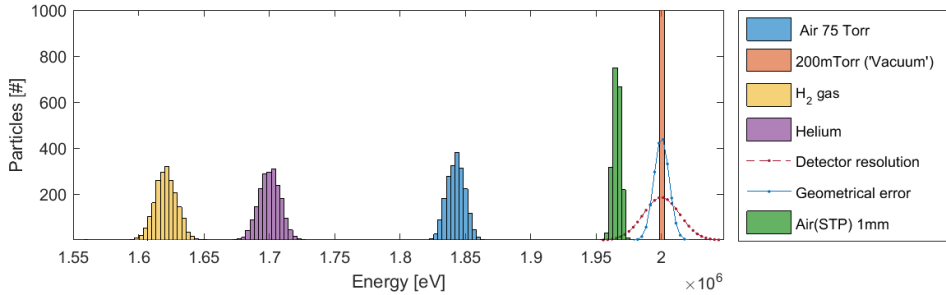


Figure 6.7. Energy loss and straggling of 2MeV tritons in different gasses, this energy is equal to the energy of a triton after 11 micron of aluminium foil, a common current collector. Results of Monte Carlo simulation of 2000 trajectories in SRIM, see appendix for program details. Bin width is 3266 eV, peak width is inversely related to particle energy due to straggling as is explained in section 2.1.5. Detector resolution is approximated by a Gaussian with standard deviation of the rated error for 5MeV alfa's, the standard deviation of geometrical resolution is assumed to be a third of the maximum error.

The idea would be to perform the experiments in an enclosed volume to be filled with helium, such an enclosure is sketched in **Figure 6.8**. This helium chamber would be flushed and filled prior to the measurement. The advantage of this set-up is that operating conditions remain unaltered, hence the introduction of this should be straightforward. Although arguably some advantage as associated with decreasing the sample to detector distance as the convolution of straggling and geometrical error is larger than the detector resolution for most energies, see **Figure 6.7** and **Figure 6.9**. Hence in the chamber three positions are available 30, 40 and 50 mm from the sample plane. These positions allow a 2.2, 1.25, 0.8 fold increase respectively, assuming a point source sample. Increasing the sample to detector distance decreases the geometric error by decreasing the detector opening angle, as was explained in **Chapter 2**. However, in a ambient pressure helium environment does not increase the measurement accuracy as straggling in the gas has become the dominant error contribution, see open symbols in **Figure 6.9**. Nonetheless this last position van be used to decrease counting rates and so called 'pile up' effects[50] in concentrated samples, see **section 2.1.4**.

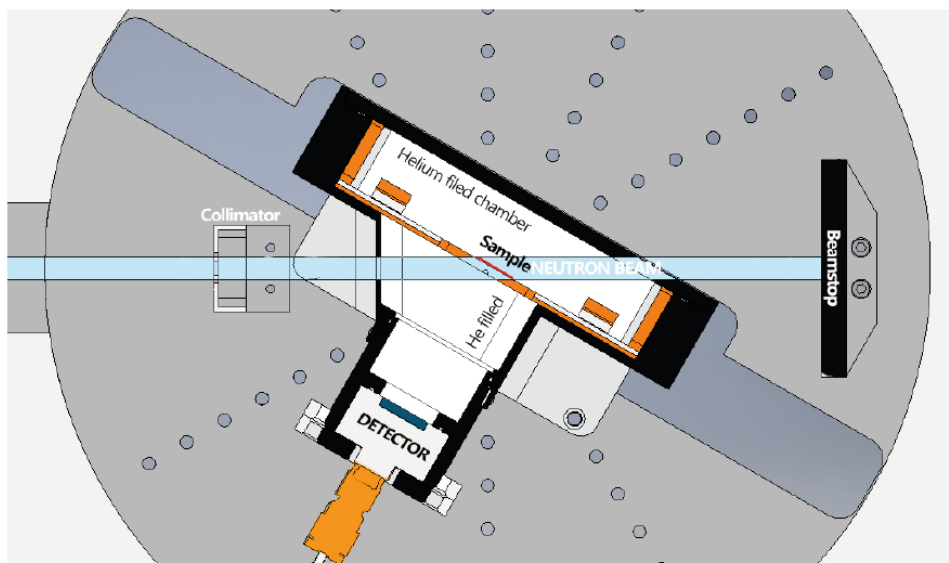


Figure 6.8 A cross section of the helium filled ‘nesting doll’ set up.

The aluminum enclosure should not significantly alter the background as at present the same alloy is used for the chamber and the absorption in the 1 mm thick entry window is negligible. However the amount of material is a little increase, for more on the activation of this set-up, see **Appendix E**. Not shown in the Figure is an extension fitting the entire detector connector assembly, as these are purposely made to leak in order to prevent damage as they are normally used under vacuum conditions.

The Russian nesting doll set-up, helium chamber inside vacuum chamber, has another advantage. As the chamber can be fed into the glovebox, a battery electrode could be harvested and measured without exposure to oxygen or water, thereby paving the way towards ex-situ measurements on instable anode material and solid electrolytes.

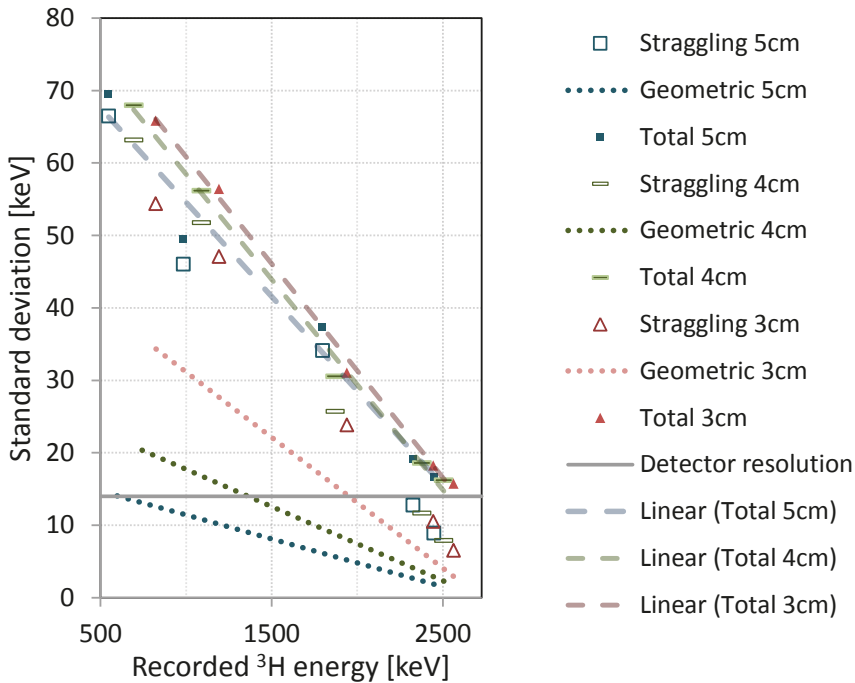


Figure 6.9. Measurement inaccuracy versus recorded tritium energy. Clearly geometric error increases with decreasing sample to detector distance. However as straggling is the dominant contributor to the deviation of the measured energy, the resolution is almost independent of the sample to detector distance, within the available range.

A second route is through altering the method for decreasing the detectors' opening angle. Instead of placing the detector at a certain distance, a multi-channel plate, a filter, with a similar ratio between length and channel diameter would yield equal geometrical resolution, see **Figure 6.10**. This set up would reduce the distance to $\sim 1\text{mm}$, hence allowing to use an ambient air environment. At these distances straggling would be significantly reduced, see **Figure 6.7**. This does mean that the detector is located in the neutron beam. This is not without consequences. The printed circuit board mount for instance contains a bromide fire retardant and bromide isotopes are prone to activation. The use of bromide should therefore be avoided. Hence the hole in the mount shown in **Figure 6.10b** and **c**. Moreover the silicon chip detector is a p-n junction, containing boron on the p-side. Almost 20% of this boron is

likely to be the ^{10}B isotope[51], able to undergo a neutron capture reaction itself. Although depletion of boron is unlikely to threaten detector function, the ions produced would affect the measurement, this however should be well defined peak and should be straightforwardly compensated for.

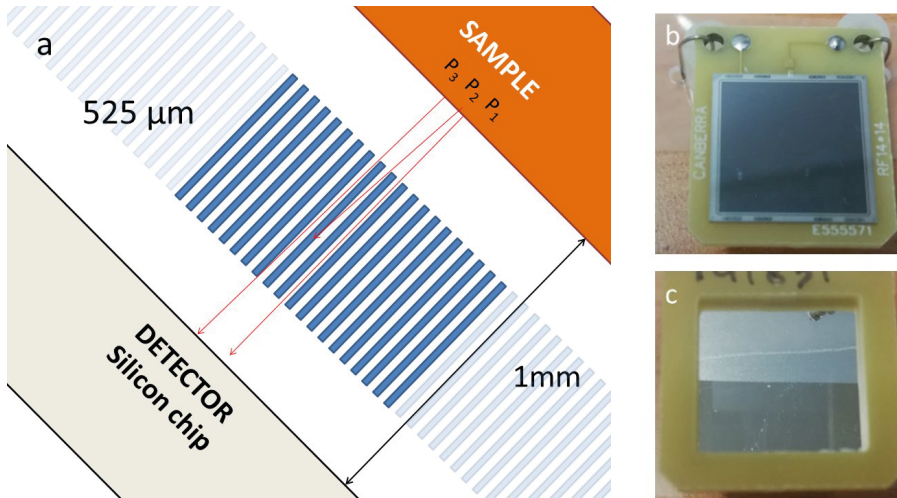


Figure 6.10 a) Collimation method, P1 makes it to the detector, P2 is filtered out and P3 penetrates part of the filter. **b&c)** show front and back of the silicon chip detector.

The filter is a standard silicon wafer, hence the $525\ \mu\text{m}$ thickness. The channel diameter should than be $50\ \mu\text{m}$, these aspect ratios can be achieved using a technique known in this field as deep reactive ion etching[52, 53]. Wall thicknesses should be minimal order to reach appreciable counting. Although the advent of high capacity anodes and cathodes, the so-called beyond Li systems ensure measurements with high count rates which do not suffer from a 50-75% decrease in intensity[5, 54]. Although the principle of operation remains largely unaltered and straggling is reduced, see **Figure 6.7**, there is a new error contribution to be considered, specifically associated with this set up. Particles can hit the wall but still reach the detector, increasing noise in the low energy region. This noise will bear a relation with the signal in the higher energy region, possibly allowing a measurement specific calibration. This process would be similar to the process explained in **section 2.3.3** designed to compensate the alfa signal.

6.3 Conclusions

Recent developments for li-ion battery oriented set-ups have been sketched here. One particularly interesting concept is based on a gas filled chamber allowing 3D particle track reconstruction. Aiming to resolve lateral concentration differences, added benefits include; increased opening angle allows for faster measurements, no need for a vacuum owing to the unique operating principal and the ability to discriminate various ionizing particles, thereby greatly reducing noise sensitivity. The results presented here are based on a first generation timepix chip. Owing to their large readout time, these chips are unable to record at rates that reach temporal resolution. However, recently a consortium of Bonn University, Nikhef and ASI have embarked on build assemblies of next generation timepix chips. These so-called 'quads' cover 28mmx28mm of active area, moreover the timepix3 chip can operate in simultaneous read and write mode. These developments allow striving for a new mode of NDP offering intrinsic 3D spatial and temporal resolution.

Eliminating the need for vacuum operation as it hinders liquid electrolyte battery operation can also be achieved alternatively. Here two concepts were presented, one of which is currently used actively. It is a Russian nesting doll type of operation. The environment of the li ion pouch cell is kept at ambient pressure, by filling the surrounding interior with helium. The introduction of this gas adds to the measurement uncertainty. Yet by putting the detector closer, counting rates increase, allowing to balance time and depth resolution.

Higher depth resolution might be achieved by using a filter to collimate the beam irradiating the detector. However this loses a large fraction of the signal. Moreover the detector would have to be placed in the neutron beam, which considering the boron in junction leads to noise and, on the long term, could lead to radiation damage. Furthermore particles traveling through part of the filter will introduce noise.

6.4 References

1. Fink, D., *Neutron Depth Profiling*, Hahn-Meitner Institute fur Kernforschung, 1996.



2. Ziegler, J.F., et al., *Technique for determining concentration profiles of boron impurities in substrates*. Journal of Applied Physics, 1972. **43**(9): p. 3809-3815.
3. Oudenhoven, J.F.M., et al., *In Situ Neutron Depth Profiling: A Powerful Method to Probe Lithium Transport in Micro-Batteries*. Advanced Materials, 2011. **23**(35): p. 4103-+.
4. Downing, R.G., et al., *Neutron Depth Profiling: Overview and Description of NIST Facilities*. Journal of Research of the National Institute of Standards and Technology, 1993. **98**(1): p. 109-126.
5. Verhallen, T.W., et al., *Operando Neutron Depth Profiling to Determine the Spatial Distribution of Li in Li-ion Batteries*. Frontiers in Energy Research, 2018. **6**(62).
6. Zhang, X.Y., et al., *Direct Observation of Li-Ion Transport in Electrodes under Nonequilibrium Conditions Using Neutron Depth Profiling*. Advanced Energy Materials, 2015. **5**(15): p. 1500498.
7. Wang, J., et al., *Profiling lithium distribution in Sn anode for lithium-ion batteries with neutrons*. Journal of Radioanalytical and Nuclear Chemistry, 2014. **301**(1): p. 277-284.
8. Lv, S., et al., *Operando monitoring the lithium spatial distribution of lithium metal anodes*. Nature Communications, 2018. **9**(1): p. 2152.
9. Liu, D.X., et al., *In Situ Quantification and Visualization of Lithium Transport with Neutrons*. Angewandte Chemie-International Edition, 2014. **53**(36): p. 9498-9502.
10. Liu, Z., et al., *Relating the 3D electrode morphology to Li-ion battery performance; a case for LiFePO₄*. Journal of Power Sources, 2016. **324**: p. 358-367.
11. Zhang, S.S., *Problem, Status, and Possible Solutions for Lithium Metal Anode of Rechargeable Batteries*. ACS Applied Energy Materials, 2018. **1**(3): p. 910-920.
12. Xu, W., et al., *Lithium metal anodes for rechargeable batteries*. Energy & Environmental Science, 2014. **7**(2): p. 513-537.
13. Seh, Z.W., et al., *Designing high-energy lithium-sulfur batteries*. Chemical Society Reviews, 2016. **45**(20): p. 5605-5634.
14. Kalhoff, J., et al., *Safer Electrolytes for Lithium-Ion Batteries: State of the Art and Perspectives*. ChemSusChem, 2015. **8**(13): p. 2154-2175.
15. Guo, Y., et al., *Reviving Lithium-Metal Anodes for Next-Generation High-Energy Batteries*. Advanced Materials, 2017. **29**(29).
16. Conder, J., et al., *Do imaging techniques add real value to the development of better post-Li-ion batteries?* Journal of Materials Chemistry A, 2018. **6**(8): p. 3304-3327.
17. Hutzenlaub, T., et al., *Three-dimensional reconstruction of a LiCoO₂ Li-ion battery cathode*. Electrochemical and Solid-State Letters, 2012. **15**(3): p. A33-A36.

18. Hutzenlaub, T., et al., *Three-dimensional electrochemical Li-ion battery modelling featuring a focused ion-beam/scanning electron microscopy based three-phase reconstruction of a LiCoO₂ cathode*. *Electrochimica Acta*, 2014. **115**: p. 131-139.
19. Nelson, J., et al., *In Operando X-ray Diffraction and Transmission X-ray Microscopy of Lithium Sulfur Batteries*. *Journal of the American Chemical Society*, 2012. **134**(14): p. 6337-6343.
20. Yang, N.-H., et al., *In Operando Transmission X-ray Microscopy Illuminated by Synchrotron Radiation for Li-Ion Batteries*. *ACS Energy Letters*, 2018. **3**(8): p. 1911-1928.
21. Liu, Y., et al., *Phase retrieval using polychromatic illumination for transmission X-ray microscopy*. *Optics express*, 2011. **19**(2): p. 540-545.
22. Wang, J., et al., *In operando tracking phase transformation evolution of lithium iron phosphate with hard X-ray microscopy*. *Nature Communications*, 2014. **5**: p. 4570.
23. Andrews, J.C., et al., *Nanoscale X-ray microscopic imaging of mammalian mineralized tissue*. *Microscopy and Microanalysis*, 2010. **16**(3): p. 327-336.
24. Meirer, F., et al., *Three-dimensional imaging of chemical phase transformations at the nanoscale with full-field transmission X-ray microscopy*. *Journal of Synchrotron Radiation*, 2011. **18**(5): p. 773-781.
25. Zhang, X., et al., *Rate-Induced Solubility and Suppression of the First-Order Phase Transition in Olivine LiFePO₄*. *Nano Letters*, 2014. **14**(5): p. 2279-2285.
26. Sedmák, P., et al., *Grain-resolved analysis of localized deformation in nickel-titanium wire under tensile load*. *Science*, 2016. **353**(6299): p. 559.
27. Borkiewicz, O.J., et al., *Best Practices for Operando Battery Experiments: Influences of X-ray Experiment Design on Observed Electrochemical Reactivity*. *The Journal of Physical Chemistry Letters*, 2015. **6**(11): p. 2081-2085.
28. Yang, Y., et al., *In Situ Electrochemistry of Rechargeable Battery Materials: Status Report and Perspectives*. *Advanced Materials*, 2017. **29**(31): p. 1606922.
29. Ganapathy, S., et al., *Operando Nanobeam Diffraction to Follow the Decomposition of Individual Li₂O₂ Grains in a Nonaqueous Li-O₂ Battery*. *The Journal of Physical Chemistry Letters*, 2016. **7**(17): p. 3388-3394.
30. Tomandl, I., et al., *High resolution imaging of 2D distribution of lithium in thin samples measured with multipixel detectors in sandwich geometry*. *Review of Scientific Instruments*, 2017. **88**(2): p. 023706.
31. Werner, L., et al., *The new neutron depth profiling instrument N4DP at the Heinz Maier-Leibnitz Zentrum*. *Nuclear Instruments and Methods in Physics Research Section A: Accelerators, Spectrometers, Detectors and Associated Equipment*, 2018.



32. He, Y., et al., *3D mapping of lithium in battery electrodes using neutron activation*. Journal of Power Sources, 2015. **287**: p. 226-230.
33. Portenkirchner, E., et al., *Tracking areal lithium densities from neutron activation – quantitative Li determination in self-organized TiO₂ nanotube anode materials for Li-ion batteries*. Physical Chemistry Chemical Physics, 2017. **19**(12): p. 8602-8611.
34. Ketzer, B., *A time projection chamber for high-rate experiments: Towards an upgrade of the ALICE TPC*. Nuclear Instruments and Methods in Physics Research Section A: Accelerators, Spectrometers, Detectors and Associated Equipment, 2013. **732**(Supplement C): p. 237-240.
35. Giomataris, Y., et al., *MICROMEGAS: a high-granularity position-sensitive gaseous detector for high particle-flux environments*. Nuclear Instruments and Methods in Physics Research Section A: Accelerators, Spectrometers, Detectors and Associated Equipment, 1996. **376**(1): p. 29-35.
36. Ligtenberg, C., et al., *Performance of a GridPix detector based on the Timepix3 chip*. Nuclear Instruments and Methods in Physics Research Section A: Accelerators, Spectrometers, Detectors and Associated Equipment, 2018. **908**: p. 18-23.
37. Bilevych, Y., et al. *New results from GridPix detectors*. in *Nuclear Science Symposium Conference Record, 2008. NSS'08. IEEE*. 2008. IEEE.
38. van der Graaf, H., *GridPix: An integrated readout system for gaseous detectors with a pixel chip as anode*. Nuclear Instruments and Methods in Physics Research Section A: Accelerators, Spectrometers, Detectors and Associated Equipment, 2007. **580**(2): p. 1023-1026.
39. Baibussinov, B., et al., *Free electron lifetime achievements in liquid Argon imaging TPC*. Journal of Instrumentation, 2010. **5**(03): p. P03005.
40. Wolverson, M., *Muons for peace*, in *Scientific American*. 2007, NPG publishing. p. 26-28.
41. Biagi, S.F., *Monte Carlo simulation of electron drift and diffusion in counting gases under the influence of electric and magnetic fields*. Nuclear Instruments and Methods in Physics Research Section A: Accelerators, Spectrometers, Detectors and Associated Equipment, 1999. **421**(1): p. 234-240.
42. Ziegler, J.F., et al., *SRIM - The stopping and range of ions in matter (2010)*. Nuclear Instruments & Methods in Physics Research Section B-Beam Interactions with Materials and Atoms, 2010. **268**(11-12): p. 1818-1823.
43. Ziegler J.F., B.J.P., *The Stopping and Range of Ions in Matter*. 1985, Boston, MA: Springer.
44. Wilson, W.D., et al., *Calculations of nuclear stopping, ranges, and straggling in the low-energy region*. Physical Review B, 1977. **15**(5): p. 2458-2468.
45. Koehler, A., et al., *Range modulators for protons and heavy ions*. Nuclear Instruments and Methods, 1975. **131**(3): p. 437-440.
46. Downing, R., *NIST Neutron Depth Profiling Facility: 2013*. Vol. 109. 2013.

47. Shi, C., et al., *Inverse iteration algorithm for neutron depth profiling*. Journal of Radioanalytical and Nuclear Chemistry, 2018. **317**(1): p. 81-85.
48. Çetiner, S.M., et al., *Development and applications of time-of-flight neutron depth profiling (TOF-NDP)*. Journal of Radioanalytical and Nuclear Chemistry, 2008. **276**(3): p. 623.
49. Nagpure, S.C., et al., *Neutron depth profiling of Li-ion cell electrodes with a gas-controlled environment*. Journal of Power Sources, 2014. **248**: p. 489-497.
50. Wetjen, M., et al., *Quantifying the Distribution of Electrolyte Decomposition Products in Silicon-Graphite Electrodes by Neutron Depth Profiling*. Journal of The Electrochemical Society, 2018. **165**(10): p. A2340-A2348.
51. Kopecky, J., *Atlas of neutron capture crosssections*. 1997, IAEA NUCLEAR DATA SECTION: VIENNA.
52. Laermer, F., et al., *Chapter 21 - Deep Reactive Ion Etching*, in *Handbook of Silicon Based MEMS Materials and Technologies (Second Edition)*, M. Tilli, et al., Editors. 2015, William Andrew Publishing: Boston. p. 444-469.
53. Gähler, R., et al., *Space-time description of neutron spin echo spectrometry*. Physica B: Condensed Matter, 1996. **229**(1): p. 1-17.
54. Cabana, J., et al., *Beyond Intercalation-Based Li-Ion Batteries: The State of the Art and Challenges of Electrode Materials Reacting Through Conversion Reactions*. Advanced Materials, 2010. **22**(35): p. E170-E192.

A.

Appendices & Other

A. Activation of elements of possible interest in battery research

All the elements without red marked disadvantages as given in the periodic table of light elements are listed below. Activation was calculated using the free NIST activation calculator. 1 mol of every element (natural abundance of isotopes) was used, exposure time was 24h to 10^8 #n/s, 1Bq equals 1 disintegration per second, b=beta, p=proton. This table can be used for a first screening. Any new set-up should always be analysed with the aid of the technical staff and the program BERAKT.

Element	reaction	product	Half life	0 hrs [MBq]	30 min [MBq]	1 hr [MBq]
Li-6	n,a	H-3	12.346 y	7.55E+04	7.55E+04	7.55E+04
Li-7	act	Li-8	0.844 s	2.51E+05	2.51E+05	
B-11	act	B-12	0.0203 s	2.60E+04	2.60E+04	
N-15	act	N-16	7.14 s	9.72E-01	9.72E-01	
O-18	act	O-19	27.1 s	1.76E+00	1.76E+00	
F-19	act	F-20	11 s	5.78E+04	5.78E+04	
Na-23	act	Na-24	15.03 h	2.14E+06	2.14E+06	2.04E+06
Na-23	act	Na-24m+	0.02 s	2.41E+06	2.41E+06	
Mg-26	act	Mg-27	9.46 m	2.17E+04	2.17E+04	2.67E+02
Al-27	act	Al-28	2.246 m	1.40E+06	1.40E+06	
Si-30	act	Si-31	2.62 h	1.87E+04	1.87E+04	1.43E+04
P-31	act	P-32	14.3 d	4.90E+04	4.90E+04	4.89E+04
S-33	n,p	P-33	25.3 d	2.37E+00	2.37E+00	2.37E+00
S-34	act	S-35	87.2 d	4.53E+02	4.53E+02	4.53E+02
S-36	act	S-37	5.1 m	1.21E+02	1.21E+02	
Cl-35	act	Cl-36	300000 y	1.28E+00	1.28E+00	1.28E+00
Cl-35	n,a	P-32	14.3 d	1.75E+01	1.75E+01	1.75E+01
Cl-35	n,p	S-35	87.2 d	1.79E+04	1.79E+04	1.79E+04
Cl-37	act	Cl-38	37.18 m	5.91E+05	5.91E+05	1.93E+05
Cl-37	act	Cl-38m+	1 s	6.57E+04	6.57E+04	
K-41	act	K-42	12.36 h	4.16E+05	4.16E+05	3.93E+05
Ca-40	n,a	Ar-37	34.8 d	2.88E+02	2.88E+02	2.88E+02
Ca-44	act	Ca-45	165 d	4.21E+02	4.21E+02	4.21E+02
Ca-46	act	Ca-47*	4.54 d	1.65E+01	1.65E+01	1.64E+01
Ca-48	act	Ca-49t	8.72 m	1.04E+04	1.04E+04	8.84E+01
Ca-48	b	Sc-49	57.3 m	1.04E+04	1.04E+04	5.04E+03

Element	reaction	product	Half life	0 hrs [MBq]	30 min [MBq]	1 hr [MBq]
Ti-50	act	Ti-51	5.8 m	5.47E+04	5.47E+04	4.21E+01
V-51	act	V-52	3.75 m	2.96E+07	2.96E+07	4.51E+02
Cr-50	act	Cr-51	27.7 d	1.07E+05	1.07E+05	1.07E+05
Cr-54	act	Cr-55	3.6 m	4.93E+04	4.93E+04	4.74E-01
Mn-55	act	Mn-56	2.58 h	7.99E+07	7.99E+07	6.11E+07
Fe-54	act	Fe-55	2.7 y	5.71E+02	5.71E+02	5.71E+02
Fe-58	act	Fe-59	44.6 d	3.55E+02	3.55E+02	3.55E+02
Co-59	act	Co-60	5.272 y	8.11E+04	8.11E+04	8.11E+04
Co-59	act	Co-60m+	10.5 m	1.13E+08	1.13E+08	2.15E+06
Zn-64	act	Zn-65	265 d	5.98E+03	5.98E+03	5.97E+03
Zn-68	act	Zn-69	56 m	1.08E+06	1.08E+06	5.13E+05
Zn-68	act	Zn-69ms	13.9 h	5.41E+04	5.41E+04	5.15E+04
Zn-70	act	Zn-71	2.4 m	2.90E+03	2.90E+03	
Zn-70	act	Zn-71m	3.9 h	2.99E+02	2.99E+02	2.51E+02
Br-79	act	Br-80	18 m	2.66E+07	2.66E+07	2.63E+06
Br-79	act	Br-80m*	4.42 h	7.24E+06	7.24E+06	6.19E+06
Br-81	act	Br-82	35.34 h	2.97E+06	2.97E+06	2.91E+06
Br-81	act	Br-82m+	6.1 m	7.12E+06	7.12E+06	7.79E+03
Sn-112	act	Sn-113	115 d	3.76E+02	3.76E+02	3.76E+02
Sn-112	act	Sn-113m+	20 m	1.91E+04	1.91E+04	2.39E+03
Sn-116	act	Sn-117m	14 d	2.57E+02	2.57E+02	2.57E+02
Sn-118	act	Sn-119m	245 d	4.13E+01	4.13E+01	4.12E+01
Sn-120	act	Sn-121	27 h	1.26E+05	1.26E+05	1.23E+05
Sn-122	act	Sn-123	129.2 d	2.65E+02	2.65E+02	2.65E+02
Sn-122	act	Sn-123m	40.1 m	2.75E+02	2.75E+02	9.76E+01
Sn-124	b	Sb-125	2.76 y	3.05E+01	3.05E+01	3.05E+01
Sn-124	act	Sn-125m	9.5 m	4.35E+04	4.35E+04	5.46E+02
Sn-124	act	Sn-125t	9.64 d	9.28E+01	9.28E+01	9.25E+01
I-127	act	I-128	24.99 m	3.73E+07	3.73E+07	7.06E+06

B. Isotopes for NDP

This is a copy of table 1.1

Table 2.1.3.i List of capture reactions relevant for NDP. Energies in keV are found within the brackets, all neutron capture cross sections are in barns and protons are abbreviated with p. Adapted from [1] and [2].

Element	%Abundance	Particles (Energies)	Cross section [barns]
³ He	0.00014	p (572) + ³ H(191)	5333
⁶ Li	7.5	3H(2727) + ⁴ He(2055)	940
⁷ Be	Radioactive	p(1438) + ⁷ Li (207)	48000
¹⁰ B	19.9	⁴ He(1472) + ⁷ Li(840) + γ [93.7%]	3837
		⁴ He(1777) + ⁷ Li(1013) [6.3%]	
¹⁴ N	99.6	¹⁴ C(42) + p (584)	1.83
¹⁷ O	0.038	¹⁴ C(404) + ⁴ He(1413)	0.24
²² Na	Radioactive	²² Ne(103) + p (2247)	31000
³³ S	0.75	³⁰ Si(411) + ⁴ He (3081)	0.19
³⁵ Cl	75.8	³⁵ S(17) + p (598)	0.49
⁴⁰ K	0.012	⁴⁰ Ar(56) + p (2231)	4.4
⁵⁹ Ni	Radioactive	⁵⁶ Fe(340) + ⁴ He(4757)	12.3

C. Data Handling

This is a description of the method available. The scripts are in a work in progress state and are by no means plug and play. Chapter 2 describes the physical reasons behind the practical steps detailed here. In the 'information and matlab scripts' folder located where the data is stored all the necessary programs are to be found as well as some older stuff, which could be relevant as a source of inspiration in more desperate times. Data handling consists of three parts, conversion from energy to depth, the standard deviation in intensity (the measurement is a Poisson distribution) and subtracting the background (normalization with respect to charged and discharged states). However first the data needs to be imported. Data can be imported from the comma separated files, however reading these one by one is time consuming. Hence users are advised to use the `ndp info` program as described in C1. After importing the data, the main line program '`...dataprocessing.m`' can be started. This program employs some nested functions (=other programs), to quickly perform sub steps and some databases which contain information on the stopping power and energy lost in the window (both obtained using SRIM/TRIM) and so on. The idea would be to adapt the mainline script to your experiment, i.e. operando/ in-situ/ ex-situ or thin layer type whilst employing the same sub steps.

C.1. Data import

To read the channel files produced, `NDPinfo` is available. `NDPinfo` is a simple program to view and convert channel data today the program is not strictly necessary but for a first view of the data it is practical. Simply run the program and click file list and 'add files' to add the desired files.

To convert click Actions and send it to the clipboard and paste in excel.

This automatically normalizes the counts to the monitor, currently 1 monitor count is 66 counts, as set in `NDPinfo`. Clicking Actions and then Sum CHN and convert: Sums the channels of the specified CHN files. This can be practical when a sample is measured multiple times. After pasting specify the number of data columns in the cell 'B2', close and save the file in your matlab directory.

Next generation NDP

Open matlab.

Use the **importxfile** script to convert data to an matlab database. Make sure the third line in the scripts corresponds to correct folder i.e. path='D:\twverhallen\My Documents\Zwavelshizzle\matlab\'. Probably does not exist on your computer.

Next call the script, to do so paste the following lines in the command window.

```
workbookFile= '...' %fill in name of your excel file
```

```
sheets=[...] %can be 1 for sheet1 or 2 for sheet2 or [1 2] for both (yes some people record so much data it does not fit one excel sheet)
```

```
savename='...' % fill the name of file you would like to create
```

```
[AllData,TimeLive,Time] = importxfile(workbookFile,sheets,savename)
```

The merit of this method is that is now made available for matlab in a consistent manner. Next make sure the stopping powers and window data are correct for your set-up. We use SRIM for this.

C.2. TRIM/SRIM Manual

In the matlab scripts developed input from the SRIM software is needed. This input is stored in a database, which is opened at start of the program. Called 'HinBatMat'. Separate from the raw data, for which a different routine is developed, described in the previous appendix. Although these first two steps can be performed in reverse order.

Install the software.

It comes in two versions 2008 and 2013, some devices do not have certain configuration file needed to operate version 2013. Computationally there are no differences.

Click SRIM.

The software package provides two functions first are the Stopping and Range tables, provide a table containing particle energy, stopping power, straggling and range, and is based on a direct calculation, second there is the availability to run monte carlo simulations (TRIM), both use effective electrons densities able the account electrons in molecular bonds when these are specified in the COMPOUND.dat. You can add your materials yourself when you follow the instructions at the top of the file, for polar solvents this is highly advisable as differences can be as big as 20% reflected in the correction factor. In present set of matlab instructions we use both functionalities. The TRIM part is used to determine the input for the 'ExtraLayer' matrix which accounts for the energy lost in the (copper/aluminum) current collector or window. When analyzing ex-situ data this is not necessary, the functionality can be avoided by changing the 'extralayer' matrix to one with two equal vectors. Finding the input for Extralayer matrix or determining the degree of straggling for different gasses, as shown in the **Figure** in chapter 6 is done as follows.

The starting window will open. Click 'TRIM' the window shown in **Figure C.1** opens.

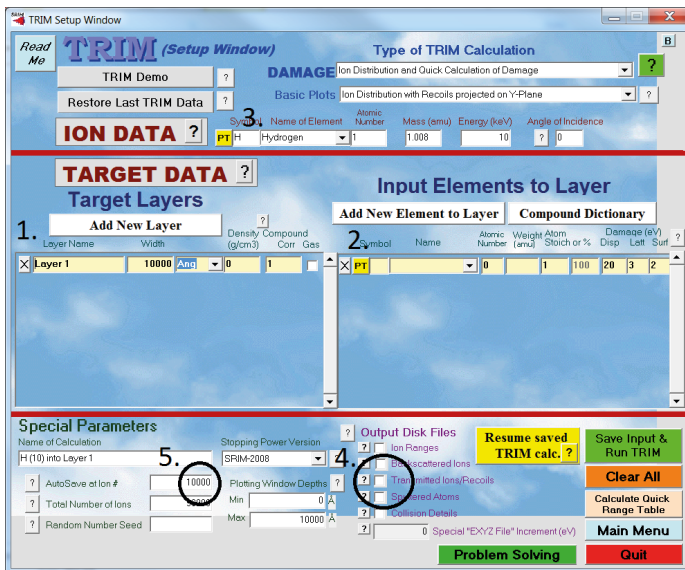


Figure C.1. Starting menu of TRIM

Next generation NDP

1. First specify a layer name, ions will encounter the layers from top to bottom.
2. Specify elements in the layer and the correct stoichiometry. Srim will calculate a density based on the elements given, this calculation is correct only for the pure metal or when a Compound is used from the program database. Hence it usually needs to be changed in step 1.
3. Now specify the ion you wish to investigate, initial kinetic energies can be found in Appendix A. Ensure to give the correct atomic weight, i.e. 3H is 3 amu
4. Check the transmitted ions box, this will allow to find energy after passing through the layers.
5. Give the number ions you want to calculate at AutoSave after.
6. Now click Save Input and Run TRIM.

Now a new window will show

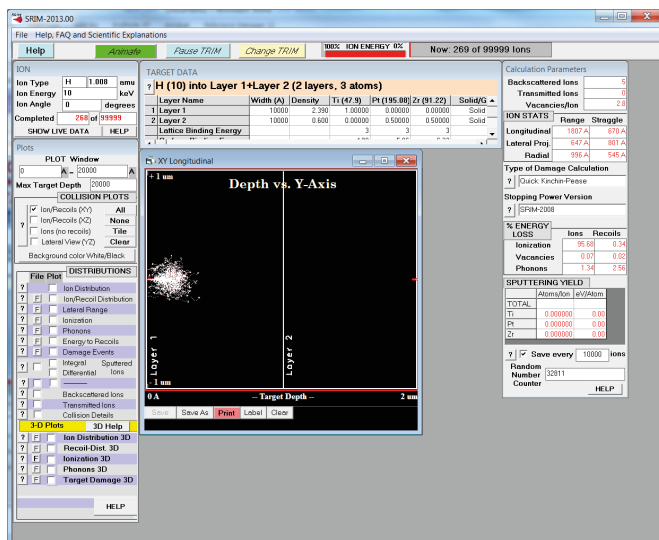


Figure C.2. TRIM calculation in action.

Make sure that the ions are transmitted, note that in the **Figure** this is NOT the case (the ion energy is too low), the white lines should cross the black



layers. Let program run until the number of ions is reached, then click pause TRIM in the top menu. The data is now stored in a file called TRANSMIT.txt.

In this file the forth column contains the particle energies after transmission. The mean allows the determination of energy lost through these layers and the variance reflects straggling. Using the matlab script 'EAverage.m' the average is easily calculated. Store this value somewhere, Excell or Matlab, and go back to TRIM.

click 'Change TRIM' Change the particle energy and run simulation again. Be sure the new calculation is stored in a new file!

The two columns E_{in} and E_{out} are used in the program in the matrix named 'ExtraLayer'. Alternatively the layer thickness is changed by clicking 'Change TRIM' give a new layer thickness and restart the calculation. Repeat this process a number of times. Now fit the resulting depth vs energy curve with a third degree polynomial. The coefficients of this curve is then used in other Matlab scripts. This method, used in Zhang et al.[5], results in a nonlinear depth axis and requires a correction of counts. The method described in Chapter 2 does result in a linear depth axis, but makes use of a table found with the Stopping and range tables part.

Start SRIM, click Stopping and range tables.



Figure C.3 SRIM input window. Add your elements or compounds. Be sure to use: the correct density, weight of the particle and units [keV/micron].

A table containing the stopping power values is made by clicking 'stopping and range tables' in opening dialogue of SRIM. Here the ion type and mass should be specified and the elements in the layer. Compounds with covalent bonds, such as the electrolyte, should be added in the compound.dat file, the program can then calculate a compound correction factor which reflects electrons associated in a bond. The resulting table shows the stopping power due to electrons as well as due to atom cores the contributions are independent and thus can be summed. The same holds for mixtures, the stopping powers of the different components can be added according to their volume ratios.

Output is a table with stopping powers (core and electrons), range and straggling as a function of particle energy. Currently only the sum of the stopping powers vs energy is used. Store as a matrix in the your general

database. Presently named 'HinBatMat'. As the stopping power is independent of the material surrounding the equation in chapter 2 can be used to add the various components of your electrode and electrolyte according to their volume ratios. This is a significant advantage over the method presented by Zhang et al. Also it allows the program to calculate the ratio electrode electrolyte in situ as detailed in chapter 2.

C.3. The mainline script.

Here we will quickly discuss the mainline script and the role of the different nested functions. The first part deals with loading the previously stored data and calculated stopping powers. Again make sure the path string (in purple) is correct. Next some constants are loaded. Give the sample size. After which the various components are assigned. Here we make the total stopping power according to the volume ratios of the separate components;

$$S_t = \sum_{i=1}^n v_i \cdot S_i \quad (C.1)$$

Next the 'stepsize' is specified. The channel width is 3.3keV, typical stopping powers are in the order of 30 keV/micron, hence choose a value above 0.1 micron, to avoid a false sense of accuracy.

Before energy is converted to depth, the data is converted back to integer counts, the originally obtained. 'makenorm' performs this feat through multiplication with the smallest measured value inversed. The values found are stored in NormVec and the converted data in NormMat.

Energy to depth conversion is done in 'NonLinInt_n', yielding 'outputdata'. This matrix contains integer data and is used to find the standard deviation. This is a measure for accuracy in the y direction. Deviation in depth interpretation (x), due to straggling, detector inaccuracy and geometrical errors are not yet incorporated.

This data is renormalized in 'DeNorm' function. Next 'Findminandmax' is used for recognition of the charged and discharged state, which are used for normalization. This outcome is also plotted. There should be sufficient differences between the two. In the last part of the script one can chose to subtract the chargedstate or normalize. This function is called 'makeSoc'.

Next generation NDP

Using the 'mode' parameter the type normalization can be set, i.e. 0 for subtracting the charged (empty) state only or 1 to normalize to the discharged state as well. This was for instance done in section 2.2.3, while in chapter 5 only the charged state was subtracted.

In the very last section a Poisson distribution based error is calculated. This reflects the error in counts and can be useful to assess whether an acceptable signal to noise ratio is reached when subtracting a background signal. Again errors in energy are not taken into account, this could be done for instance by using an iterative deconvolution algorithm.

Text in bold refers to Matlab scripts found in;

`\tnw\rrrrid\rrr\Fame\NDP\Data\Information&matlab scripts\Datahandling scripts`

D. Supporting Information to Chapter 3

Electrode preparation

The LiFePO₄ cathodes were prepared by thoroughly mixing carbon coated LiFePO₄ (140 nm, Phostech) powder with PVDF (Aldrich), and Super P carbon black (TIMCAL) in a 90:5:5 weight ratio using NMP as solvent with a solid to solvent mass ratio of 1:3. For templated electrodes approximately 40 wt% NaHCO₃ (Aldrich) is added to the electrode slurry. First, the bicarbonate salt was stirred in NMP solvent forming a sodium carbonate suspension. Later 5 wt% PVDF was added into the NMP and NaHCO₃ suspension. Once the PVDF was dissolved, the carbon coated LiFePO₄ and the carbon (black Super P) were added and thoroughly mixed. The resulting slurry was casted using different doctor blade thicknesses onto carbon coated aluminum foil. The electrodes are dried at 50 °C for 48 to 72 hours in a vacuum oven to evaporate the NMP. To enhance good electronic contact between active materials and carbon black the dried electrodes are mechanically compressed using a roller hand press leading to approximately 60% increase of the compaction of all electrodes. After mechanical compaction the NaHCO₃ templated electrodes are washed with demineralized water which reacts with the NaHCO₃ towards water soluble NaOH and gaseous CO₂, resulting in a compacted but porous electrode. The gas formation is visible as tiny gas bubbles evolving at the electrode surface. After washing the electrodes were dried for few hours in vacuum oven. Further details can be found in a prior publication[3].

Battery Preparation and Testing

Battery cells were assembled in vacuum flange type electrochemical cells under argon atmosphere (< 0.1 ppm O₂ / H₂O). Lithium metal was used as anode and glass fiber disks (Whatman) as separators. The electrolyte used was 1.0 Molar LiPF₆ in EC/DMC (ethylene carbonate and dimethyl carbonate in a 1:1 volume ratio) (Novolyte, battery grade). The cells were tested at variable charge rate between C/20 up to 20 C within a voltage window of 4.3 and 2.5 V vs Li/Li⁺ using a Maccor battery cycler. For the NDP measurements, both standard and templated electrodes were disassembled from the test

cells and thoroughly washed using DMC (dimethyl carbonate) solvent to remove the residual lithium salt and organic impurities.

FIB-SEM Sample Preparation and Tomography

Three-phase 3D reconstruction was performed on both a templated electrode processed via NaHCO_3 templating and a pristine electrode processed via conventional method (referred to as compacted electrode in the following text). A commercial two-part silicone resin (ELASOSIL RT 604, Wacker, Germany) was infiltrated into the electrode cavities (the porous electrode is filled with electrolyte when sealed as a battery) to provide image contrast between the infiltrated porosity and the present carbonaceous materials (carbon and binder). The resin infiltrated sample was then cured for 24 hours at room temperature and cut in to cuboid shape. A triple ion-beam cutter (Leica EM TIC 3X) was employed for sample polishing, **Figure D.1a**), to obtain a smooth top surface in order to minimize curtain effects for FIB milling. For a typical polishing process, the ion guns were operated at 4 KV accelerating voltage with 2 mA ion current for 8 hours polishing. Finally, a ~ 30 nm osmium coating was deposited on the sample to minimize charging effects during the following FIB-SEM data collection. An FEI Helios FIB-SEM (FEI Company, OR, USA) was employed for the 3D data collection. As shown in **Figure D.1 b**), a “U” shape trench was milled to expose sample volume for FIB slicing and SEM imaging. The coordinate system shown in the **Figure D.1 b**) provides spatial information of the 3D volume and its location relative to the current collector and separator, necessary for performing directional connectivity and tortuosity. The Z direction is the FIB slicing direction, while XY plane is for SEM image collection. Moreover, the current collector is adjacent to the right YZ plane of the 3D data set. Backscattered electron signal is collected using through-the-lens detector (TLD) detector for imaging. Considering the feature size of interest, the pixel size of the SEM images was chosen as 15.6 nm and the slice thickness as 20 nm. A total of 321 consecutive images were collected for each template and compacted sample for following 3D reconstruction.

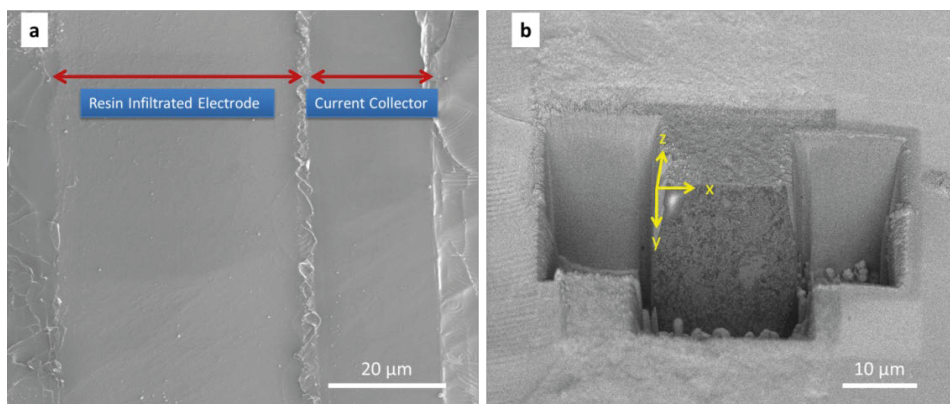


Figure D.1. a) SEM image of the polished LiFePO_4 electrode sample top surface. b) A “U” shape trench milled on the electrode. The coordinate system is also shown to indicate the FIB slicing direction (z) and SEM image collection plane (x-y plane).

Neutron Depth Profiling

SRIM[4] was used to calculate the energy loss of the ^3H particles originating at different depths in the electrode. A third order polynomial was fitted on these results to yield a calibration relation between the energy of the tritons and the depth of the capture reaction. From the depth dependent energy loss of the tritons that was determined with SRIM the energy dependent stopping power of the electrode system (LiFePO_4 coating) was determined by fitting a third order polynomial on the with SRIM calculated values. The ^3H spectra reported in the manuscript are converted using the fully charged and fully discharged states as background and reference states. By subtracting the fully (C/50) charged state spectrum ($\text{Li}_{x=0}\text{FePO}_4$), shown in **Figure D.2**, from all the spectra the background is eliminated and by normalizing on the fully discharged state ($\text{Li}_{x=1}\text{FePO}_4$) the average Li composition is obtained. Because the ^3H and ^4He spectra overlap, as shown in chapter 2, these need to be separated to reflect the Li-ion concentration. This can be achieved by making use of the large difference in stopping power, being much larger for the ^4He ions as demonstrated in Figure D. In combination with the depth calibration and stopping power correction this results in the Li-ion concentration profiles as a function of the electrode depth.

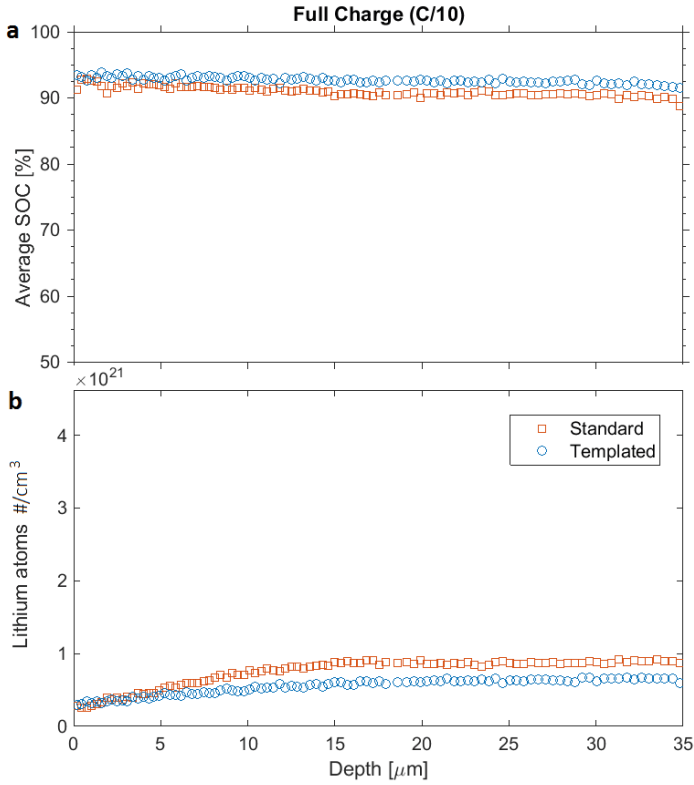


Figure D.2 Fully charged electrodes after C/10. **a)** Percentage of the state of charge compared to the pristine state, indicating 9.7% inactive LiFePO_4 for the standard and 7.8% for the templated electrode. **b)** Measured Lithium concentration showing the concentration drop at 0 micron, defining the end of the electrode, the interface with the electrolyte.

E. Deactivation of the Matroesjka

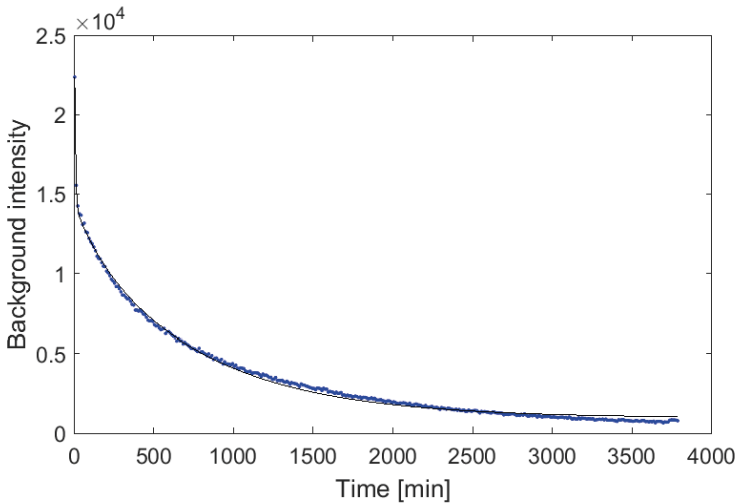


Figure E.1. Radioactive decay of neutron activated isotopes in the Matroesjka containing a pouch battery cell with copper current collectors as measured by the silicon detector.

Fit, black line, was build up from a series of exponential functions, which reflect the decay of the activated isotopes. According to;

$$f(t) = A_1 e^{-t/t_{1/2}} + A_2 e^{-t/t_{1/2}} + A_3 e^{-t/t_{1/2}} + A_4 e^{-t/t_{1/2}} \quad (\text{E.1})$$

Where the recorded activities are fitting parameters.

Isotope	Origin	Half life	Constants (A)
Al-27	Current collector, Matroesjka, Pouch material	2.3 min	$<10^{-6}$
Cu-63	Current collector	5.5 m	$2 \cdot 10^4$
Cu-65	Current collector	12.7 h	$1.2 \cdot 10^4$
Mn-55	Matroesjka	2.58 h	$1.9 \cdot 10^3$

F. Selected SLDs

Table F.1 Scattering length densities of materials and notes, relevant for lithium ion battery research, NIST activation calculator.

Material	SLD [10^{-6} A]	Notes
Li	-0.874	SLD increases with ^6Li content, however absorption reduces signal!
^7Li	-1.01	
^6Li	0.927	
Separators		
Celgard (C_3H_6) _n	-0.322	Reducing H content is beneficial for contrast vs Li.
Solupor ($\text{C}_2\text{F}_2\text{H}_2$) _n	3.221	
Teflon (C_2F_4) _n	4.8	
Solvents		
DMC, $\text{OC}(\text{OCH}_3)_2$	5.189	For solvents the same is true, however fluorinated solvents have different chemical properties, deuteration may be preferable, but is expensive.
DMC, $\text{OC}(\text{OCD}_3)_2$	1.067	
EC, $(\text{CD}_2\text{O})_2\text{CO}$	5.53	
EC, $(\text{CH}_2\text{O})_2\text{CO}$	2.022	
Salts		
LiPF_6	2.209	Salt with high SLD could be used to increase contrast vs Li, and match separator/solvent
LiNO_3	5.171	
LiTFSi	2.332	

References

1. Downing, R.G., et al., *Neutron Depth Profiling: Overview and Description of NIST Facilities*. Journal of Research of the National Institute of Standards and Technology, 1993. **98**(1): p. 109-126.
2. Shi, C., et al., *Inverse iteration algorithm for neutron depth profiling*. Journal of Radioanalytical and Nuclear Chemistry, 2018. **317**(1): p. 81-85.
3. Singh, D.P., et al., *Facile Micro Templating LiFePO₄ Electrodes for High Performance Li-Ion Batteries*. Advanced Energy Materials, 2013. **3**(5): p. 572-578.
4. Ziegler, J.F., M.D. Ziegler, and J.P. Biersack, Nucl. Instrum. Methods B, 2010. **268**: p. 1818-1823.
5. Zhang, X.Y., et al., *Direct Observation of Li-Ion Transport in Electrodes under Nonequilibrium Conditions Using Neutron Depth Profiling*. Advanced Energy Materials, 2015. **5**(15): p. 1500498.

Dankwoord

Nu wil ik graag aantal mensen bedanken, allereerst natuurlijk Marnix, voor de kans om een dit traject in te gaan, maar ook voor je 'zeg nooit nee' houding waardoor ik zoveel verschillende projecten heb kunnen doen. In adem door moet ik ook Erik noemen, zonder wie ik Marnix niet had leren kennen en ik niet verslingerd was geraakt aan Li-ion batterijen. En Fokko natuurlijk, die er mede voor gezorgd heeft dat er Delft überhaupt 'geNDPt' wordt en onder andere hoofdstuk 5 uiteindelijk is gerealiseerd. Ook Harry ben ik het een en ander verschuldigd, zonder hem geen 3D-NP!

Maar om de dag door te komen was het wellicht belangrijker dat er tegelijkertijd met mij 4 fantastische collega's starten, Niek, Zhaolong, Alexandros en Peter-Paul. Vier uitersten, qua mens en achtergrond, maar met ieder van jullie had ik super interessante discussies over elektrochemica en batterijen als geheel. En over het leven of je ouders, je vriendin, je bier of je CV (ketel). Naast deze kern waren er natuurlijk nog veel meer mensen belangrijk voor een goede werksfeer; Martijn, Violetta, Remco, Swapna, Yaolin, Michi, ik heb heel veel gelachen en zonder jullie hadden de afgelopen vier jaar er heel anders uit gezien. Nu dient zich alweer een volgende generatie aan, het is goed om te zien dat de druk van het veld jullie niet uit het veld slaat! Het kan ook bijna niet anders, met zo'n groot fan van team uitjes als Marnix aan het hoofd, dan wordt het zeker een interessante ervaring worden! Ik moet zeggen dat ik stiekem jaloers op jullie ben, zoveel tijd en ruimte voor leuke experimenten nog voor je!

Na zo'n dag is thuis komen natuurlijk super fijn, zeker aangezien Anna daar ook woont! Zonder haar had dit boekje er heel anders uitgezien en was het vast niet zo'n stress-vrije periode geweest. Ook mijn ouders en familie wil ik bedanken, zonder jullie trots en steun was ik nooit zo vrij geweest om zo lang te blijven studeren. Daarnaast was ik altijd omringd door zeer hechte vrienden groepen; de Boyzz, The 4ce en Dons&Staal, het was geniaal.

Van dit boekje was heel weinig terecht gekomen als er niet zoveel ondersteuning was van de collega's op het RID. Doordat iedereen bereid is



om te luisteren en te fantaseren komen er iedere dag weer nieuwe, interessante projecten van de grond. Deze omgeving is bijzonder waardevol en zal ik op zeker moment enorm gaan missen. Wim, Steven en Chris, bedankt voor jullie hulp met de SANS/SESANS experimenten! En Zhou Zhou en Lambert, laten we hopen dat de Gridpix experimenten ergens toe leiden, voor nu hebben we in ieder geval lol gehad en veel geleerd. Michel, Frans en Martin zonder jullie hulp bij het ontwerpen en onderhouden van alle opstellingen en monster voorbereidingen was er zekerste weten niet zoveel gemeten!

Acknowledgements

Now I would like to give a big shout out to some people that helped realize this amazing book. First and foremost, there is Marnix, without his 'can do'/'never say so' approach I would have started so many different projects! Thanks to Erik for getting me hooked on batteries and introducing me to Marnix. Next I would like thank Fokko, initializing NDP on batteries in Delft and his contribution to chapter 5. Also Harry has been an important driver behind the 3D NP project (chapter 6), for which I am very grateful.

Besides these pillars I was lucky enough to start at the same time with four amazing colleagues Niek, Zhaolong, Alexandros and Peter-Paul, you really helped me get through the day. Four extremes, in terms of people and background, but with each of you I had super interesting discussions about electrochemistry or the equation editor in word, life or your parents, your girlfriend, your beer or your CV (boiler). In addition to this omnipresent 'core', their many more people were important for a good working atmosphere; Martijn, Violetta, Remco, Swapna, Yaolin, Michi, I laughed a lot and without you, the last four years would have looked very different. Now a new generation is starting, it is good to see that the pressure from the field does not restrain you! It can hardly be otherwise, with such a team-outings fan as Marnix at the head, it surely an interesting experience! I must say that I am secretly jealous of you, so much time and space for fun experiments ahead!

After such a day, it is nice to be home, especially since Anna also lives there! Without her, this book would have looked very different and it would probably not have been such a stress-free period. I would also like to thank my parents and family, without your pride and support I would never have been free to continue studying for so long. In addition, I was always surrounded by very close groups of friends; the Boyzz, The 4ce and Dons & Staal, this is amazing and I consider myself to be very lucky!

Very little of this booklet would have been finished if there wasn't as much support from the colleagues at the RID. Because everyone is willing to listen and to fantasize, new, interesting projects are started every day. This



environment is precious and I will miss it enormously at some point. Wim, Steven and Chris, thank you for your help in the SESANS/SANS experiments, hopefully this will one day lead to something! The same holds for cultural heritage project with Zhou Zhou and Lambert, so far we have had an interesting and fun number of experiments. Michel, Frans and Martin without your help in the design and maintenance of all setups and sample preparations, there were certainly not as much measured!

Publications

- 2015 Xiaoyu Zhang, **Tomas W. Verhallen**, Freek Labohm and Marnix Wagemaker; Direct Observation of Li-Ion Transport in Electrodes under Non-equilibrium Conditions Using Neutron Depth Profiling, *Advanced Energy Materials*, (2015) (Cover article) DOI: 10.1002/aenm.201500498
- 2016 **Tomas W. Verhallen**, Zhao Liu, Deepak P. Singh, Hongqian Wang, Marnix Wagemaker, Scott Barnett; Relating the 3D electrode morphology to Li-ion battery performance; a case for LiFePO₄, *Journal of Power Sources*, 324, (2016) p358–367 DOI: 10.1016/j.jpowsour.2016.05.097
- 2017 Peter Paul R. M. L. Harks, Carla B. Robledo, **Tomas W. Verhallen**, Peter H. L. Notten, Fokko M. Mulder; The Significance of Elemental Sulfur Dissolution in Liquid Electrolyte Lithium Sulfur Batteries; *Advanced Energy Materials*, (2017) p1601-1635. DOI: 10.1002/aenm.201601635
- 2018 Shasha Lv, **Tomas Verhallen**, Alexandros Vasileiadis, Frans Ooms, Yaolin Xu, Zhaolong Li, Zhengcao Li and Marnix Wagemaker; Operando monitoring the Lithium spatial distribution of Li-metal anodes; *Nature Communications*, volume 9, (2018)
- 2018 **Tomas Verhallen**, Shasha Lv, Marnix Wagemaker; Operando Neutron Depth Profiling to Determine the Spatial Distribution of Li in Li-ion Batteries; *Front. Energy Res.*, 03 July 2018 | <https://doi.org/10.3389/fenrg.2018.00062>
- 2019 Alexander Ledovskikh, **Tomas Verhallen**, Marnix Wagemaker, The non-ohmic nature of intercalation materials and the consequences for charge transport limitations, *Energy Storage Materials Journal*, March 2018, 10.1016/j.ensm.2019.01.006
- 2019 D. M. Cunha, T. A. Hendriks, A. Vasileiadis, C. M. Vos, **T. Verhallen**, D. P. Singh, M. Wagemaker, M. Huijben, Doubling Reversible Capacities in Epitaxial Li₄Ti₅O₁₂ Thin Film Anodes for Microbatteries; *ACS Applied Energy Materials* 2019.
- 2019 Liu, Ming; Cheng, Zhu; Qian, Kun; **Verhallen, Tomas**; Wang, Chao; Wagemaker, Marnix, Efficient Li-metal plating/stripping in carbonate electrolytes by a combined gel polymer and LiNO₃ electrolyte approach, monitored by operando Neutron Depth Profiling, *Chemistry of Materials*. May 2019
- 2019 **Tomas W. Verhallen**, Peter-Paul R.M.L. Harks, Chandramohan George, Fokko M. Mulder and Marnix Wagemaker, Spatio-temporal Quantification of lithium both in Electrode and in Electrolyte with atomic precision via Operando Neutron Absorption, *Advanced Energy Materials*, under review